

CHARACTERIZATION AND DIAGNOSTIC TECHNIQUES FOR
OPTIMIZATION OF WATER MANAGEMENT OF PROTON EXCHANGE
MEMBRANE FUEL CELL

A THESIS SUBMITTED TO
THE GRADUATE SCHOOL OF NATURAL AND APPLIED SCIENCES
OF
MIDDLE EAST TECHNICAL UNIVERSITY

SEVLER GÖKÇE AVCIOĞLU

IN PARTIAL FULFILLMENT OF THE REQUIREMENTS
FOR
THE DEGREE OF DOCTOR OF PHILOSOPHY
IN
CHEMICAL ENGINEERING

SEPTEMBER 2016

Approval of the thesis:

**CHARACTERIZATION AND DIAGNOSTIC TECHNIQUES FOR
OPTIMIZATION OF WATER MANAGEMENT OF PROTON EXCHANGE
MEMBRANE FUEL CELL**

submitted by **SEVLER GÖKÇE AVCIOĞLU** in partial fulfillment of the requirements for the degree of **Doctor of Philosophy in Chemical Engineering Department, Middle East Technical University** by,

Prof. Dr. Gülbin Dural Ünver _____
Dean, Graduate School of **Natural and Applied Sciences**

Prof. Dr. Halil Kalıpçılar _____
Head of Department, **Chemical Engineering**

Prof. Dr. İnci Eroğlu _____
Supervisor, **Chemical Engineering Department, METU**

Asst. Prof. Dr. Berker Fıçıcılar _____
Co-supervisor, **Chemical Engineering Department, OMU**

Examining Committee Members:

Assoc. Prof. Dr. Ayşe Bayrakçeken Yurtcan _____
Chemical Engineering Department, AU

Prof. Dr. İnci Eroğlu _____
Chemical Engineering Department, METU

Assoc. Prof. Dr. Serkan Kınal _____
Chemical Engineering Department, METU

Asst. Prof. Dr. Ramiz Gültekin Akay _____
Chemical Engineering Department, KU

Assoc. Prof. Dr. Görkem Külâh _____
Chemical Engineering Department, METU

Date: 2/09/2016

I hereby declare that all information in this document has been obtained and presented in accordance with academic rules and ethical conduct. I also declare that, as required by these rules and conduct, I have fully cited and referenced all material and results that are not original to this work.

Name, Last Name : SEVLER GÖKÇE AVCIOĞLU

Signature : _____

ABSTRACT

CHARACTERIZATION AND DIAGNOSTIC TECHNIQUES FOR OPTIMIZATION OF WATER MANAGEMENT OF PROTON EXCHANGE MEMBRANE FUEL CELL

Avcıođlu, Gökçe Sevler

Ph.D., Department of Chemical Engineering
Supervisor: Prof. Dr. İnci Erođlu
Co-supervisor: Asst. Prof. Dr. Berker Fıçıcılar

September 2016, 253 pages

Proton exchange membrane fuel cell (PEMFC) is the most promising candidate for transportation, stationary, and portable applications due to low operating temperature, high power density, simple, and modular construction, and quiet operation. For enhanced performance and durability, providing efficient water management in each component of the PEM fuel cell is essential. This study is motivated by the need to develop a water management strategy that facilitates excess water removal from catalyst layer (CL).

Seven different parameters were studied on the scope of this dissertation. The effect of Pt percentage in the commercial catalyst; Pt loading of catalyst layers; membrane electrode assembly (MEA) configurations altering with hydrophobic nanoparticle inclusion in catalyst layers; various hydrophobic nanoparticles; O₂/air as an oxidant in the cathode side was investigated. In the first part, Polytetrafluoroethylene (PTFE) was added to the CL prepared with a commercial catalyst including 20 wt % Pt; in the second and third part, polytetrafluoroethylene (PTFE), fluorinated ethylene propylene (FEP), poly (tetrafluoroethylene-co-

perfluoro propyl vinyl ether) (PFA) were added to catalyst layer prepared with a commercial catalyst including 70 wt. % Pt.

The increase in the Pt percentage of commercial catalyst improves the cell performance. Hydrophobic nanoparticles in the catalyst layers prepared with 20 wt. % Pt/C, enhanced the cell performance above high current densities, indicating improved water management. Created hydrophobic channels through catalyst layers provided two-phase flow. High airflow rate prevents water accumulation in the pores of the gas diffusion layer of the cathode.

Keywords: Proton exchange membrane fuel cells, electrocatalyst, catalyst layer, hydrophobic nanoparticle, water management

ÖZ

PROTON DEĞİŞİM ZARLI YAKIT PİLİNDE SU YÖNETİMİNİN TANILAMA VE KARAKTERİZASYON TEKNİKLERİ İLE OPTİMİZASYONU

Avcıoğlu, Gökçe Sevler

Doktora, Kimya Mühendisliği Bölümü

Tez Yöneticisi: Prof. Dr. İnci Eroğlu

Ortak Tez Yöneticisi: Yard. Doç. Dr. Berker Fıçıcılar

Eylül 2016, 253 sayfa

Proton değişim zarlı (PEM) yakıt pilleri, düşük sıcaklıkta çalışabilmesi, yüksek güç yoğunluğu elde edilebilmesi, basit olması, kolay kullanımı ve sessiz çalışmasından dolayı ulaşımda, yerleşik hayatta ve taşınabilir cihazlarda kullanım için en çok umut vadeden yakıt pilidir. Uzun süre dayanıklılık ve yüksek performans için PEM yakıt pilinin her bir bileşeninde etkili bir su yönetimi sağlamak esastır. Bu çalışma, katalizör tabakasındaki fazla suyun atılmasının kolaylaştırılması için bir su yönetim stratejisinin geliştirilmesine duyulan ihtiyaçtan yola çıkarak gerçekleştirilmiştir.

Bu tez kapsamında yedi ayrı parametre çalışıldı. Ticari katalizör içerisindeki Pt yüklemesinin, katalizör tabakalarındaki Pt yüklemesinin, katalizör tabakalarında hidrofobik nanoparçacık içerme durumuna göre değişen MEA yapısının, farklı hidrofobik nanoparçacıkların, katot tarafında oksitleyici gaz olarak O₂/havanın etkisi incelenmiştir.

Bu çalışmanın ilk bölümünde, kütlece % 20 Pt içeren ticari katalizör ile hazırlanmış katalizör tabakasına, iki basamaklı katalizör hazırlama yöntemi ile

Politetrafuloroetilen (PTFE) eklenmiştir; ikinci ve üçüncü bölümde ise, kütlece % 70 Pt içeren ticari katalizör ile hazırlanmış katalizör tabakasına, Politetrafuloroetilen (PTFE), florlanmış etilen propilen (FEP), poli (tetrafloroetilen-co-perfloropropil vinil eter) (PFA) eklenmiştir.

Ticari katalizördeki Pt yüzdesinin artması hücre performansını arttırmıştır. Düşük Pt yüklü ticari katalizör ile hazırlanmış hidrofobik nanoparçacık içeren katalizör tabakaları hücre performansını yüksek akım yoğunluğunda arttırmıştır. Bu iyileştirilmiş su yönetimini olduğunu gösterir. Katalizör tabakalarında oluşturulan hidrofobik kanallar 2 fazlı akışı sağlamıştır. Yüksek hava akış hızı katot tarafındaki gaz difüzyon tabakasında su birikmesin engel olmuştur.

Anahtar Kelimeler: Proton değişim zarlı yakıt pilleri, elektrokatalizör, katalizör tabakası, hidrofobik nanopartikül, su yönetimi

Dedicated to
Struggle for bringing Peace, Freedom, and Justice to the Middle East

ACKNOWLEDGMENTS

I would like to thank my supervisors Prof. Dr. Inci Eroglu and Asst. Prof. Dr. Berker Ficicilar for their guidance and encouragement. I also would like to thank my supervisors for their patience, respect, supports, advice, kindness, friendship, positive intent, and motivation during my research studies. I would like to thank Dr. Serdar Erkan for his technical help on experimental techniques of fuel cells. I thank Assoc. Prof. Dr. Serkan Kincal, Dr. Assoc. Prof. Ayse Bayrakeceken and Assoc. Prof. Dr. Yilser Devrim for their valuable suggestions and comments.

I thank Turgay for his love, patience, and his respect for my lifestyle. He always supports my dreams and future plans. I also thank my mother, father, brother, aunt and cousins for their endless love, patience, respect, confidence, and being with me all the time. I am there where I want to be, which is related to you (my family). I also thank my mother in law and co-sister in law for their endless patience and support. They added all the years to my education, which they could not spend for their education.

This study was supported by Middle East Technical University Scientific Research Found Projects (project number: BAP-03-04-2013-002), and Turkish Scientific Research Council (project number: 113M205).

I thank Department of Chemical Engineering of METU for providing technical support on the XRD, and nitrogen physisorption analysis, METU Central Lab for TGA-DTA, ICP_MS, SEM, EDX, and TEM analyses of catalysts. I also acknowledge to National Nanotechnology Research Center of Bilkent University for TEM analysis.

TABLE OF CONTENTS

ABSTRACT	v
ÖZ	vii
ACKNOWLEDGMENTS	x
TABLE OF CONTENTS	xi
LIST OF TABLES	xiv
LIST OF FIGURES	xvii
LIST OF SYMBOLS AND ABBREVIATIONS	xxvii
CHAPTERS	
1. INTRODUCTION	1
1.1. Polymer Exchange Membrane Fuel Cells.....	3
1.2. Proton Movement across the Membrane electrode Assembly.....	5
1.3. Water Transport Mechanisms across the MEA	6
1.4. Hydrophobicity in the Catalyst Layers	8
1.5. Objective of the Work.....	10
2. HIGH-PERFORMANCE PEM FUEL CELL CATALYST LAYERS WITH HYDROPHOBIC CHANNELS	13
2.1. Introduction.....	13
2.2. Materials and Methods.....	16
2.3. Results and Discussions	20
2.4. Conclusions	39
3. EFFECT OF PTFE NANOPARTICLES IN CATALYST LAYER WITH HIGH Pt LOADING ON PEM FUEL CELL PERFORMANCE	41
3.1. Introduction.....	41
3.2. Materials and Methods.....	44

3.3. Results and Discussions	47
3.4. Conclusions.....	66
4. INFLUENCE OF FEP NANOPARTICLES IN CATALYST LAYER ON WATER MANAGEMENT AND PERFORMANCE OF PEM FUEL CELL WITH HIGH Pt LOADING	67
4.1. Introduction.....	67
4.2. Materials and Methods.....	71
4.3. Results and Discussion	72
4.4. Conclusions.....	89
5. UNDERSTANDING THE EFFECTS OF HYDROPHOBIC, HIGH Pt LOADED CATALYST LAYERS INCLUDING PFA NANOPARTICLES ON MASS TRANSPORT AND PERFORMANCE OF PEM FUEL CELL.....	91
5.1. Introduction.....	91
5.2. Materials and Methods.....	93
5.3. Results and Discussion	94
5.4. Conclusions.....	111
6. DIAGNOSTIC CHARACTERISATION OF HYDROPHOBIC CATALYST LAYERS INCLUDING PTFE NANOPARTICLES OF HIGH-PERFORMANCE PEM FUEL CELL.....	113
6.1. Introduction.....	114
6.2. Materials and Methods.....	114
6.3. Results and Discussions.....	120
6.4. Conclusions.....	157
7. CHARACTERIZATION OF HYDROPHOBIC CATALYST LAYERS INCLUDING FEP NANOPARTICLES IN THE SCOPE OF WATER MANAGEMENT AND PERFORMANCE OF PEM FUEL CELL	159
7.1. Introduction.....	159
7.2. Materials and Methods.....	160
7.3. Results and Discussions.....	161
7.4. Conclusions.....	193

8. DETERMINATION THE EFFECTS OF HYDROPHOBIC CATALYST LAYERS INCLUDING PFA NANOPARTICLES TO WATER MANAGEMENT AND PERFORMANCE OF PEM FUEL CELL	195
8.1. Introduction	195
8.2. Materials and Methods	196
8.3. Results and Discussions	197
8.4. Conclusions	228
9. CONCLUSIONS AND RECOMMENDATIONS.....	231
REFERENCES.....	237
CURRICULUM VITAE.....	249

LIST OF TABLES

TABLES

Table 2.1 Pt, Nafion, and PTFE loadings in catalyst layers	17
Table 2.2 Physical and electrochemical characterization of powders of commercial catalyst, Pt/C (ETEK), commercial catalyst impregnated with Nafion (without PTFE), commercial catalyst impregnated with Nafion and 30 wt % PTFE (30PTFE_AC).....	23
Table 2.3 The non-linear regression parameters for 0-D model of equation 2.5.....	34
Table 3.1 Pt, Nafion, and PTFE loadings in catalyst layers	46
Table 3.2 Parameters of equivalent circuit modeling of EIS spectra of MEA1 at H ₂ /O ₂ gas-feeding mode.....	52
Table 3.3 Parameters of equivalent circuit modeling of EIS spectra of MEA2 at H ₂ /O ₂ gas-feeding mode.....	57
Table 3.4 Parameters of equivalent circuit modeling of EIS spectra of MEA1 at H ₂ /Air gas-feeding mode.....	61
Table 3.5 Parameters of equivalent circuit modeling of EIS spectra of MEA1 at H ₂ /Air gas-feeding mode.....	65
Table 4.1 Pt, Nafion, and FEP loadings in catalyst layers.....	71
Table 4.2 Parameters of equivalent circuit modeling of EIS spectra of MEA1 at H ₂ /O ₂ gas-feeding mode.....	75
Table 4.3 Parameters of equivalent circuit modeling of EIS spectra of MEA2 at H ₂ /O ₂ gas-feeding mode.....	81
Table 4.4 Parameters of equivalent circuit modeling of EIS spectra of MEA1 at H ₂ /Air gas-feeding mode.....	85
Table 4.5 Parameters of the equivalent circuit modeling of MEA2 at H ₂ /Air gas-feeding mode	88
Table 5.1 Pt, Nafion, and PFA loadings in catalyst layers	93

Table 5.2 Parameters of equivalent circuit modeling of EIS spectra of MEA1 at H ₂ /O ₂ gas-feeding mode	98
Table 5.3 Parameters of equivalent circuit modeling of EIS spectra of MEA2 at H ₂ /O ₂ gas-feeding mode	103
Table 5.4 Parameters of equivalent circuit modeling of EIS spectra of MEA1 at H ₂ /Air gas-feeding mode	107
Table 5.5 Parameters of the equivalent circuit modeling of MEA2 at H ₂ /Air gas- feeding mode	111
Table 6.1 Pt, Nafion, and PTFE loadings in catalyst layers.....	115
Table 6.2 Physical characterization values of powders of commercial catalyst (Pt/C), commercial catalyst impregnated with Nafion (without PTFE), commercial catalyst impregnated with different Nafion and PTFE loadings	128
Table 6.3 Parameters of equivalent circuit modeling of EIS spectra of MEA1 at H ₂ /O ₂ gas-feeding mode	139
Table 6.4 Parameters of equivalent circuit modeling of EIS spectra of MEA2 at H ₂ /O ₂ gas-feeding mode	145
Table 6.5 Parameters of equivalent circuit modeling of EIS spectra of MEA1 at H ₂ /Air gas-feeding mode	150
Table 6.6 Parameters of equivalent circuit modeling of EIS spectra of MEA1 at H ₂ /Air gas-feeding mode	154
Table 7.1 Pt, Nafion, and FEP loadings in catalyst layers	160
Table 7.2 Physical characterization values of powders of commercial catalyst (Pt/C), commercial catalyst impregnated with Nafion (without FEP), commercial catalyst impregnated with different Nafion and FEP loadings.....	169
Table 7.3 Parameters of equivalent circuit modeling of EIS spectra of MEA1 at H ₂ /O ₂ gas-feeding mode	177
Table 7.4 Parameters of equivalent circuit modeling of EIS spectra of MEA2 at H ₂ /O ₂ gas-feeding mode	182
Table 7.5 Parameters of equivalent circuit modeling of EIS spectra of MEA1 at H ₂ /Air gas-feeding mode	186
Table 7.6 Parameters of equivalent circuit modeling of EIS spectra of MEA1 at H ₂ /Air gas-feeding mode	190

Table 8.1 Pt, Nafion, and PFA loadings in catalyst layers	196
Table 8.2 Physical characterization values of powders of commercial catalyst (Pt/C), commercial catalyst impregnated with Nafion (without PFA), commercial catalyst impregnated with different Nafion and PFA loadings	204
Table 8.3 Parameters of equivalent circuit modeling of EIS spectra of MEA1 at H ₂ /O ₂ gas-feeding mode	212
Table 8.4 Parameters of equivalent circuit modeling of EIS spectra of MEA2 at H ₂ /O ₂ gas-feeding mode	217
Table 8.5 Parameters of equivalent circuit modeling of EIS spectra of MEA1 at H ₂ /Air gas-feeding mode	221
Table 8.6 Parameters of equivalent circuit modeling of EIS spectra of MEA2 at H ₂ /Air gas-feeding mode	225

LIST OF FIGURES

FIGURES

Figure 1.1 Types of fuel cells and its application fields (https://ec.europa.eu/research/rtdinfo/42/01/print_article_1317_en.html)..	2
Figure 1.2 A schematic of a proton exchange membrane fuel cell	3
Figure 1.3 PEM fuel cell components; 1) Squeezing Bolts, 2) Gaskets 3) Graphite plates 4) Gold coated conductor plates 5) Thermocouple Insert Hole 6) Voltage Measurement Banana Plug 7) Heater	4
Figure 1.4 Proton transport in Nafion membrane a) Direct proton transport at low water content b) Vehicular mechanism from high water content to low water content c) Grotthus mechanism at high water content.....	6
Figure 1.5 Main water transport mechanisms across the in a PEM fuel cell	7
Figure 1.6 Micro-meso and meso-macro channeling through catalyst layer with and without hydrophobic agent	8
Figure 1.7 Liquid water accumulation in the gas channels	9
Figure 1.8 Catalyst aggregate including hydrophobic agent providing distinct pathways for gas and liquid	10
Figure 2.1 Thermogravimetric analyses for powders of commercial catalyst (Pt/C), commercial catalyst impregnated with Nafion (without PTFE), and commercial catalyst impregnated with Nafion and 30 wt % PTFE (30PTFE_AC). The measurements were performed in air	20
Figure 2.2 Differential thermal analysis curves for powders of commercial catalyst (Pt/C), commercial catalyst impregnated with Nafion (without PTFE), commercial catalyst impregnated with Nafion and 30 wt % PTFE (30PTFE_AC). The measurements were performed in air	22
Figure 2.3 XRD patterns of powders of commercial catalyst (Pt/C), commercial catalyst impregnated with Nafion (without PTFE), and commercial catalyst impregnated with Nafion and 30 wt % PTFE (30PTFE_AC).....	24

Figure 2.4 Adsorption/desorption isotherms for powders of commercial catalyst (Pt/C), commercial catalyst impregnated with Nafion (without PTFE), commercial catalyst impregnated with Nafion and 30 wt % PTFE (30PTFE_AC)	27
Figure 2.5 Pore size distributions for powders of commercial catalyst Pt/C (ETEK), commercial catalyst impregnated with Nafion (without PTFE), and commercial catalyst impregnated with Nafion and 30 wt % PTFE (30PTFE_AC)	28
Figure 2.6 Cyclic voltammograms of commercial catalyst (Pt/C), commercial catalyst impregnated with Nafion (without PTFE), and commercial catalyst impregnated with Nafion and 30 wt % PTFE (30PTFE_AC).....	30
Figure 2.7 iR corrected polarization curves and power density vs. current density curves for commercial catalyst (Pt/C), commercial catalyst impregnated with Nafion (without PTFE), commercial catalyst impregnated with Nafion and 30 wt % PTFE (30PTFE_AC).....	33
Figure 2.8 SEM images of powders of a) commercial catalyst (Pt/C), b) commercial catalyst impregnated with Nafion (without PTFE), and c) commercial catalyst impregnated with Nafion and 30 wt % PTFE (30PTFE_AC).....	36
Figure 2.9 SEM images of cross-section of the membrane electrode assemblies for a)commercial catalyst (Pt/C), b) commercial catalyst impregnated with Nafion (without PTFE), and c) commercial catalyst impregnated with Nafion and 30 wt % PTFE (30PTFE_AC).....	37
Figure 2.10 TEM Images of powders of a)commercial catalyst (Pt/C), b) commercial catalyst impregnated with Nafion (without PTFE), and c) commercial catalyst impregnated with Nafion and 30 wt % PTFE (30PTFE_AC).....	38
Figure 3.1 Polarization and power density curves of PEMFC for MEA1. Pt loading of anode and cathode electrodes was 1.2 mgPt/cm ² . Both anode and cathode catalyst layers coated with PTFE nanoparticles. PEMFC was operated at H ₂ /O ₂ gas-feeding mode	48
Figure 3.2 Electrochemical impedance spectra obtained for running fuel cell at 0.5 V. Pt loading of anode and cathode electrodes was 1.2 mgPt/cm ² . Both anode and cathode catalyst layers were coated with PTFE nanoparticles. H ₂ /O ₂ gas-feeding mode was used	50

Figure 3.3 Equivalent circuit model for measured impedance spectra a) impedance spectra with two arcs b) impedance spectra with one arc.....	51
Figure 3.4 Polarization and power density curves of PEMFC for MEA2. Pt loading of anode and cathode electrodes was 1.2 mgPt/cm ² . Cathode catalyst layer was coated with PTFE nanoparticles. PEMFC was operated at H ₂ /O ₂ gas feeding mode	54
Figure 3.5 Electrochemical impedance spectra obtained for running fuel cell at 0.5 V. Pt loading of anode and cathode electrodes was 1.2 mgPt/cm ² . Cathode catalyst layer was coated with PTFE nanoparticles. PEMFC was operated at H ₂ /O ₂ gas-feeding mode	56
Figure 3.6 Polarization and power density curves of PEMFC for MEA1. Pt loading of anode and cathode electrodes was 1.2 mgPt/cm ² . Both anode and cathode catalyst layers were coated with PTFE nanoparticles. PEMFC was operated at H ₂ /Air gas-feeding mode	59
Figure 3.7 Electrochemical impedance spectra obtained for running fuel cell at 0.5 V. Pt loading of anode and cathode electrodes was 1.2 mgPt/cm ² . Both anode and cathode catalyst layers were coated with PTFE nanoparticles. PEMFC was operated at H ₂ /Air gas-feeding mode	60
Figure 3.8 Polarization and power density curves of PEMFC for MEA2. Pt loading of anode and cathode electrodes was 1.2 mgPt/cm ² . Cathode catalyst layer was coated with PTFE nanoparticles. PEMFC was operated at H ₂ /Air gas feeding mode	63
Figure 3.9 Electrochemical impedance spectra obtained for running fuel cell at 0.5 V. Pt loading of anode and cathode electrodes was 1.2 mgPt/cm ² . Cathode catalyst layer was coated with PTFE nanoparticles. PEMFC was operated at H ₂ /Air gas-feeding mode	64
Figure 4.1 . Polarization and power density curves of PEMFC for MEA1. Pt loading of anode and cathode electrodes was 1.2 mgPt/cm ² . Both anode and cathode CLs were coated with FEP nanoparticles. PEMFC was operated at H ₂ /O ₂ gas-feeding mode	73
Figure 4.2 Electrochemical impedance spectra obtained for running fuel cell at 0.5 V. Pt loading of anode and cathode electrodes was 1.2 mgPt/cm ² . Both	

anode and cathode CLs were coated with FEP nanoparticles. PEMFC was operated at H ₂ /O ₂ gas-feeding mode	74
Figure 4.3 Polarization and power density curves of PEMFC for MEA2. Pt loading of anode and cathode electrodes was 1.2 mgPt/cm ² . Cathode catalyst layer was coated with FEP nanoparticles. PEMFC was operated at H ₂ /O ₂ gas-feeding mode	78
Figure 4.4 Electrochemical impedance spectra obtained for running fuel cell at 0.5 V. Pt loading of anode and cathode electrodes was 1.2 mgPt/cm ² . Cathode catalyst layer was coated with FEP nanoparticles. H ₂ /O ₂ gas-feeding mode was used	80
Figure 4.5 Polarization and power density curves of PEMFC for MEA1. Pt loading of anode and cathode electrodes was 1.2 mgPt/cm ² . Both anode and cathode catalyst layer were coated with FEP nanoparticles. PEMFC was operated at H ₂ /Air gas-feeding mode	82
Figure 4.6 Electrochemical impedance spectra obtained for running fuel cell at 0.5 V. Pt loading of anode and cathode electrodes was 1.2 mg Pt/cm ² . Both anode and cathode catalyst layer were coated with FEP nanoparticles. PEMFC was operated at H ₂ /Air gas-feeding mode	84
Figure 4.7 Polarization and power density curves of PEMFC for MEA2. Pt loading of anode and cathode electrodes was 1.2 mgPt/cm ² . Cathode catalyst layer was coated with FEP nanoparticles. PEMFC was operated at H ₂ /Air gas-feeding mode	86
Figure 4.8 Electrochemical impedance spectra obtained for running fuel cell at 0.5 V. Pt loading of anode and cathode electrodes was 1.2 mgPt/cm ² . The only cathode catalyst layer was coated with FEP nanoparticles. PEMFC was operated at H ₂ /Air gas-feeding mode	88
Figure 5.1 Polarization and power density curve for PEMFC for MEA1. Pt loading of anode and cathode electrodes was 1.2 mgPt/cm ² . Both anode and cathode catalyst layer were coated with PFA nanoparticles. PEMFC was operated at H ₂ /O ₂ gas-feeding mode	95
Figure 5.2 Electrochemical impedance spectra for running fuel cell obtained at 0.5 V. Pt loading of anode and cathode electrodes was 1.2 mgPt/cm ² . Both	

anode and cathode catalyst layer were coated with PFA nanoparticles. PEMFC was operated at H ₂ /O ₂ gas-feeding mode	97
Figure 5.3 Polarization and power density curves of PEMFC for MEA2. Pt loading of anode and cathode electrodes was 1.2 mgPt/cm ² . The only cathode catalyst layer was coated with PFA nanoparticles. PEMFC was operated at H ₂ /O ₂ gas-feeding mode	101
Figure 5.4 Electrochemical impedance spectra for running fuel cell obtained at 0.5 V. Pt loading of anode and cathode electrodes was 1.2 mgPt/cm ² . The only cathode catalyst layer was coated with PFA nanoparticles. H ₂ /O ₂ gas- feeding mode was used.....	102
Figure 5.5 Polarization and power density curves of PEMFC for MEA1. Pt loading of anode and cathode electrodes was 1.2 mgPt/cm ² . Both anode and cathode catalyst layers were coated with PFA nanoparticles. PEMFC was operated at H ₂ /Air gas-feeding mode.	105
Figure 5.6 Electrochemical impedance spectra obtained for running fuel cell at 0.5 V. Pt loading of anode and cathode electrodes was 1.2 mg Pt/cm ² . Both anode and cathode catalyst layers were coated with PFA nanoparticles. PEMFC was operated at H ₂ /Air gas-feeding mode	106
Figure 5.7 Polarization and power density curves of PEMFC for MEA2. Pt loading of anode and cathode electrodes was 1.2 mgPt/cm ² . PFA nanoparticles were coated on only cathode catalyst layer. PEMFC was operated at H ₂ /Air gas-feeding mode	109
Figure 5.8 Electrochemical impedance spectra obtained running fuel cell at 0.5 V. Pt loading of anode and cathode electrodes was 1.2 mgPt/cm ² . The only cathode catalyst layer was coated with PFA nanoparticles. PEMFC was operated at H ₂ /Air gas-feeding mode	110
Figure 6.1 Adsorption/desorption isotherms for powders of commercial catalyst (Pt/C), commercial catalyst impregnated with Nafion (without PTFE), commercial catalyst impregnated with different Nafion and PTFE loadings	120
Figure 6.2 Pore size distributions for powders of commercial catalyst (Pt/C), commercial catalyst impregnated with Nafion (without PTFE), and	

commercial catalyst impregnated with different Nafion and PTFE loadings	121
Figure 6.3 XRD patterns of powders of commercial catalyst (Pt/C), commercial catalyst impregnated with Nafion (without PTFE), and commercial catalyst impregnated with different Nafion and PTFE loadings	124
Figure 6.4 Cyclic voltammograms of commercial catalyst (Pt/C), commercial catalyst impregnated with Nafion (without PTFE), and commercial catalyst impregnated with different Nafion and PTFE loadings	125
Figure 6.5 TEM images of powders of a)Pt/C, b) without PTFE, c) 5PTFE, d) 10PTFE, e) 10PTFE_2, f) 20PTFE, g) 30PTFE, h) 40PTFE	130
Figure 6.6 SEM images of powders of a)Pt/C, b) without PTFE, c) 5PTFE, d) 10PTFE, e) 10PTFE_2, f) 20PTFE, g) 30PTFE, h) 40PTFE	132
Figure 6.7 Polarization and power density curves of PEMFC for MEA1. Pt loading of anode and cathode electrodes was 0.4 mgPt/cm ² . PTFE nanoparticles were coated with both anode and cathode catalyst layers. H ₂ /O ₂ gas- feeding mode was used.....	134
Figure 6.8 Electrochemical impedance spectra obtained for a running fuel cell at 0.5 V. Pt loading of anode and cathode electrodes was 0.4 mgPt/cm ² . Both anode and cathode catalyst layers were coated with PTFE nanoparticles. H ₂ /O ₂ gas-feeding mode was used	136
Figure 6.9 Polarization and power density curves of PEMFC for MEA2. Pt loading of anode and cathode electrodes was 0.4 mgPt/cm ² . PTFE nanoparticles were coated on only cathode catalyst layer. PEMFC was operated at H ₂ /O ₂ gas feeding mode	141
Figure 6.10 Electrochemical impedance spectra obtained at 0.5 V. Pt loading of anode and cathode electrodes was 0.4 mgPt/cm ² . PTFE nanoparticles were coated on only cathode catalyst layer. PEMFC was operated at H ₂ /O ₂ gas- feeding mode	144
Figure 6.11 Polarization and power density curves of PEMFC for MEA1. Pt loading of anode and cathode electrodes was 0.4 mgPt/cm ² . Both anode and cathode catalyst layers include PTFE nanoparticles. PEMFC was operated at H ₂ /Air gas-feeding mode	147

Figure 6.12 Electrochemical impedance spectra obtained for a running fuel cell at 0.5 V. Pt loading of anode and cathode electrodes was 0.4 mgPt/cm ² . Both anode and cathode catalyst layers were coated with PTFE nanoparticles. PEMFC was operated at H ₂ /Air gas-feeding mode	149
Figure 6.13 Polarization and power density curves of PEMFC for MEA2. Pt loading of anode and cathode electrodes was 0.4 mgPt/cm ² . PTFE nanoparticles were coated on only cathode catalyst layer. PEMFC was operated at H ₂ /Air gas feeding mode	152
Figure 6.14 Electrochemical impedance spectra obtained for running fuel cell at 0.5 V. Pt loading of anode and cathode electrodes was 0.4 mgPt/cm ² . Cathode catalyst layer was coated with PTFE nanoparticles. PEMFC was operated at H ₂ /Air gas-feeding mode	153
Figure 6.15 SEM images of the cross-section of the MEAs for a) without PTFE with 1.2 mg/cm ² Pt loading, b) without PTFE with 0.4 mg/cm ² Pt loading, c) 5PTFE_AC with 1.2 mg/cm ² d) 10PTFE_2_AC with 0.4 mg/cm ²	156
Figure 7.1 Adsorption/desorption isotherms for powders of commercial catalyst (Pt/C), commercial catalyst impregnated with Nafion (without FEP), commercial catalyst impregnated with different Nafion and FEP loadings	161
Figure 7.2 Pore size distributions for powders of commercial catalyst (Pt/C), commercial catalyst impregnated with Nafion (without FEP), and commercial catalyst impregnated with different Nafion and FEP loadings	162
Figure 7.3 XRD patterns of powders of commercial catalyst (Pt/C), commercial catalyst impregnated with Nafion (without FEP), and commercial catalyst impregnated with different Nafion and FEP loadings	165
Figure 7.4 Cyclic voltammograms of commercial catalyst (Pt/C), commercial catalyst impregnated with Nafion (without FEP), and commercial catalyst impregnated with different Nafion and FEP loadings	166
Figure 7.5 TEM images of powders of a)Pt/C, b) without FEP, c) 5FEP, d) 10FEP, e) 10FEP_2, f) 20FEP, g) 30FEP, h) 40FEP	171
Figure 7.6 SEM images of powders of a) Pt/C, b) without FEP, c) 5FEP, d) 10FEP, e) 10FEP_2, f) 20FEP, g) 30FEP, h) 40FEP	172

Figure 7.7 Polarization and power density curves of PEMFC for MEA1. Pt loading of anode and cathode electrodes was 0.4 mgPt/cm ² . Both anode and cathode catalyst layers were coated with FEP nanoparticles. H ₂ /O ₂ gas-feeding mode was used.....	174
Figure 7.8 Electrochemical impedance spectra obtained for a running fuel cell at 0.5 V. Pt loading of anode and cathode electrodes was 0.4 mgPt/cm ² . Both anode and cathode catalyst layers were coated with FEP nanoparticles. H ₂ /O ₂ gas-feeding mode was used	176
Figure 7.9 Polarization and power density curves of PEMFC for MEA2. Pt loading of anode and cathode electrodes was 0.4 mgPt/cm ² . Cathode catalyst layer was coated with FEP nanoparticles. PEMFC was operated at H ₂ /O ₂ gas feeding mode	179
Figure 7.10 Electrochemical impedance spectra obtained at 0.5 V. Pt loading of anode and cathode electrodes was 0.4 mgPt/cm ² . FEP nanoparticles were coated on only cathode catalyst layer. PEMFC was operated at H ₂ /O ₂ gas-feeding mode	181
Figure 7.11 Polarization and power density curves of PEMFC for MEA1. Pt loading of anode and cathode electrodes was 0.4 mgPt/cm ² . Both anode and cathode catalyst layers were coated with FEP nanoparticles. PEMFC was operated at H ₂ /Air gas-feeding mode	183
Figure 7.12 Electrochemical impedance spectra obtained for a running fuel cell at 0.5 V. Pt loading of anode and cathode electrodes was 0.4 mgPt/cm ² . Both anode and cathode catalyst layers were coated with FEP nanoparticles. PEMFC was operated at H ₂ /Air gas-feeding mode.....	185
Figure 7.13 Polarization and power density curves of PEMFC for MEA2. Pt loading of anode and cathode electrodes was 0.4 mgPt/cm ² . Cathode catalyst layer was coated with FEP nanoparticles. PEMFC was operated at H ₂ /Air gas feeding mode	188
Figure 7.14 Electrochemical impedance spectra obtained for running fuel cell at 0.5 V. Pt loading of anode and cathode electrodes was 0.4 mgPt/cm ² . Cathode catalyst layer was coated with FEP nanoparticles. PEMFC was operated at H ₂ /Air gas-feeding mode.....	189

Figure 7.15 SEM images of the cross-section of the MEAs for a) without FEP with 1.2 mg/cm ² Pt loading, b) without FEP with 0.4 mg/cm ² Pt loading, c) 5FEP_AC with 1.2 mg/cm ² d) 5FEP_AC with 0.4 mg/cm ²	192
Figure 8.1 Adsorption/desorption isotherms for powders of commercial catalyst (Pt/C), commercial catalyst impregnated with Nafion (without PFA), commercial catalyst impregnated with different Nafion and PFA loadings	197
Figure 8.2 Pore size distributions for powders of commercial catalyst (Pt/C), commercial catalyst impregnated with Nafion (without PFA), and commercial catalyst impregnated with different Nafion and PFA loadings	199
Figure 8.3 XRD patterns of powders of commercial catalyst (Pt/C), commercial catalyst impregnated with Nafion (without PFA), and commercial catalyst impregnated with different Nafion and PFA loadings.....	201
Figure 8.4 Cyclic voltammograms of commercial catalyst (Pt/C), commercial catalyst impregnated with Nafion (without PFA), and commercial catalyst impregnated with different Nafion and PFA loadings.....	202
Figure 8.5 TEM images of powders of a)Pt/C, b) without PFA, c) 5PFA, d) 10PFA, e) 10PFA_2, f) 20PFA, g) 30PFA h) 40PFA	206
Figure 8.6 SEM images and energy-dispersive X-ray spectroscopy (EDX) of powders of a) Pt/C, b) without PFA c) 5PFA, d) 10PFA, e) 10PFA_2, f) 20PFA, g) 30PFA and h) 40PFA.....	208
Figure 8.7 Polarization and power density curves of PEMFC for MEA1. Pt loading of anode and cathode electrodes was 0.4 mgPt/cm ² . Both anode and cathode catalyst layers coated with PFA nanoparticles. H ₂ /O ₂ gas-feeding mode was used.....	210
Figure 8.8 Electrochemical impedance spectra obtained for a running fuel cell at 0.5 V. Pt loading of anode and cathode electrodes was 0.4 mgPt/cm ² . Both anode and cathode catalyst layers were coated with PFA nanoparticles. H ₂ /O ₂ gas-feeding mode was used.....	211
Figure 8.9 Polarization and power density curves of PEMFC for MEA2. Pt loading of anode and cathode electrodes was 0.4 mgPt/cm ² . Cathode catalyst layer was coated with PFA nanoparticles. H ₂ /O ₂ gas-feeding mode was used	214

Figure 8.10 Electrochemical impedance spectra obtained at 0.5 V. Pt loading of anode and cathode electrodes was 0.4 mgPt/cm ² . Cathode catalyst layer were coated with PFA nanoparticles. PEMFC was operated at H ₂ /O ₂ gas-feeding mode	216
Figure 8.11 Polarization and power density curves of PEMFC for MEA1. Pt loading of anode and cathode electrodes was 0.4 mgPt/cm ² . Both anode and cathode catalyst layers were coated with PFA nanoparticles. PEMFC was operated at H ₂ /Air gas-feeding mode	219
Figure 8.12 Electrochemical impedance spectra obtained for a running fuel cell at 0.5 V. Pt loading of anode and cathode electrodes was 0.4 mgPt/cm ² . Both anode and cathode catalyst layers were coated with PFA nanoparticles. PEMFC was operated at H ₂ /Air gas-feeding mode.....	220
Figure 8.13 Polarization and power density curves of PEMFC for MEA2. Pt loading of anode and cathode electrodes was 0.4 mgPt/cm ² . Cathode catalyst layer was coated with PFA nanoparticles. PEMFC was operated at H ₂ /Air gas feeding mode	223
Figure 8.14 Electrochemical impedance spectra obtained for a running fuel cell at 0.5 V. Pt loading of anode and cathode electrodes was 0.4 mgPt/cm ² . Both anode and cathode catalyst layers were coated with PFA nanoparticles. PEMFC was operated at H ₂ /Air gas-feeding mode.....	224
Figure 8.15 SEM images of the cross-section of the MEAs for a) without PFA with 1.2 mg/cm ² Pt loading, b) without PFA with 0.4 mg/cm ² Pt loading, c) 5PFA_C with 1.2 mg/cm ² d) 20PFA_C with 0.4 mg/cm ²	227

LIST OF SYMBOLS AND ABBREVIATIONS

Symbols

d_{Pt} : Average Platinum diameter (nm)

$d_{pore_{avg}}$: Average Pore Diameter (nm)

E_{cell} : Raw voltage (V)

$E_{iR-free}$: iR corrected cell voltage (V)

E_{OCV} : Open circuit voltage (V)

ESA: Electrochemical Surface Area (m^2/g)

F: Faraday's constant (C/mol)

i : Raw current density (A/cm^2)

i_L : Limiting current density (A/cm^2)

i_0 : Exchange current density (A/cm^2)

K: Scherrer constant

L_{Pt} : Pt loading on glassy carbon disc electrode (mg/cm^2)

n: Number of electrons involved in the reaction

$Q_{H(avg)}$: Average charge density of adsorption and desorption charges on glassy carbon disc electrode (mC/cm^2)

$Q_{H(ref)}$: Specific charge determined for the adsorption of one monolayer of hydrogen on an atomically flat polycrystalline Pt electrode ($\mu C/cm^2$)

R: Universal gas constant (J/mol K)

R_{ct} : Charge transfer resistance ($\Omega.cm^2$)

R_{HF} : High-frequency resistance ($\Omega.cm^2$)

R_i : Internal resistance ($\Omega.cm^2$)

R_{mt} : Mass transfer resistance ($\Omega \cdot \text{cm}^2$)
 SA_{Pt} : Total surface area of Pt particles (m^2/g)
 SA_{BET} : BET Surface Area (m^2/g)
 T : Cell temperature ($^{\text{K}}$)
 U_{Pt} : Platinum Utilization (%)
 $V_{poreCum}$: Cumulative Pore Volume (cm^3/g)

Greek Letters

α : Transfer coefficient
 β : Full width of the strongest diffraction peak at half height (radian)
 λ : Wavelength of incident X-rays (nm)
 ρ : Density of Pt particles (g/cm^3)
 θ_{β} : Bragg angle (radian)

Abbreviations

aCL: Catalyst Layer of Anode
AEO: Annual Energy Outlook
AFCs: Alkaline Fuel Cells
aGDL: Gas Diffusion Layer of Anode
aMPL: Microporous Layer of Anode
BET: Brunauer–Emmett–Teller
BJH: Barrett Joyner Halenda
C: Capacitance
cCL: Catalyst Layer of Cathode
cGDL: Gas Diffusion Layer of Cathode
CL: Catalyst Layer

cMPL: Microporous Layer of Cathode

CPE: Constant Phase Element

CV: Cyclic Voltammetry

DMFC: Direct Methanol Fuel Cells

DSO: Dimethyl Silicone Oil

DTA: Differential Thermal Analyses

EDX: Energy-dispersive X-ray spectroscopy

ETFE: Ethylene tetrafluoroethylene

FEP: Fluorinated ethylene propylene

GDL: Gas Diffusion Layer

ICP_MS: Inductively-Coupled Plasma spectrometer-Mass Spectrometer

IPA: Isopropyl Alcohol

MCFCs: Molten Carbonate Fuel Cells

MEA: Membrane Electrode Assembly

MPL: Microporous Layer

PAFCs: Phosphoric Acid Fuel Cells

PE: Polyethylene

PEMFCs: Proton Exchange Membrane Fuel Cells

PFA: Poly(tetrafluoroethylene-co-perfluoro propyl vinyl ether)

PTFE: Polytetrafluoroethylene

PVDF: Polyvinylidene fluoride

PVF: Polyvinyl fluoride

SEM: Scanning Electron Microscopy

SOFCs: Solid Oxide Fuel Cells

TEM: Transmission Electron Microscopy

TGA: Thermogravimetric Analysis

XRD: X-ray Diffractograms

CHAPTER 1

INTRODUCTION

Due to change in consuming habits and technology development industrial, transportation and residential energy demand have been growing every day. In according to Annual Energy Outlook (AEO) 2012 a major part (77%) of energy demand is assumed to be supplied by fossil fuels and renewable energy resources supply only 14% of the demand till 2035 (<http://www.instituteforenergyresearch.org>). However, consuming fossil fuels leads to increase in carbon dioxide emissions, which make the planet, encounter with climate change. Searching for clean, efficient, renewable energy resources except fossil fuels makes fuel cells to have been much attention owing to their high efficiencies and low emissions compared to internal combustion engines.

PEM fuel cells are being applied in transportation from 1kW to 100 kW; stationary from 0.5 to 400kW, and portable power generation from 5-20kW (<http://www.fuelcelltoday.com>).

Sir William Groove first invented the fuel cell in 1839, however; practically, the first fuel cell was used in the Gemini space mission of U.S. Space Program in 1962. Nowadays, fuel cells have successfully used in various transportation and residential application as an energy carrier (Barbir 2005).

Figure 1.1 illustrates the types of and application fields of fuel cells. Fuel cells are classified according to the electrolyte employed: proton exchange membrane fuel cells (PEMFC), solid oxide fuel cells (SOFC), alkaline fuel cells (AFC), phosphoric acid fuel cells (PAFC) molten carbonate fuel cells (MCFC), direct methanol fuel cells (DMFC)

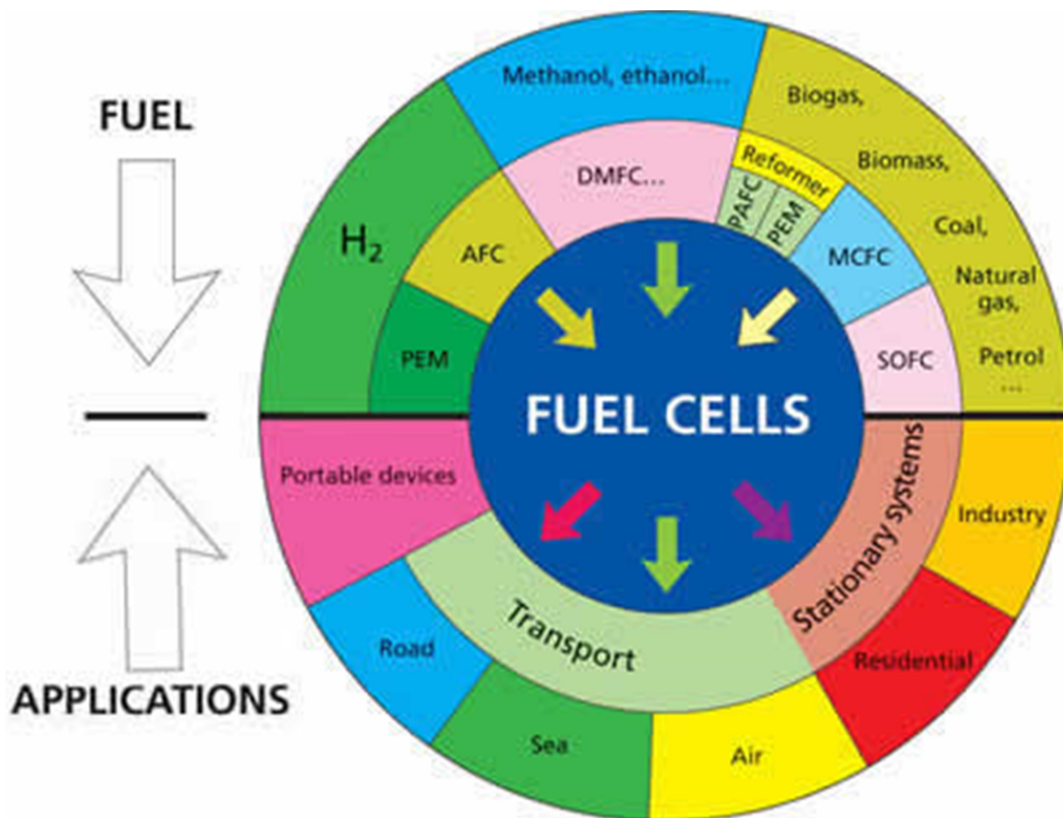


Figure 1.1 Types of fuel cells and its application fields (https://ec.europa.eu/research/rtdinfo/42/01/print_article_1317_en.html)

Among these fuel cell types PEMFC is the most promising candidate for transportation, stationary, and portable applications owing to low operating temperature, high power density, simple, and modular construction, and quiet operation. In a PEMFC a proton conductive polymer membrane is used as an electrolyte, which is impermeable to gasses. On the both sides of the membrane, there are two electrically conductive electrodes. One side of these electrodes, which looks towards the membrane, was coated with catalyst particles. Electrochemical reactions take place at the surface of the catalyst at the interface between the electrolyte and the membrane. Hydrogen, which is fed to the anode side of the cell, consists of one electron and one proton. Protons travel through the ionomer membrane whereas electrons travel through the electrodes, through current collectors and outside circuit and come back meet with the protons. Protons passed through the membrane, electrons come through outside circuit and oxygen fed on the cathode

side meet and produce water. Then produced water as a product of the electrochemical reaction besides heat is exhausted with the excess flow of air from the cathode side of the cell.

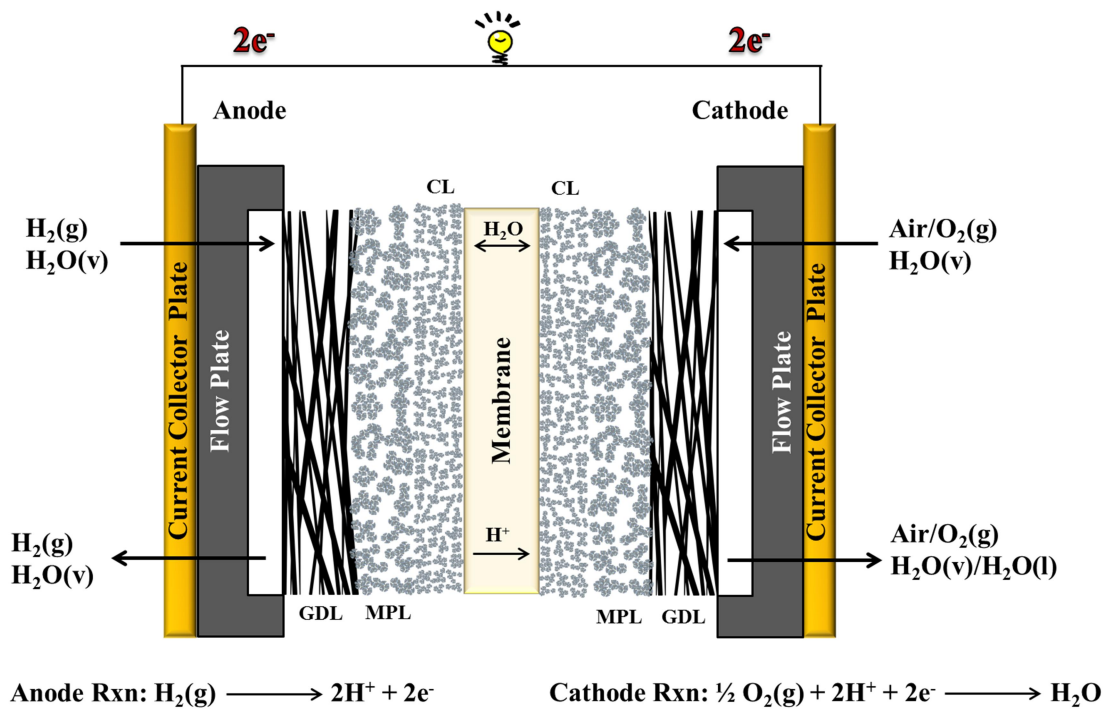


Figure 1.2 A schematic of a proton exchange membrane fuel cell

1.1. Polymer Exchange Membrane Fuel Cells

The fuel cell is an electrochemical device that directly converts chemical energy stored in fuels to electricity with the continuous fuel supply. In a PEMFC a proton conductive polymer membrane is used as an electrolyte, which is impermeable to gasses. On the both sides of the membrane, there are two electrically conductive electrodes. One side of these electrodes, which looks towards the membrane, was coated with catalyst particles. Electrochemical reactions take place at the surface of the catalyst at the interface between the electrolyte and the membrane. Hydrogen that is fed to the anode side of the cell consists of one electron and one proton. Protons travel through the ionomer membrane whereas electrons

travel through the electrodes, through current collectors and outside circuit and come back meet with the protons.

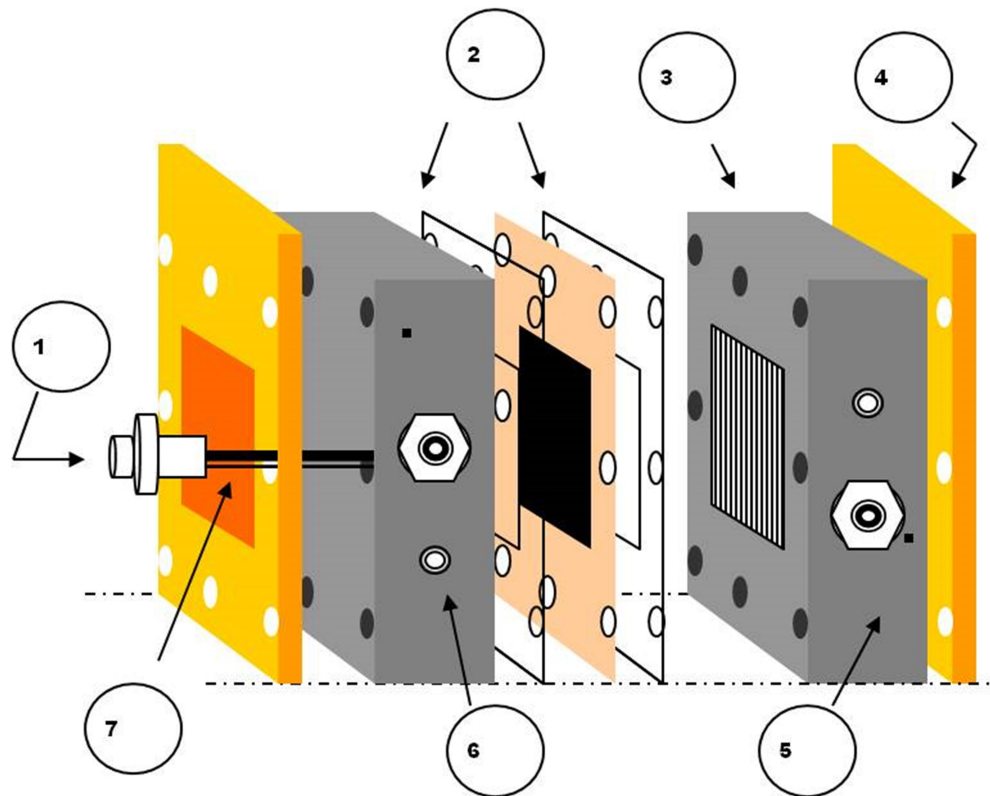


Figure 1.3 PEM fuel cell components; 1) Squeezing Bolts, 2) Gaskets 3) Graphite plates 4) Gold coated conductor plates 5) Thermocouple Insert Hole 6) Voltage Measurement Banana Plug 7) Heater

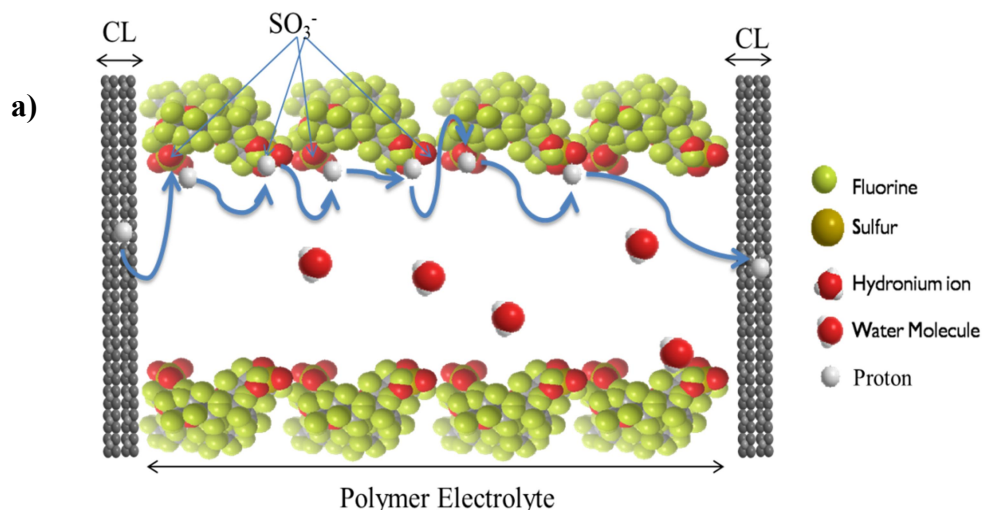
Protons passed through the membrane, electrons come through outside circuit and oxygen fed on the cathode side meet and produce water. Then produced water as a product of the electrochemical reaction besides heat is exhausted with the excess flow of air from the cathode side of the cell. Figure 1.3 illustrates the components of PEM fuel cell. The main part of the proton exchange membrane fuel cells is a membrane, which conducts proton via water molecules. On the both sides of the membrane, there is a porous electrode, which is coated with Pt on the one side at the interface between the GDL and the membrane. In the literature, the membrane sandwiched between two electrodes is called as a membrane electrode assembly

(MEA). A gasket on the both sides also surrounds the MEA in order to prevent the gas leakage. The MEA and gaskets are squeezed between bipolar plates which allow gas penetrate into the MEA by the gas channels on it. There is also an end plate generally used as a current collector on the both sides of the bipolar plates.

1.2. Proton Movement across the Membrane electrode Assembly

Conduction of protons from the anode to the cathode side of the cell is the main parameter that affects the performance of a proton exchange membrane fuel cell. The proton conduction depends on the water uptake of the membrane. Because as the electrolyte membrane absorbs water this water accumulates around the SO_3^- ions and by the help of the weak interaction between the water and the protons or SO_3^- ions and protons, they can move through the membrane. Figure 1.4 illustrates the proton movement mechanisms in the PFSA membrane.

Water and thermal management have a great impact on the performance of a PEM fuel cell. In order to obtain an efficient water and thermal management strategy, water transport and thermal scattering should be understood clearly.



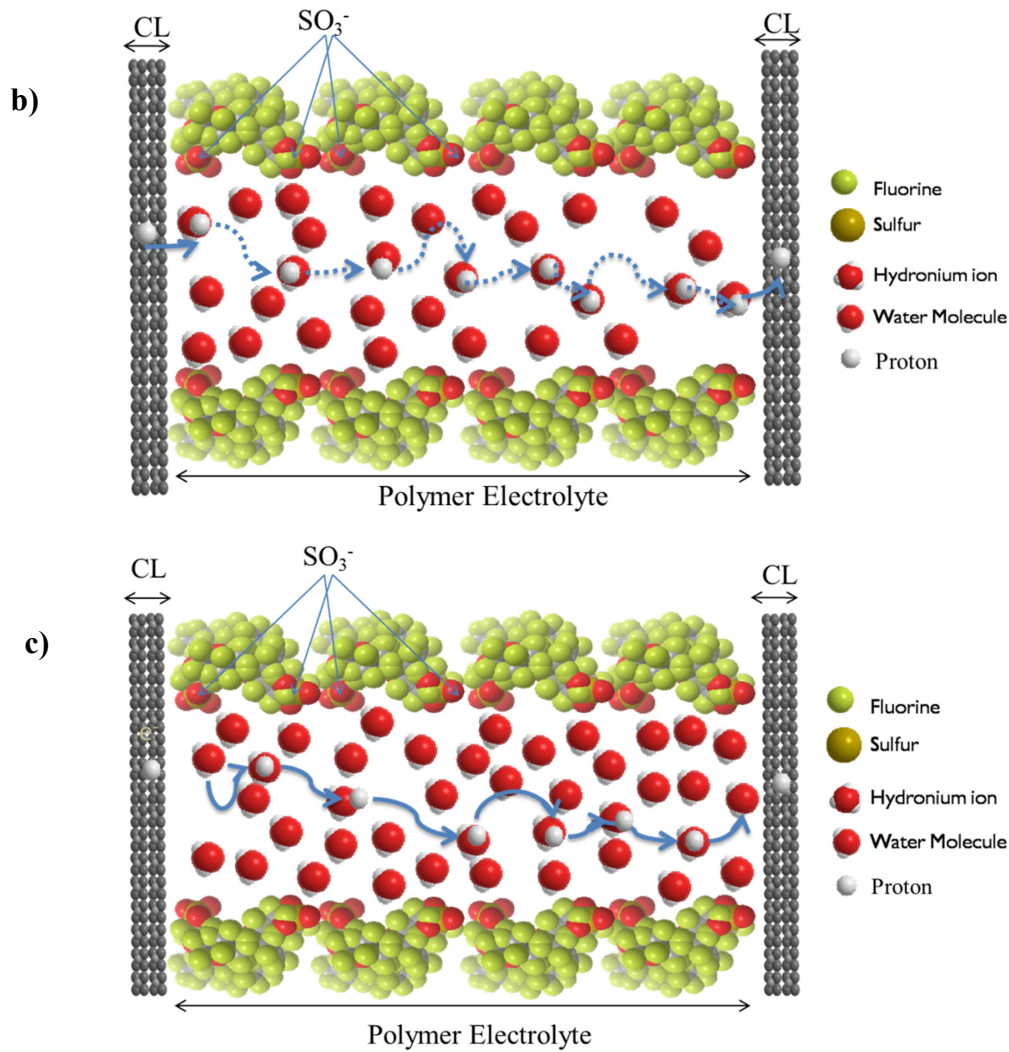


Figure 1.4 Proton transport in Nafion membrane a) Direct proton transport at low water content b) Vehicular mechanism from high water content to low water content c) Grotthus mechanism at high water content

The humidified reactant gasses sent to the cell provide the humidification of the membrane. Besides, water is produced in the cCL by the oxygen reduction reaction.

1.3. Water Transport Mechanisms across the MEA

Figure 1.5 illustrates the water movements through the cell. There are two main water movements through the MEA in a PEM fuel cell; electro-osmotic drag and back diffusion (Jiao & Li 2011).

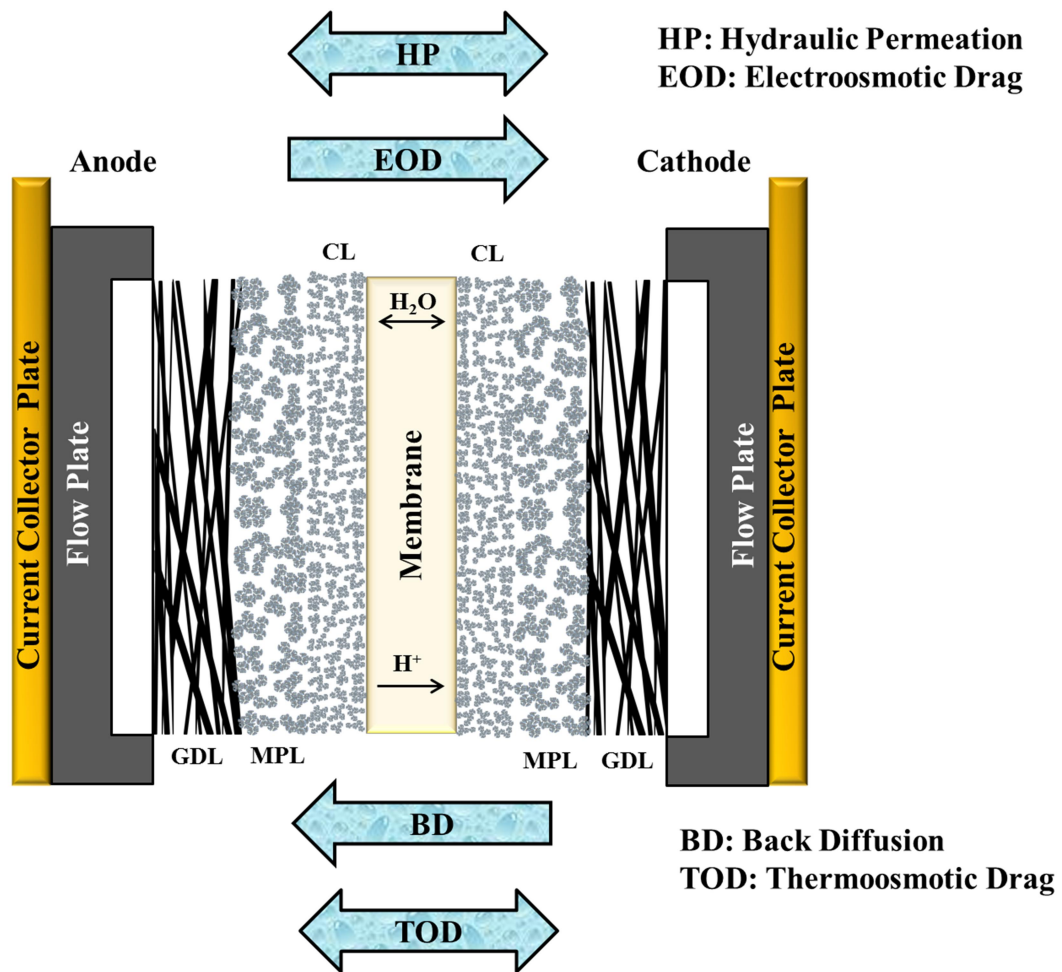


Figure 1.5 Main water transport mechanisms across the in a PEM fuel cell

In the electro-osmotic drag, protons are moved with the movement of water molecules that enters the system by hydrogen through the membrane (Pivovar 2006). The latter water transport mechanism is the back diffusion. In this mechanism, proton moves from the cathode to the anode by the water concentration gradient (Dai et al. 2009). Other two water transport mechanisms are called hydraulic permeation and thermo-osmotic diffusion (Dai et al. 2009). Hydraulic permeation occurs owing to the pressure difference between the anode and cathode; water moves from the high-pressure region to the low-pressure region. Thermo-osmotic drag occurs when one or two temperature differences or more occurs between the anode and cathode sides of the cell (Kim & Mench 2009).

1.4. Hydrophobicity in the Catalyst Layers

In order to obtain high-performance membrane should have been saturated with water. However, if the water produced by oxygen reduction reaction present as larger amounts it will block these empty spaces and prevents the oxygen from reaching the active catalyst sites. Consequently, cell performance decreases.

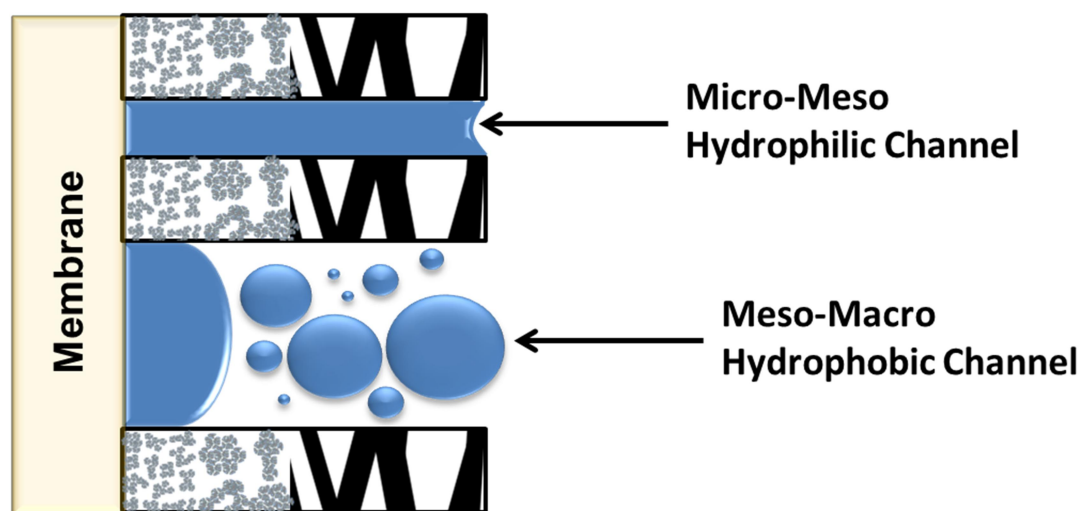


Figure 1.6 Micro-meso and meso-macro channeling through catalyst layer with and without hydrophobic agent

To prevent performance loss besides providing a better control of the water movement constituting specific passageways for electron and ionic conduction should be provided. Figure 1.6 illustrates the micro-meso and meso-macro channeling through CL with and without a hydrophobic agent.

Otherwise, if distinct pathways are not provided, product water in the pores of CL flow through GDL of the cathode. While water moved from CL to the gas diffusion layer of the cathode, it condenses and blocks the pores. Consequently, liquid water filled the pores prevents oxygen/air diffusion through pores. This will lead to a decrease in reaction rate, because, active catalyst sites can never meet with the reactant gas. Figure 1.7 illustrates liquid water accumulation in the gas channels.

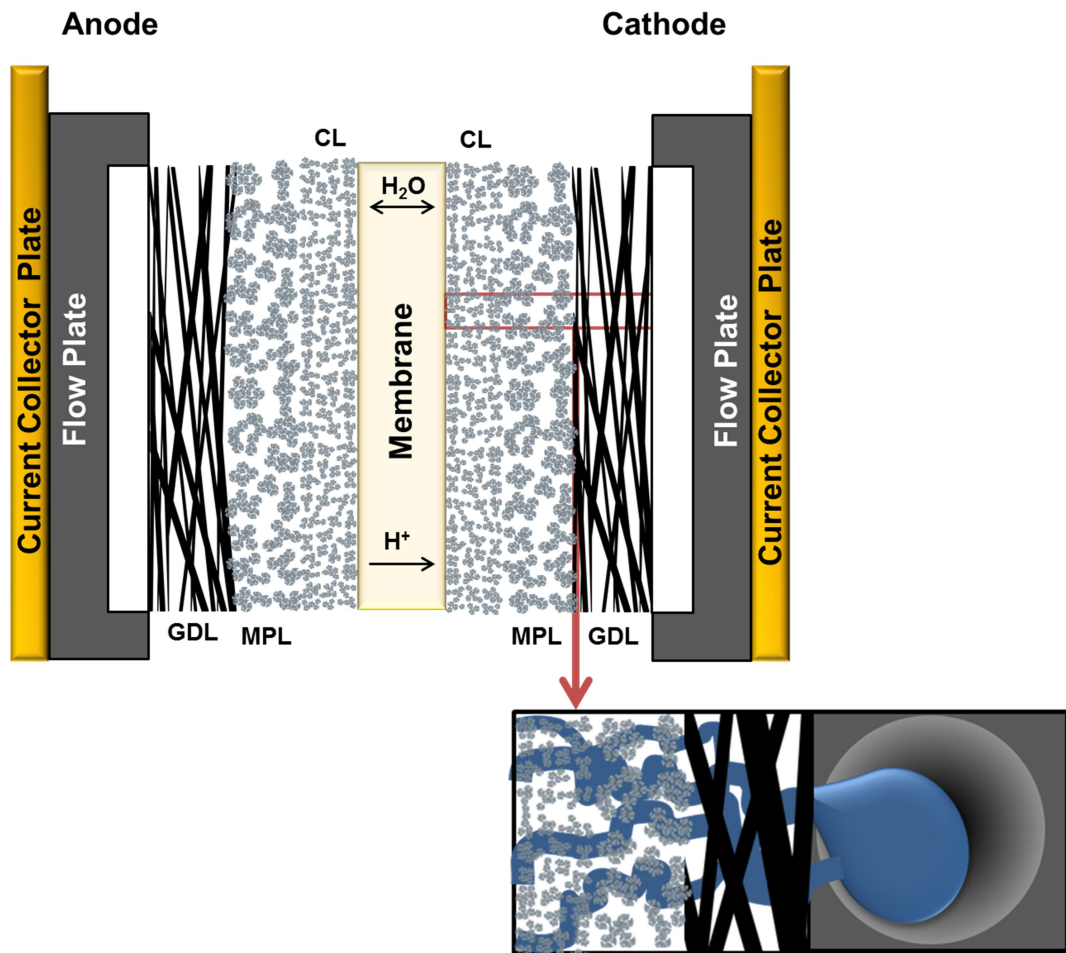


Figure 1.7 Liquid water accumulation in the gas channels

In order to provide distinct pathways, hydrophobic agents can be added to the catalyst ink. By this way, excess water removal can be facilitated. In addition, the portion of the reactant gasses access to active catalyst sites is increased. Figure 1.8 shows the catalyst aggregate including hydrophobic agent providing distinct pathways for gas and liquid. However, (Friedmann & Van Nguyen 2010), revealed that in the case of Polytetrafluoroethylene (PTFE) addition to the CL, PTFE nanoparticles occupy the active catalyst sites instead of Nafion, therefore the performance decreases. They proposed a preparation method completed the ink in two steps. In this method, Nafion was added in the steps and PTFE was added in the second step, by this way, being the occupation of the active catalyst by PTFE nanoparticles were diminished.

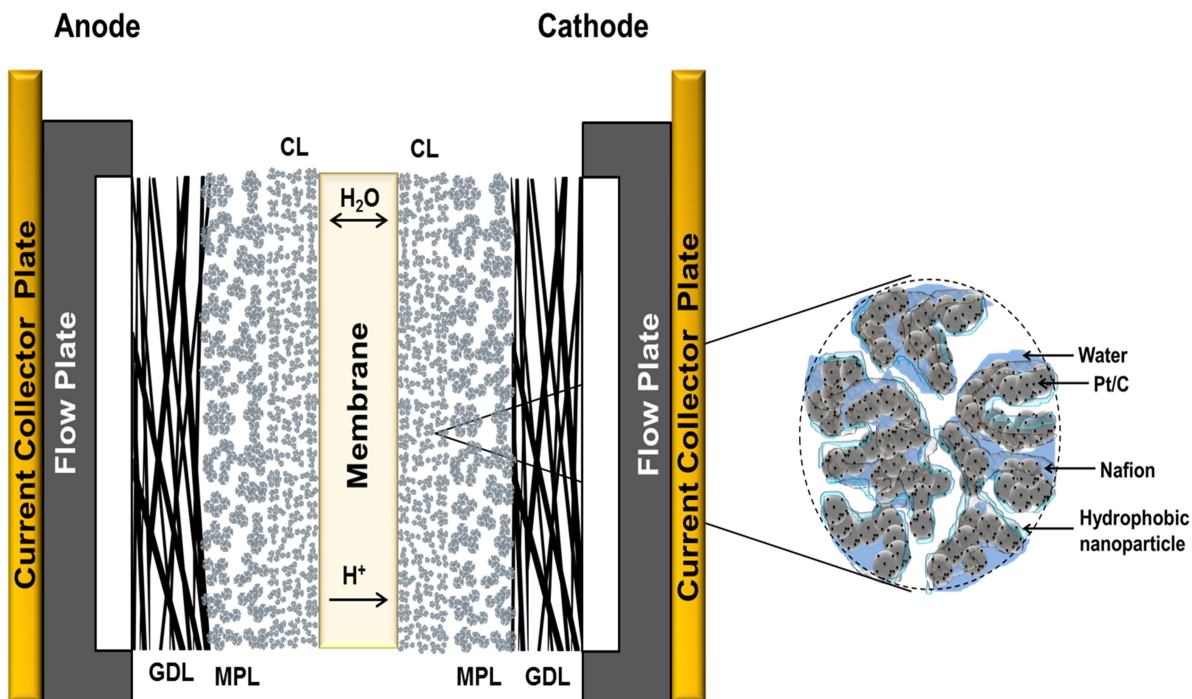


Figure 1.8 Catalyst aggregate including hydrophobic agent providing distinct pathways for gas and liquid

1.5. Objective of the Work

The objective of this work is to obtain high performance with hydrophobic CLs prepared by ultrasonic coating technique with low Pt-containing (20 wt %) and high Pt-containing (70 wt %) commercial catalyst with the higher (1.2 mg Pt/cm²) and the lower (0.4 mg Pt/cm²) Pt loading.

Here, we also investigated the effect of hydrophobic nanoparticle addition into the CL to enhance water management in high-performance PEM fuel cells. The experimental design has been used to optimize the composition of the CL. Fuel cell performance tests were carried out to determine the highest performance. Reaction kinetics and mass transport limitations were investigated with electrochemical impedance spectroscopy.

In the present study, commercial catalysts were used as Pt source because of reproducibility. The performance of hydrophobic CLs prepared with low Pt content enhanced, however, hydrophobic CLs prepared high Pt content commercial catalyst

did not improve performance with respect to CLs without a hydrophobic agent. This indicated that commercial catalyst may also include a hydrophobic agent. Therefore, further addition of hydrophobic nanoparticles caused a performance decrease. Catalyst powder could be prepared by microwave irradiation technique (Bayrakceken et al. 2008; Fiçicilar et al. 2009), supercritical deposition technique (Bayrakçeken et al. 2008). As a future work, catalyst powder can be prepared by the methods mentioned above, and then the performance of the hydrophobic CLs is studied.

CHAPTER 2

HIGH-PERFORMANCE PEM FUEL CELL CATALYST LAYERS WITH HYDROPHOBIC CHANNELS*

Proton exchange membrane fuel cell performance has been enhanced with efficient water management by modification of the structure of the CLs. In this study, PTFE was added to the anode and cathode CLs by using two-step catalyst ink preparation method. Physical and electrochemical characterization of CLs with hydrophobic nanoparticles was investigated via TGA-DTA, XRD, nitrogen physisorption, SEM, TEM, EDX analysis, and cyclic voltammetry technique. In addition, performance tests of MEAs were carried out. Catalyst layer structure after performance tests was observed by SEM analysis.

2.1. Introduction

PEM fuel cells are promising power generators for stationary, automotive industry, and portable applications. However, challenges in cost, fuel storage, performance losses, and durability make barriers to commercialization of PEM fuel cells. For enhanced performance and durability, providing efficient water and thermal management in each component of the PEM fuel cell is essential. There are two major factors affecting PEM fuel cell performance. One is the sluggish reduction reaction, which leads to kinetic limitations. The other one is water-flooding leading

* Avcioglu, G.S. et al., 2015. High performance PEM fuel cell catalyst layers with hydrophobic channels. *International Journal of Hydrogen Energy*, 40(24), pp.7720–7731.

to mass transport limitations especially at high current densities on the cathode side. Various water management strategies have been developed for each component of the fuel cell. Flow channel design (Van Nguyen & Knobbe 2003; Trabold et al. 2006; Owejan et al. 2007; Li et al. 2007; Bunmark et al. 2010; Martins Belchor et al. 2012), stoichiometric gas flow rate (Weng et al. 2007), structure of GDL (Owejan et al. 2007; Song et al. 2014; Joo et al. 2014; Benziger et al. 2005; Li et al. 2008; Ji & Wei 2009; Dai et al. 2009; Yau et al. 2011; Park et al. 2012) and microporous layer (MPL) addition (Blanco & Wilkinson 2014; Chen et al. 2004; Cho & Mench 2012; Kitahara et al. 2014; Kitahara et al. 2012; Lee et al. 2012; Nam et al. 2009; Pasaogullari & Wang 2004; Qi & Kaufman 2002; Wang et al. 2006; Wang & Van Nguyen 2010; Weber & Newman 2005) have been studied extensively. However, the role of the CL structure on water management has not been explored in detail due to its complexity. Furthermore, among these specific areas, cCL has a primary impact on water balance in addition to cell performance, since water is produced in this layer.

In the CL, electrons travel through electrically conductive carbon support and protons travel through the Nafion ionomer. On the other hand, the reactant gasses travel through the voids. In addition to produced water, water vapor enters the CL with the humidified reactant gasses, accumulates through the voids, and condenses due to a temperature gradient, which results in oxidant transport limitation. When water accumulates through the void spaces of the CL, it blocks the voids; as a result, reactant gasses cannot reach active catalyst sites. This leads to mass transport limitations and decreases the cell performance. Therefore, CL structure has to be designed in such a way that in addition to electrons and protons, a reactant gas, and liquid water should easily travel throughout the porous media. For this purpose, distinct pathways for gas and liquid transport should be provided through the CL. Hydrophobic nanoparticles can be added to the CL structure to provide two-phase flow. Common base polymers such as; polytetrafluoroethylene (PTFE), fluorinated ethylene propylene (FEP), poly(tetrafluoroethylene-co-perfluoro propyl vinyl ether) (PFA), polyvinylidene fluoride (PVDF), ethylene tetrafluoroethylene (ETFE), polyvinyl fluoride (PVF), polyethylene (PE) (Gubler et al. 2005), and polystyrene (Vinodh et al. 2010) can be used as hydrophobic nanoparticles.

In earlier studies, PTFE was used as a binder in CLs. However, due to its lack of proton conductivity, Nafion was started to be used as a binder instead of PTFE (Wilson & Gottesfeld 1992; Uchida 1996; Uchida 1995). Catalyst layer structure has been altered via the addition of hydrophobic nanoparticles on the purpose of providing optimum gas and liquid transport while maintaining three-phase boundary layer. Nguyen et al. (Nguyen et al. 2006), developed a process that created CL structure which provided optimum transport path for electronic, ionic, gas and liquid phase with PTFE nanoparticles via two-step preparation method. Friedmann and Nguyen (Friedmann & Nguyen 2008; Friedmann & Van Nguyen 2010), have proven the relation between the CL structure and the composition. In recent studies, dimethyl silicon oil (DSO) was used as a hydrophobic nanoparticle through the CL because of its oxygen permeable structure (Li et al. 2010). Among various DSO concentrations, the maximum performance was obtained at 0.5 mg/cm² loading (Li et al. 2010). Furthermore, PEM fuel cells with DSO-loaded CL on GDL at cathode side have improved performance in both humidified and dry feed conditions (Li & Chan 2013). PTFE loading via chess and strip patterns on the CL was also studied, and it was found that loading with different patterns has no effect on the performance of thin CLs (Therdthianwong et al. 2012).

The objective of this work is to enhance PEMFC performance by constructing mesoporous hydrophobic channels through the CL with the addition of PTFE nanoparticles using two-step catalyst ink preparation method. To validate that the desired structure is achieved by this two-step catalyst preparation method and the effect of PTFE deposition on the ionic and electronic network, physical, morphological, and electrochemical characterization techniques such as TGA-DTA XRD, nitrogen physisorption, cyclic voltammetry, SEM, TEM, are carried out. Fuel cell performance tests are carried out to investigate the effect of hydrophobic nanoparticle addition to the CL on the mass transport limitation.

2.2. Materials and Methods

2.2.1. Catalyst Ink Preparation

Three different types of catalysts were studied. The commercial catalyst was Pt/C (20 wt % Pt on Vulcan XC-72R, ETEK Inc., USA). Catalyst ink without PTFE was prepared by mixing wet Pt/C catalyst with Nafion solution (15 wt % 1100 EW, Ion Power, Inc., USA) and then adding a mixture of 80/20 (v/v) isopropyl alcohol (Sigma-Aldrich Co. LLC., USA)/water. Nafion amount in the catalyst ink without PTFE was 33 wt % on dry basis. Catalyst ink was mixed for 24 h in a water bath with a magnetic stirrer at room temperature. 30PTFE_AC catalyst ink was prepared via two-step preparation method (Friedmann & Nguyen 2008). The initial step was the same as described above. After mixing step, catalyst ink autoclaved in a vacuum oven (Model: EV 018, Nuve Inc., Turkey). With the sample, the oven was heated from room temperature to 134 °C. It was held for 20 min at 134 °C. Then the oven was cooled down to 75 °C and hold for 20 min more at 75 °C. Afterward, the oven was cooled down to room temperature. In the second step, the dry catalyst was mixed with water and Nafion solution, PTFE dispersion (45.5 wt %), and a mixture of 80/20 (v/v) isopropyl alcohol (IPA)/water for 24 h in a water bath with a magnetic stirrer at room temperature. The weight ratios of Nafion and PTFE amounts were 30 wt% in 30PTFE_AC catalyst ink. It should be noted that the mixture was mixed in an ultrasonic bath for 15 min after each addition. The ratio of IPA and distilled water mixture (ml) to total catalyst weight (g) in the catalyst inks was adjusted to 10/1. The ratio of total volume of distilled water (ml) to total catalyst weight (g) in the catalyst ink was set to 10.4/1. Catalyst ink was dried in an oven under atmospheric pressure at 40 °C for 12 h and then was kept under vacuum at 110 °C for 6 h.

2.2.2. MEA Configuration

Performance testing was carried out with membrane electrode assembly configurations in which PTFE nanoparticles in anode and CL on water transport mechanism was investigated. The Pt, Nafion, and PTFE nanoparticle loadings on CLs for prepared MEAs are summarized in Table 2.1.

Table 2.1 Pt, Nafion, and PTFE loadings in catalyst layers

Catalyst Ink	Loading (mg/cm ²)		
	Pt	Nafion	PTFE
Pt/C	0.4	-	-
without PTFE	0.4	0.90	-
30PTFE	0.4	1.50	1.50

Numbers before PTFE synonym represent the weight percentage of PTFE in the CL on a dry basis. For example, 30PTFE_AC represents the MEA that has 30 wt % PTFE on both anode and cathode CLs.

2.2.3. Physical Characterization

Physical and morphological characterization of the catalysts was performed by using TGA-DTA, Nitrogen physisorption, XRD, SEM, TEM, and EDX analyses.

2.2.3.1. TGA and DTA analysis

A modular simultaneous TGA&DTA thermal analyzer (SETSYS Evolution TGA-DTA/DSC, Seteram Instrumentation, France) performed thermogravimetrically (TGA) and differential thermal analyses (DTA) of catalysts. Aluminum pans were used in all experiments. For TGA and DTA analyses, samples were heated from room temperature to 1000 °C with a heating ramp of 3 °C/min under airflow.

2.2.3.2. Nitrogen physisorption analysis

Brunauer–Emmett–Teller (BET) surface area, pore size distribution, and pore volume characterization were performed with a surface area analyzer (Micromeritics TriStar II 3020 V1.04, Particle & Surface Sciences Pty. Limited, Australia). All samples were degassed at 110 °C for 3 h before analysis. Adsorption/desorption isotherms were measured at -196 °C. Pore size distribution data were calculated from desorption branches of nitrogen isotherms by the Barrett Joyner Halenda (BJH) method.

2.2.3.3. XRD analysis

The X-ray diffractograms (XRD) of the catalysts were determined by an X-Ray Diffractometer (PW1840 of M/s Philips NV, Netherlands) equipped with a Cu X-ray tube and a multilayer mirror (0.154 nm for Cu-K α 1 radiation). X-ray emission spectra of the X-ray tube were filtered using a Ni absorber. XRD measurements were performed in a range of 5° to 90° with a 2 θ step of 0.1. The diffractometer was operated at 30 kV and 24 mA Cu-K α radiation. In order to determine the Pt crystallite size, MDI Jade 5.0 program was used.

2.2.3.4. SEM analysis

Scanning Electron Microscopy (SEM) images for powders of commercial catalyst (Pt/C), commercial catalyst impregnated with Nafion (without PTFE), and commercial catalyst impregnated with Nafion and 30 wt % PTFE (30PTFE_AC) were taken by using high-resolution scanning electron microscope system (FEI QUANTA 400F Field Emission, FEI Company, USA) included secondary electrons (SE) in high vacuum modes. Energy-dispersive X-ray spectroscopy (EDX) of the catalyst samples were obtained by the instrument. In order to provide conductivity, ultrathin (5 nm) coating of gold/palladium alloy was deposited on samples by low vacuum sputter coating. Coated samples were fixed on aluminum holder before analysis. SEM images of membrane electrode assemblies (MEAs) were obtained by using high-resolution scanning electron microscope system (FEI QUANTA 400F Field Emission, FEI Company, USA) included secondary electrons (SE) in high vacuum modes. The images were taken from the cross section of the membrane electrode assemblies. Samples were prepared by submerging half of the MEA into liquid nitrogen then breaking it into two parts. Ultrathin (5 nm) coating of gold/palladium alloy was deposited on samples by low vacuum sputter coating to provide conductivity. Coated samples were fixed on aluminum holder before analysis.

2.2.3.5. TEM analysis

Transmission electron microscopy (TEM) images for powders of commercial catalyst (Pt/C), commercial catalyst impregnated with Nafion (without PTFE), and commercial catalyst impregnated with Nafion and 30 wt % PTFE (30PTFE_AC

were taken by using a conventional transmission electron microscope system (FEI Tecnai G2 F30 HRTEM, FEI Company, USA) operated at 200 kV. Samples used for TEM analysis were prepared by suspending the catalyst powder in ethanol and mixing with an ultrasonic probe. As the homogeneous mixture was obtained, the sample was loaded on the carbon-covered grid and dried completely before analysis.

2.2.4. Electrochemical Characterization

Electrochemical characterization of catalysts was performed by cyclic voltammetry experiments. The experiments were repeated until the similar voltammograms were obtained.

2.2.4.1. Cyclic voltammetry analysis

Cyclic voltammetry (CV) measurements were performed in a three-electrode cell containing 0.1 M HClO₄ at 20 °C temperature. Bipotentiostat (Pine AFCBP1, Pine Instrument Company, USA) was used for the experiments. Working electrode was a glassy carbon disk with a 0.5 cm diameter cavity inserted into a Teflon holder. The reference electrode was made up of Ag/AgCl, filled with 0.1 M KCl solution and the counter electrode was a platinum wire. Prior to experiments, the electrolyte was purged with N₂ for 30 min. Experiments were performed under N₂ atmosphere. Working electrode was polished with 5-micron Alumina slurry (Micropolish, Buehler, ITW Company, USA) on a polisher (Microcloth, Buehler, ITW Company, USA) after every experiment. Platinum loading on working electrode was fixed at 28 μg Pt/cm². The concentration of the cyclic voltammetry ink of commercial catalyst (Pt/C) was fixed at 4 mgcat/ml. The concentration of cyclic voltammetry inks of without PTFE and 30PTFE_AC catalysts were fixed at 8 mgcat/ml. The ink of the catalysts was prepared by mixing the catalysts with the mixture of 20/80 (v/v) 1,2 Propandiol/water. The deposited aliquot volume of powders of commercial catalyst (Pt/C), commercial catalyst impregnated with Nafion (without PTFE), and commercial catalyst impregnated with Nafion and 30 wt % PTFE (30PTFE_AC) were 7.68, 5.62, and 8.80 mL, respectively. The aliquots were left overnight to dry under ambient atmosphere. Cyclic voltammograms were recorded at 50 mV/s scan

rate from -0.28 V to 1.2 V. Potentials were referenced to normal hydrogen electrode for Ag/AgCl reference electrode at 25 °C.

2.3. Results and Discussions

2.3.1. Physical Characterization

2.3.1.1. Thermogravimetric analysis

Thermogravimetric analyses were performed to investigate the limits of the thermal stability of the catalysts in addition to estimating Pt content in the catalysts, roughly.

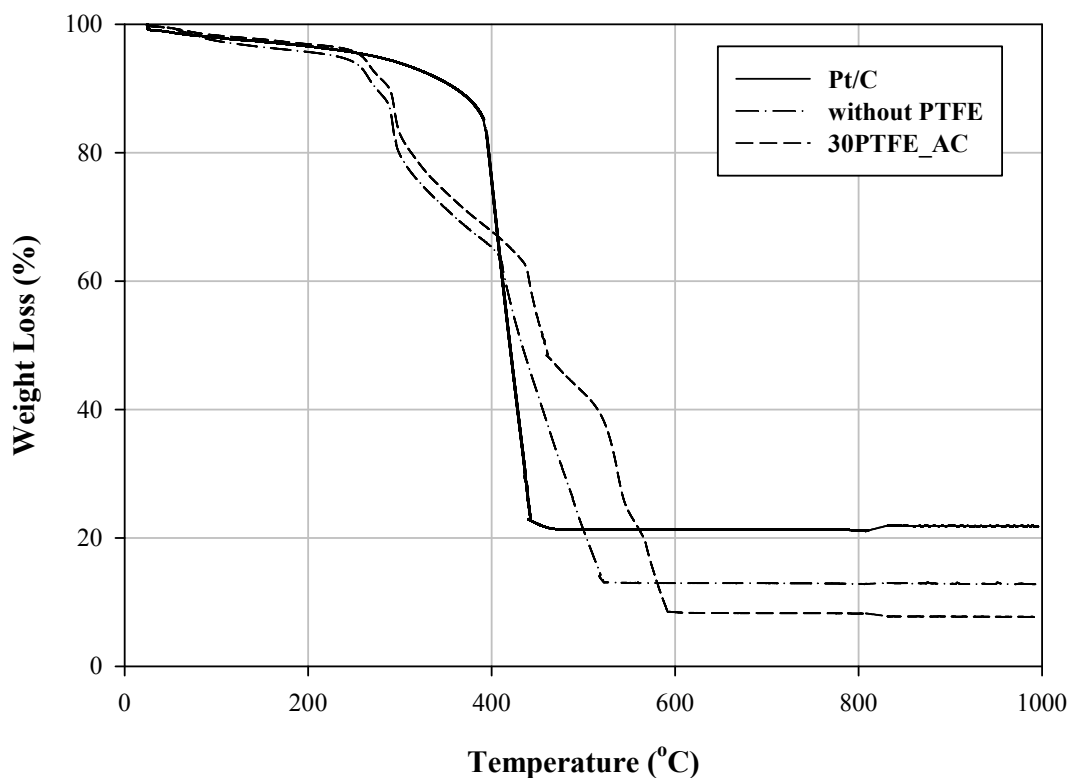


Figure 2.1 Thermogravimetric analyses for powders of commercial catalyst (Pt/C), commercial catalyst impregnated with Nafion (without PTFE), and commercial catalyst impregnated with Nafion and 30 wt % PTFE (30PTFE_AC). The measurements were performed in air

Weight loss curves of thermogravimetric analyses for powders of commercial catalyst (Pt/C), commercial catalyst impregnated with Nafion (without PTFE), and commercial catalyst impregnated with Nafion and 30 wt % PTFE (30PTFE_AC) are given in Figure 2.1. The final weight percentage of the catalyst corresponds to its Pt content. As it is summarized in Table 2.2; commercial catalyst (Pt/C) has 21 wt % Pt, commercial catalyst impregnated with Nafion (without PTFE) has 13 wt % Pt and commercial catalyst impregnated with Nafion and 30 wt % PTFE (30PTFE_AC) has 8 wt % Pt. There were three distinctive weight loss regions for commercial catalyst. In the first region, from room temperature to 360 °C, there was a little weight loss (10 wt %) observed. Only, water and volatile species were removed. In the second region, significant weight loss (69 wt %) occurred between 360 and 470 °C. This loss was attributed to Pt catalyzed carbon oxidation (Baturina et al. 2006). Vulcan XC-72 carbon black decomposes between 550 °C and 750 °C however; Pt accelerated decomposition of carbon black. In the third region, the sample reached a constant weight that reflected Pt weight percentage (21 wt %) in the commercial catalyst.

The weight loss curve of commercial catalyst impregnated with Nafion was divided into four distinctive regions. In the first region, volatiles (6 wt %) were removed. In the second region, weight loss (27 wt %) was observed between 230 and 380 °C which was attributed to Nafion decomposition. Even though Nafion decomposes between the temperature range of 350 and 550 °C (Samms et al. 1996; Devrim et al. 2013), Pt accelerated its decomposition (Baturina et al. 2006). Another significant weight loss (54 wt %) occurred between 380 and 530 °C due to Pt catalyzed carbon oxidation. After 530 °C, the sample weight stabilized, remained mass reflected Pt amount (13 wt %).

There were five distinctive weight loss regions for 30PTFE_AC. In the first region, 3.6 wt % of the catalyst were lost due to decomposition of volatiles. In the second region, Nafion (weight loss 26.4 wt %) was decomposed between 230 and 380 °C. Significant weight loss (30 wt %) due to Pt-catalyzed carbon oxidation occurred between 380 and 510 °C in the third region. According to the thermogravimetric analysis of pure PTFE, decomposition should begin at 260 °C, while significant decomposition occurs above 400 °C (Samms et al. 1996) and continues up to 590 °C (Devrim et al. 2013). The weight loss (32 wt %) observed between 510 and 590 °C was mainly due to PTFE decomposition. Remained mass (8

wt %) reflected Pt amount in the 30PTFE_AC. Compared to commercial catalyst impregnated with Nafion (without PTFE), PTFE addition increased the thermal stability of the catalyst.

2.3.1.2. Differential thermal analysis

DTA analyses were performed in order to determine decomposition temperatures of carbon, Nafion, and PTFE. Curves of differential thermal analysis for powders of commercial catalyst (Pt/C), commercial catalyst impregnated with Nafion (without PTFE), commercial catalyst impregnated with Nafion and 30 wt % PTFE (30PTFE_AC) are shown in Figure 2.2. DTA curve for powder of the commercial catalyst (Pt/C) had one major peak appeared between 360 and 470 °C, which reflected the decomposition of Vulcan XC-72R (Baturina et al. 2006).

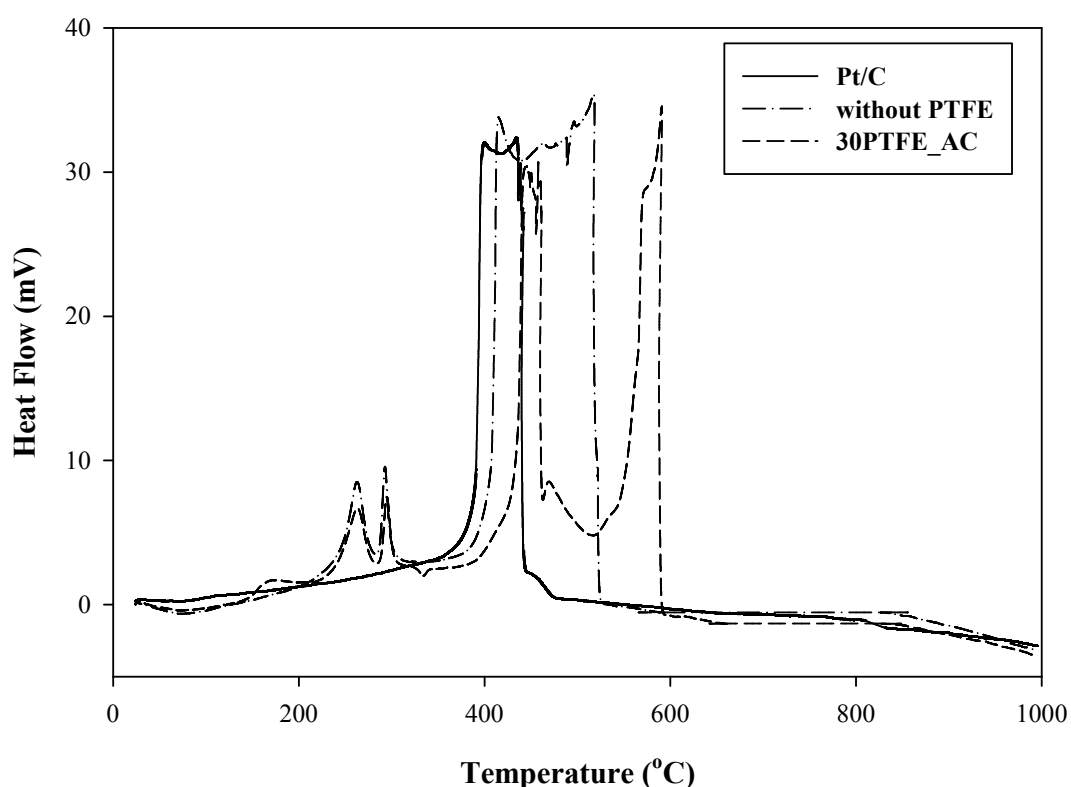


Figure 2.2 Differential thermal analysis curves for powders of commercial catalyst (Pt/C), commercial catalyst impregnated with Nafion (without PTFE), commercial catalyst impregnated with Nafion and 30 wt % PTFE (30PTFE_AC). The measurements were performed in air

On the other hand, three exothermic peaks occurred at DTA curve of commercial catalyst impregnated with Nafion (without PTFE). The first two, between 230 and 380 °C, reflected decomposition of Nafion while the third peak, between 380 and 530 °C, represented decomposition of Vulcan XC-72R. There were four exothermic peaks occurred at DTA curve of 30PTFE_AC. The first two peaks appeared between 230 and 380 °C represented Nafion decomposition. The third peak with higher intensity occurred between 380 and 510 °C represented carbon decomposition. The fourth peak occurred between 510 °C and 590 °C represented PTFE decomposition. TGA and DTA analysis verified the composition of catalysts synthesized in the present work.

Table 2.2 Physical and electrochemical characterization of powders of commercial catalyst, Pt/C (EOTEK), commercial catalyst impregnated with Nafion (without PTFE), commercial catalyst impregnated with Nafion and 30 wt % PTFE (30PTFE_AC)

	Pt/C	Without PTFE	30PTFE
Pt wt % (theoretical value)	20	14	8
Pt wt %^a	21	13	8
d_{Ptavg}^b (nm)	2.7	3.9	3.5
SA_{Pt}^b (m²/g)	103	71	79
ESA^c (m²/g)	77	70	45
U_{Pt}^c (%)	75	99	56
SA_{BET}^d (m²/g)	166	50	12
V_{poreCum}^d (cm³/g)	0.27	0.1	0.04
V_{pporeCum}^d (cm³/g)	0.13	0.02	0.01
V_{sporeCum}^d (cm³/g)	0.14	0.08	0.03
dpore_{avg}^d (nm)	3.7	14.1	14.2

^a Determined by TGA analysis

^b Calculated from XRD data

^c Calculated from Cyclic Voltammetry data

^d Calculated from nitrogen physisorption data

2.3.1.3. XRD analysis

XRD patterns for powders of commercial catalyst (Pt/C), commercial catalyst impregnated with Nafion (without PTFE), commercial catalyst impregnated with Nafion and 30 wt % PTFE (30PTFE_AC) are shown in Figure 2.3. All of the

patterns clearly show the presence of the elemental platinum with the five characteristic peaks of face centered cubic crystalline platinum. The Bragg angles of ca. 40°, 46°, 67°, 81°, 86° correspond to (111), (200), (220), (311) (He 1997; Pozio et al. 2002), and (222) (Zhang et al. 2010) Pt facets, respectively.

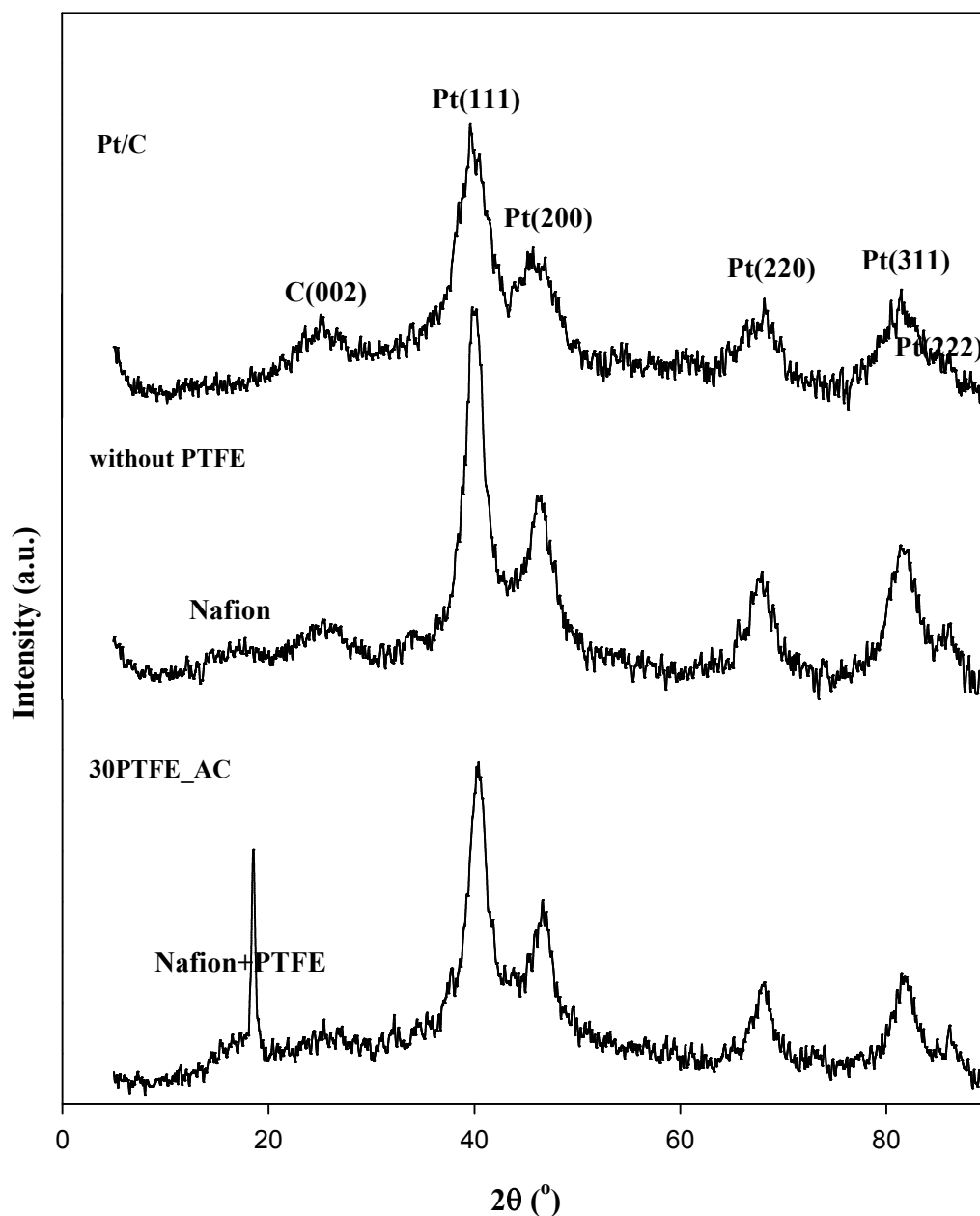


Figure 2.3 XRD patterns of powders of commercial catalyst (Pt/C), commercial catalyst impregnated with Nafion (without PTFE), and commercial catalyst impregnated with Nafion and 30 wt % PTFE (30PTFE_AC)

The intensity of diffraction peak of Pt (222) was weak only in the pattern of Pt/C catalyst. The peak at ca. 25° Bragg angle observed for all patterns corresponds to the hexagonal graphite structures, (002), of Vulcan XC-72R support material used by ETEK (He 1997), (Li et al. 2003). This rather wide and shallow carbon peak indicated that XC-72R was an amorphous carbon material with small regions of crystallinity (Li et al. 2003). The peak appeared at the diffraction pattern for powder of commercial catalyst impregnated with Nafion (without PTFE) at ca. 17° Bragg angle was attributed to poly-fluorocarbon chains of Nafion ionomer (Jung et al. 2003). The broadness of the Nafion peak pointed out the amorphous structure of the polymer. The sharp peak occurred at ca. 18.4° Bragg angle corresponded to a crystalline component of PTFE (Lebedev et al. 2010). Nafion and PTFE peaks were overlapped at the diffraction pattern for powder of 30PTFE_AC catalyst, since corresponding Bragg angles of Nafion and PTFE were very close to each other.

Average diameter of Pt crystallite was calculated using Scherrer formula as below:

$$d_{Pt} = \frac{K\lambda}{\beta \cos(\theta_{\beta})} \quad 0.1$$

d_{Pt} is the average Pt crystallite size (nm), K is the Scherrer constant (depends on the crystallite shape; for spherical particles with cubic symmetry it is 0.94), λ is the wavelength of incident X-rays (0.154 nm for Cu- $K_{\alpha 1}$ radiation), β is the full width of the strongest diffraction peak at half height (radians), θ is the Bragg angle at the position of peak the maximum (radian)

Total Pt surface area was calculated using the equation below, considering particles have spherical shape:

$$SA_{Pt} = \frac{6000}{\rho_{Pt} d_{Pt}} \quad 0.2$$

SA_{Pt} is the total surface area of Pt particles (m^2/g), d_{Pt} is the average Pt crystallite size (nm), and ρ_{Pt} is the density of Pt particles (21.4 g/cm^3). In order to

determine the Pt crystallite size from diffraction patterns, MDI Jade 5.0 program was used.

Average Pt crystallite size of powders of commercial catalyst (Pt/C), commercial catalyst impregnated with Nafion (without PTFE), and 30PTFE_AC were 2.7 nm, 3.9 nm, and 3.5 nm and total Pt surface area were 103m²/g, 71m²/g, and 79m²/g, respectively (Table 2.2). Nafion impregnation caused agglomeration of Pt particles. However, further PTFE addition did not increase the average particle diameter; even Pt agglomeration had been reduced. By heat treatment after Nafion impregnation, the ionomer phase was steam annealed onto the catalyst particles to cover all accessible catalyst surface areas. Since the catalysts particles were already covered by the ionomer, PTFE could no longer block the active catalyst sites thus placed itself into the voids (Friedmann & Van Nguyen 2010). Total Pt surface area and average particle diameter of commercial catalyst (Pt/C), obtained from XRD data, were compatible with the literature values (Pozio et al. 2002; Antolini et al. 2001; Prabhuram et al. 2004; Zhang et al. 2011).

2.3.1.4. Nitrogen physisorption analysis

Figure 2.4 illustrates nitrogen adsorption/desorption isotherms for powders of commercial catalyst (Pt/C), commercial catalyst impregnated with Nafion (without PTFE), commercial catalyst impregnated with Nafion and 30 wt % PTFE (30PTFE_AC). All isotherms are compatible with isotherm of Type IV according to IUPAC classification which is typical for the mesoporous structure of catalysts (Brunauer et al. 1940; Sing 1985). Furthermore, the hysteresis loops with steep and parallel adsorption-desorption branches were denoted as Type H1 according to IUPAC classification, indicating the formation of open-ended unconnected pores (Do 1998; Thomas & Thomas 2015).

BET surface area was calculated from nitrogen physisorption data for Pt/C (166 m²/g), Pt/C-Nafion (50 m²/g), and 30PTFE_AC (12 m²/g) catalysts are tabulated in Table 2.2. Zhang et al. (Zhang et al. 2011), obtained similar BET surface area for powders of commercial catalyst (Pt/C), commercial catalyst impregnated with Nafion (without PTFE). Nafion ionomer addition to the commercial catalyst (Pt/C) decreased 70% of the BET surface area by blocking 67% of the cumulative pore volume. BJH desorption average pore diameter of commercial catalyst

impregnated with Nafion (without PTFE) (14.1 nm) was bigger than the commercial catalyst (Pt/C) (3.7 nm); while BJH desorption cumulative pore volume (0.1 cm³/g) was less than the Pt/C catalyst (0.3 cm³/g). These results showed that some of the mesopores have been blocked and new mesopores with larger diameters have been formed. The addition of PTFE nanoparticles decreased 76 % of the BET surface area for powder of commercial catalyst impregnated with Nafion (without PTFE) and blocked 60% of the cumulative pore volume (0.04 cm³/g). BJH desorption average pore diameter (14.2 nm) remained constant while cumulative pore volume decreased which was the further evidence to blockage of the pores with the addition of PTFE nanoparticles.

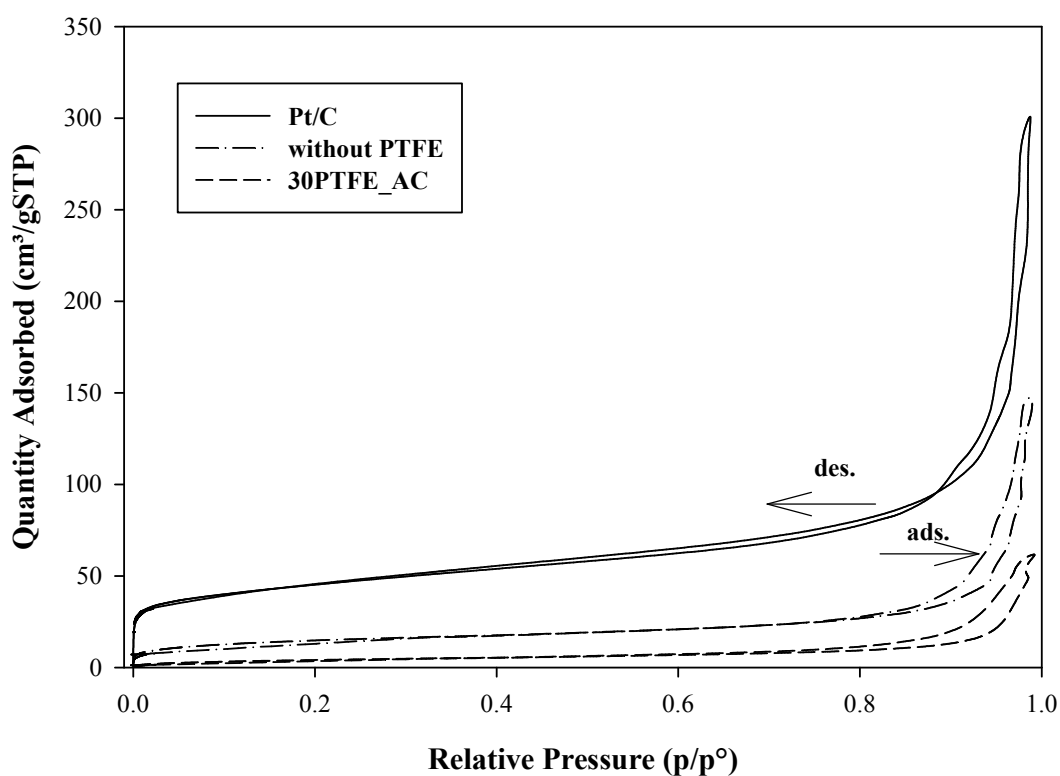


Figure 2.4 Adsorption/desorption isotherms for powders of commercial catalyst (Pt/C), commercial catalyst impregnated with Nafion (without PTFE), commercial catalyst impregnated with Nafion and 30 wt % PTFE (30PTFE_AC)

The pore structure of the CL was divided into two typical pore distributions; primary and secondary pores (Watanabe et al. 1985). Primary pores work as a reaction volume and the secondary pores work as main gas channels (Watanabe et al. 1985). Pore diameters of all catalysts (see Figure 2.5) were spread into meso/macroporous region and were mainly distributed from 0.01 to 0.1 μm . Pores from 0.02 to 0.04 μm were defined as primary pores, pores from 0.04 to 0.1 μm were defined as secondary pores (Uchida 1996; Uchida 1995). Impregnation of Nafion ionomer into commercial catalyst (Pt/C) lessened the volume of the primary (70%) and of the secondary (32%) pores. Therefore, both reaction volume and gas channel volume decreased. Further addition of PTFE to commercial catalyst impregnated with Nafion (without PTFE) further blocked primary pores (32%) almost completely; whereas the volume of the secondary pores (68%) decreased. Furthermore, remained pores mainly distributed from 0.05 to 0.1 μm .

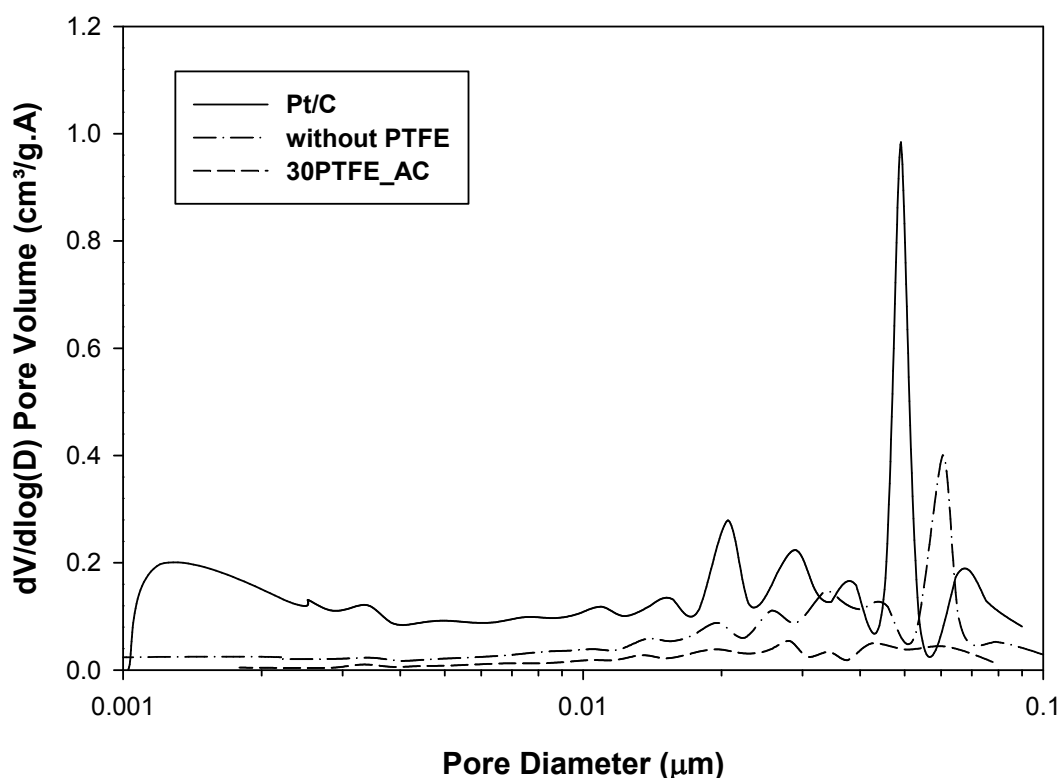


Figure 2.5 Pore size distributions for powders of commercial catalyst Pt/C (E TEK), commercial catalyst impregnated with Nafion (without PTFE), and commercial catalyst impregnated with Nafion and 30 wt % PTFE (30PTFE_AC)

The pore distribution results indicate that both Nafion and PTFE addition to the CL structure decreased reaction volume. In addition to that, Nafion and PTFE addition to the CL structure caused structural changes, which were more pronounced by Nafion addition.

2.3.2. Electrochemical Characterization

2.3.2.1. Cyclic voltammetry analysis

Figure 2.6 illustrates cyclic voltammograms of commercial catalyst (Pt/C), commercial catalyst impregnated with Nafion (without PTFE), commercial catalyst impregnated with Nafion and 30 wt % PTFE (30PTFE_AC). Hydrogen adsorption/desorption peaks observed from 0.0 to 0.3 V both for the anodic and cathodic directions. Pt oxidation was observed between 0.7 and 1.2 V at the cathodic direction and Pt reduction was observed at 0.9 and 0.4 V at anodic direction. The peak observed between 0.4 and 0.7 V at the cathodic direction of voltammogram for Pt/C catalyst indicated carbon oxidation. This peak revealed that carbon amount in the commercial catalyst (Pt/C) was higher than the required amount which can lead to carbon corrosion, accordingly, lead to a decline in cell performance in long-term studies (Şayin et al. 2012). Electrochemical surface area was calculated from cyclic voltammetry analysis by using the following equation:

$$ESA = \frac{Q_{H_{avg}}}{Q_{H_{ref}} L_{Pt}} 10^{-1} \quad 0.3$$

ESA is the electrochemical surface area (m^2/g), $Q_{H(avg)}$ is the average charge density of adsorption and desorption charges (mC/cm^2) on glassy carbon disc electrode, L_{Pt} is the Pt loading on glassy carbon disc electrode (mg/cm^2), $Q_{H(ref)}$ is the specific charge determined by the adsorption of one monolayer of hydrogen on an atomically flat polycrystalline Pt electrode ($210 \mu C/cm^2$)

Pt utilization of the catalysts was calculated by using the equation below;

$$U_{Pt} = \frac{ESA}{SA_{Pt}} 100 \quad 0.4$$

where U_{Pt} is the Pt utilization of the catalyst (%), ESA is the electrochemical surface area of the catalyst determined by cyclic voltammetry (m^2/g), SA is the total surface area of Pt particles (m^2/g).

Commercial catalyst (Pt/C) had the highest electrochemical surface area ($77 m^2/g$) compared to commercial catalyst impregnated with Nafion (without PTFE), and 30PTFE_AC.

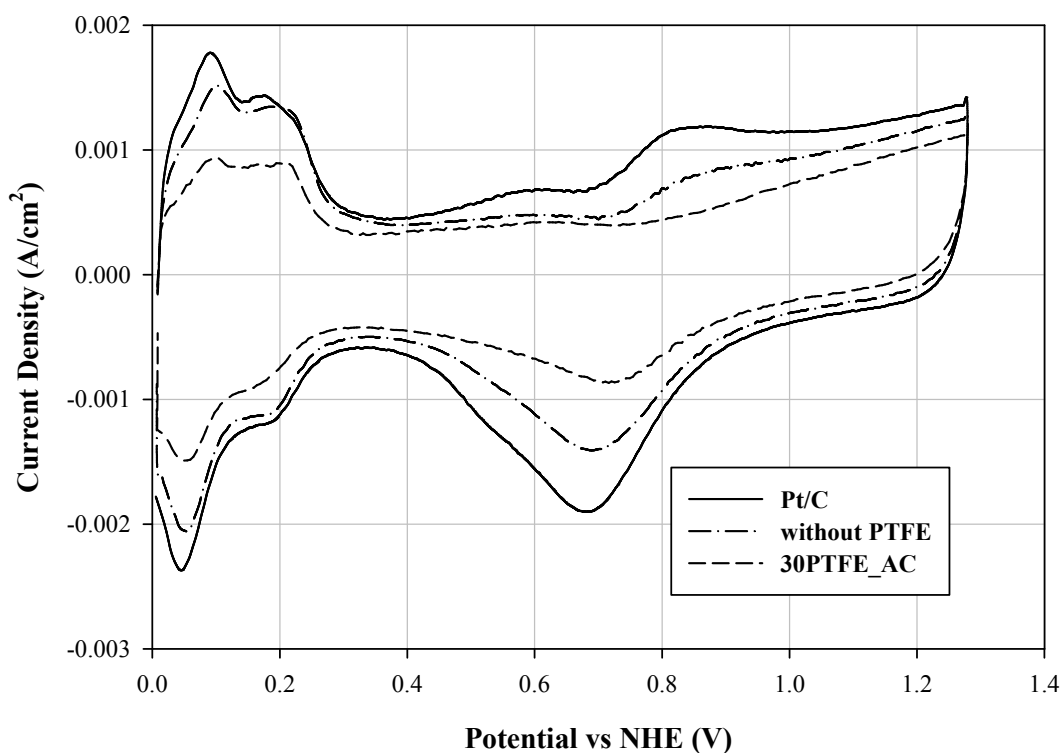


Figure 2.6 Cyclic voltammograms of commercial catalyst (Pt/C), commercial catalyst impregnated with Nafion (without PTFE), and commercial catalyst impregnated with Nafion and 30 wt % PTFE (30PTFE_AC)

This was attributed to the highest total Pt surface area in the commercial catalyst (Pt/C). Schmidt et al. (Schmidt & Gasteiger 1998), obtained similar electrochemical surface area ($69 \text{ m}^2/\text{g}$) for Pt/C catalyst with the same Pt loading ($28 \text{ mg}/\text{cm}^2$) on glassy carbon disk. Nafion addition to the commercial catalyst (Pt/C) decreased the electrochemical surface area ($70 \text{ m}^2/\text{g}$). Although the total Pt surface area of commercial catalyst impregnated with Nafion (without PTFE) was lower than the commercial catalyst (Pt/C), Pt utilization of commercial catalyst impregnated with Nafion (without PTFE) (99%) was higher than the commercial catalyst (75%). This result could be interpreted as Nafion impregnation caused Pt agglomeration; however, enhanced Pt utilization. Cheng et al. (Cheng et al. 1999), obtained 77.8% Pt utilization when the electrode was sufficiently immersed with Nafion, which was lower than the Pt utilization obtained for commercial catalyst impregnated with Nafion (without PTFE) in this study. Electrochemical surface area of 30PTFE_AC was $45 \text{ m}^2/\text{g}$ while Pt utilization was 56%. Decrease in the electrochemical surface area and Pt utilization with PTFE addition to commercial catalyst impregnated with Nafion (without PTFE) was attributed to the disruption of three-phase boundary and blockage of active sites. Song et al. (Song et al. 2010), also reported that PTFE addition decreased the electrochemical surface area, but enhanced the diffusion process in the CL.

2.3.3. Performance Tests

PEM fuel cell tests were also performed to determine the electrocatalytic activity of the prepared catalysts in the fuel cell environment. Raw cell voltage vs. current density data of three different catalysts were fitted to a sufficiently accurate approximation of the fuel cell polarization curve the equation given below:

$$E_{\text{cell}} = E_{\text{OCV}} - \frac{RT}{\alpha F} \ln \left(\frac{i}{i_0} \right) - \frac{RT}{nF} \ln \left(\frac{i_L}{i_L - i} \right) - iR_i \quad 0.5$$

where E_{cell} is the raw voltage (V), E_{OCV} is the open circuit voltage (V), R is the universal gas constant ($8.314 \text{ J}/\text{mol K}$), T is the cell temperature (K), α is the transfer coefficient, F is the Faraday's constant ($96,485 \text{ C}/\text{mol}$), i is the raw current

density (A/cm^2), i_0 is the exchange current density (A/cm^2), n is the number of electrons involved in reaction which is 2, i_L is the limiting current density (A/cm^2), R_i is the internal resistance ($\Omega.cm^2$)

A more quantitative assessment of the oxygen reduction reaction kinetics on PEMFC performance can be achieved by examining the resistance corrected cell voltages (Gasteiger et al. 2005). $E_{iR-free}$:

$$E_{iR-free} = E_{cell} + iR_i \quad 0.6$$

Figure 2.7 illustrates iR corrected polarization curves and power vs current density plots for the commercial catalyst (Pt/C), commercial catalyst impregnated with Nafion (without PTFE), commercial catalyst impregnated with Nafion and 30 wt % PTFE (30PTFE_AC). The effect of PTFE addition to the catalyst can be seen much clearly in Figure 2.7. The maximum power density was $0.32 W/cm^2$ obtained at the current density of $0.70 A/cm^2$ at $0.45 V$ for 30PTFE_AC. The power density was $0.28 W/cm^2$ obtained at the current density of $0.60 A/cm^2$ at $0.45 V$ for commercial catalyst impregnated with Nafion (without PTFE) and $0.13 W/cm^2$ at the current density $0.35 A/cm^2$ and $0.30 V$ for Pt/C catalyst. These results were in accordance with the previous studies carried out Pt/C commercial catalyst (Bayrakceken et al. 2008; Şengül et al. 2008). Results of TGA analysis indicated that Pt content of these catalysts was different. The commercial catalyst had 20 wt % Pt on Vulcan XC-72R carbon support. However, the addition of Nafion decreased the Pt amount to 13 wt % (commercial catalyst impregnated with Nafion) and further addition of PTFE decreased Pt amount to 8 wt %. We adjusted the same Pt loading as $0.4 mg/cm^2$ for on gas diffusion electrodes. Although ultrasonic coating was a very effective method, the decrease in Pt percent in the catalysts caused an increase of the thickness of the active layer (Erkan & Eroglu 2015). Therefore, the performance of the MEA was slightly negatively affected at low current densities from further mass transfer limitation. It should be emphasized that we observed a significant positive effect of Nafion addition to the catalyst on performance in all current density range and the addition of PTFE had a further enhancement on performance, especially at higher current densities. Qi and Kaufman (Qi & Kaufman 2002) who had also used

commercial 20 wt % Pt/C catalyst (E TEK) obtained 1.25 A/cm^2 at 0.45 V with higher catalyst loading as 1.7 mg/cm^2 . Li et al. (Li et al. 2010), obtained 1.50 A/cm^2 at 0.45 V performance with DSO loaded CL which had 0.4 mg/cm^2 Pt loading. Li et al., (Li & Chan 2013) also reported 0.75 A/cm^2 at 0.45 V performance with DSO loaded cCL on MPL and on gas diffusion media with a 0.5 mg/cm^2 Pt loading. Song et al. (Song et al. 2010), observed 1.0 A/cm^2 at 0.45 V performance with 5 wt % PTFE included CL with 0.4 mg/cm^2 Pt loading on each side (50 wt % Pt/C Johnson Matthey) in an H_2/Air fuel cell. Friedmann et al. (Friedmann & Nguyen 2008; Friedmann & Van Nguyen 2010) obtained 1.15 A/cm^2 at 0.45 V by using Tanaka Pt/C with 46 wt % of Pt for the cathode catalyst ink preparation.

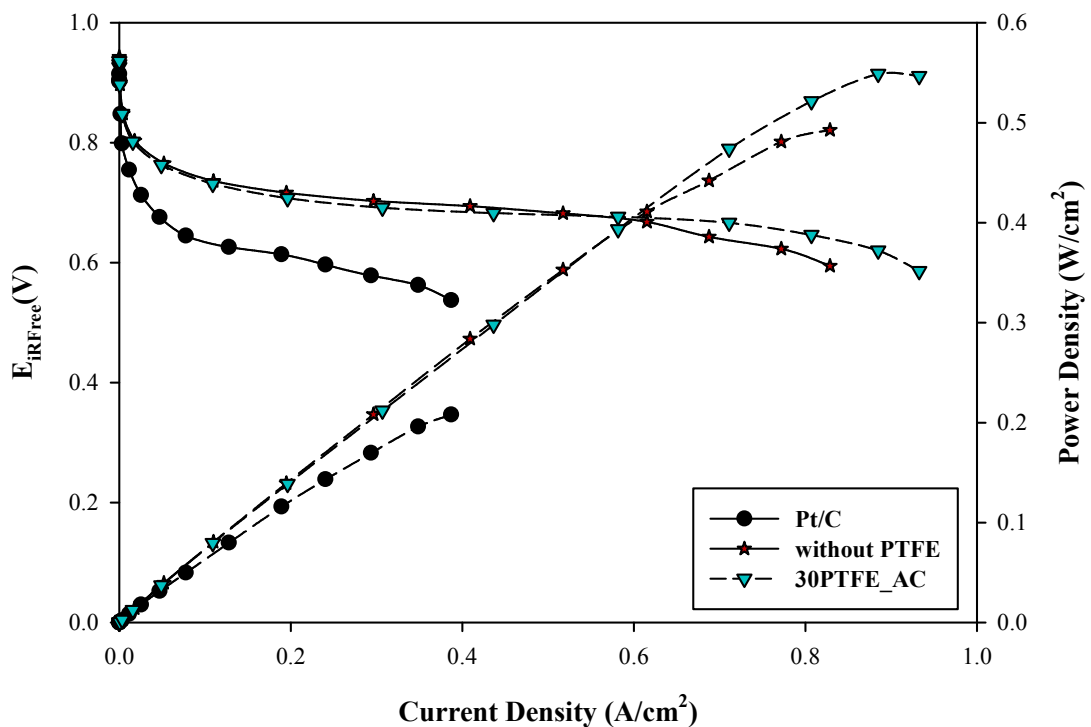


Figure 2.7 iR corrected polarization curves and power density vs. current density curves for commercial catalyst (Pt/C), commercial catalyst impregnated with Nafion (without PTFE), commercial catalyst impregnated with Nafion and 30 wt % PTFE (30PTFE_AC)

They reported that optimal compositions of the cCL were Carbon:Nafion:PTFE=1:0.875:0.875 and Carbon:Nafion:PTFE=1:1.375:0.375 with a catalyst loading of 0.55 and 0.45 mg/cm^2 , respectively. With these compositions,

their fuel cells had peak powers of 0.60 and 0.52 W/cm² and limiting current densities greater than 1.50 A/cm². They showed the advantage of the structure of the CL prepared with the two-step method compared to the conventional one-step method.

The values of the model parameters of Equation (5) α , i_0 , i_L and R_i are listed in Table 2.3. The transfer coefficient α was 0.82 for both commercial catalyst (Pt/C) and commercial catalyst impregnated with Nafion and 30 wt % PTFE (30PTFE_AC), while it was increased to 0.95 for commercial catalyst impregnated with Nafion (without PTFE).

Table 2.3 The non-linear regression parameters for 0-D model of equation 2.5

	α	$i_0 \cdot 10^{-4}$ (A/cm ²)	i_L (A/cm ²)	R_i (Ω cm ²)
Pt/C	0.82	0.55	0.39	0.64
Without PTFE	0.95	1.2	0.83	0.36
30PTFE AC	0.82	2.4	0.91	0.26

High values of α indicate that all of these catalysts were effective. The exchange current density was 0.055 mA/cm² for commercial catalyst (Pt/C), 0.12 mA/cm² for commercial catalyst impregnated with Nafion (without PTFE), and 0.24 mA/cm² for 30PTFE_AC. The increase in exchange current density indicated faster kinetics. The limiting current density was 0.39 A/cm² for the commercial catalyst (Pt/C); it was doubled to 0.83 A/cm² by Nafion impregnation and even further increased current density to 0.91 mA/cm² with PTFE addition. Internal resistance R_i was 0.64 Ω cm² for the commercial catalyst (Pt/C), Nafion impregnation almost halved the value to 0.36 Ω cm², it was further decreased to 0.26 Ω cm² by the addition of PTFE nanoparticles. These results indicated the significance of Nafion ionomer, which enhanced proton conduction, on cell performance. Polarization curves showed that activation losses of commercial catalyst impregnated with Nafion (without PTFE) and 30PTFE_AC were lower than the activation losses of commercial catalyst (Pt/C). This can be interpreted as the usage of the active catalyst sites through the CLs of commercial catalyst (Pt/C) was lower compared to commercial

catalyst impregnated with Nafion (without PTFE) and 30PTFE_AC catalysts due to lack of Nafion ionomer. iR corrected voltage results revealed that mass transport limitations of 30PTFE_AC became lower than the commercial catalyst impregnated with Nafion (without PTFE) after 0.60 A/cm^2 . At the same time, the power density of 30PTFE_AC catalysts became higher, compared to the power density of commercial catalyst impregnated with Nafion (without PTFE). This result indicated that mesoporous hydrophobic channels in the CL provided decreasing mass transport limitations at higher current densities, by this way, the power density of 30PTFE_AC enhanced.

(Song et al. 2010) reported that the exchange current density, limiting current density, and internal resistance for 5 wt % PTFE loaded catalyst was 0.265 mA/cm^2 , 0.943 mA/cm^2 , and $0.596 \text{ } \Omega\text{cm}^2$, respectively, where transfer coefficient was assumed to be 0.5. These results pointed out that as the PTFE weight percentage increased, the exchange current density and limiting current density remained constant, while internal resistance decreased.

2.3.4. SEM Analysis

2.3.4.1. SEM images of catalyst powders

SEM images of powders of commercial catalyst (Pt/C), commercial catalyst impregnated with Nafion (without PTFE), commercial catalyst impregnated with Nafion and 30 wt % PTFE (30PTFE_AC) are shown in Figure 2.8. The dark gray color reflected the Pt particles in the catalyst while black holes reflected void spaces. The particles in the commercial catalyst (Pt/C) was the smallest considering commercial catalyst impregnated with Nafion (without PTFE) and 30PTFE_AC (Figure 2.8-a1). Catalyst agglomeration occurred with Nafion addition to Pt/C catalyst was clearly observed from Figure 2.8-b1. Decline in void spaces of commercial catalyst impregnated with Nafion (without PTFE) was also examined from Figure 2.8-b1. The agglomeration was also present in the 30PTFE_AC structure (Figure 2.8-c1). On the other hand, enlargement of the void spaces in 30PTFE_AC was clearly observed when compared to catalyst without PTFE. In

addition to that, there were net-like solid blocks through the CL, which was another sign of structural changes; occurred in the 30PTFE_AC.

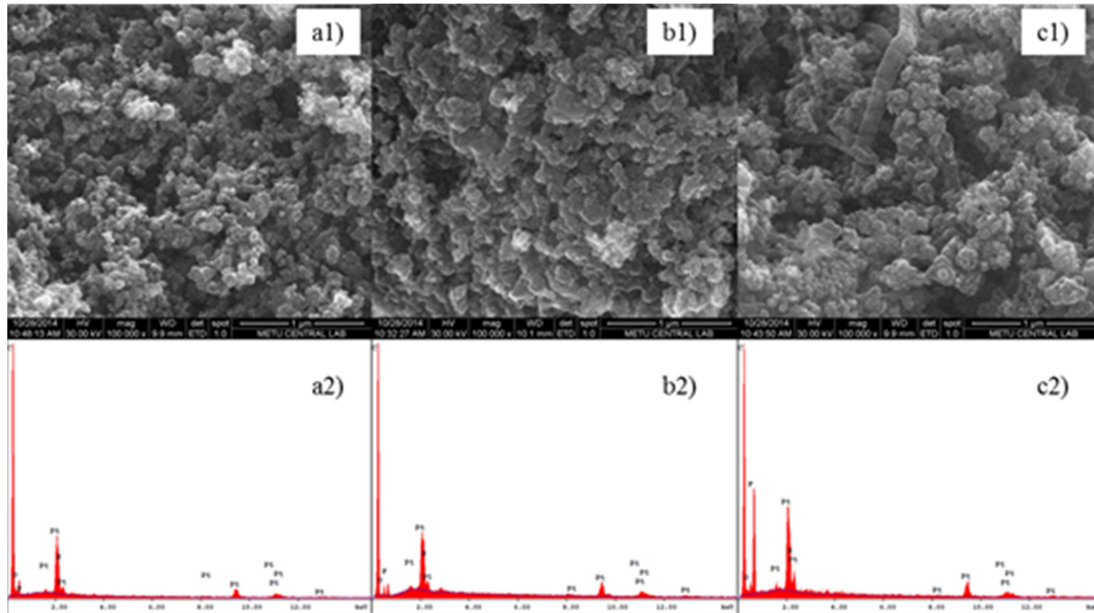


Figure 2.8 SEM images of powders of a) commercial catalyst (Pt/C), b) commercial catalyst impregnated with Nafion (without PTFE), and c) commercial catalyst impregnated with Nafion and 30 wt % PTFE (30PTFE_AC)

EDX results represented the relative amount of the chemical compounds in the catalysts. For commercial catalyst (Pt/C), only, Pt, carbon, and oxygen peaks appeared in the EDX results (Figure 2.8-a2); while fluoride and sulfur peaks appeared in addition to Pt, carbon, and oxygen peaks for commercial catalyst impregnated with Nafion (without PTFE) (Figure 2.8-b2) and 30PTFE_AC (Figure 2.8-c2) catalysts.

2.6.2. SEM images of the MEAs

SEM images of cross section area of the membrane electrode assemblies for MEAs prepared with commercial catalyst (Pt/C), commercial catalyst impregnated with Nafion (without PTFE), and commercial catalyst impregnated with Nafion and 30 wt % PTFE (30PTFE_AC) are shown in Figure 2.9. The membrane, catalyst and

gas diffusion layers are separated from each other with two-sided arrows on the images.

Surface morphology of MEA of commercial catalyst (Pt/C) after fuel cell testing is shown in Figure 2.9-a1. Electrodes were peeled off from the membrane due to the absence of Nafion in the CL. Some parts of the CL remained on the membrane shown with a red (in web version) arrow on the image, while the other part remained on the electrode. The thickness of the membrane was not same at the whole cross-section area, indicating the altered membrane structure due to swelling. Surface morphology of the MEA of commercial catalyst impregnated with Nafion (without PTFE) after fuel cell testing is shown in Figure 2.9-b1. Membrane deformation due to swelling was severe for this MEA compared to 30PTFE_AC. Catalyst layer embed in the membrane showed with red arrows on the image. Surface morphology of the MEA after fuel cell testing of 30PTFE_AC is shown in Figure 2.9-c1. Membrane deformation due to swelling was not as significant as the other catalysts.

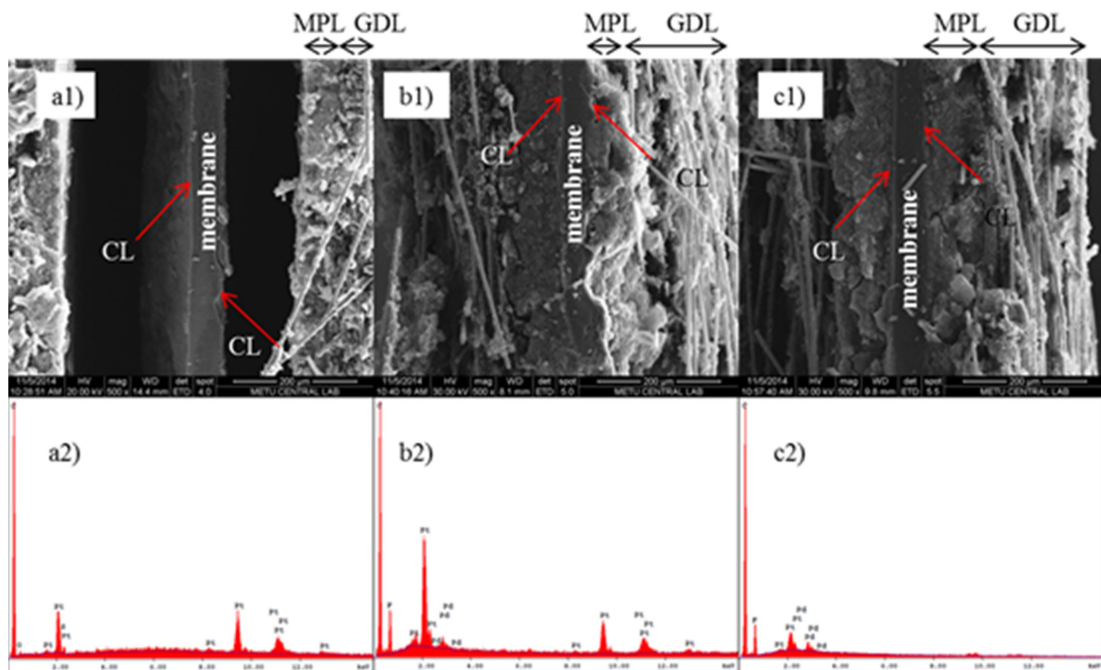


Figure 2.9 SEM images of cross-section of the membrane electrode assemblies for a) commercial catalyst (Pt/C), b) commercial catalyst impregnated with Nafion (without PTFE), and c) commercial catalyst impregnated with Nafion and 30 wt % PTFE (30PTFE_AC)

This was attributed to the enhanced water management through the cross section of the MEA provided by mesoporous hydrophobic channels through both anode and cathode side. In the EDX analysis of commercial catalyst (Pt/C) (Figure 2.9-a2), Pt, carbon, and oxygen peaks appeared clearly. On the other hand, In the EDX analyses of commercial catalyst impregnated with Nafion (without PTFE) and 30PTFE_AC, fluorine, sulfur peaks appeared in addition to Pt, carbon, and oxygen peaks.

2.3.5. TEM Analysis

TEM images of powders of commercial catalyst (Pt/C), commercial catalyst impregnated with Nafion (without PTFE), commercial catalyst impregnated with Nafion and 30 wt % PTFE (30PTFE_AC) are shown in Figure 2.10. Red-circled (in web version) parts on the images are illustrated in Figure 2.10-a2, -b2, and -c2 with higher magnified images.

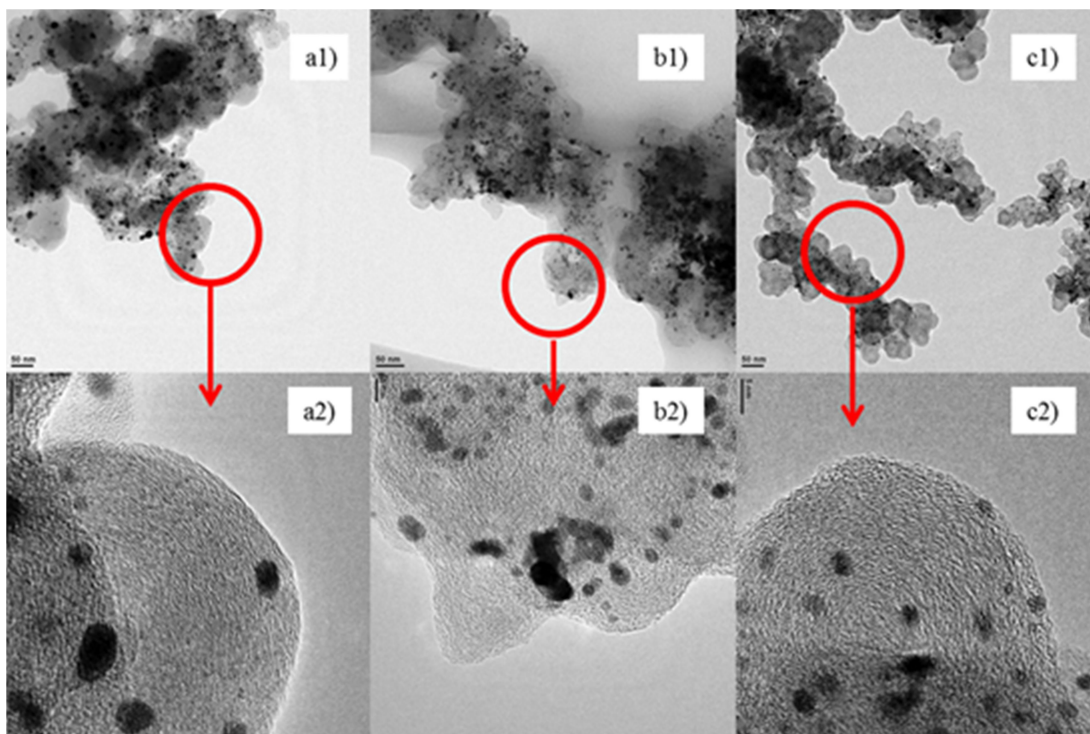


Figure 2.10 TEM Images of powders of a)commercial catalyst (Pt/C), b) commercial catalyst impregnated with Nafion (without PTFE), and c) commercial catalyst impregnated with Nafion and 30 wt % PTFE (30PTFE_AC)

The spherical black dots in bright-field TEM images of the catalysts indicated the dispersed Pt particles on gray carbon spheres. Pt agglomerates were observed on the image of the commercial catalyst (Pt/C) revealed the non-uniform distribution of Pt particles through the catalyst. When Nafion ionomer was added to the commercial catalyst (Pt/C), more uniform distribution of Pt particles on carbon support was provided (Figure 2.10-b1). Nafion ionomer placed around carbon spheres were detected on the higher magnified image of commercial catalyst impregnated with Nafion (without PTFE). However, the image shows that the film thickness of the Nafion ionomer was not uniform around the carbon spheres. Structural changes occurred with PTFE addition to the commercial catalyst impregnated with Nafion (without PTFE) can be revealed from the carbon spheres, which are more apparent in Figure 2.10-c1. The homogeneous dispersion of Nafion ionomer on carbon spheres was deduced from the uniform film thickness, which can be observed from Figure 2.10-c2.

2.4. Conclusions

From the results obtained in this study, the following conclusions can be drawn with respect to the addition of Nafion and PTFE nanoparticles on the structure of Pt/C catalyst and performance of fuel cell.

1. PTFE nanoparticle addition to catalyst does not accelerate catalyst decomposition. Furthermore, it increases the thermal stability of the catalyst.

2. Nafion impregnation to commercial catalyst (Pt/C) increases Pt agglomeration and decreases total Pt surface area. On the other hand, it decreases electrochemical surface area, however, enhances Pt utilization. PTFE addition to a catalyst with two-step preparation method diminishes Pt agglomeration but decreases total Pt surface area and electrochemical surface area as well as Pt utilization.

3. Nafion and PTFE addition to the catalyst cause structural changes. Therefore, BET surface area and cumulative pore volume decrease, however, average pore diameter increases.

4. Nafion addition to the catalyst affects the performance of PEMFC positively in all current density range. PTFE addition enhances the performance of PEMFC, especially at higher current densities.

Future works will focus on increasing Pt content for the cathode catalyst ink such as Pt/C above 45 wt %. In addition, more studies have to be made on the hydrophobic characteristic of the annealed catalyst and the CL.

CHAPTER 3

EFFECT OF PTFE NANOPARTICLES IN CATALYST LAYER WITH HIGH Pt LOADING ON PEM FUEL CELL PERFORMANCE[†]

In this chapter, PTFE was added to CL structure. This modification was aimed at facilitating excess water removal from the cCL with high Pt loading (1.2 mg/cm²). The weight percentage of PTFE in the catalyst inks varied from zero to 30. Membrane electrode assemblies were prepared with a commercial catalyst containing 70 wt % Pt on carbon, by ultrasonic spray coating technique. PEM fuel cell performance testing was carried out with two different membrane electrode assembly configuration in order to identify the effect of PTFE in the anode and cathode catalyst layer structures on water transport mechanism and cell performance. In the first configuration (MEA1), PTFE nanoparticles were added to anode and cathode catalyst layers. In the second configuration (MEA2), PTFE nanoparticles were added only on cCL. PEM fuel cell tests were carried out at both H₂/O₂ and H₂/Air gas-feeding modes.

3.1. Introduction

PEM fuel cells are preferable in some applications than other fuel cell types because of its simplicity, quiescence, and quick start up. The only product of the

[†] Avcioglu, G.S. et al., 2016. Effect of PTFE nanoparticles in catalyst layers with high Pt loading on PEM fuel cell performance. *International Journal of Hydrogen Energy*, 41(23), pp.10010–10020.

reaction, which is generated in cCL of a PEM fuel cell, is water. PEM fuel cells are used commercially in portable applications. In order to widen its application field, understanding the water transport across the membrane electrode assembly is essential. Cathode catalyst layer is one of the most important components, where the oxygen reduction reaction takes place. Furthermore, cCL has a primary impact on water management due to water generation in this layer. When the water is generated in excess amount in the cathode side, it fills the voids and hinders gas transport leading to reactant starvation. For higher performances, Nafion ionomer in the CL should be fully saturated, however; excess liquid water should be removed. For this purpose, distinct pathways for gas and liquid transport should be provided in order to reduce reactant starvation. Hydrophobic nanoparticles can be added to the CL structure to create two-phase flow. By this way, excess water removal can be facilitated and reactants can easily access active catalyst sites.

In earlier studies, PTFE was used as a binder in CLs, however, due to its lack of proton conductivity, Nafion was started to be used as a binder (Wilson & Gottesfeld 1992; Uchida 1995; Uchida 1996). Nguyen et al. (Nguyen et al. 2006) developed a catalyst ink preparation process in order to provide optimum transport path for electronic, ionic, gas and liquid phase in hydrophobic CL with PTFE nanoparticles. Friedmann and Nguyen (Friedmann & Nguyen 2008; Friedmann & Van Nguyen 2010) studied various catalyst ink compositions. They reported that catalyst inks prepared with the weight ratios of Nafion: Teflon: C = 0.875:0.875:1 and Nafion:Teflon:C=1.375:0.375:1, using 46 wt % Pt/C yielded higher performance.

The fabrication technique of membrane electrode assembly (MEA) significantly affects the performance and durability of PEM fuel cell. Ultrasonic spray coating technique has been used for manufacturing different sizes of gas diffusion electrodes up to 400 cm² with commercial Pt/C catalysts having different platinum content (Erkan & Eroglu 2015). In this technique, catalyst ink has been sprayed onto the GDL using an ultrasonic spray coating instrument operating at 48 kHz. The coating process was fully computer controlled and it was programmed according to the coating area, spray flow rate, and multiple layer coating. The performance of electrodes has been tested in a single PEM fuel cell. The power densities reached with the new method were 0.53, 0.74, 0.77, and 0.88 W/cm² for 20

wt %, 40 wt %, 50 wt %, 70 wt % Pt/C catalyst, respectively. The platinum loading was kept constant at 0.4 mg Pt/cm². The power density increased 2.5 times compared to spraying of catalyst ink with air pressure atomizing spray gun. Uniform thin film has been achieved with the ultrasonic coating method. Multiple layer formation retained the porosity of the electrode, impeded flooding on the electrode surface during the coating process, and enhanced transport of reactant during the fuel cell operation. Therefore, high performance, reproducible and large area electrodes could be manufactured by ultrasonic spray coating technique.

PEMFC performance can be enhanced by constructing mesoporous hydrophobic channels through the CL with the addition of PTFE nanoparticles using two-step catalyst ink preparation method. To validate the proposed structure, the effect of PTFE deposition on the ionic and electronic network was investigated by physical, morphological, and electrochemical characterization techniques such as TGA, DTA, XRD, nitrogen physisorption, cyclic voltammetry, SEM, TEM (Avcioglu et al. 2015). Fuel cell performance tests were carried out to investigate the effect of hydrophobic nanoparticle addition to the CL on performance. Avcioglu et al. (Avcioglu et al. 2015), reported that the maximum power density was 0.32 W/cm² obtained at 0.45 V for 30PTFE_AC, 0.28 W/cm² at 0.45 V for Pt/C-Nafion catalyst and 0.13 W/cm² at 0.30 V for commercial catalyst (Pt/C). These results were in accordance with the studies carried out Pt/C commercial catalyst (Bayrakceken et al. 2008; Gasteiger et al. 2005). Results of TGA analysis indicated that Pt content of these catalysts was different. The commercial catalyst had 20 wt % Pt on Vulcan XC-72R carbon support. However, the addition of Nafion decreased the Pt amount to 13 wt % (Pt/C-Nafion) and further addition of PTFE decreased Pt amount to 8 wt%. In all cases, Pt loading was adjusted to 0.4 mg/cm² on gas diffusion electrodes. Although ultrasonic coating is a very effective method, the decrease in Pt percentage in the catalyst ink causes an increase of the electrode thickness (Erkan & Eroglu 2015). Therefore, the performance of the MEA was slightly negatively affected at low current densities from further mass transfer limitation. It has been emphasized that a significant positive effect of Nafion addition to the CL on performance in all current density range and the addition of PTFE had a further enhancement on performance, especially at higher current densities. Qi and Kaufman (Qi & Kaufman 2002) who had also used commercial 20 wt% Pt/C catalyst (E-TEK) obtained 1.25

A/cm² at 0.45 V with a higher catalyst loading of 1.7 mg/cm². Mukerjee et al. (Mukerjee et al. 1993) reported that the performance of the cell was enhanced when the platinum content of the commercial electrocatalyst was increased. This was attributed to active layer thickness. By reducing the thickness of the active layer, mass-transport and ohmic resistances within the active layer were substantially reduced and thus higher power densities were attained in the cells.

The objective of this work is to obtain high performance with hydrophobic CLs prepared by ultrasonic coating technique with high Pt-containing commercial catalyst (70 wt % Pt/C) with a higher Pt load (1.2 mg Pt/cm²). Here, we also investigated the effect of PTFE nanoparticle addition into the CL to enhance water management in high-performance PEM fuel cells. The experimental design has been used to optimize the composition of the CL. Fuel cell performance tests were carried out to determine the highest performance. Reaction kinetics and mass transport limitations were investigated with electrochemical impedance spectroscopy.

3.2. Materials and Methods

3.2.1. Catalyst Ink Preparation

The commercial catalyst was 70 wt % Pt on a carbon support. Catalyst ink of CLs without PTFE was prepared by adding water, Nafion solution (15 wt% 1100 EW, Ion Power, Inc., USA) and isopropyl alcohol (IPA) (Sigma-Aldrich Co. LLC., USA) to Pt/C catalyst, respectively. Then, catalyst ink was mixed for 24 h in a water bath with a magnetic stirrer at room temperature. Hydrophobic catalyst inks were prepared via two-step preparation method (Friedmann & Nguyen 2008). In the first step, the catalyst was wetted with water, and then half amount of Nafion solution was added. The ink was mixed for 24 h in a water bath with a magnetic stirrer at room temperature. After mixing step, catalyst ink was dried in an oven (Binder GmbH, Germany). With the sample, the oven was heated from room temperature to 135 °C. It was held for 20 min at 135 °C, cooled down to 75 °C and hold for 20 min further at 75 °C. Afterward, it was cooled down to room temperature. In the second step, the dried catalyst ink was wetted with water and remained half of Nafion solution was added. Finally, PTFE dispersion (10 wt %), and IPA were added to the

ink, respectively. The prepared ink was mixed for 24 h in a water bath with a magnetic stirrer at room temperature. Nafion fraction parameter (Antolini et al. 1999) (Nafion amount on dry basis) in the catalyst inks was fixed at 0.3. The weight percentage of PTFE in the catalyst ink varied 5 wt %, 10 wt %, 20 wt %, 30 wt % on dry basis. The ratio of total volume of water (ml) to total catalyst weight (g) in the catalyst ink was adjusted to 200. The ratio of total volume of IPA (ml) to the total volume of water (ml) in the catalyst ink was set to three. For characterization, catalyst ink was dried in an oven under atmospheric pressure at 40 °C for 96 h and then was kept at 110 °C for 3 h.

3.2.2. Performance Tests

Catalyst inks were coated onto 34 BC gas diffusion layers (SGL Technologies GmbH, Germany) by using Sono-Tek ultrasonic coating instrument (ExactaCoat DMC-2100, Sono-Tek Corporation, USA). The operating frequency was 48 kHz. Before coating, catalyst inks were inserted into a syringe pump and then were sprayed on the GDL at a flow rate of 0.3 ml/min. Gas diffusion layers were 315 mm thick and were hydrophobized with 5 wt % PTFE with standard MPL on one side. The Pt loading of anode and cathode electrodes was kept 1.2 mg Pt/cm² for all catalysts. After coating, electrodes were hot pressed onto the Nafion 212 membrane (Ion Power, Inc., USA) at 135 °C for 5min at 20 bars on the active area. The fabricated MEA was placed in a single cell with an active area of 5 cm² (Model: FC05-01 SP REF, Electro-Chem Inc., USA). Silicon gaskets (0.18 mm) were placed on both anode and cathode sides of the membrane between MEA and graphite plates consist of mixed serpentine flow fields. A single cell was tightened with a torque of 1.7 Nm on each bolt from corners. Performance tests were carried out by using a fuel cell test station. External humidification system was included in the test station. Reactant gasses were passing through a water column of a humidifier bottle, whereas temperatures of anode and cathode humidifiers were adjusted to 70 °C. Fuel cell temperature was adjusted to 70.2 °C. Back pressure (3 psi) was applied on both anode and cathode exhaust of the cell. The fuel cell was operated at both H₂/O₂ and H₂/Air gas feeding modes. The volumetric flow rate for hydrogen and oxygen was 0.1 slpm, and for air was 0.6 slpm. For MEA conditioning, the cell was operated at 0.3 V for 1 h, then at 0.5 V for 3.5 h. At the end of every hour, the cell was kept at

OCV for 5 min, and then at 0.1 V for 5 min. Data for polarization curve were taken for three times using a visual basic program. Cell voltage varied from 1 to 0.3 V with a step size of 0.05 V for each MEA.

3.2.3. MEA Configuration

Performance testing was carried out with two different membrane electrode assembly configurations. By this way, the effect of PTFE nanoparticles in anode and CL on water transport mechanism was investigated, separately. In the first configuration (MEA1), PTFE nanoparticles were coated with both anode and cathode catalyst layers. In the second configuration (MEA2), PTFE nanoparticles were coated only on cCL. The Pt, Nafion, and PTFE nanoparticle loadings on CLs for prepared MEAs are summarized in Table 3.1.

Table 3.1 Pt, Nafion, and PTFE loadings in catalyst layers

Catalyst Ink	Loading (mg/cm ²)		
	Pt	Nafion	PTFE
without PTFE	1.20	0.80	-
30PTFE	1.20	1.40	1.40
20PTFE	1.20	1.11	0.74
10PTFE	1.20	0.93	0.31
5PTFE	1.20	0.85	0.14

Numbers before PTFE synonym represent the weight percentage of PTFE in the CL on a dry basis. For example, 5PTFE represents the CL prepared with the ink containing 5 wt % PTFE on a dry basis. On the other hand, 30PTFE_AC represents the MEA that has 30 wt % PTFE on both anode and cathode catalyst layers. 30PTFE_C represents the MEA that had 30 wt % PTFE on only cCL.

3.2.4. Electrochemical Impedance Spectroscopy Analysis

A frequency response analyzer (FCI4/Series G, Gamry Instruments, USA) was connected to an electronic load (RBL 488, TDI-Dynaload, TDI Power, USA). A voltage follower circuit was used to isolate grounds and unwanted current flow between the output signal from the FRA and the analog input to the load. The sweeping frequency was ranged from 4 kHz down to 0.1 Hz with 10 points/decade. The amplitude of the AC current was kept at 5 % of the DC current for H₂/O₂ feeding mode and 10 % of the DC current for H₂/Air feeding mode. The impedance measurement was obtained at galvanostatic mode. Real and imaginary parts of frequency response were measured at fast mode to minimize fluctuations. After the data of polarization curve were obtained, the cell was held at 0.5 V for 1 h for stabilization, then real and imaginary part of frequency responses of the Nyquist plot was measured at 0.5 V. Equivalent circuit modeling was done with Echem Analyst software. Initial guesses of the Simplex method was used to the model to experimental data.

3.3. Results and Discussions

3.3.1. Effect of PTFE Loading on Performance and Running Electrochemical Impedance Spectrum of PEMFC at H₂/O₂ Gas-feeding Mode

PTFE Loaded Catalyst Layers on Both Electrodes (MEA1):

Polarization and power density curves for CLs with four different PTFE loadings, working at H₂/O₂ gas-feeding mode are shown in Figure 3.1. The performances of PTFE loaded CLs were compared with CLs without PTFE. Kinetically controlled region (<0.1 A/cm²) of polarization curves gives information about the intrinsic activity of cCL. The current density at 0.9 V for CLs without PTFE was 79 mA/cm². The current density at the same voltage for 5PTFE_AC was 76 mA/cm². Current densities of CLs without PTFE and 5PTFE_AC are very close to each other. This shows us that PTFE nanoparticles in 5PTFE_AC did not decrease Pt utilization significantly.

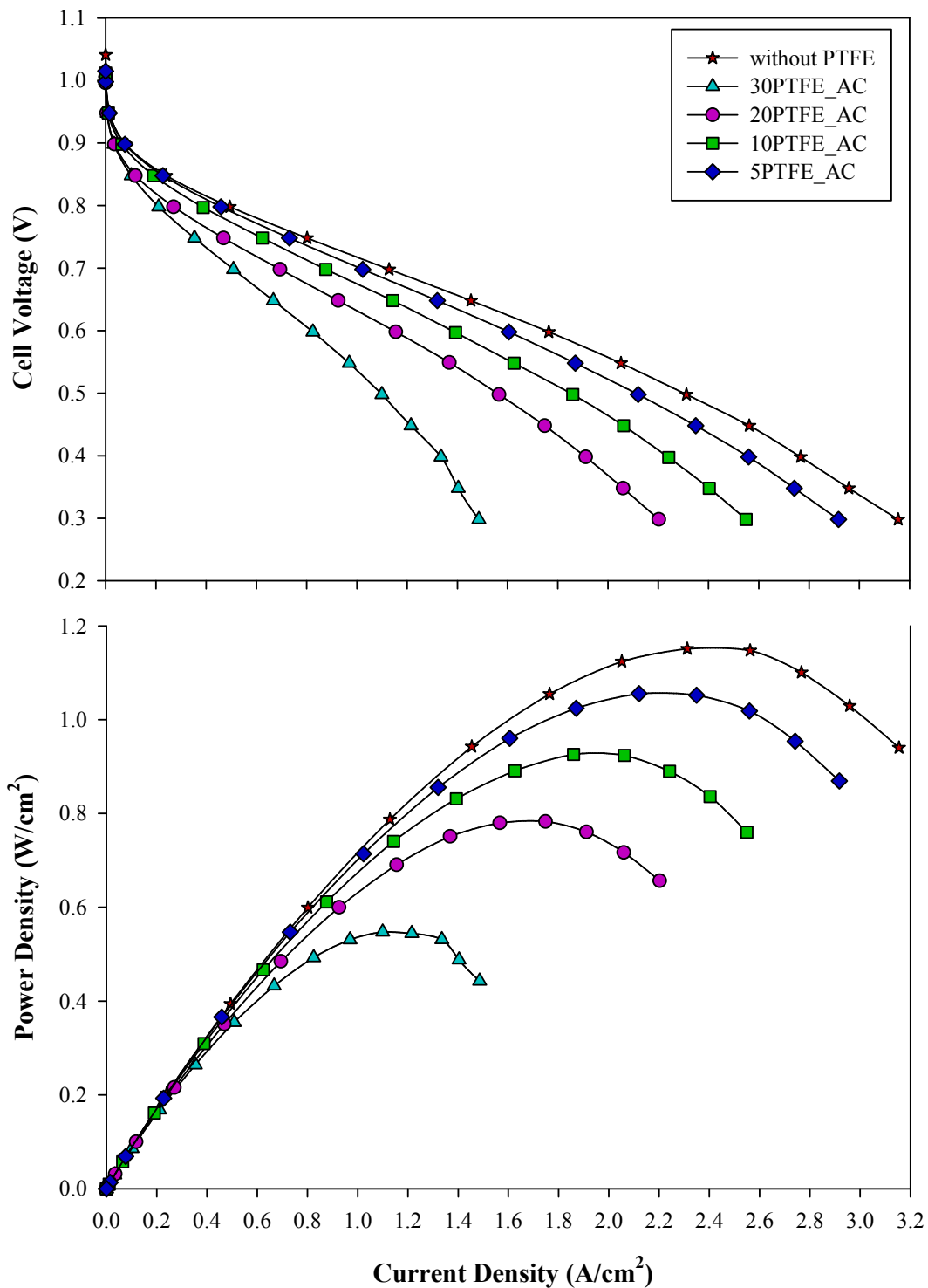


Figure 3.1 Polarization and power density curves of PEMFC for MEA1. Pt loading of anode and cathode electrodes was $1.2 \text{ mgPt}/\text{cm}^2$. Both anode and cathode catalyst layers coated with PTFE nanoparticles. PEMFC was operated at H_2/O_2 gas-feeding mode

10PTFE_AC had 64 mA/cm² at 0.9 V, while 20PTFE_AC and 30PTFE_AC had 35 and 33 mA/cm² current densities at 0.9 V, respectively. As PTFE loading on CLs increased, Pt utilization decreased due to the isolation of Pt and carbon particles by PTFE nanoparticles. The maximum power density at 0.45 V was 1.15 W/cm² for CLs without PTFE. Erkan et al. (Erkan & Eroglu 2015) obtained 0.88 W/cm² the maximum power density keeping Pt loading 0.4 mg/cm² on the CLs, which was prepared with 70 wt % Pt/C by an ultrasonic coating technique. Although in the present study, CLs were prepared with the same commercial catalyst and coating technique, performance was enhanced. The difference between performances of CLs without PTFE is attributed to the differences in ink preparation and MEA conditioning techniques. 5PTFE_AC had a closer performance to CLs without PTFE with a power density of 1.05 W/cm² at 0.45 V. Song et al. (Song et al. 2010), studied with hydrophobic CLs with different PTFE weight percentages while keeping Pt loading at 0.4 mg/cm². They obtained ca. 0.47 W/cm² power density for 5 wt % PTFE in CLs at 0.45 V. Catalyst loading was three-fold in the present study caused an increase in electrode thickness, which causes higher mass and ohmic resistances. The performance was twofold than the result of their study. This is attributed to 2-step ink preparation method, which diminishes PTFE nanoparticles settled on electronic and ionic network leading to a reduction in active catalyst surface area. Electrode preparation technique has also a significant impact on cell performance.

Ultrasonic coating technique used in this study also led to enhanced performance. Power density of 10PTFE_AC was 0.92 W/cm², while power densities of 20PTFE_AC, and 30PTFE_AC were 0.78, and 0.54 at 0.45 V, respectively. As PTFE amount in the CLs increased, Pt utilization decreased, and therefore power density decreased, gradually.

Figure 3.2 illustrates EIS spectra of MEA1 measured at 0.5 V. Thin film diffusion has a preponderant effect on mass transport at this voltage (Ciureanu & Roberge 2001). Impedance spectrum for all CLs shows a high-frequency arc followed by a low-frequency arc. The first arc at high frequencies is accounted for charge transfer process, and latter is accounted for mass-transport processes (Yuan et al. 2007). The intercept of the high-frequency impedance arc on the real axis represents the total ohmic resistance of the cell.

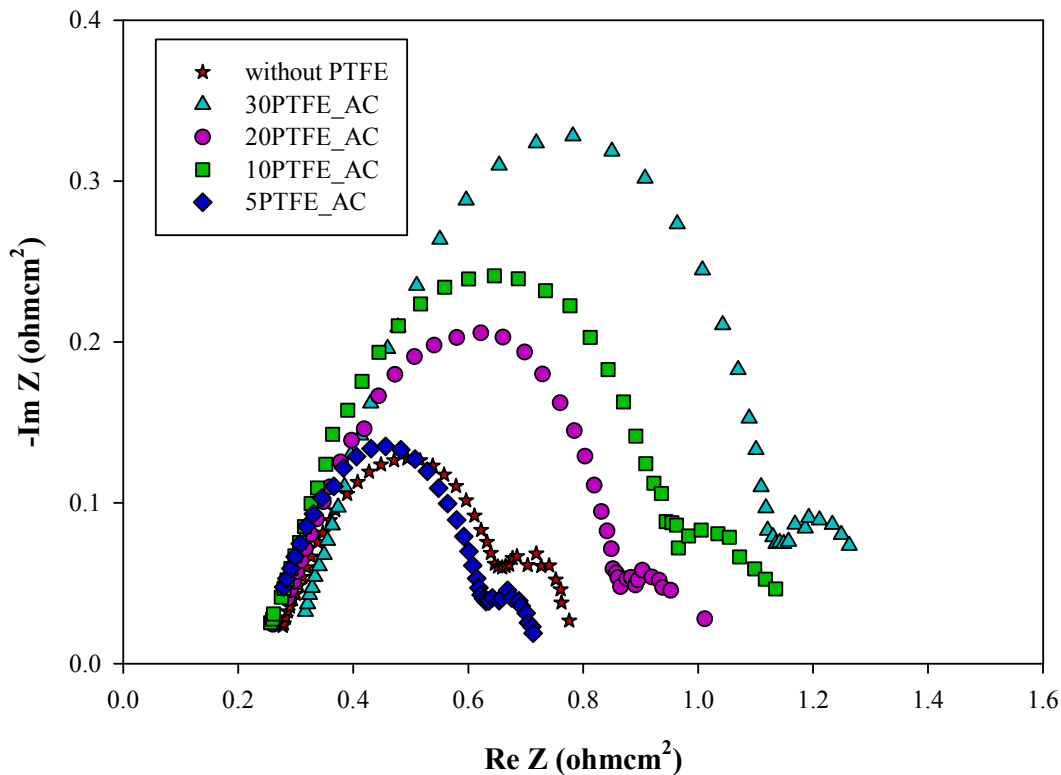


Figure 3.2 Electrochemical impedance spectra obtained for running fuel cell at 0.5 V. Pt loading of anode and cathode electrodes was 1.2 mgPt/cm^2 . Both anode and cathode catalyst layers were coated with PTFE nanoparticles. H_2/O_2 gas-feeding mode was used

The total ohmic resistance of the cell (R_{HF}) is expressed as the sum of the contributions from uncompensated contact resistances; resistance to ion migration within the electrolyte, resistance to electron transport within the cell components (electrodes, GDL, and flow field/current collectors) (Cooper & Smith 2006). High frequency arc, representing the charge transfer resistance (R_{ct}), which is responsible for processes occurring mainly in the cCL: interfacial charge transfer and mass transport of Air/O_2 in the pores of the CL (agglomerate diffusion) and in the Nafion layer surrounding the catalyst particles (thin film diffusion) (Ciureanu & Roberge 2001). Electrode kinetics is controlled by agglomerate diffusion above 0.6 V, while thin film diffusion acts as a rate-determining step below 0.6 V (Park et al. 2006). There are various approaches to the appearance of low-frequency arc (LF), including i) mass-transport limitations of gas phase within the backing (Springer et al. 1996) ii)

mass transport limitation at interface between electrode, electrolyte and gas phase (Kurzweil & Fischle 2004) iii) back diffusion of water (Paganin et al. 1998). Whereas low-frequency arc represents Nernst impedance (thin film diffusion), while linear impedance is representing Warburg diffusion (infinite diffusion) (Wagner et al. 1998). To determine R_{HF} , R_{ct} , and R_{mt} , measured electrochemical impedance spectra were evaluated using equivalent circuits representing reaction steps. The equivalent circuit of impedance spectra with two arcs is shown in Figure 3.3a. The equivalent circuit was resistances series with the three-time constants of parallel R/C. The cathode was represented by two-time constants; one for charge transfer, the other for mass transfer, while anode was represented with one time constant for charge transfer.

The equivalent circuit of impedance spectra with one arc is shown in Figure 3.3b. The cathode and anode were represented with one-time constant for charge transfer. The capacitance (C) was replaced by CPE (constant phase element) because; the capacitance due to double layer charging is distributed along the length of the pores in the porous electrode (Ciureanu et al. 2003).

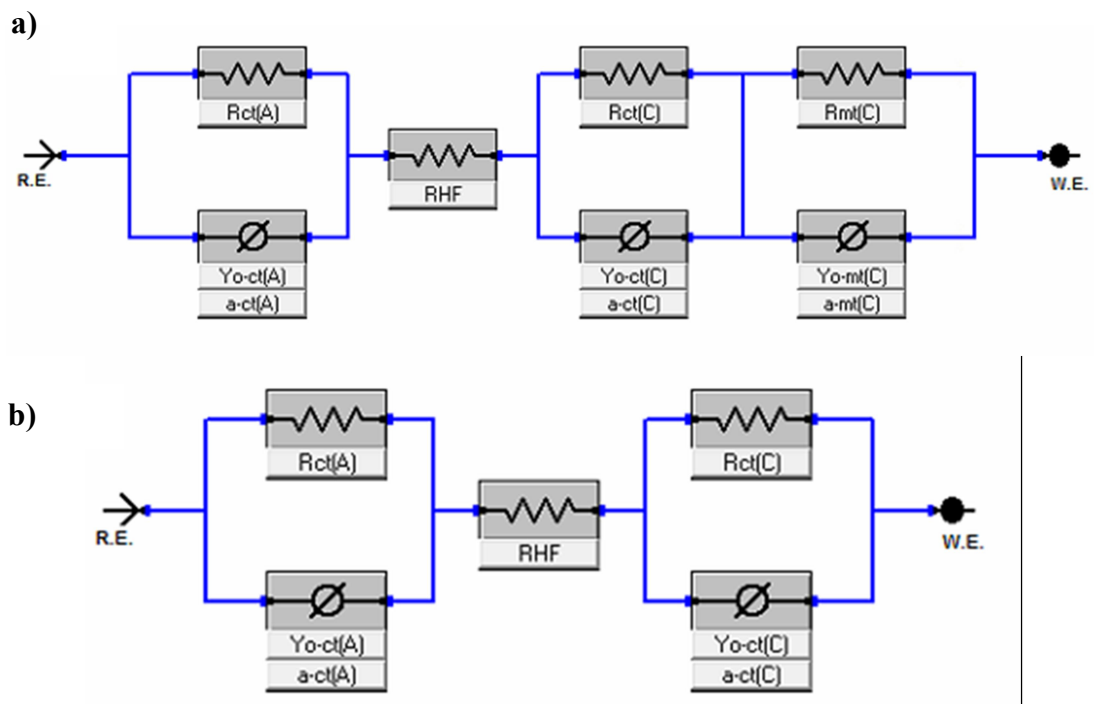


Figure 3.3 Equivalent circuit model for measured impedance spectra a) impedance spectra with two arcs b) impedance spectra with one arc

Parameters of equivalent circuit modeling of EIS spectra for MEA1 are listed in Table 3.2. 5PTFE_AC had the lowest high-frequency resistance ($0.23 \Omega\text{cm}^2$), which indicates the lowest ohmic resistance of membrane. As PTFE percentage was increased, high-frequency resistances increased, gradually. 5PTFE_AC had also the lowest charge ($0.36 \Omega\text{cm}^2$) at cathode and mass transfer resistance ($0.05 \Omega\text{cm}^2$), which pointed out the highest reaction rate and the lowest water saturation in the cathode GDL.

Table 3.2 Parameters of equivalent circuit modeling of EIS spectra of MEA1 at H₂/O₂ gas-feeding mode

MEA Type	O ₂			
	R _{HF} (Ωcm^2)	R _{ct} (A)(Ωcm^2)	R _{ct} (C)(Ωcm^2)	R _{mt} (Ωcm^2)
without PTFE	0.26	0.03	0.39	0.11
MEA1				
30PTFE_AC	0.28	0.23	0.63	0.16
20PTFE_AC	0.26	0.21	0.41	0.11
10PTFE_AC	0.24	0.13	0.61	0.16
5PTFE_AC	0.23	0.08	0.36	0.05

This indicates that PTFE nanoparticles in CLs of 5PTFE_AC provided meso-macro hydrophobic channeling, which provides enhanced water management compared to CLs without PTFE. Cho and Mench (Cho & Mench 2012) reported that the MPL mitigates flooding in the cathode side through enhanced transport of water to the anode side, however, the total water content stored in the cell is slightly affected by the presence of the MPL. In the present study, GDL consists of an MPL with a 5 wt % PTFE. Therefore, when 5 wt % PTFE added on cCL, hydrophobic channels in the cCL promoted capillary water flow via hydraulic connections among pores between CL and MPL, consequently, water removal rate in cCL increased. Cho and Mench (Cho & Mench 2012) also reported that on the anode side, the MPL increases tolerance to drier gas conditions by acting as a barrier to water removal from aCL. When 5 wt % PTFE were added to aCL, the retention time of water molecules captured in aCL was increased. Therefore, membrane humidification was

enhanced in terms of stability. 30PTFE_AC had the highest mass transfer ($0.16 \Omega\text{cm}^2$), charge transfer at cathode ($0.63 \Omega\text{cm}^2$), and high frequency resistance ($0.28 \Omega\text{cm}^2$). Higher PTFE amount in CL reduced Pt utilization leading to decreased amount of product water. When the water generation rate is low, a continuous hydraulic connection among water in pores is not formed, and therefore the product water is widely spread over the GDL in the isolated droplet form, increasing water saturation in the porous media (Cho & Mench 2012). Although 10PTFE_AC had lower PTFE amount, it had higher charge transfer resistance at cathode ($0.61 \Omega\text{cm}^2$) and mass transfer resistance ($0.16 \Omega\text{cm}^2$) than the charge transfer resistance at cathode ($0.41 \Omega\text{cm}^2$) and mass transfer resistance ($0.11 \Omega\text{cm}^2$) of 20PTFE_AC. 10PTFE_AC had lower PTFE loading in CLs, consequently, it had higher Pt utilization than 20PTFE_AC leading to higher water generation rate. This caused flooding at catalyst/electrolyte interface, which hinders oxygen diffusion. On the other hand, rendering cCL more hydrophobic promotes a higher capillary pressure, leading to higher water removal rate from cCL. In the case of 20PTFE_AC, due to increased hydrophobicity, when charge transfer resistance of aCL was considered, this is interpreted that the amount of water purged from cCL towards aCL was higher than 10PTFE_AC, which caused diminished blockage of pores in cGDL of 20PTFE_AC.

PTFE Loaded Catalyst Layer on Cathode Electrodes (MEA2):

Polarization and power density curves for MEA2 with four different PTFE loadings in CLs, working at H₂/O₂ gas-feeding mode are illustrated in Figure 3.4. Only cCL was loaded with PTFE nanoparticles in this configuration. The performances of PTFE loaded cCLs were compared with CLs without PTFE. The current density at 0.9 V for CLs without PTFE was 79 mA/cm². The current density at the same voltage for 5PTFE_C was 35 mA/cm². Current densities for 10PTFE_C, 20PTFE_C, and 30PTFE_C were 31, 29, and 35 mA/cm² at 0.9 V, respectively. For all PTFE loaded CLs intrinsic activities were similar and almost half the value of CLs without PTFE. The maximum power density at 0.45 V was 1.15 W/cm² for CLs without PTFE. 5PTFE_C had a power density of 1.09 W/cm² at 0.45 V. Similarity in power densities indicates that decrease in Pt utilization was not significant for 5PTFE_C. Power density for 10PTFE_C at 0.45 V was 0.96 W/cm².

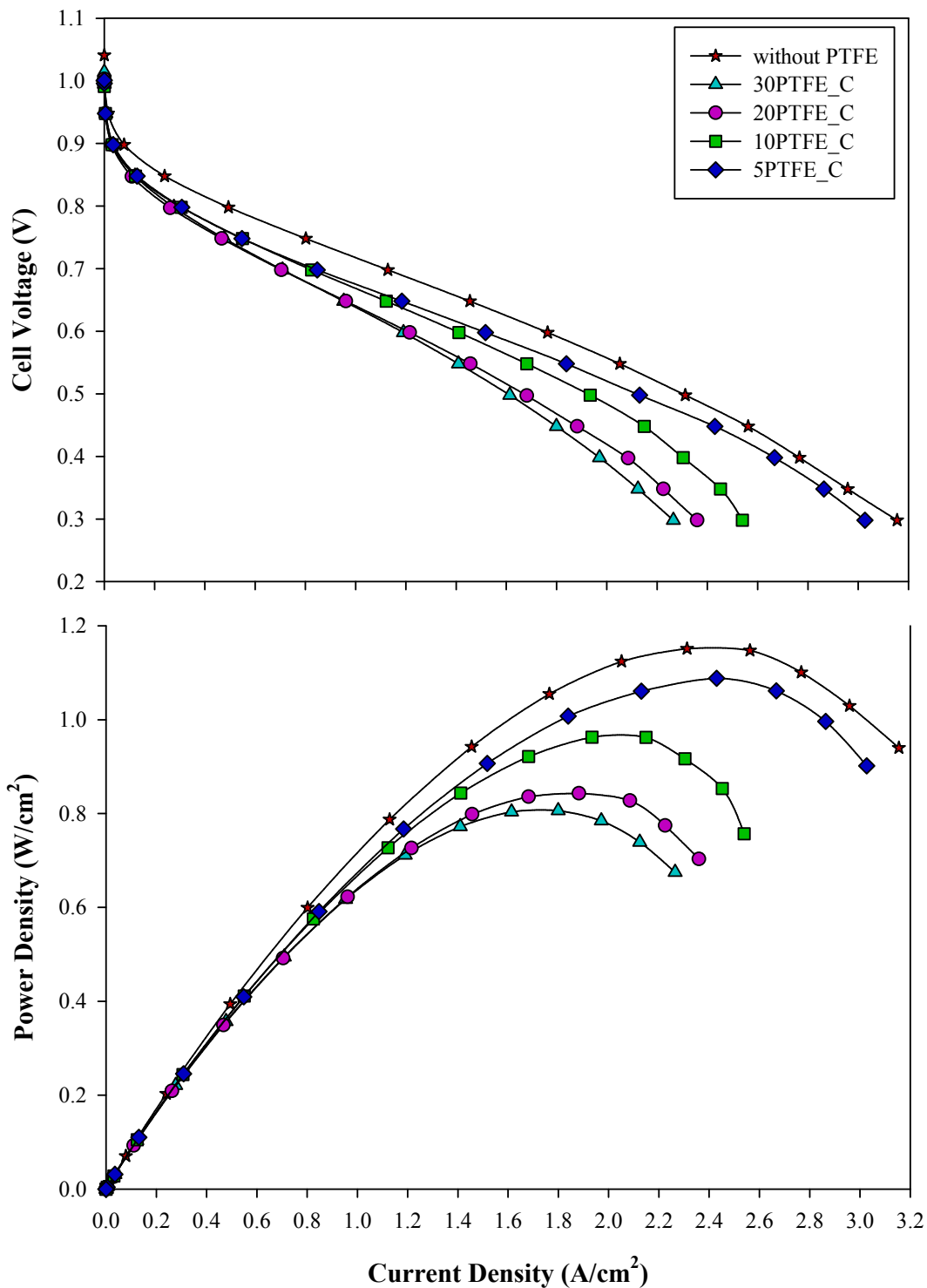


Figure 3.4 Polarization and power density curves of PEMFC for MEA2. Pt loading of anode and cathode electrodes was $1.2 \text{ mgPt}/\text{cm}^2$. Cathode catalyst layer was coated with PTFE nanoparticles. PEMFC was operated at H_2/O_2 gas feeding mode

Therdthianwong et al. (Therdthianwong et al. 2012) obtained ca. 0.45, 0.40, and 0.38 W/cm² for 0.1, 0.25 and 0.5 mg/cm² Pt loadings, respectively with 10 wt % PTFE in cCL at 0.45 V, working at H₂/O₂ gas-feeding mode. Although Pt loading in this study much higher which leading to additional ohmic and mass transport resistances, power density obtained for 10PTFE_C was higher more than two-fold. This is attributed to 2-step ink preparation method, which promotes PTFE nanoparticles settled in voids between catalyst agglomerates. By this way, disruption of electronic and ionic network and a decline in Pt utilization minimized. Therdthianwong et al. (Therdthianwong et al. 2012) also compared the performance of PTFE added cCL with catalyst layers without PTFE. They obtained enhanced performance with PTFE added cCL. They used a commercial catalyst with 20 wt % Pt/C while preparing the CLs. In our previous study (Avcioglu et al. 2015), we also used the same commercial catalyst with the same Pt/C percentage. We have added 30 wt % PTFE on both CLs. We also yielded higher performance with CLs including 30 wt % PTFE compared to CLs without PTFE. However, in this study, the performance of the cCLs even with 5 wt % PTFE was lower than the performance of CLs without PTFE. This is attributed to the high Pt percentage in the commercial catalyst, because, as Pt percentage increases in the commercial catalyst, total catalyst surface area per unit mass of the catalyst decreases (Marr & Li 1999). Furthermore, Platinum to Carbon ratio for 20 wt % Pt/C catalyst was 0.25, while it is 2 for 70 wt % P/C catalyst, which is almost ten times higher. Therefore, in the present study, when PTFE nanoparticles were added to CLs even if 2 step-catalyst ink preparation method were used, they occupied electronic and ionomer network that caused a loss in the electrochemical surface area or disruption of the network. Power densities for 20PTFE_C and 30PTFE_C at 0.45 V were 0.84 and 0.81 W/cm², respectively. The lowest power density was obtained for 30PTFE_C, which is attributed to the lowest Pt utilization.

Figure 3.5 illustrates EIS spectra of MEA2 measured at 0.5 V. Parameters of equivalent circuit modeling of EIS spectra of MEA2 are shown in Table 3.3.

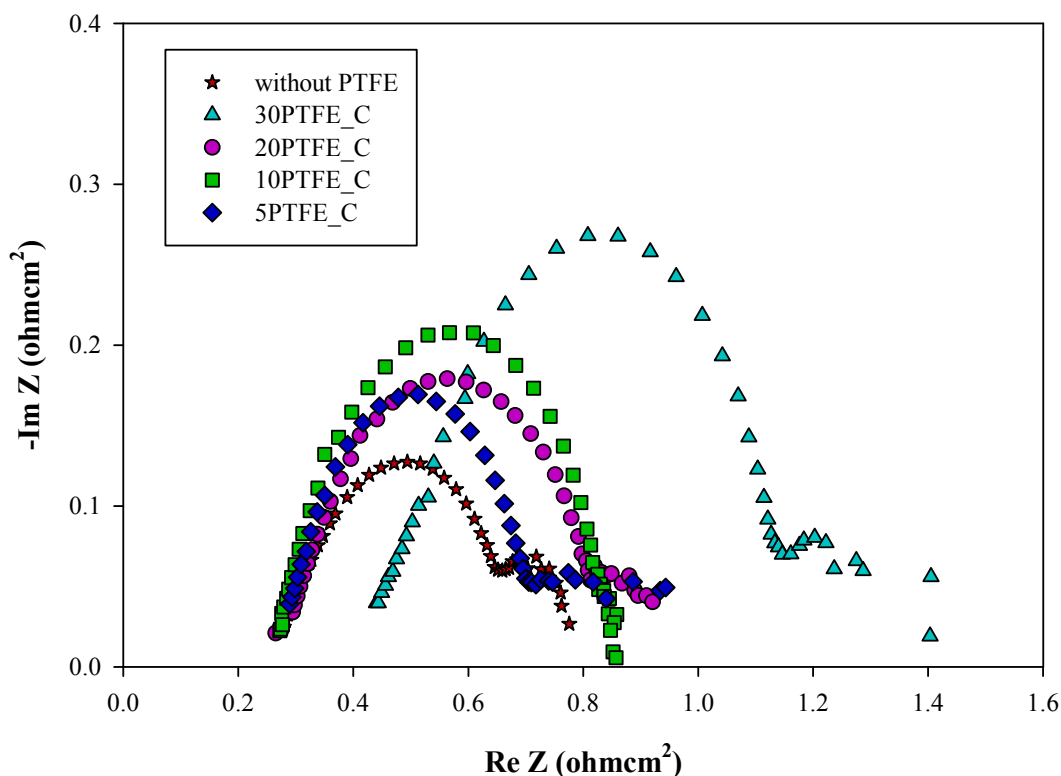


Figure 3.5 Electrochemical impedance spectra obtained for running fuel cell at 0.5 V. Pt loading of anode and cathode electrodes was 1.2 mgPt/cm^2 . Cathode catalyst layer was coated with PTFE nanoparticles. PEMFC was operated at H_2/O_2 gas-feeding mode

Impedance spectra of CLs except 10 PTFE_C demonstrates a high-frequency arc followed by a low-frequency arc. The high-frequency resistance of 5PTFE_C ($0.23 \text{ } \Omega\text{cm}^2$) was the lowest, while R_{HF} of 30PTFE_C ($0.41 \text{ } \Omega\text{cm}^2$) was the highest. The initial higher value of R_{HF} of 30PTFE_C is attributed to lack of water at anode side (Freire & Gonzalez 2001). 30PTFE_C had higher hydrophobicity than other cCLs, this, led to increased rate of back diffusion of water. When aCL contained no PTFE nanoparticles, whereas cCL was highly hydrophobic, water molecules arrived at anode side by back diffusion of water purged more rapidly because of reduced retention time. The exhausted liquid water towards the pores of anode GDL hindered humidified gas access to aCL, leading anode dehydration. On the other hand, higher mass transfer of 30PTFE_C ($0.21 \text{ } \Omega\text{cm}^2$) is attributed to the unformed hydraulic connection among water molecules in pores of cathode electrode due to low water

generation rate. 5PTFE_C had the highest charge resistance at the cathode ($0.67 \Omega\text{cm}^2$), which was also higher than charge resistance of 30PTFE_C at the cathode ($0.63 \Omega\text{cm}^2$). The higher hydrophobicity in the cCL of 30PTFE_C increased back diffusion rate of water, which diminished the amount of water surrounding the agglomerates in the CL.

Table 3.3 Parameters of equivalent circuit modeling of EIS spectra of MEA2 at H_2/O_2 gas-feeding mode

MEA Type	O_2			
	$R_{\text{HF}} (\Omega\text{cm}^2)$	$R_{\text{ct}} (\text{A})(\Omega\text{cm}^2)$	$R_{\text{ct}} (\text{C})(\Omega\text{cm}^2)$	$R_{\text{mt}} (\Omega\text{cm}^2)$
without PTFE MEA2	0.26	0.03	0.39	0.11
30PTFE_C	0.41	0.12	0.63	0.21
20PTFE_C	0.27	0.01	0.56	0.10
10PTFE_C	0.24	0.13	0.51	-
5PTFE_C	0.23	0.06	0.67	0.21

In the case of 5PTFE_C, when considering charge transfer resistance at aCL ($0.06 \Omega\text{cm}^2$) together with mass transfer resistance ($0.21 \Omega\text{cm}^2$), water amount in the aGDL was lower than 30PTFE_C. In other words, the back diffusion rate of water was lower, thus, higher water amount in the CL caused flooding and made oxygen difficult to diffuse through the thin film of Nafion ionomer to reach the active surface area. 10PTFE_C had the lowest charge transfer resistance at the cathode ($0.51 \Omega\text{cm}^2$) among PTFE included CLs in addition to that its impedance spectrum was a lack of low-frequency arc. This reveals that distributed paths for gas and water transport were constructed in the CL, thus, mass transfer resistance due to flooding at cathode GDL was eliminated, leading to higher reaction rate.

3.3.2. Effect of PTFE Loading on Performance and Running Electrochemical Impedance Spectrum of PEMFC at H₂/Air Gas-feeding Mode

PTFE Loaded Catalyst Layer on Both Electrodes (MEA1):

Figure 3.6 illustrates polarization and power density curves obtained for MEA1 at H₂/Air gas feeding mode. Performances of all MEAs reduced by half, when the air was used instead of oxygen due to decreased partial pressure of the oxygen. It is well-known that increase in partial pressure of oxygen, not only enhances the electrode kinetics but also reduces the mass transport limitations (Ticianelli et al. 1988). Performances of PTFE loaded CLs were compared with CLs without PTFE. The current density at 0.9 V for CLs without PTFE was 39 mA/cm². The current density at the same voltage for 5PTFE_AC was 37 mA/cm². That value was very close to the value of CLs without PTFE. In the case of H₂/O₂ gas feeding mode, 5PTFE_AC had also similar intrinsic activity compared with CLs without PTFE. This reveals that 5PTFE_AC yielded higher performance at both feeding mode. 10PTFE_AC, 20PTFE_AC, and 30PTFE_AC had 25, 12, and 8 mA/cm² current densities at 0.9 V, respectively. As PTFE loading on CLs increased, Pt utilization decreased gradually. The maximum power density at 0.45 V was 0.61 W/cm² at the current density of 1.35 A/cm² for CLs without PTFE. 5PTFE_AC had a power density of 0.55 W/cm² at 0.45 V. Song et al. (Song et al. 2010), obtained ca. 0.34 W/cm² power density for 5 wt % PTFE in both CLs at 0.45 V for 0.4 mg/cm² Pt loading, working at H₂/Air gas-feeding mode. Although the same PTFE loading was used in CLs, power density in this study was higher. This is attributed to 2-step ink preparation method (Friedmann & Nguyen 2008; Friedmann & Van Nguyen 2010). In the first step of this method, ionomer phase is steam-annealed onto the catalyst particles to cover all accessible catalyst surface areas. By this way, Nafion phase does not go back into the solution when isopropyl alcohol or water is added to the ionomer-coated catalyst material. In the second step, the additional ionomer is used to crosslink the individual agglomerates which are already covered with annealed Nafion. This assures high ionic conductivity between agglomerates, which enhances cell performance.

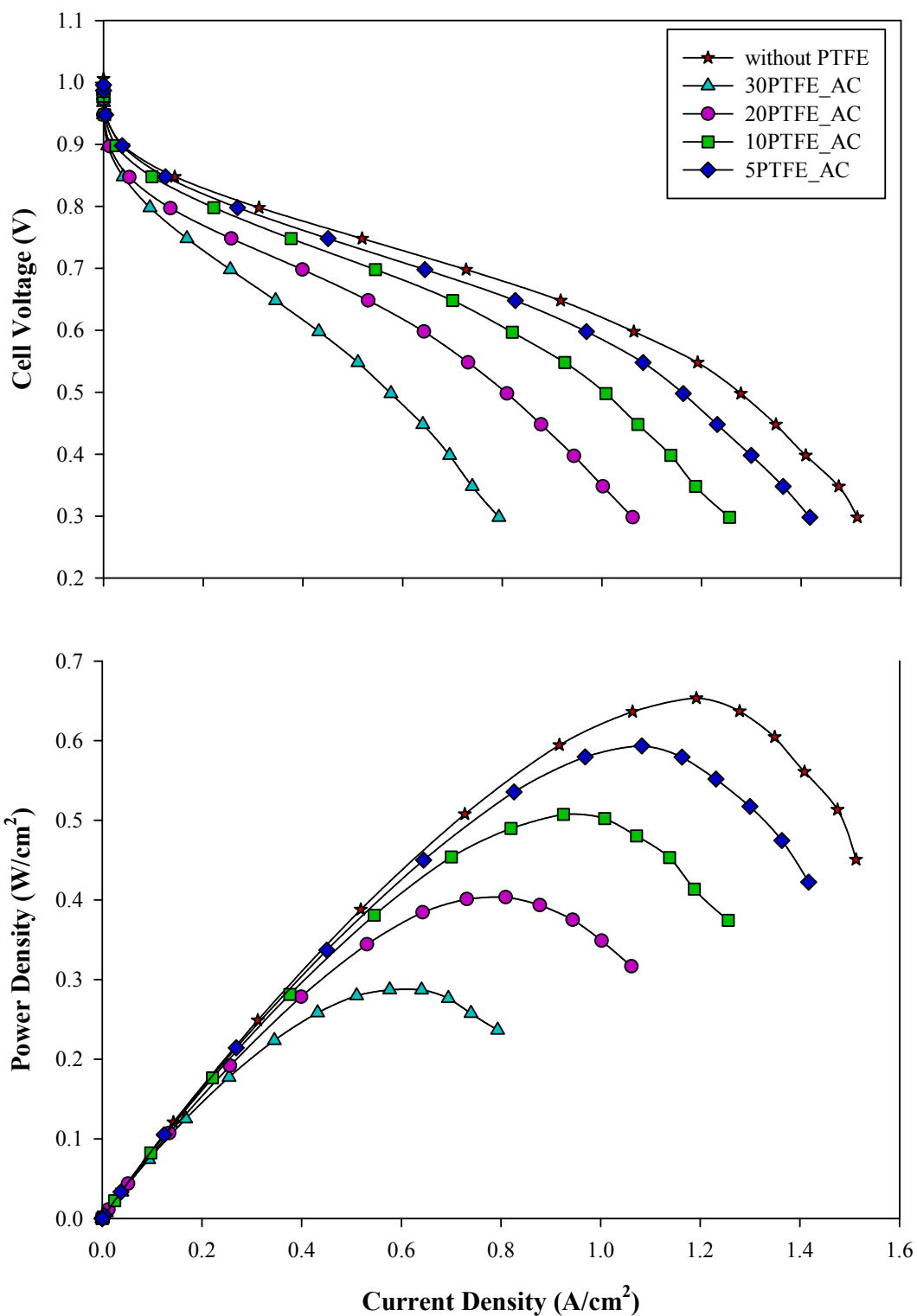


Figure 3.6 Polarization and power density curves of PEMFC for MEA1. Pt loading of anode and cathode electrodes was 1.2 mgPt/cm². Both anode and cathode catalyst layers were coated with PTFE nanoparticles. PEMFC was operated at H₂/Air gas-feeding mode

Furthermore, PTFE nanoparticles settled mostly in voids between agglomerates, leading to enhanced water removal. Power densities of 10PTFE_AC, 20PTFE_AC, and 30PTFE_AC were 0.48, 0.39, and 0.29 W/cm² at 0.45 V, respectively. As PTFE amount in the CL increased, performances decreased, gradually, due to reduced Pt utilization.

Figure 3.7 illustrates EIS spectra of MEA1 measured at 0.5 V. Parameters of equivalent circuit modeling of EIS spectra of MEA1 are shown in Table 3.4.

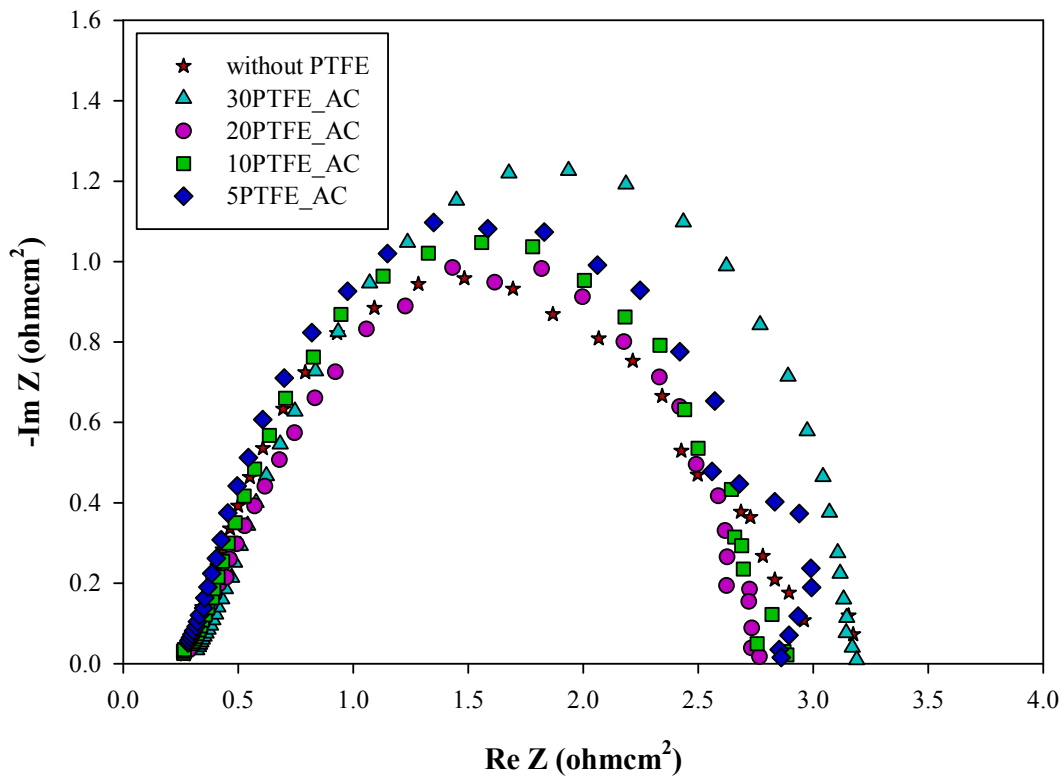


Figure 3.7 Electrochemical impedance spectra obtained for running fuel cell at 0.5 V. Pt loading of anode and cathode electrodes was 1.2 mgPt/cm². Both anode and cathode catalyst layers were coated with PTFE nanoparticles. PEMFC was operated at H₂/Air gas-feeding mode

Impedance spectra of all CLs demonstrate only one arc at high-frequency data range. This means that mass transport limitations associated with gas access to triple phase boundary were diminished. This is attributed to the high airflow rate, because, when it is generally much higher than the stoichiometric flow, it prevents

cathode over flooding (Ciureanu & Roberge 2001) via promoting back diffusion of water. 5PTFE_AC had the lowest high-frequency resistance ($0.24 \Omega\text{cm}^2$). As PTFE weight percentage in the CLs increased, high-frequency resistances increased, gradually. The decrease in partial pressure of oxygen caused reduced reaction rate, accordingly, the rate of water generation decreased.

Charge transfer resistances at cCLs of all MEAs increased more than 6 times which also indicates reduced reaction kinetics. 20PTFE_AC had the lowest charge transfer resistance at the cathode ($1.85 \Omega\text{cm}^2$). This is interpreted that higher hydrophobicity coupled with high airflow rate, increased back diffusion rate of water, leading to reduced amount of product water in the pores of cCL. The highest charge transfer resistance at the cathode ($2.51 \Omega\text{cm}^2$) was obtained for CLs without PTFE. Higher water generation due to the highest Pt utilization caused flooding in the CL. Furthermore, back diffusion of the rate of water was lower, causing severe flooding in the cCL. Higher water amount increased the film thickness of water molecules covering agglomerates, the hindering diffusion rate of oxygen.

Table 3.4 Parameters of equivalent circuit modeling of EIS spectra of MEA1 at H₂/Air gas-feeding mode

MEA Type	Air		
	R _{HF} (Ωcm^2)	R _{ct} (A) (Ωcm^2)	R _{ct} (C) (Ωcm^2)
without PTFE MEA1	0.25	0.11	2.51
30PTFE_AC	0.30	0.52	2.38
20PTFE_AC	0.27	0.63	1.85
10PTFE_AC	0.25	0.31	2.25
5PTFE_AC	0.24	0.26	2.26

PTFE Loaded Catalyst Layer on Cathode Electrode (MEA2):

Figure 3.8 illustrates polarization and power density curves obtained for MEA2 at H₂/Air gas feeding mode. Performances of all MEAs reduced by half, compared to MEAs operated with H₂/O₂ feeding mode. The current density at 0.9 V

for CLs without PTFE was 39 mA/cm^2 . The highest catalytic activity was obtained for CLs without PTFE. Current densities at the same voltage for 5PTFE_C, 10PTFE_C, and 20PTFE_C were similar and 23, 21, and 21 mA/cm^2 , respectively. 30PTFE_C had the lowest current density (10 mA/cm^2) at the same voltage. The maximum power density was 0.61 W/cm^2 at 0.45 V, which was obtained for CLs without PTFE. 5PTFE_C had a power density of 0.52 W/cm^2 , while power density of 10PTFE_C was 0.43 W/cm^2 at 0.9 V. Friedman et al. (Friedmann & Van Nguyen 2010), obtained ca. 0.52 W/cm^2 power density for the cCL with 10 wt % PTFE at 0.45 V for lower Pt loading at H₂/Air gas-feeding mode. They also prepared the catalyst ink with 2-step preparation method. They obtained higher power density for reduced Pt loading. Lower performance in this study is attributed to the negative impact of high Pt loading. This is because, as Pt loading (1.2 mg/cm^2) increases, electrode thickness increases. Thicker electrodes lead higher diffusion resistances, this cause reactant starvation, localized dehydrated or flooded regions in the CL. Moreover, underpenetrated locals through the CL caused reduced active catalyst sites. Furthermore, they operated fuel cell with high airflow rate and interdigitated flow field, which creates higher gas pressure on the both anode and cathode sides to minimize the influence of flooding in the GDLs on the performance of the CLs. In their study, temperatures of anode and cathode humidifiers were also 20 °C higher than cell temperature. When external humidification is used, as the anode and cathode humidification temperatures are higher than cell temperature, performance enhances (Wang et al. 2003). Power density of 20PTFE_C was 0.48 W/cm^2 at 0.45 V. Friedman et al. (Friedmann & Van Nguyen 2010), obtained ca. 0.60 W/cm^2 power density for 23 wt % PTFE in cCL for 0.55 mg Pt/cm^2 loading. Platinum to carbon ratio was 0.86 in their study, while it was 2.0 in this study. The lower performance of 20PTFE_C is attributed to higher Pt loading together with high Pt percentage in the commercial catalyst, which led to decreased Pt utilization. The power density of 30PTFE_C was 0.30 W/cm^2 at 0.45 V. As PTFE amount in the cCL increased, performance decreased. Friedman et al. (Friedmann & Van Nguyen 2010), obtained ca. 0.50 W/cm^2 power density for the cCL with 27.7 wt % PTFE at 0.45 V for 0.48 mg/cm^2 Pt loading, which has also higher performance than 30PTFE_C as expected.

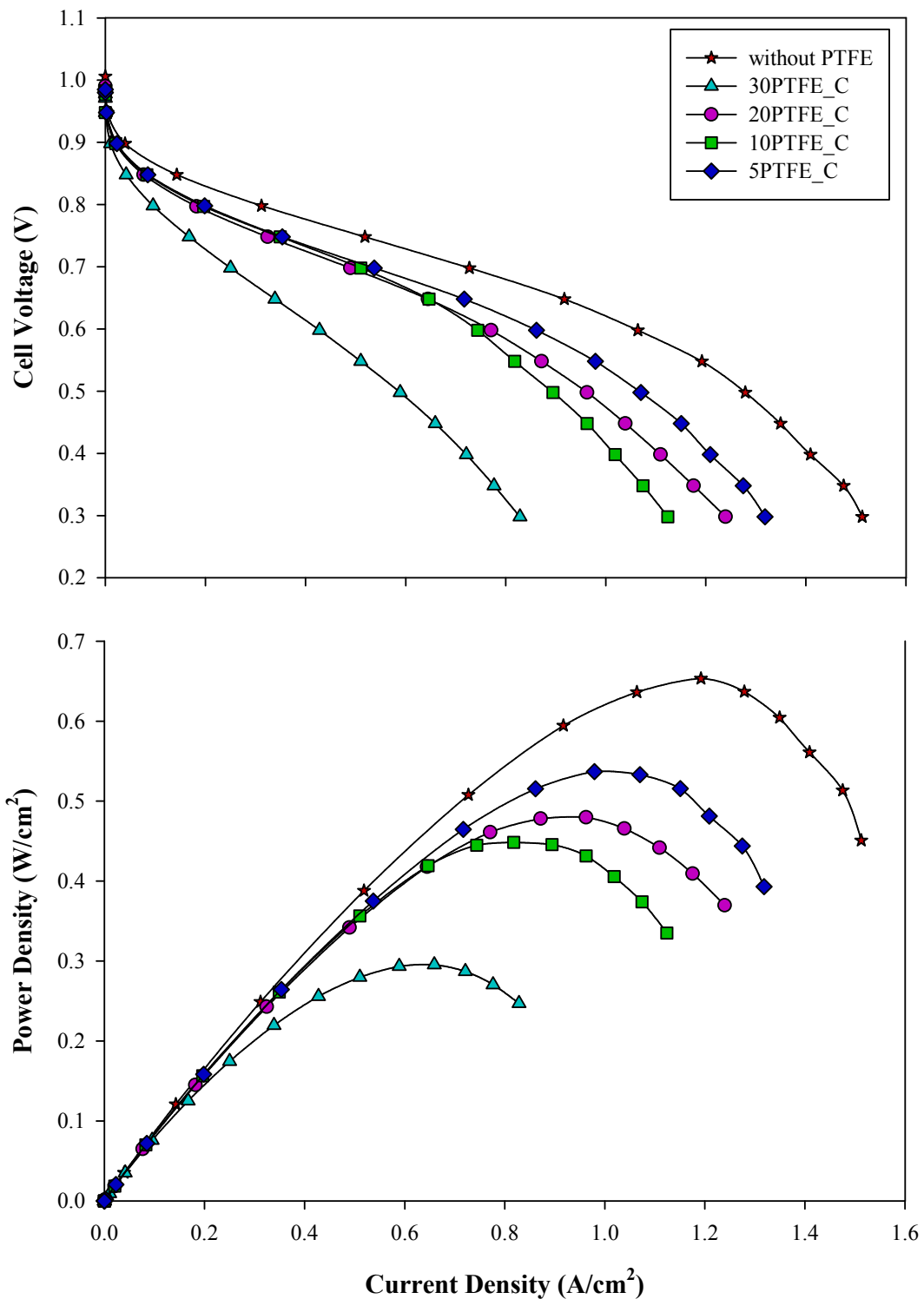


Figure 3.8 Polarization and power density curves of PEMFC for MEA2. Pt loading of anode and cathode electrodes was $1.2 \text{ mgPt}/\text{cm}^2$. Cathode catalyst layer was coated with PTFE nanoparticles. PEMFC was operated at H_2 /Air gas feeding mode

Figure 3.9 illustrates EIS spectra of MEA2 measured at 0.5 V. Impedance spectra of all CLs demonstrate only one arc at high-frequency data range.

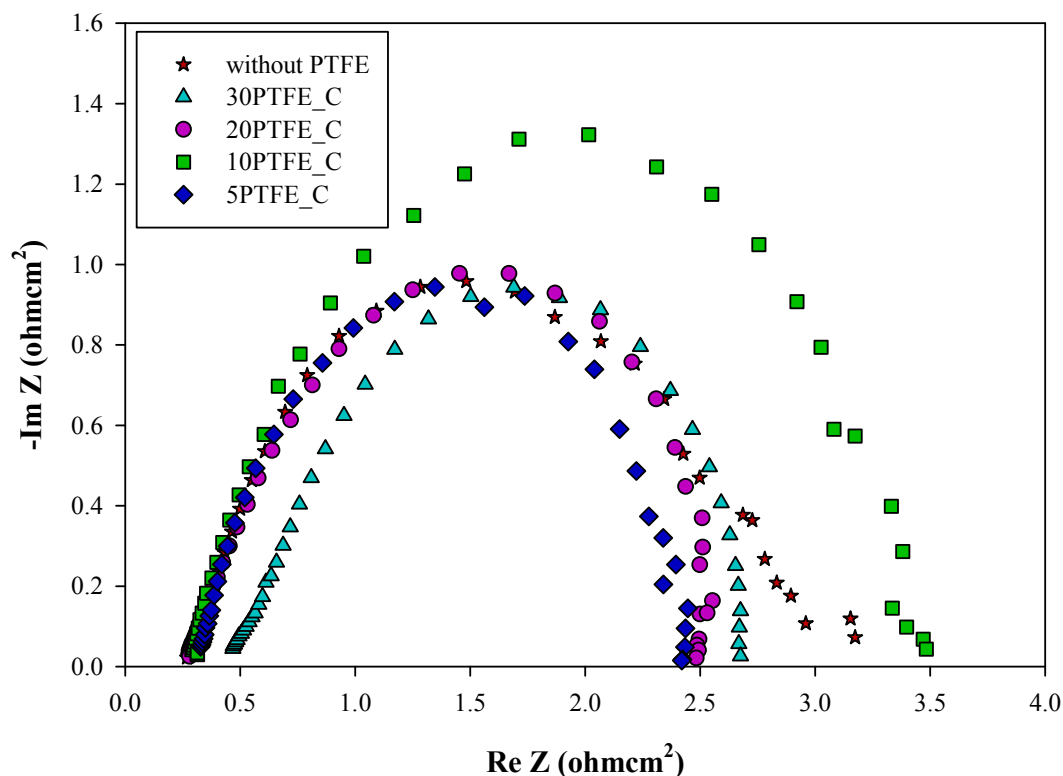


Figure 3.9 Electrochemical impedance spectra obtained for running fuel cell at 0.5 V. Pt loading of anode and cathode electrodes was 1.2 mgPt/cm^2 . Cathode catalyst layer was coated with PTFE nanoparticles. PEMFC was operated at H_2/Air gas-feeding mode

Mass transport limitations associated with water blocking the pores of cGDL were diminished also in this MEA configuration. This is attributed to the high airflow rate. Parameters of equivalent circuit modeling of EIS spectra of MEA2 are shown in Table 3.5. Catalyst layers without PTFE had the lowest high-frequency resistance ($0.25 \text{ } \Omega\text{cm}^2$), while 30PTFE_C had the highest high-frequency resistance ($0.43 \text{ } \Omega\text{cm}^2$) due to anode dehydration. Higher hydrophobicity at cCL of 30PTFE_C promoted dragging higher amount of condensed water from cathode to anode side.

Table 3.5 Parameters of equivalent circuit modeling of EIS spectra of MEA1 at H₂/Air gas-feeding mode

MEA Type	Air		
	R _{HF} (Ωcm ²)	R _{ct} (A)(Ωcm ²)	R _{ct} (C)(Ωcm ²)
without PTFE	0.25	0.11	2.51
MEA2			
30PTFE_C	0.43	0.42	1.86
20PTFE_C	0.26	0.59	1.72
10PTFE_C	0.27	0.51	2.63
5PTFE_C	0.27	0.16	2.00

Accumulated water in the aGDL blocked the pores by constructing a capillary barrier to humidified gas fed. Charge transfer resistances at the cathode of all CLs increased more than 6 times which also indicates reduced reaction kinetics as encountered with previous experiment set. 20PTFE_C had the lowest charge transfer resistance at cathode (1.72 Ωcm²) and the highest charge transfer resistance at the anode (0.59 Ωcm²). The highest charge transfer resistance at the anode is attributed to the higher amount of water carried with back diffusion, blocking the pores and hindering hydrogen diffusion. On the other hand, the lowest charge transfer resistance at the cathode is attributed to the higher back diffusion rate of water coupled with the lower amount of product water. Furthermore, 20PTFE_C had lower charge transfer resistance at the cathode (1.72 Ωcm²) than charge transfer resistance of 10PTFE_C (2.63 Ωcm²) and charge transfer resistance 5PTFE_C (2.00 Ωcm²), despite containing higher PTFE amount. This is interpreted that higher hydrophobicity coupled with high airflow rate, promoting increased back diffusion rate of water. On the other hand, water generation rate was lower than 10PTFE_C and 5PTFE_C due to reduced Pt utilization. As back diffusion rate was higher, the active surface area was used more effectively due to thin liquid water around catalyst agglomerates, which enhanced gas diffusion. Charge transfer resistance at the cathode of 10PTFE_C (2.63 Ωcm²) was higher with respect to 5PTFE_C (2.00 Ωcm²). This is pointed out the disrupted ionic network, leading to the lowest reaction rate.

3.4. Conclusions

From the results obtained in this study, the following conclusions can be drawn with respect to the addition of PTFE nanoparticles to the CL on the performance of fuel cell. Pt percentage in the commercial catalyst has a great impact on cell performance for catalyst inks containing. PTFE nanoparticles, because, as Pt percentage increases in the commercial catalyst, total catalyst surface area per unit mass of the catalyst decreases. Therefore, the even low amount of PTFE is added to catalyst ink, Pt utilization decreases, leading to lower performance.

2-step ink preparation method enhances performance with steam-annealed catalyst agglomerates. By this method, PTFE nanoparticles settling on active catalyst surface can be diminished.

Electrode preparation technique has a great impact on cell performance. Ultrasonic coating technique used in this study helps improving cell performance.

PTFE nanoparticles in CLs of 5PTFE_AC provide meso-macro hydrophobic channeling, which promotes enhanced water management compared to CLs without PTFE at H₂/O₂ feeding mode.

Mass transfer resistance due to flooding at cathode GDL can be eliminated when 10 wt % PTFE is added on only cCL at H₂/O₂ feeding mode.

When 20 wt % PTFE is used for both MEA configurations at H₂/Air feeding mode, charge transfer resistance at the cathode can be minimized, due to promoted back diffusion rate of water provided with high hydrophobicity and high air flow rate.

When 30 wt % PTFE is included only on cCL at both feeding modes due to higher hydrophobicity on the cathode side, the back diffusion rate of water increase. Consequently, water molecules arrived at anode side by increased exhaust more rapidly because of reduced retention time, which led to higher high-frequency resistance.

High airflow rate promotes increased back diffusion rate of water, diminishing flooding at cGDL.

CHAPTER 4

INFLUENCE OF FEP NANOPARTICLES IN CATALYST LAYER ON WATER MANAGEMENT AND PERFORMANCE OF PEM FUEL CELL WITH HIGH Pt LOADING

In this chapter, fluorinated ethylene propylene (FEP) nanoparticles were added to CL to facilitate excess water removal from the triple phase boundary in high Pt loading (1.2 mg/cm^2) PEMFC electrodes. The loading of FEP in the catalyst ink was varied from zero to 30-weight percentage. High-performance electrodes for anode and cathode were prepared by ultrasonic spray coating technique with a commercial catalyst containing 70 wt % Pt on carbon. Different MEAs were prepared in order to differentiate the influence of hydrophobic nanoparticles on water transport and cell performance. In the first configuration (MEA1), FEP nanoparticles were added to both anode and cathode catalyst layers. In the second configuration (MEA2), FEP nanoparticles were added only to cCL. PEM fuel cell tests were carried out at both H_2/O_2 and H_2/Air gas-feeding modes.

4.1. Introduction

Significant progress has been reported in increasing PEMFC performance and durability. This progress had been enabled by discovering new materials and manufacturing methods for the MEA, which is composed of the PEM, CLs, and GDLs. In a PEMFC, hydrogen and oxygen are combined electrochemically. Hydrogen oxidizes at the anode, releasing proton and electrons. The generated protons are transported across the membrane and the electrons across the external

circuit. At the cCL, protons and the electrons react with oxygen to generate water; therefore, it has a primary impact on water management (Weber et al. 2014). At a triple phase boundary of both CLs, carbon conducts electrons, while Nafion ionomer conducts protons, and voids allow oxygen/air gas to access active catalyst sites. However, in order to provide better proton conduction, the water concentration in the voids of agglomerates should be optimum. In other words, Nafion ionomer in the CL should be fully saturated with liquid water in order to provide the highest proton conduction. Otherwise, liquid water fills the voids, covers the agglomerates and consequently, hinders gas transport, and leads to reactant starvation. In order to reduce reactant starvation, distinct pathways for gas and liquid transport should be provided. For this purpose, hydrophobic nanoparticles are incorporated to the CL to create two-phase flow.

Fluoropolymers used to construct the membrane backbone can be used as a hydrophobic agent in the CLs. Fuel cell membranes have been prepared with different fluoropolymer films, such as Polytetrafluoroethylene (PTFE), Fluorinated ethylene propylene (FEP), Perfluoroalkoxy alkanes (PFA), Ethylene tetrafluoroethylene (ETFE), Polyvinylidene fluoride (PVDF) and Polyvinyl fluoride (PVF) (Chen et al. 2006). FEP-based membrane showed the highest proton conductivity corresponds for its higher water uptake, indicating the presence of more hydrophilic sites within the hydrophobic base film for proton transport.

Staiti et al (Staiti et al. 1992), investigated fluorinated ethylene propylene (FEP) as a hydrophobic agent in GDL. They examined the dependence of water transport on the hydrophobicity of the electrodes, and correlations among water transport and internal resistance, gas diffusion, and electrochemical activity of the cell. In their study, CL contained 0.5 mg Pt/cm^2 and 40 wt % of PTFE; the diffusion layer contained an FEP loading varying in the range 0-60 wt %. They found that FEP loading in the carbon paper plays an important role in controlling water transport by influencing both the ionic resistance as well as the diffusion phenomena. Lim and Wang, (Lim & Wang 2004) investigated effects of FEP content within a carbon paper, used as the gas diffusion layer of the cathode (cGDL), on power performance of an H_2/Air PEMFC. Carbon papers treated with different contents of fluorinated ethylene propylene (FEP) ranging from 10 to 40 wt %. They found that under all humidification conditions, a membrane-electrode assembly (MEA) consisting of 10

wt % FEP-impregnated GDL showed higher power densities than 30 wt % FEP-impregnated one.

Yan et al (Yan et al. 2007) investigated the effects of electrode fabrication processes and material parameters on cell performance of PEM by adding an MPL produced by coating FEP as the hydrophobic material onto to traditional GDL to enhance the ability of water management. FEP nanoparticles in the gas diffusion and microporous layers were varying from 10 to 30 wt %. They found that the GDL made of the carbon paper of 10wt % FEP with an MPL of 20 wt % FEP resulted in the best cell performance. Liu et al (Liu et al. 2009) investigated the effect of FEP (varying from 0-50 wt %) on thickness, contact angle, air permeability, and surface and through-plane resistivity. They found that GDL produced using a 5 wt % FEP concentration yielded the highest performance at an operating temperature of 80 °C. Yan et al (Yan et al. 2010), studied the effect of the screen-printing and spraying processes and constituent materials; carbon paper as backing, Acetylene Black carbon, XC-72R carbon or BP2000 as carbon powders, and 10–50 wt % FEP as hydrophobic agent for MPLs on the performance of PEMFCs. They concluded that optimal FEP content maximized MEA power output, due to a compromise between reduced gas permeation resistance and increased the contact resistance between the MPL and CL when FEP content increased.

Park et al (Park & Popov 2011), characterized physical properties of a commercially available GDL prepared with carbon paper or carbon cloth and examined how the GDLs treated with FEP affect water management and oxygen flow during PEM fuel cell operation. They reported that the hydrophobic MPL deposition onto carbon paper appreciably enhances the resistance to water flow through the GDL due to smaller pores and higher surface energy in the MPL. FEP has also been used as the binder for preparing the MPL ink instead of PTFE (Park & Park 2012). They indicated that the properties of FEP, such as low friction and non-reactivity, were the same as those of PTFE; however; FEP is advantageous than PTFE. FEP can be formed into desired shapes more easily because, it is softer than PTFE (melting temperature of FEP is 260°C) and it has low viscosity, which helps easy coating. The performances of FEP (10 wt %) treated GDLs with and without MPL yielded higher performance than PTFE treated GDLs with and without MPL. Latorrata et al (Latorrata et al. 2014) investigated MPL properties consist of FEP

used in order to replace PTFE in terms of static contact angle values and morphology. They found that FEP-treated MPLs showed a superhydrophobic surface that led to reducing significantly mass transfer limitations, both at low and high relative humidity (RH). Therefore, cell performances enhanced the fuel cell assembled with GDLs containing FEP reached the highest power density.

Forner-Cuenca et al (Forner-Cuenca et al. 2015) reported a new fabrication method of commercial GDLs treated with FEP based on radiation grafting for preparing novel GDL materials with patterned wettability properties. They proposed a material design consisting of defined patterned hydrophobic regions providing a dry transport pathway not limited by mass transport (decreased tortuosity) for reactant gasses to reach the CL. Intermittent hydrophilic regions of the proposed material provide a separate pathway for product water to leave the cell. Their results emphasized the potential of the new proposed material to significantly improve the performance and reduce the flooding without the addition of an MPL.

Modestov et al (Modestov et al. 2009) investigated the influence of FEP in CL of the performance of PBI-based MEA for a high-temperature PEM fuel cell. They tried FEP and Nafion as catalyst binders, which differed substantially in wettability and aggregation, and aimed at finding its optimal concentration. They found that low-frequency capacitance measurements with GDEs of PBI-based MEAs at 160°C showed that catalyst electrochemical surface area (ESA) was independent of binder used, Nafion or FEP, and of the binder concentration.

The objective of this work is to investigate the influence of FEP nanoparticles in CLs as a hydrophobic agent in a low-temperature PEM fuel cell. The electrodes were prepared by ultrasonic coating technique with high Pt-containing commercial catalyst (70 wt % Pt/C) with a high Pt loading (1.2 mg Pt/cm²). Fuel cell performance tests were carried out to determine the influence of FEP nanoparticles on high-performance PEM fuel cells. Impedance spectroscopy results have revealed the influence of FEP nanoparticles on reaction kinetics and water management.

4.2. Materials and Methods

Ink preparation, electrochemical characterization methods in addition to performance tests are same as explained in Chapter 3.

4.2.1. MEA Configuration

Performance testing was carried out with two different membrane electrode assembly configurations. By this way, the effect of FEP nanoparticles in anode and CL on water transport mechanism was investigated, separately. In the first configuration (MEA1), FEP nanoparticles were coated with both anode and cathode catalyst layers. In the second configuration (MEA2), FEP nanoparticles were coated only on cCL. The Pt, Nafion, and FEP nanoparticle loadings on CLs for prepared MEAs are summarized in Table 4.1.

Table 4.1 Pt, Nafion, and FEP loadings in catalyst layers

Catalyst Ink	Loading (mg/cm ²)		
	Pt	Nafion	FEP
without FEP	1.20	0.80	-
30FEP	1.20	1.40	1.40
20FEP	1.20	1.11	0.74
10FEP	1.20	0.93	0.31
5FEP	1.20	0.85	0.14

Numbers before FEP synonym represent the weight percentage of FEP in the CL on a dry basis. For example, 5FEP represents the CL prepared with the ink containing 5 wt % FEP on a dry basis. On the other hand, 30FEP_AC represents the MEA that has 30 wt % FEP on both anode and cathode catalyst layers. Moreover, 30FEP_C represents the MEA that had 30 wt % FEP on the only cCL.

4.3. Results and Discussion

4.3.1. Effect of FEP Loading on Performance and Running Electrochemical Impedance Spectrum of PEMFC at H₂/O₂ Gas-feeding Mode

FEP Loaded Catalyst Layers on Both Electrodes (MEA1):

Polarization and power density curves for CLs with four different Nafion and FEP loadings, working at H₂/O₂ gas-feeding mode are shown in Figure 4.1. The performances of FEP loaded CLs were compared with CLs without FEP. Kinetically controlled region ($<0.1 \text{ A/cm}^2$) of polarization curves gives information about Pt utilization of cCL. The current density at 0.9V for CLs without FEP was 79 mA/cm^2 . The highest current density at the same voltage among FEP included CLs was obtained for 10FEP_AC (76 mA/cm^2). Moreover, 10FEP_AC had a higher current density than 5FEP_AC (70 mA/cm^2) at 0.9V despite having higher FEP amount in the CLs. Current densities at 0.9V for 20FEP_AC (33 mA/cm^2) and 30FEP_AC (35 mA/cm^2) were very similar to each other. The highest intrinsic activity was obtained for CLs without FEP, while the lowest was obtained for 20FEP_AC and 30FEP_AC. This indicated that as the FEP weight percentage increased, Pt utilization decreased due to the isolation of Pt and carbon particles by FEP nanoparticles. The maximum power density at 0.45 V was 1.15 W/cm^2 for CLs without FEP. 5FEP_AC and 10FEP_AC had closer performances to CLs without FEP with power densities of 0.91 W/cm^2 and 0.89 W/cm^2 at 0.45 V, respectively. Power densities of 20FEP_AC, and 30FEP_AC at 0.45V were 0.61 , and 0.53 W/cm^2 , respectively. In chapter 3, PTFE nanoparticles were used instead of FEP nanoparticles as a hydrophobic agent in the CLs with the same Pt loading. Power densities for 5PTFE_AC, 10PTFE_AC, 20PTFE_AC, and 30PTFE_AC were 1.05 , 0.92 , 0.78 , and 0.54 W/cm^2 , respectively. Slightly higher power densities were obtained with PTFE nanoparticles.

As FEP weight percentage in the CLs was increased, power density decreased. However, 10FEP_AC exhibited higher power density than 5FEP_AC at current densities greater than 1.6 A/cm^2 , indicating more effective hydrophobic channel formation with 10 wt % FEP nanoparticles.

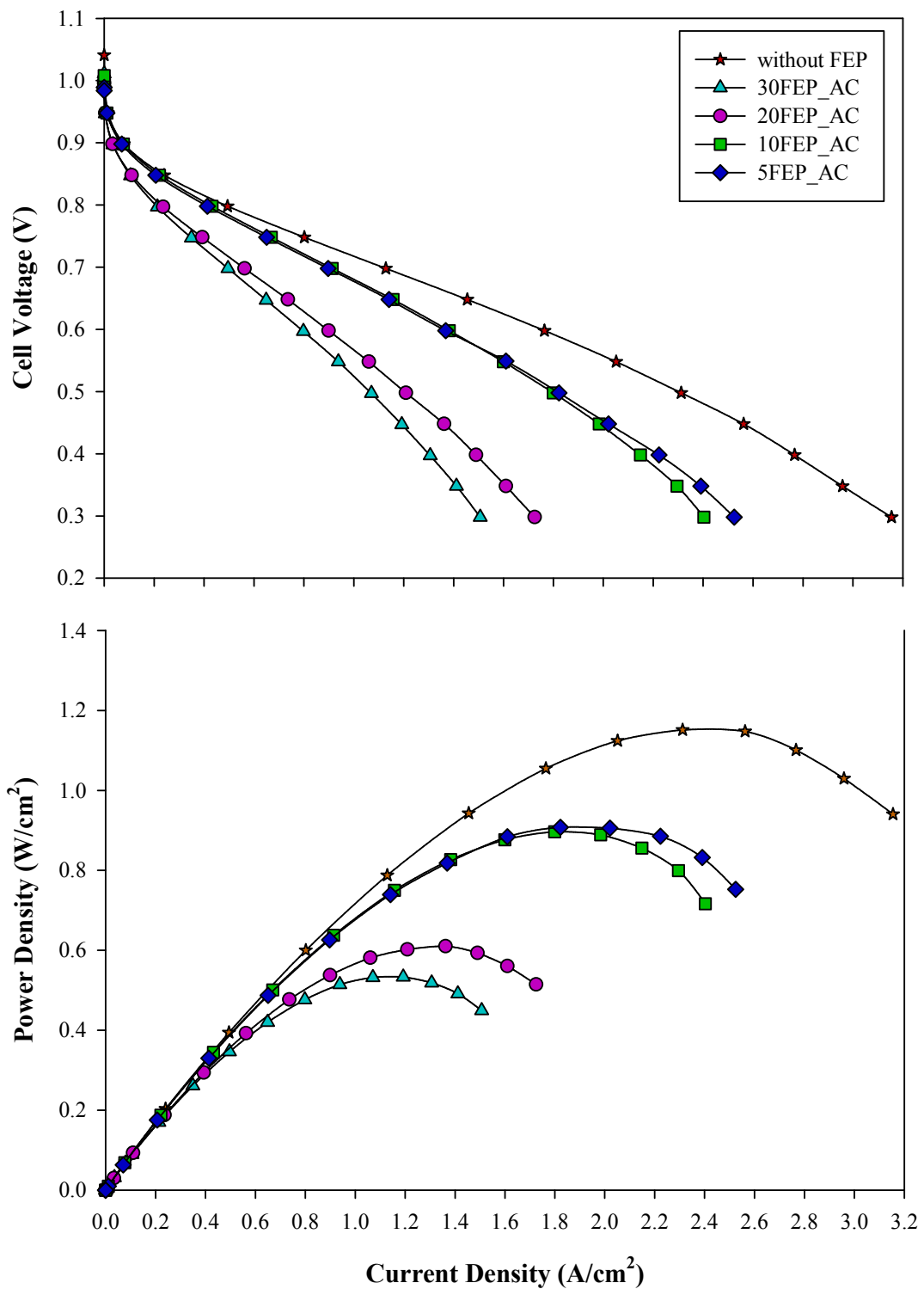


Figure 4.1 Polarization and power density curves of PEMFC for MEA1. Pt loading of anode and cathode electrodes was $1.2 \text{ mgPt}/\text{cm}^2$. Both anode and cathode CLs were coated with FEP nanoparticles. PEMFC was operated at H_2/O_2 gas-feeding mode

This result indicated that when FEP nanoparticles were used as a hydrophobic agent, 5 wt % in the CL could not be enough to mitigate flooding in the CL as PTFE nanoparticles at H₂/O₂ feeding mode. This is attributed to the higher hydrophilic properties of FEP nanoparticles with respect to PTFE nanoparticles, which affect the water removal from the CLs.

Figure 4.2 illustrates EIS spectra of MEA1 measured at 0.5 V. Impedance spectra for all CLs show a high-frequency arc followed by a low-frequency arc. The first arc at high frequencies is accounted for charge transfer process, and latter is accounted for mass-transport processes (Yuan et al. 2007).

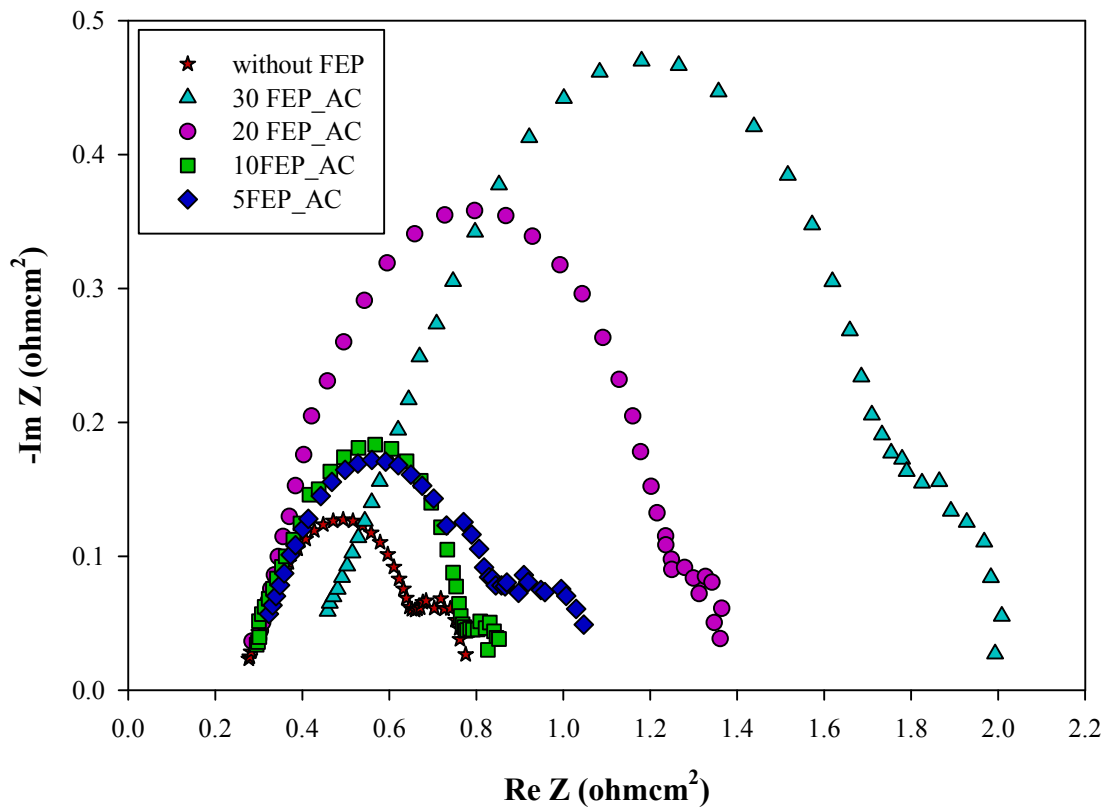


Figure 4.2 Electrochemical impedance spectra obtained for running fuel cell at 0.5 V. Pt loading of anode and cathode electrodes was 1.2 mgPt/cm². Both anode and cathode CLs were coated with FEP nanoparticles. PEMFC was operated at H₂/O₂ gas-feeding mode

The intercept of the high-frequency impedance arc on the real axis represents the total ohmic resistance of the cell. The total ohmic resistance of the cell (R_{HF}) is expressed as the sum of the contributions from uncompensated contact resistances; resistance to ion migration within the electrolyte, resistance to electron transport within the cell components (electrodes, GDL, and flow field/current collectors) (Cooper & Smith 2006). High frequency arc, representing the charge transfer resistance (R_{ct}), which is responsible for processes occurring in the cCL: interfacial charge transfer and mass transport of Air/O₂ in the pores of the CL (agglomerate diffusion) and in the Nafion layer surrounding the catalyst particles (thin film diffusion) (Ciureanu & Roberge 2001). The low-frequency arc (LF), can include: i) mass-transport limitations of gas phase within the backing (Springer et al. 1996) ii) mass transport limitation at interface between electrode, electrolyte and gas phase (Kurzweil & Fischle 2004) iii) back diffusion of water (Paganin et al. 1998). Parameters of equivalent circuit modeling of EIS spectra for MEA1 are listed in Table 4.2.

Table 4.2 Parameters of equivalent circuit modeling of EIS spectra of MEA1 at H₂/O₂ gas-feeding mode

MEA Type	O ₂			
	R_{HF} (Ωcm^2)	R_{ct} (A) (Ωcm^2)	R_{ct} (C) (Ωcm^2)	R_{mt} (Ωcm^2)
without FEP MEA1	0.26	0.03	0.39	0.11
30FEP_AC	0.43	0.15	1.20	0.20
20FEP_AC	0.28	0.04	0.94	0.11
10FEP_AC	0.26	0.08	0.43	0.09
5FEP_AC	0.25	0.06	0.50	0.12

In the present study, GDL consists of an MPL with 5 wt % PTFE on both anode and cathode side. When FEP nanoparticles were added in the cCL, hydrophobic channels were constructed, which allowed gas to access to active catalyst sites, by increasing capillary pressure. Produced water first condenses and/or flows in the larger hydrophilic pores, after the hydrophilic pores are flooded, water will eventually penetrate into first the larger hydrophobic pores and then to smaller

ones, which will be the least prone to flooding due to the highest capillary pressure (Dai et al. 2009). Since the fraction of hydrophobic pores was increased, water saturation in the hydrophilic pores increased. Increased water saturation provided the construction of hydraulic connections among pores promoted liquid transport. This is known as internally connected capillary liquid flow or funicular regime (Cho & Mench 2010).

High-frequency resistances of all MEA's except 30FEP_AC were similar. Moreover, 5FEP_AC had the lowest high-frequency resistance ($0.25 \Omega\text{cm}^2$), which indicated the lowest ohmic resistance of membrane among all MEAs. Hydrophobic nanoparticles in the cCL of 5FEP_AC promoted back diffusion of liquid water, while hydrophobic channels in the anode CL was increasing the retention time of liquid water in the aCL by increasing capillary pressure. This led to increasing in water concentration at aCL/membrane interface. On the other hand, while the high-frequency resistances of all CLs were similar, 30FEP_AC had a very higher value ($0.43 \Omega\text{cm}^2$), which was shifted to the right to the axes of the real impedance. This is attributed to the dehydrated anode (Le Canut et al. 2006; Freire & Gonzalez 2001). PFSA polymer membrane surface is strongly hydrophobic when it is in contact with water vapor (whether saturated or not), and it becomes hydrophilic when in contact with liquid water (Jiao & Li 2011). Therefore, the decrease in membrane hydration is associated with decreased concentration of liquid water at CL/membrane interface at the anode side. While rendering CL more hydrophobic, fraction of hydrophobic pores increased, and thus, water condensation in the pores of the CL decreased. Because, in a hydrophobic pore the liquid water pressure should overcome both the surface tension of the hydrophobic pores of the CL and the pressure to drive the liquid flow against the gas flow (Benziger et al. 2005), while in a hydrophilic pore the liquid water pressure should only overcome the pressure to drive the flow against gas flow. Increased hydrophobicity led to negative or zero capillary pressure causes the hydrophobic pores full of hydrogen gas saturated with water vapor (Weber et al. 2004), which resulted in decreased membrane hydration.

10FEP_AC had the lowest charge transfer resistance at the cathode ($0.43 \Omega\text{cm}^2$) among FEP included CLs, while mass transfer resistance ($0.09 \Omega\text{cm}^2$) was the lowest among all CLs. This pointed out the highest reaction rate among FEP included CLs and the lowest water saturation in the cathode GDL among all CLs.

This indicates that 10FEP_AC mitigated flooding via promoting capillary water flow besides, providing two-phase flow to allow gas access. Although 10FEP_AC had a higher amount of FEP in the CLs than 5FEP_AC, it had lower charge transfer resistance at cathode ($0.43 \Omega\text{cm}^2$) and lower mass transfer resistance ($0.09 \Omega\text{cm}^2$) than the charge transfer resistance at cathode ($0.50 \Omega\text{cm}^2$) and mass transfer resistance of 5FEP_AC ($0.12 \Omega\text{cm}^2$). Rendering cCL more hydrophobic increased capillary pressure, however, after once liquid water penetrates into a hydrophobic pore, water droplets are easily transported (Benziger et al. 2005), which leading to higher water removal rate from cCL (Cho & Mench 2012), and therefore mitigates flooding. Increasing FEP weight percentage in the CLs more than 10 wt % (20FEP_AC and 30FEP_AC) charge transfer resistance at cCL was increased more than two times. Higher FEP weight percentage in the CL reduced Pt utilization leading to decreased in the amount of product water, increasing water saturation in the porous media (Cho & Mench 2012). The highest mass transfer resistance was obtained for 30FEP_AC ($0.20 \Omega\text{cm}^2$), which indicated higher water saturation in the pores of cGDL blocking pathways for gas transport. Furthermore, increase in the fraction of hydrophobic pores caused to increase water saturation in the hydrophilic pores and around catalyst agglomerates. This was resulted in increased diffusion thickness for oxygen to reach triple phase boundary leading to increasing in charge transfer resistance. 30FEP_AC had also the highest charge transfer at anode side ($0.43 \Omega\text{cm}^2$). When FEP nanoparticles were added into the aCL, Pt utilization decreased. This caused an increase in charge transfer resistance at aCL. On the other hand, as hydrophobicity increased, capillary pressure increased, which made the barrier to the liquid water at the CL/membrane interface.

FEP Loaded Catalyst Layer on Cathode Electrode (MEA2):

Polarization and power density curves for MEA2 with four different FEP loadings in cCLs, working at H_2/O_2 gas-feeding mode are illustrated in Figure 4.3. Performances of FEP loaded cCLs were compared with CLs without FEP. The current density at 0.9V for CLs without FEP was 79 mA/cm^2 . Current density for 10FEP_C at the same voltage was closest to CLs without FEP with a value of 74 mA/cm^2 .

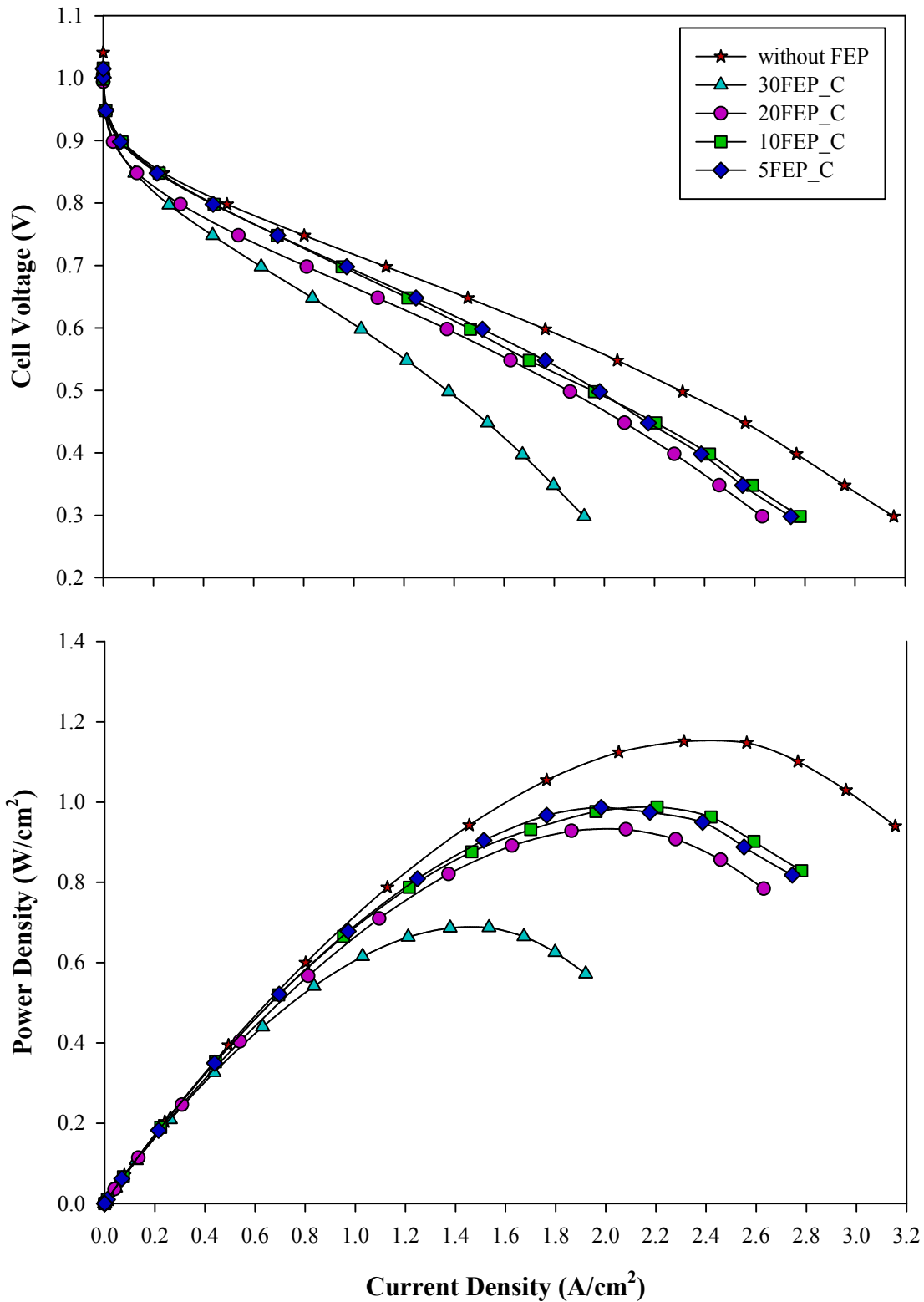


Figure 4.3 Polarization and power density curves of PEMFC for MEA2. Pt loading of anode and cathode electrodes was 1.2 mgPt/cm². Cathode catalyst layer was coated with FEP nanoparticles. PEMFC was operated at H₂/O₂ gas-feeding mode

In spite of containing higher FEP weight percentage in the cCL, 10FEP_C had higher intrinsic activity than 5FEP_C (68 mA/cm²). On the other hand, 20FEP_C, and 30FEP_C had 43, and 39 mA/cm² current densities at 0.9 V, respectively, which were the lowest intrinsic activities indicating lower Pt utilization. The maximum power density at 0.45 V was obtained as 1.15 W/cm² for CLs without FEP. The highest power densities closest to CLs without FEP were attained for 10FEP_C (0.99 W/cm²) and for 5FEP_C (0.97 W/cm²) at 0.45 V. Power densities for 20FEP_C (0.93 W/cm²) were also closer to CLs without FEP. Furthermore, above 1.8 A/cm², 10FEP_C had higher performance than 5FEP_C, indicating enhanced water management at higher current densities. In chapter 3, we also studied the same commercial catalyst with the same Pt percentage. We have prepared hydrophobic CLs with PTFE nanoparticles. For the experiments carried out with MEAs, which only cCL was hydrophobic, the performance of the MEA decreased with increasing PTFE weight percentage. Although 10FEP_C had a higher FEP weight percentage in the cCL with respect to 5FEP_C, higher performance was attained. Moreover, the power density of 20FEP_C was also closer to 10FEP_C and 5FEP_C, although higher FEP weight percentage in the cCL. This is attributed to the higher value of water uptake of FEP nanoparticles compared to PTFE nanoparticles. Higher water uptake led to enhanced hydraulic connection between agglomerates for proton transport. The lowest power density at 0.45V was obtained for 30FEP_C (0.69 W/cm²) due to the lowest Pt utilization.

Figure 4.4 illustrates EIS spectra of MEA2 measured at 0.5 V. Parameters of equivalent circuit modeling of EIS spectra of MEA2 are shown in Table 4.3. Impedance spectrum of all CLs demonstrates a high-frequency arc followed by a low-frequency arc. High-frequency resistances of all CLs were similar; however, the high-frequency resistance of 20FEP_C (0.26 Ωcm²) was the lowest and same with CLs without FEP, while the high-frequency resistance of 30FEP_C was the highest (0.28 Ωcm²). This similarity indicated that ohmic resistances for all MEAs were similar. Charge transfer resistances for 10FEP_C (0.26 Ωcm²) and 5FEP_C (0.27 Ωcm²) at cathode were similar to each other and the lowest among all CLs. Although 10FEP_C had higher FEP weight percentage in the cCL, it had a lower charge transfer resistance than 5FEP_C. This is attributed to the higher mass transfer resistance of 5FEP_C (0.18 Ωcm²). Water generation rate at cCL of 5FEP_C was

higher than 10FEP_C, which gave rise to increasing in water saturation in the pores of GDL of the cathode, hindering oxygen diffusion. Despite having lower Pt utilization, 10FEP_C ($0.26 \Omega\text{cm}^2$) and 5FEP_C ($0.27 \Omega\text{cm}^2$) had lower charge transfer resistances than CLs without FEP ($0.39 \Omega\text{cm}^2$), indicating higher reaction rate. This is attributed to the decreased diffusion limitations due to decreased water concentration in the pores of CL film depending on the decreased film thickness of water surrounding catalyst agglomerates.

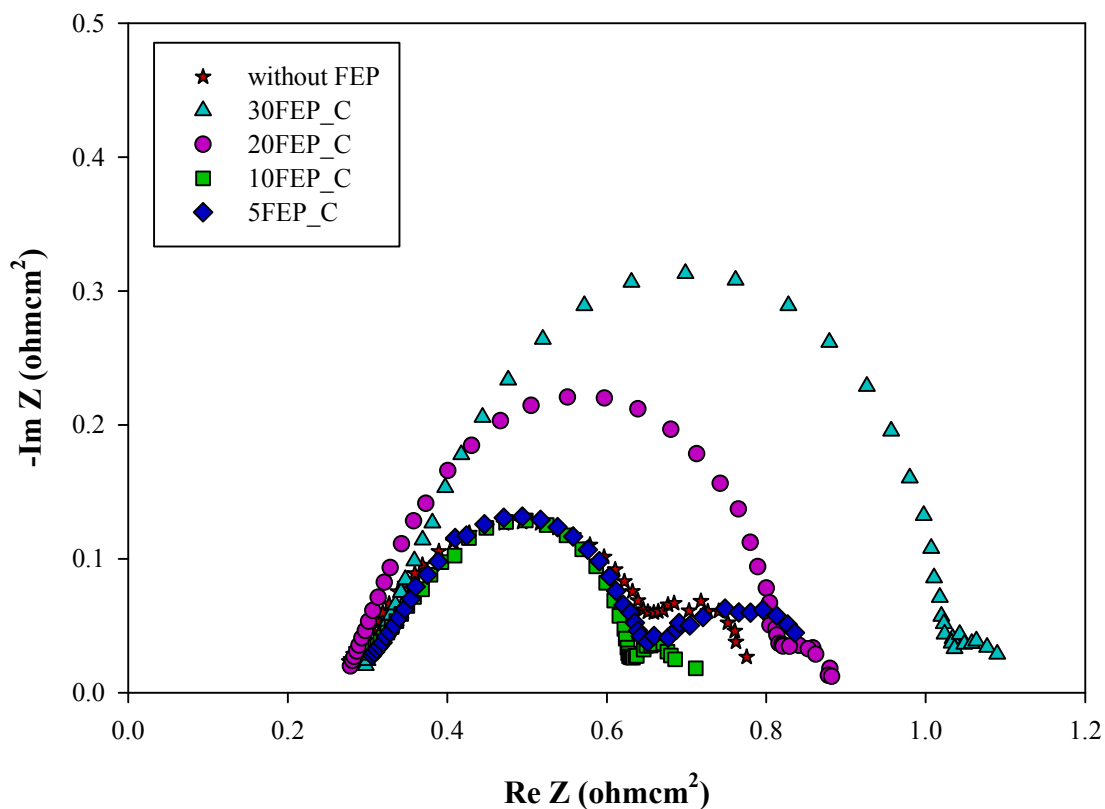


Figure 4.4 Electrochemical impedance spectra obtained for running fuel cell at 0.5 V. Pt loading of anode and cathode electrodes was 1.2 mgPt/cm^2 . Cathode catalyst layer was coated with FEP nanoparticles. H_2/O_2 gas-feeding mode was used

This indicates that enhanced water management was provided with distributed paths for gas and water transport through the CL, which allowed gas access to triple phase boundary besides, excess water removal. As FEP weight

percentage in the cCL exceeded 10 wt %, charge transfer resistance increased almost two times, however, mass transfer resistances slightly decreased. The increase in charge transfer resistance of 20FEP_C ($0.51 \Omega\text{cm}^2$) and 30FEP_C ($0.63 \Omega\text{cm}^2$) is attributed to decreased Pt utilization. Furthermore, the decrease in the mass transfer resistance is attributed to the lower water concentration, which was retained in the hydrophilic structure of FEP nanoparticles.

Table 4.3 Parameters of equivalent circuit modeling of EIS spectra of MEA2 at H₂/O₂ gas-feeding mode

MEA Type	O ₂			
	R _{HF} (Ωcm^2)	R _{ct} (A) (Ωcm^2)	R _{ct} (C) (Ωcm^2)	R _{mt} (Ωcm^2)
without FEP MEA2	0.26	0.03	0.39	0.11
30FEP_C	0.28	0.12	0.63	0.07
20FEP_C	0.26	0.06	0.51	0.06
10FEP_C	0.27	0.08	0.26	0.10
5FEP_C	0.27	0.14	0.27	0.18

4.3.2. Effect of FEP Loading on Performance and Running Electrochemical Impedance Spectrum of PEMFC at H₂/Air Gas-feeding Mode

FEP Loaded Catalyst Layers on Both Electrodes (MEA1):

Figure 4.5 illustrates polarization and power density curves obtained for MEA1 at H₂/Air gas feeding mode. Performances of all MEAs reduced by half when the air was used instead of oxygen due to decreased partial pressure of the oxygen. It is well-known that increase in partial pressure of oxygen, not only enhances the electrode kinetics but also reduces the mass transport limitations (Ticianelli et al. 1988). Performances of FEP loaded CLs were compared with CLs without FEP. The current density at 0.9V for CLs without FEP was 39 mA/cm². The highest intrinsic activity was obtained for CLs without FEP. 5FEP_AC (30 mA/cm²) and 10FEP_AC (30 mA/cm²) had same intrinsic activities, which were lower than CLs without FEP.

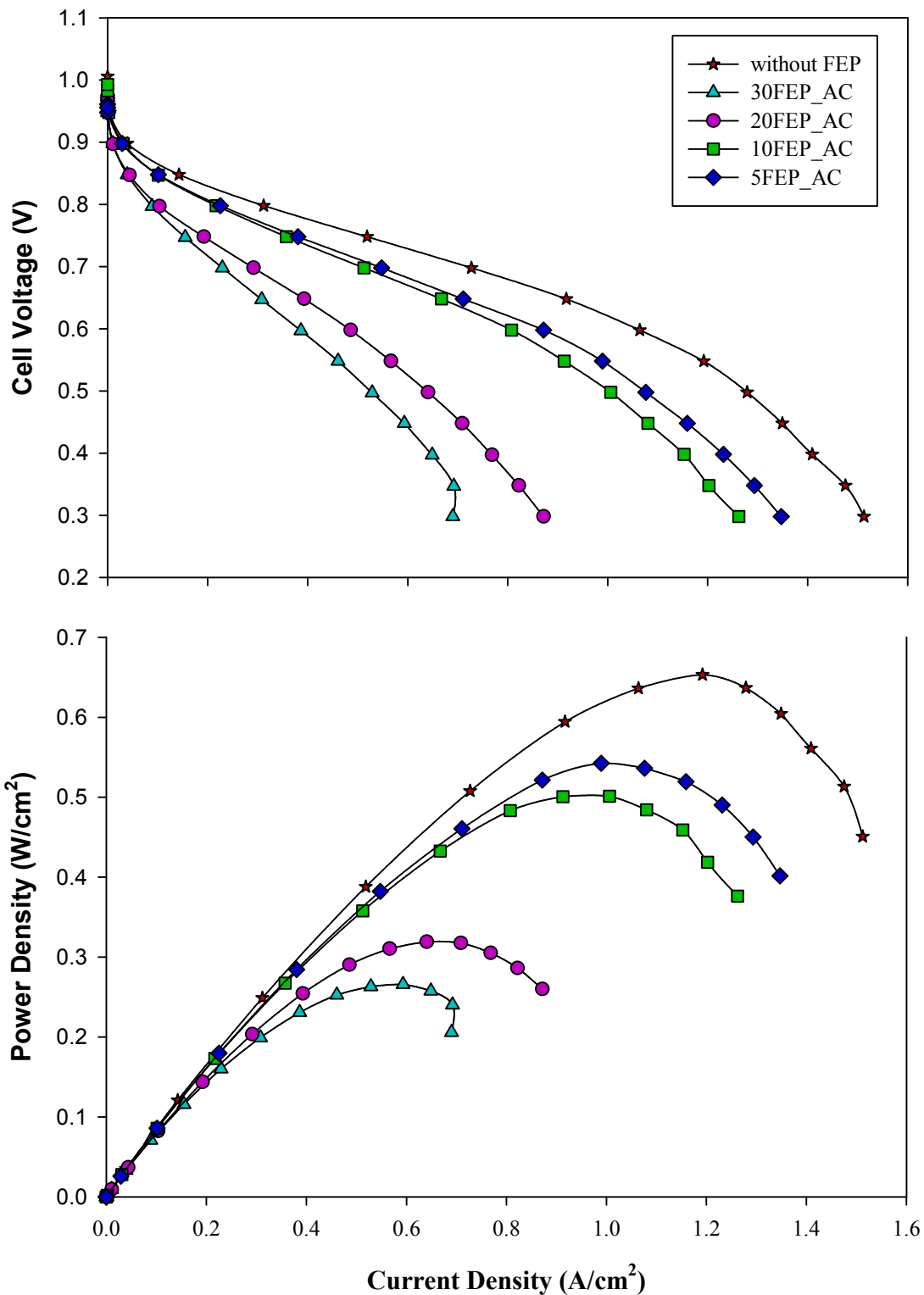


Figure 4.5 Polarization and power density curves of PEMFC for MEA1. Pt loading of anode and cathode electrodes was $1.2 \text{ mgPt}/\text{cm}^2$. Both anode and cathode catalyst layer were coated with FEP nanoparticles. PEMFC was operated at H_2 /Air gas-feeding mode

As FEP loading on CLs increased, Pt utilization decreased. Therefore, current densities of 20FEP_AC (10 mA/cm^2) and 30FEP_AC (10 mA/cm^2) were the lowest at 0.9 V. The maximum power density at 0.45 V was 0.60 W/cm^2 obtained for CLs without FEP. 5FEP_AC and 10FEP_AC had power densities of 0.52 and 0.48 W/cm^2 at 0.45 V. Power densities of 20FEP_AC, and 30FEP_AC were the lowest and 0.32, and 0.27 W/cm^2 at 0.45 V, respectively. As FEP weight percentage in the CLs increased, performances decreased, gradually. However, although weight percentage of FEP nanoparticles in 10FEP_AC was higher than 5FEP_AC, similar performances were attained. Similarly, performances of 30FEP_AC and 20FEP_AC were close to each other. This is attributed to similar Pt utilizations.

Figure 4.6 illustrates EIS spectra of MEA1 measured at 0.5 V. Impedance spectrum of all CLs demonstrates only one arc at the high-frequency range. Mass transport limitation at the cCL was diminished, which is attributed to the high airflow rate. When air flow rate is generally much higher than the stoichiometric flow, it prevents cathode over flooding (Ciureanu & Roberge 2001) via promoting back diffusion of water. Charge transfer resistances of all CLs at both anode and cathode were increased at least more than 2 times compared to H_2/O_2 feeding mode, which indicates reduced reaction kinetics. The decrease in partial pressure of oxygen caused reduced reaction rate, accordingly, the rate of water generation decreased. Because, when oxygen was fed with nitrogen to the cell, oxygen had to diffuse also through the nitrogen to reach the triple phase boundary. This caused a decrease in reaction rate. High-frequency resistance of CLs without FEP ($0.25 \text{ } \Omega\text{cm}^2$), 5FEP_AC ($0.26 \text{ } \Omega\text{cm}^2$), and 10FEP_AC ($0.23 \text{ } \Omega\text{cm}^2$) were similar and lower than high-frequency resistances of 20FEP_AC ($0.31 \text{ } \Omega\text{cm}^2$) and 30FEP_AC ($0.38 \text{ } \Omega\text{cm}^2$). This means that humidification of membrane decreased when FEP amount in the CLs increased. Decrease in membrane hydration is associated with decreased concentration of liquid water at CL/membrane interface at the anode side. One of the reasons to decrease in membrane hydration is decrease in water generation rate at cCL, because, when the weight percentage of FEP nanoparticles increased, Pt utilization in the cCL decreased. Even if back diffusion rate of water was higher due to higher hydrophobicity, a lower amount of water retained at CL/membrane interface, and this amount was not sufficient for the completely humidified membrane. On the other hand rendering aCL more hydrophobic increased water

purge rate due to higher capillary pressure, accordingly, water retention time at CL/membrane interface decreased. This also led to decrease in membrane hydration. Furthermore, PFSA polymer membrane surface is strongly hydrophobic when it is in contact with water vapor (Jiao & Li 2011).

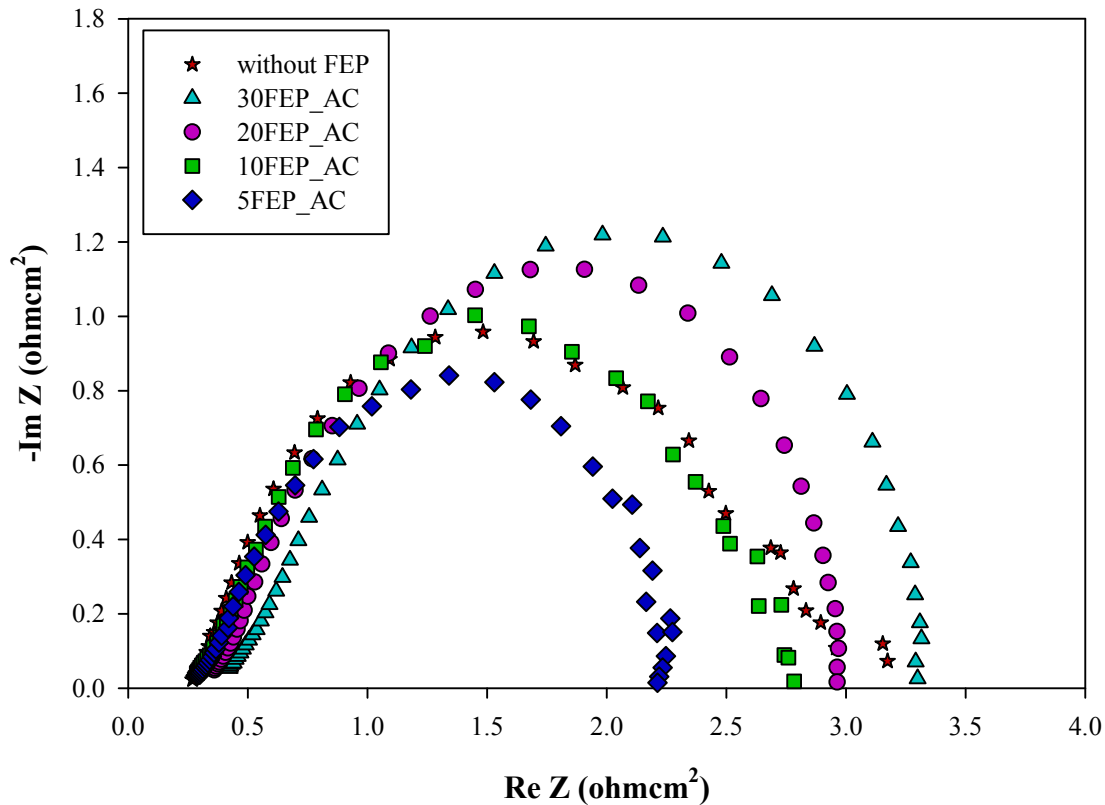


Figure 4.6 Electrochemical impedance spectra obtained for running fuel cell at 0.5 V. Pt loading of anode and cathode electrodes was 1.2 mg Pt/cm². Both anode and cathode catalyst layer were coated with FEP nanoparticles. PEMFC was operated at H₂/Air gas-feeding mode

Parameters of equivalent circuit modeling of EIS spectra of MEA1 are shown in Table 4.4. While rendering CL more hydrophobic, fraction of hydrophobic pores increased, and thus, water condensation in the pores of the CL decreased due to negative or zero capillary pressure. This caused the hydrophobic pores full of hydrogen saturated with water vapor (Weber et al. 2004), which resulted in decreased membrane hydration. 5FEP_AC had the lowest charge transfer resistance

at the cathode ($1.72 \Omega\text{cm}^2$) among all CLs, while 30FEP_AC ($2.43 \Omega\text{cm}^2$) had the highest. Rendering cCL more hydrophobic resulted in decreased Pt utilization. This led to lower water amount in the cCL coupled with high airflow rate. Although CLs without FEP have higher Pt utilization than 20FEP_AC, 10FEP_AC, and 5FEP_AC, charge transfer resistance at the cathode ($2.51 \Omega\text{cm}^2$) was higher than 20FEP_AC ($2.32 \Omega\text{cm}^2$), 10FEP_AC ($2.13 \Omega\text{cm}^2$), and 5FEP_AC ($1.72 \Omega\text{cm}^2$). This indicated that 5, 10, and 20 wt % of FEP nanoparticles in the cCL mitigate flooding, which led to higher reaction rate than CLs without FEP. On the other hand, as the weight percentage of FEP nanoparticles exceeded 10, charge transfer resistance at cathode increased due to decreased Pt utilization.

Table 4.4 Parameters of equivalent circuit modeling of EIS spectra of MEA1 at H₂/Air gas-feeding mode

MEA Type	Air		
	R _{HF} (Ωcm^2)	R _{ct} (A) (Ωcm^2)	R _{ct} (C) (Ωcm^2)
without FEP MEA1	0.25	0.11	2.51
30FEP_AC	0.38	0.53	2.43
20FEP_AC	0.31	0.37	2.32
10FEP_AC	0.23	0.36	2.13
5FEP_AC	0.26	0.29	1.72

FEP Loaded Catalyst Layer on Cathode Electrode (MEA2):

Figure 4.7 illustrates polarization and power density curves obtained for MEA2 at H₂/Air gas feeding mode. Performances of all MEAs reduced by half, compared to MEAs operated with H₂/O₂ reaction gasses. The current density at 0.9V for CLs without FEP, which had no FEP in CLs, was 39 mA/cm². The highest intrinsic activity obtained for CLs without FEP. Current densities at the same voltage for 5FEP_C and 10FEP_C were identical and 30 mA/cm². 20FEP_C and 30FEP_C also had identical current densities (10 mA/cm²) at the same voltage. As FEP weight percentage increased, Pt utilization decreased, accordingly, performances decreased, gradually.

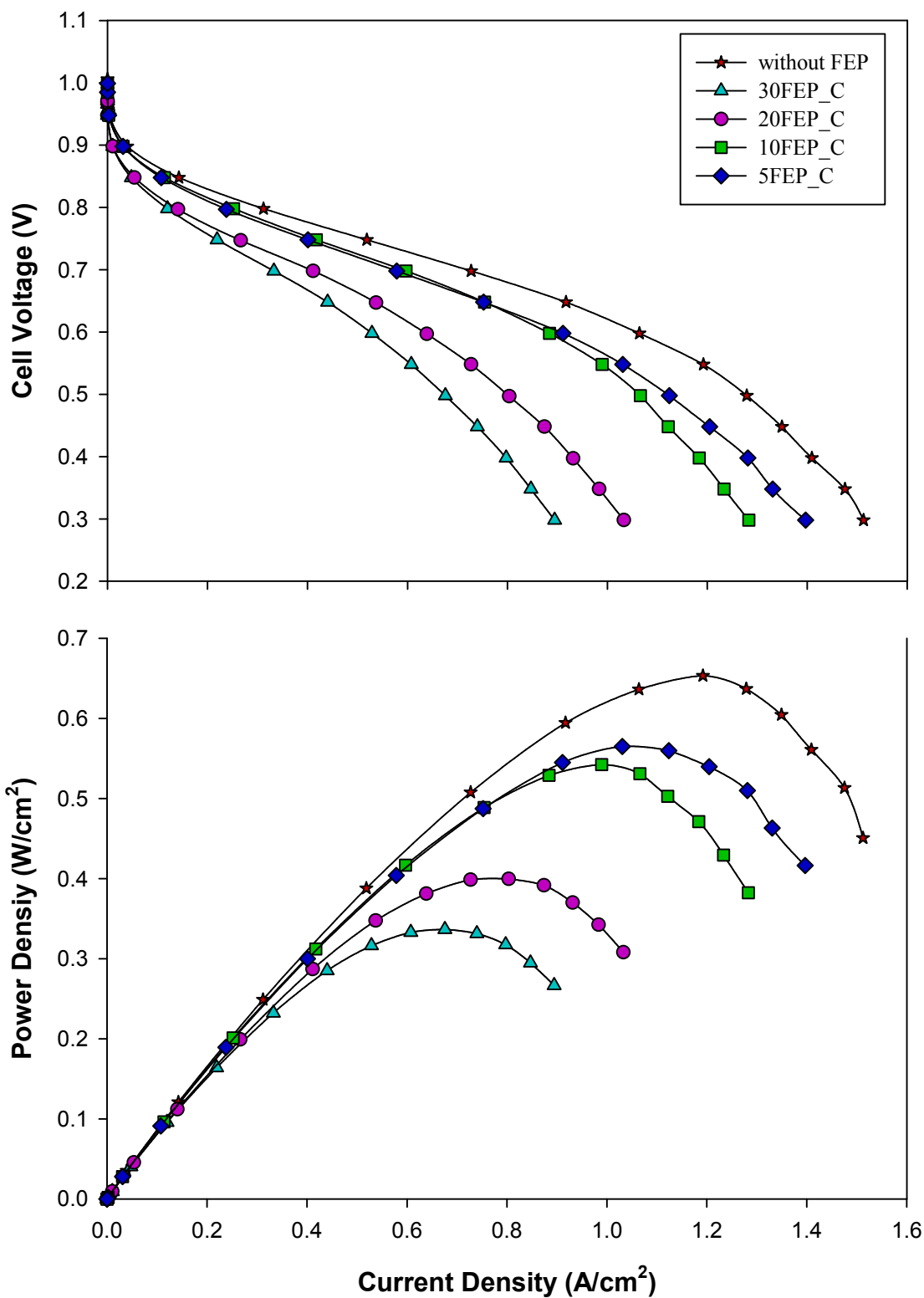


Figure 4.7 Polarization and power density curves of PEMFC for MEA2. Pt loading of anode and cathode electrodes was $1.2 \text{ mgPt}/\text{cm}^2$. Cathode catalyst layer was coated with FEP nanoparticles. PEMFC was operated at H_2 /Air gas-feeding mode

The maximum power density was 0.60 W/cm^2 at 0.45 V for CLs without FEP. 5FEP_C had a power density of 0.54 W/cm^2 at 0.45 V . Power density of 10FEP_C was 0.50 W/cm^2 at 0.45 V . Friedman et al (Friedmann & Van Nguyen 2010), obtained ca. 0.52 W/cm^2 power density at 0.45 V for lower P loading at the cCL with 10 wt % PTFE at H_2/Air gas-feeding mode. They also prepared the catalyst ink with 2-step preparation method. Although Pt loading (1.2 mg/cm^2) was three-fold in our study, power densities of cathode CLs were very similar. This is attributed to the higher hydrophilic properties of FEP nanoparticles according to PTFE nanoparticles. Moreover, FEP nanoparticles can be easily shaped compared to PTFE nanoparticles; have a lower viscosity (Park & Park 2012), leading to enhanced homogeneity in Pt distribution. Power density of 20FEP_C and 30FEP_C were 0.39 W/cm^2 and 0.30 W/cm^2 at 0.45 V .

Figure 4.8 illustrates EIS spectra of MEA2 measured at 0.5 V . Impedance spectrum of all CLs demonstrates only one arc at high-frequency data range. Mass transport limitations associated with water accumulation in the pores of GDL of cathode diminished also in this MEA configuration. This is attributed to the high airflow rate, because when air flow rate was higher than stoichiometric flow rate, it prevents cathode over flooding (Ciureanu & Roberge 2001) via promoting back diffusion of water. High-frequency resistances of all CLs were similar, while the high-frequency resistance of 10FEP_C was the lowest ($0.24 \text{ } \Omega\text{cm}^2$) and high-frequency resistance of 5FEP_C was the highest ($0.28 \text{ } \Omega\text{cm}^2$). Charge transfer resistances at the cathode of all CLs increased more than 4 times, which also indicates reduced reaction kinetics compared to H_2/O_2 feeding mode.

The lowest charge transfer resistance at cathode was obtained for 5FEP_C ($1.69 \text{ } \Omega\text{cm}^2$). Although, CLs without FEP have higher Pt utilization than 20FEP_C, and 5FEP_C, charge transfer resistance ($2.51 \text{ } \Omega\text{cm}^2$) was higher than 20FEP_C ($2.25 \text{ } \Omega\text{cm}^2$), and 5FEP_C ($1.69 \text{ } \Omega\text{cm}^2$). This indicated that 20, and 5 wt % of FEP nanoparticles in the cCL mitigate flooding, which led to higher reaction rate at the triple phase boundary than CLs without FEP. The highest charge transfer resistance at cathode was obtained for 10FEP_C ($3.13 \text{ } \Omega\text{cm}^2$). This may point out the disrupted ionic network, leading to the lowest reaction rate.

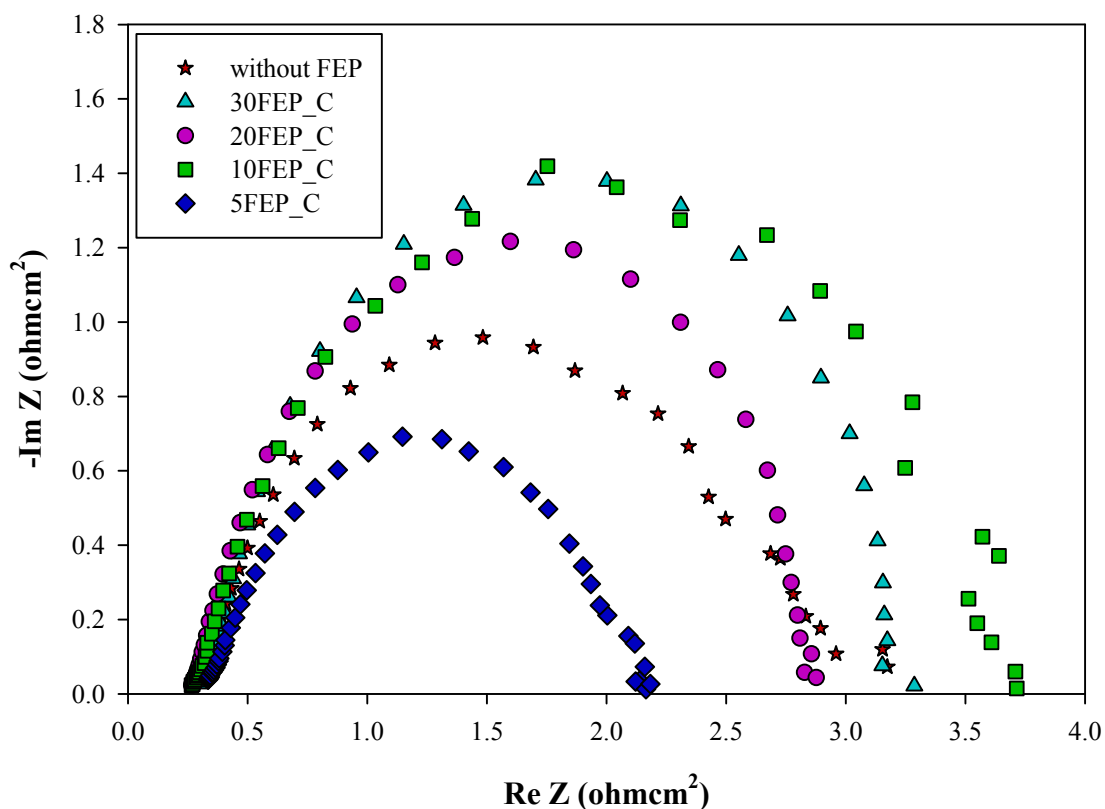


Figure 4.8 Electrochemical impedance spectra obtained for running fuel cell at 0.5 V. Pt loading of anode and cathode electrodes was 1.2 mgPt/cm^2 . The only cathode catalyst layer was coated with FEP nanoparticles. PEMFC was operated at H_2/Air gas-feeding mode

Parameters of equivalent circuit modeling of EIS spectra of MEA2 are shown in Table 4.5.

Table 4.5 Parameters of the equivalent circuit modeling of MEA2 at H_2/Air gas-feeding mode

MEA Type	Air		
	$R_{HF} (\Omega\text{cm}^2)$	$R_{ct} (A) (\Omega\text{cm}^2)$	$R_{ct} (C) (\Omega\text{cm}^2)$
without FEP MEA2	0.25	0.11	2.51
30FEP_C	0.27	0.28	2.66
20FEP_C	0.26	0.35	2.25
10FEP_C	0.24	0.22	3.13
5FEP_C	0.28	0.16	1.69

4.4. Conclusions

FEP nanoparticles in the cCLs of 10FEP_C, 5FEP_C at H₂/O₂ feeding mode and in the CLs of 20FEP_AC, 10FEP_AC, 5FEP_AC, 20FEP_C, and 5FEP_C at H₂/Air feeding mode provide meso-macro hydrophobic channeling, which mitigates flooding compared to CLs without FEP.

For anode and cCL including 30 wt % FEP nanoparticles (30FEP_AC), capillary pressure increased due to high hydrophobicity, the accordingly liquid water concentration at anode CL/membrane interface decreased and this caused membrane dehydration.

The influence of FEP nanoparticles incorporated to the CL confirms the results obtained with PTFE nanoparticles. However, due to its higher hydrophilic properties FEP nanoparticles might be more advantageous at lower amounts.

CHAPTER 5

UNDERSTANDING THE EFFECTS OF HYDROPHOBIC, HIGH Pt LOADED CATALYST LAYERS INCLUDING PFA NANOPARTICLES ON MASS TRANSPORT AND PERFORMANCE OF PEM FUEL CELL

In this chapter, poly(tetrafluoroethylene-co-perfluoro vinyl ether) (PFA) nanoparticles were added to CL to facilitate excess water removal from the triple phase boundary in high Pt loading (1.2 mg/cm^2) PEMFC electrodes. The loading of PFA in the catalyst ink was varied from zero to 30 weight percentage. High-performance electrodes for anode and cathode were prepared by ultrasonic spray coating technique with a commercial catalyst containing 70 wt % Pt on carbon. Different membrane electrode assemblies (MEAs) were prepared in order to differentiate the influence of hydrophobic nanoparticles on water transport and cell performance. In the first configuration (MEA1), PFA nanoparticles were added to both anode and cathode catalyst layers. In the second configuration (MEA2), PFA nanoparticles were added only to cCL. Anode catalyst layer prepared with commercial catalyst (Pt/C) impregnated with Nafion ionomer. PEM fuel cell tests were carried out at both H_2/O_2 and H_2/Air gas-feeding modes.

5.1. Introduction

Significant progress has been reported in increasing PEMFC performance and durability in the literature. This progress had been enabled by discovering new materials and manufacturing methods for the membrane electrode assembly (MEA), which is composed of the proton exchange membrane (PEM), catalyst and gas

diffusion layers. In a PEMFC, hydrogen and oxygen are combined electrochemically. Hydrogen oxidizes at the anode, releasing proton and electrons. The generated protons are transported across the membrane and the electrons across the external circuit. At the cCL, protons and the electrons react with oxygen to generate water; therefore, it has a primary impact on water management (Weber et al. 2014). In CLs, electrochemical reactions take place at triple phase boundaries where, electrons, protons, and reactant gasses meet. At a triple phase boundary, carbon conducts electrons, while Nafion ionomer conducts protons and voids allow a reactant gas to access active catalyst sites. In order to provide better proton conduction, Nafion ionomer in CLs should be fully saturated with liquid water in order to provide the highest proton conduction. However, the water concentration in pores of agglomerates and around the agglomerates should be optimum. Otherwise, liquid water fills the pores, covers the agglomerates and consequently, hinders gas transport, and leads to reactant starvation. One strategy to reduce reactant starvation at active catalyst sites due to water accumulation is to create distinct pathways for gas and liquid transport. For this purpose, hydrophobic nanoparticles are incorporated to the CL to create two-phase flow.

Fluoropolymers used to construct the hydrophobic backbone of fuel cell membranes can be used as a hydrophobic agent in the CLs. Chen et al (Chen et al. 2006) prepared fuel cell membranes with different fluoropolymer films, such as Polytetrafluoroethylene (PTFE), Fluorinated ethylene propylene (FEP), Perfluoroalkoxy alkanes (PFA), Ethylene tetrafluoroethylene (ETFE), Polyvinylidene fluoride (PVDF) and Polyvinyl fluoride (PVF). They found that PFA-based membranes are promising for fuel cell applications due to their good combination of physicochemical, structural, and thermal properties. In the literature, PFA-based films for the fuel cell membrane preparations has been investigated by different research groups (Nasef et al. 2000; Rager et al. 2002; Nasef & Saidi 2002; Nasef & Saidi 2003; Chen et al. 2006; Lappan et al. 2007; Kang et al. 2009; Kang et al. 2010; Fei et al. 2012; Nasef 2014; Shin et al. 2014). The research group (Shin et al. 2014; Latorrata et al. 2014) were tested three different fluorinated polymers in order to replace PTFE: PFA and FEP were applied to make MPLs hydrophobic. They found that at high relative humidity (RH), FEP- and PFA- based MPLs could manage quite well the increasing amount of water if compared with PTFE-MPLs,

due to higher hydrophobicity. Therefore, PFA_MPLs enhance the cell behavior upon increasing RH, an occurrence, which reveals the good water management ability, certainly superior to that of PTFE-based MPLs.

The objective of this work is to investigate the influence of PFA nanoparticles in CLs as a hydrophobic agent in a low-temperature single PEM fuel cell. The electrodes were prepared by ultrasonic coating technique with high Pt-containing commercial catalyst (70 wt % Pt/C) with a high Pt loading (1.2 mg Pt/cm²). Fuel cell performance tests were carried out to determine the influence of PFA nanoparticles on high-performance PEM fuel cells. Impedance spectroscopy results have revealed the influence of PFA nanoparticles on reaction kinetics and water management.

5.2. Materials and Methods

Ink preparation, electrochemical characterization methods, and performance tests are the same as explained in Chapter 3.

5.2.1. MEA Configuration

Performance testing was carried out with two different membrane electrode assembly configurations. By this way, the effect of PFA nanoparticles in anode and cathode CL on water transport mechanism was investigated separately. Electrocatalyst (Pt/C), Nafion, and PFA nanoparticle loadings on CLs for prepared MEAs are summarized in Table 5.1.

Table 5.1 Pt, Nafion, and PFA loadings in catalyst layers

Catalyst Ink	Loading (mg/cm ²)		
	Pt	Nafion	PFA
without PFA	1.20	0.80	-
30PFA	1.20	1.40	1.40
20PFA	1.20	1.11	0.74
10PFA	1.20	0.93	0.31
5PFA	1.20	0.85	0.14

In the first configuration (MEA1), PFA nanoparticles were coated with both anode and cathode catalyst layers. In the second configuration (MEA2), PFA nanoparticles were coated only on the cCL. Numbers before PFA synonym represent the weight percentage of PFA in the CL on a dry basis. For example, 5PFA represents the CL prepared with the ink containing 5 wt % PFA on a dry basis.

5.3. Results and Discussion

5.3.1. Effect of PFA Loading on Performance and Running Electrochemical Impedance Spectrum of PEMFC at H₂/O₂ Gas-feeding Mode

PFA Loaded Catalyst Layers on Both Electrodes (MEA1):

Polarization and power density curves for CLs with four different Nafion and PFA loadings, working at H₂/O₂ gas-feeding mode are shown in Figure 5.1. The performances of PFA loaded CLs were compared with CLs without PFA. Kinetically controlled region ($<0.1 \text{ A/cm}^2$) of polarization curves gives information about Pt utilization of cCL. The current density at 0.9V for CLs without PFA was 79 mA/cm^2 . The highest current density at the same voltage among PFA included CLs was obtained for 5PFA_AC (70 mA/cm^2). 10PFA_AC (60 mA/cm^2) had lower current density than 5PFA_AC. Current densities at 0.9V for 20PFA_AC (52 mA/cm^2) and 30PFA_AC (56 mA/cm^2) were very similar to each other. The highest intrinsic activity was obtained for CLs without PFA, while the lowest was obtained for 20PFA_AC and 30PFA_AC. This indicated that as the PFA weight percentage increased, Pt utilization decreased due to the isolation of Pt and carbon particles by PFA nanoparticles. The maximum power density at 0.45 V was 1.15 W/cm^2 for CLs without PFA. As PFA weight percentage increased, power density decreased, gradually. 5PFA_AC and 10PFA_AC had closer performances to CLs without PFA with power densities of 0.96 W/cm^2 and 0.82 W/cm^2 at 0.45 V, respectively. Power densities of 20PFA_AC and 30PFA_AC at 0.45V were similar and found as 0.65, and 0.69 W/cm^2 , respectively.

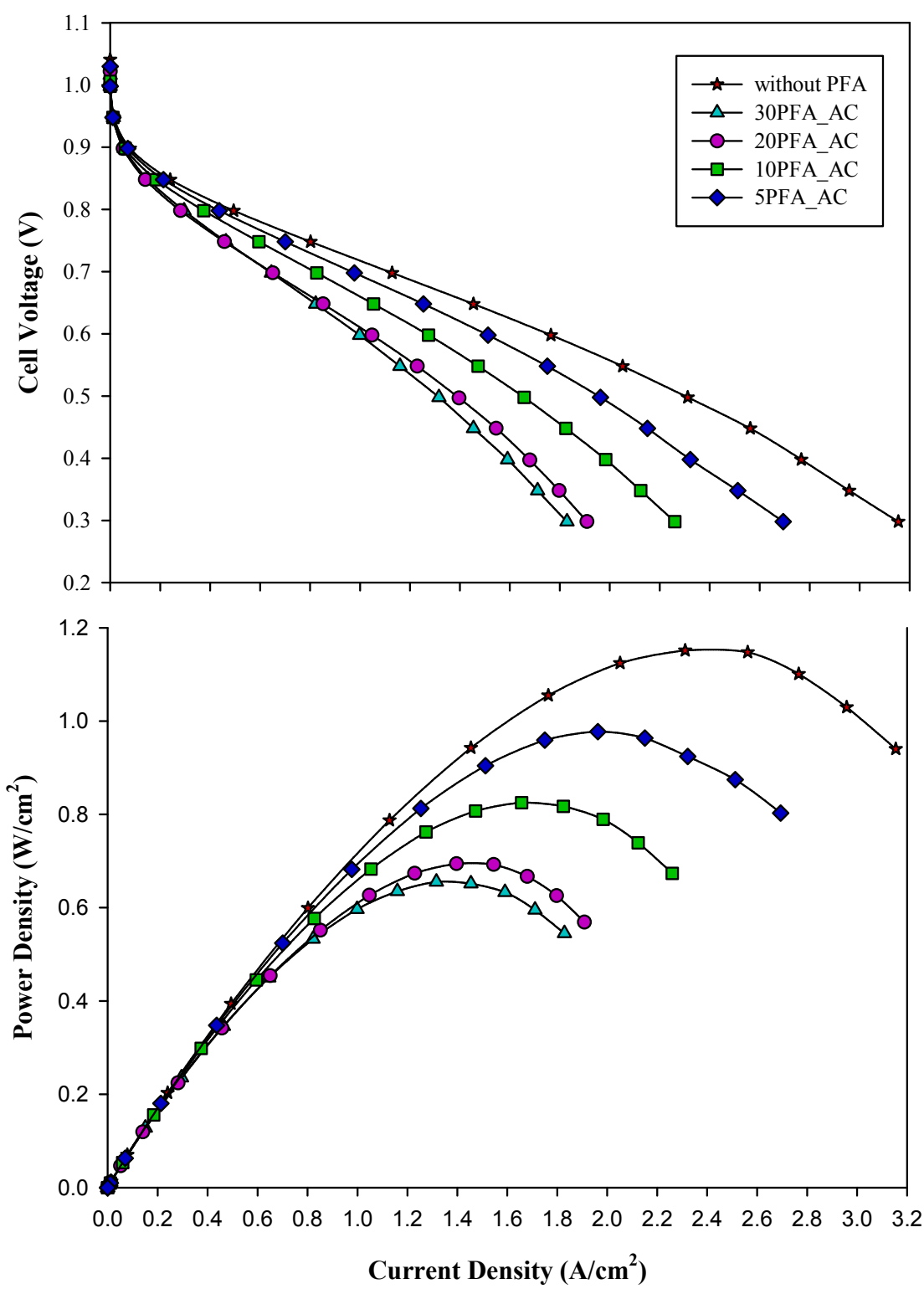


Figure 5.1 Polarization and power density curve for PEMFC for MEA1. Pt loading of anode and cathode electrodes was 1.2 mgPt/cm². Both anode and cathode catalyst layer were coated with PFA nanoparticles. PEMFC was operated at H₂/O₂ gas-feeding mode

As PFA weight percentage in the CLs was increased, Pt utilization decreased, consequently, power density decreased, gradually. Power densities for CLs obtained for PTFE were as follow: 5PTFE_AC (1.05 W/cm²), 10PTFE_AC (0.92 W/cm²), 20PTFE_AC (0.78 W/cm²) and 30PTFE_AC (0.54 W/cm²). Power density attained for CLs prepared with PTFE nanoparticles decreases gradually, in accordance with an increase in PTFE amount. On the other hand, power densities for CLs obtained for FEP nanoparticles were as follow: 5FEP_AC (0.91 W/cm²), 10FEP_AC (0.89 W/cm²), 20FEP_AC (0.61 W/cm²) and 30FEP_AC (0.53 W/cm²). Catalyst layers with 10 wt % FEP nanoparticles demonstrated improved performance than expected. Although 10FEP_AC included a higher amount of FEP, its performance was closer to 5FEP_AC.

Figure 5.2 illustrates EIS spectra of MEA1 measured at 0.5 V. Impedance spectra for all CLs show a high-frequency arc followed by a low-frequency arc. The first arc at high frequencies is accounted for charge transfer process, and latter is accounted for mass-transport processes (Yuan et al. 2007). The intercept of the high-frequency impedance arc on the real axis represents the total ohmic resistance of the cell. The total ohmic resistance of the cell (R_{HF}) is expressed as the sum of the contributions from uncompensated contact resistances; resistance to ion migration within the electrolyte, resistance to electron transport within the cell components (electrodes, gas diffusion layer, and flow field/current collectors) (Cooper & Smith 2006). High frequency arc, representing the charge transfer resistance (R_{ct}), which is responsible for processes occurring in the cCL: interfacial charge transfer and mass transport of Air/O₂ in the pores of the CL (agglomerate diffusion) and in the Nafion layer surrounding the catalyst particles (thin film diffusion) (Ciureanu & Roberge 2001). In the cathode side, MPL mitigates flooding through enhanced transport of water from cathode towards the anode side, while on the anode side, acts as a barrier to water removal (Cho & Mench 2012). When PFA nanoparticles were added in the cCL, hydrophobic channels increasing capillary pressure were constructed, which allowed gas to access to active catalyst sites. Produced water first condenses and/or flows in the larger hydrophilic pores, after the hydrophilic pores are flooded, water will eventually penetrate into first the larger hydrophobic pores and then to smaller ones, which will be the least prone to flooding due to the highest capillary pressure (Dai et al. 2009). Since the fraction of hydrophobic pores was increased, water

saturation in the hydrophilic pores increased. Increased water saturation provided the construction of hydraulic connections among pores, which promoted liquid transport. This is known as internally connected capillary liquid flow or funicular regime (Cho & Mench 2010). It should be noted that GDL consists of an MPL with 5 wt % PTFE on both anode and cathode side.

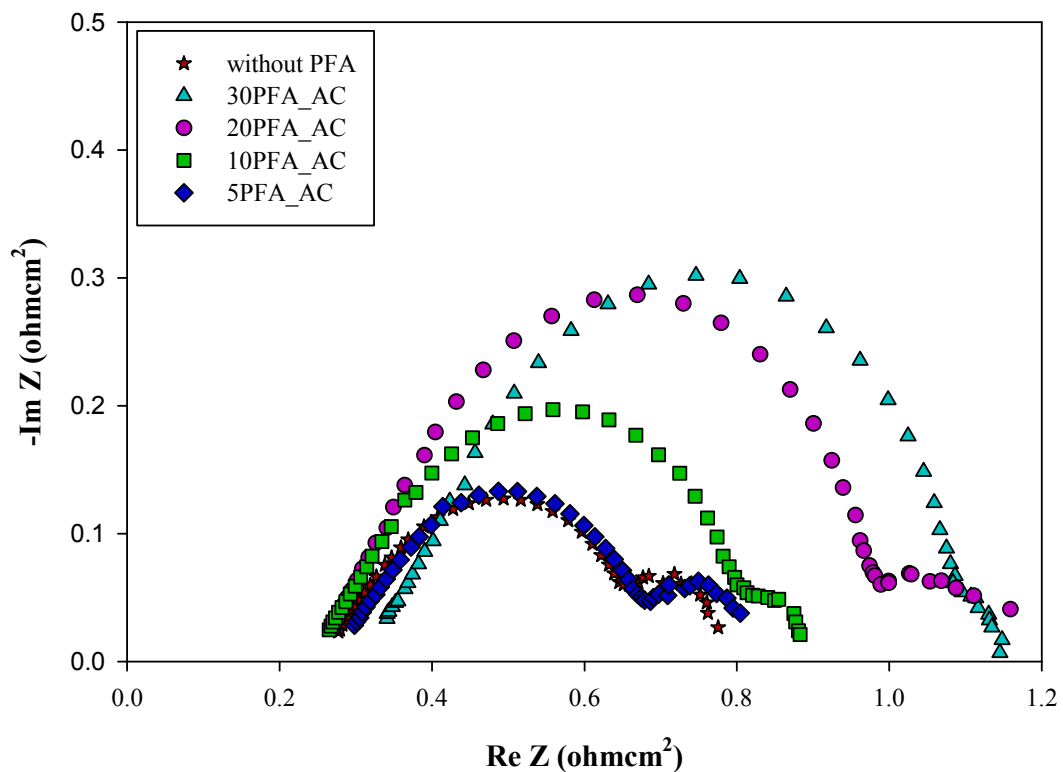


Figure 5.2 Electrochemical impedance spectra for running fuel cell obtained at 0.5 V. Pt loading of anode and cathode electrodes was 1.2 mgPt/cm^2 . Both anode and cathode catalyst layer were coated with PFA nanoparticles. PEMFC was operated at H_2/O_2 gas-feeding mode

Parameters of equivalent circuit modeling of EIS spectra for MEA1 are listed in Table 5.2. High-frequency resistances of all MEA's were similar. Moreover, 10PFA_AC had the lowest high-frequency resistance ($0.20 \text{ } \Omega\text{cm}^2$), which indicated the lowest ohmic resistance of membrane among all MEAs. This is attributed to hydrophobic channels in the aCL of 10PFA_AC increasing the retention time of

liquid water at the aCL/membrane interface by increasing capillary pressure. This led to increasing in water concentration at aCL/membrane interface. 30PFA_AC had the highest high-frequency resistance ($0.29 \Omega\text{cm}^2$), which was shifted to the right to the axes of the real impedance. This is attributed to the dehydrated anode (Le Canut et al. 2006);(Freire & Gonzalez 2001). PFSA polymer membrane surface is strongly hydrophobic when it is in contact with water vapor (whether saturated or not), and it becomes hydrophilic when it is in contact with liquid water (Jiao & Li 2011). Therefore, the decrease in membrane hydration is associated with decreased concentration of liquid water at CL/membrane interface at the anode side. While rendering CL more hydrophobic, a fraction of hydrophobic pores increased, and thus, water condensation in the pores of the CL decreased. Because, in a hydrophobic pore the liquid water pressure should overcome both the surface tension of the hydrophobic pores of the CL and the pressure to drive the liquid flow against the gas flow (Benziger et al. 2005), while in a hydrophilic pore the liquid water pressure should only overcome the pressure to drive the flow against gas flow. Increased hydrophobicity led to higher capillary pressure, causing the hydrophobic pores full of hydrogen gas saturated with water vapor (Weber et al. 2004). This may result in membrane dehydration.

Table 5.2 Parameters of equivalent circuit modeling of EIS spectra of MEA1 at H₂/O₂ gas-feeding mode

MEA Type	O ₂			
	R _{HF} (Ωcm^2)	R _{ct} (A)(Ωcm^2)	R _{ct} (C)(Ωcm^2)	R _{mt} (Ωcm^2)
without PFA MEA1	0.26	0.03	0.39	0.11
30PFA_AC	0.29	0.20	0.62	0.03
20PFA_AC	0.25	0.19	0.55	0.16
10PFA_AC	0.20	0.10	0.53	0.06
5PFA_AC	0.26	0.11	0.32	0.13

5PFA_AC had the lowest charge transfer resistance ($0.32 \Omega\text{cm}^2$) at cathode among all CLs, which is pointed out the highest reaction rate among all CLs. This indicates that 5PFA_AC mitigated flooding in the CL via promoting capillary water

flow. As PFA amount in the CLs increased, charge transfer resistance at both anode and cathode increased. Higher PFA weight percentage in the CL reduced Pt utilization leading to decreased amount of product water. Since the water generation rate was low, a continuous hydraulic connection among water in pores was not formed, and therefore the product water was widely spread over the GDL in the isolated droplet form, increasing water saturation in the porous media (Cho & Mench 2012). The highest mass transfer resistance was obtained for 20PFA_AC ($0.16 \Omega\text{cm}^2$) coupled with high charge transfer resistance at the cathode ($0.55 \Omega\text{cm}^2$) indicated higher water saturation in the pores of cGDL blocking pathways for gas transport. Although 30PFA_AC include the highest PFA amount, the lowest mass transfer resistance ($0.03 \Omega\text{cm}^2$) was attained. Moreover, 30PFA_AC had the highest charge transfer resistance at the cathode ($0.62 \Omega\text{cm}^2$). 30PFA_AC had the lowest power density among all CLs due to the lowest electrochemically active sites. Therefore, less water produced which that might cause an increase in charge transfer resistance. On the other hand, the hydrophilic structure of PFA nanoparticles in the CL absorbed water molecules; therefore, the water concentration in the cGDL was lower and occupation of the pores of cGDL by water droplets decreased. Therefore, reactant gas transported from pores of the cGDL freely. In addition to that, an increase in the fraction of hydrophobic pores caused to increase water saturation in the hydrophilic pores and around catalyst agglomerates. This was resulted in increased diffusion thickness for oxygen to reach triple phase boundary leading to increasing in charge transfer resistance at the cathode. 30PFA_AC had also the highest charge transfer at the anode side ($0.20 \Omega\text{cm}^2$). When PFA nanoparticles were added into the anode CL, electrochemically active sites decreased causing the increase in the charge transfer resistance at the aCL. Rendering aCL more hydrophobic led water molecules accumulated in hydrophilic pores causing diffusion limitations for hydrogen gas to reach active sites.

PFA Loaded Catalyst Layer on Cathode Electrode (MEA2):

Polarization and power density curves for MEA2 with four different PFA loadings in cCLs, working at H₂/O₂ gas-feeding mode are illustrated in Figure 5.3. Performances of PFA loaded cCLs were compared with CLs without PFA. The current density at 0.9V for CLs without PFA was 79 mA/cm². Current density for 5PFA_C (76 mA/cm²) at the same voltage was closest to CLs without PFA. 10PFA_C had lower intrinsic activity than 5PFA_C with a value of 68 mA/cm². On the other hand, 20PFA_C, and 30PFA_C had identical current densities (50 mA/cm²) current densities at 0.9 V, respectively, which were the lowest intrinsic activities indicating lower Pt utilization. The maximum power density at 0.45 V was 1.15 W/cm² obtained for CLs without PFA. Power densities attained for 10PFA_C (1.04 W/cm²) and for 5PFA_C (1.03 W/cm²) at 0.45 V very similar and closest values to CLs without PFA. Above 1.9 A/cm², 10PFA_C had a slightly higher performance than 5PFA_C, indicating enhanced water management at higher current densities. The lowest power density was obtained for 20PFA_C and 30PFA_C due to the lowest Pt utilization. On the other hand, although 30PFA_C (0.84 W/cm²) had a higher PFA weight percentage, it had higher power density than 30PFA_C (0.87 W/cm²) at 0.45 V. The enhanced power density of 30PFA_C is attributed to the higher hydrophilic properties of PFA nanoparticles leading to higher proton conductivity despite consisting of lower electrochemical active sites.

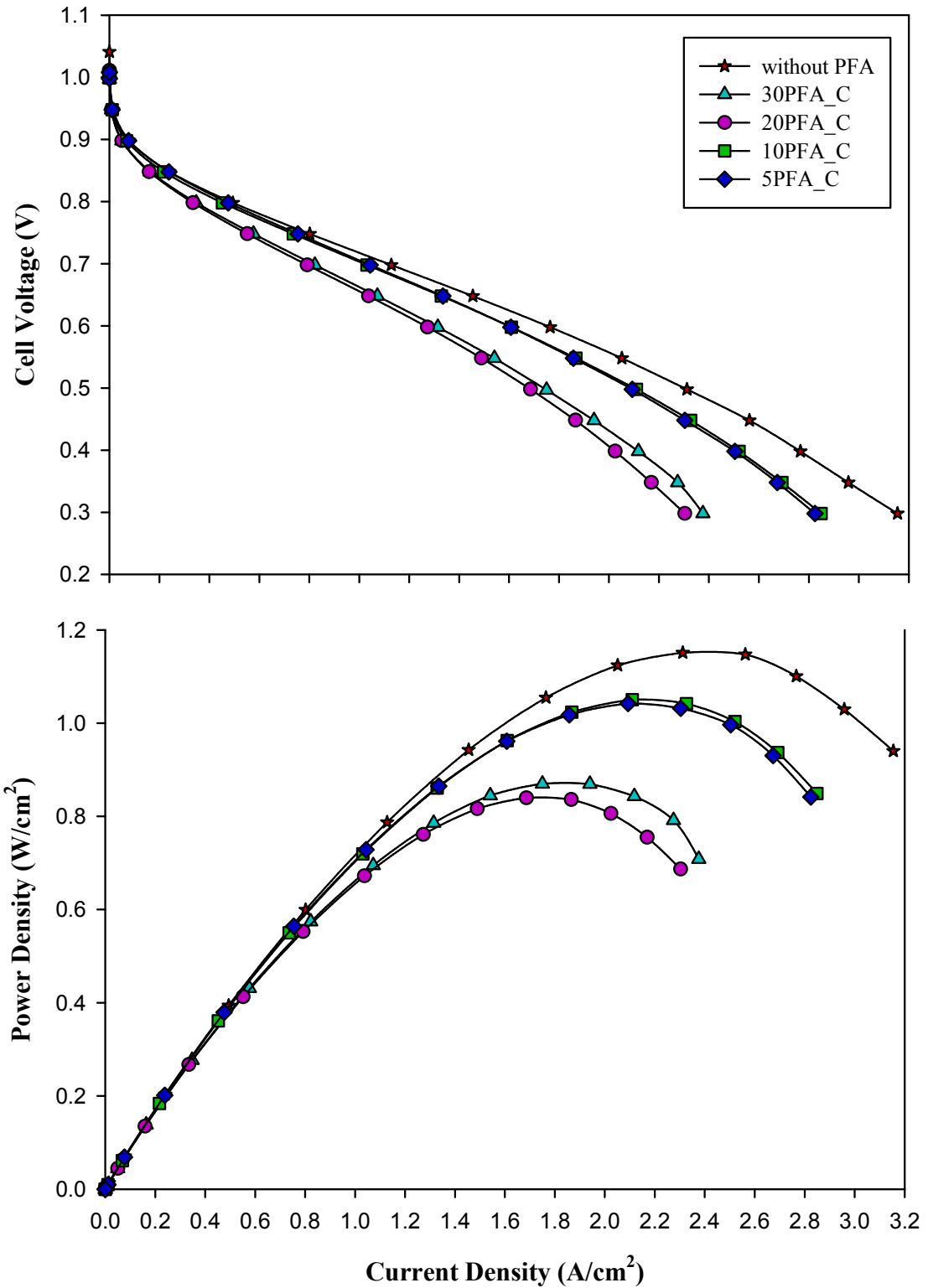


Figure 5.3 Polarization and power density curves of PEMFC for MEA2. Pt loading of anode and cathode electrodes was $1.2 \text{ mgPt}/\text{cm}^2$. Cathode catalyst layer was coated with PFA nanoparticles. PEMFC was operated at H_2/O_2 gas-feeding mode

Figure 5.4 illustrates EIS spectra of MEA2 measured at 0.5 V. Parameters of equivalent circuit modeling of EIS spectra of MEA2 are shown in Table 5.3. Impedance spectrum of all CLs demonstrates a high-frequency arc followed by a low-frequency arc. High-frequency resistances of all CLs were similar. The high-frequency resistance of 10PFA_C ($0.24 \Omega\text{cm}^2$) was the lowest among all CLs, while the high-frequency resistance of 30PFA_C ($0.28 \Omega\text{cm}^2$) was the highest. This indicated that ohmic resistances for all MEAs were similar.

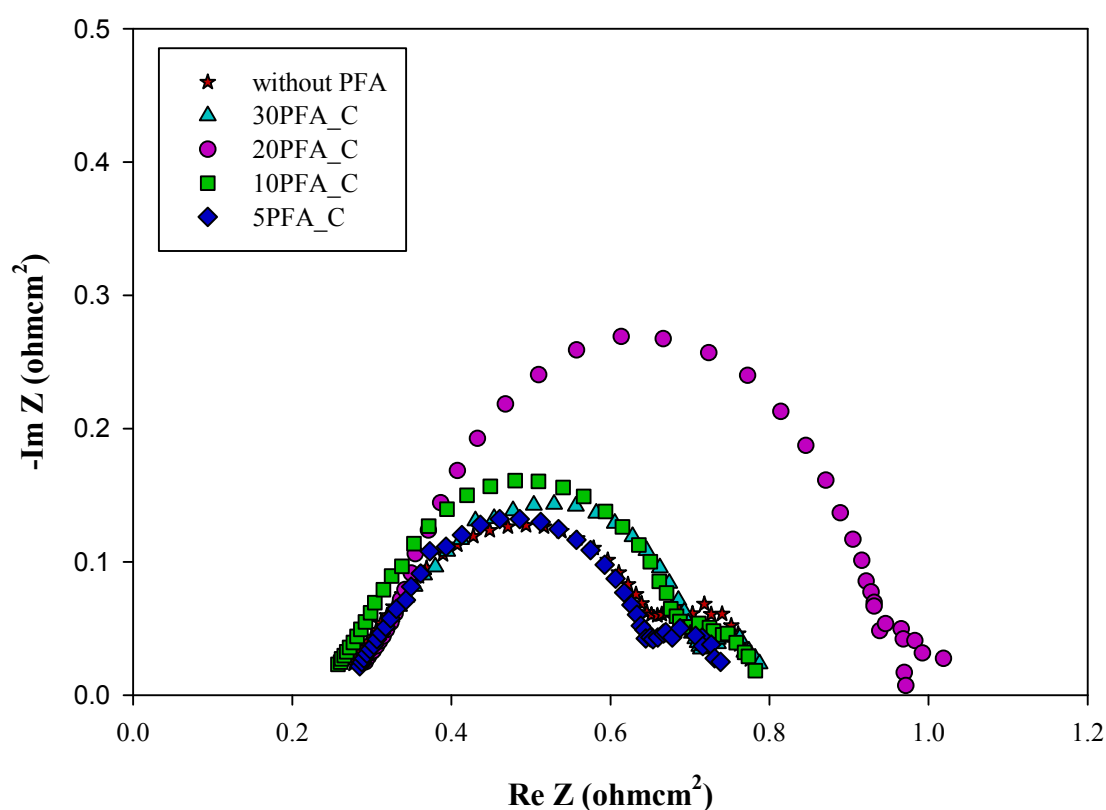


Figure 5.4 Electrochemical impedance spectra for running fuel cell obtained at 0.5 V. Pt loading of anode and cathode electrodes was 1.2 mgPt/cm^2 . Cathode catalyst layer was coated with PFA nanoparticles. H_2/O_2 gas-feeding mode was used

Charge transfer resistance for 5PFA_C at the cathode ($0.32 \Omega\text{cm}^2$) was the lowest among all CLs while mass transfer resistance of 5PFA_C ($0.09 \Omega\text{cm}^2$) was also lower than CLs without PFA. Although 5PFA_C had lower Pt utilization, it had

a higher reaction rate with respect to CLs without PFA. This indicates that enhanced water management provided with distributed paths for gas and water transport through the CL, which allowed gas access to the triple phase boundary. Furthermore, excess water removal was facilitated. The highest charge transfer resistance at cathode side was obtained for 20PFA_C ($0.61 \Omega\text{cm}^2$). The lowest cell performance was also obtained for 20PFA_AC. Higher charge transfer resistance caused a decrease in the cell performance. Despite having higher PFA amount, 30PFA_C had lower charge transfer resistances ($0.46 \Omega\text{cm}^2$) than and 20PFA_C ($0.61 \Omega\text{cm}^2$), indicating higher reaction rate. Therefore, 20PFA_C (0.84 W/cm^2) had lower power density than 30PFA_C (0.87 W/cm^2) at 0.45 V. All mass transfer resistances were lower than mass transfer resistances of CLs without PFA ($0.11 \Omega\text{cm}^2$). This indicated the volume of the blocked pores distributed along the cGDL was lower than pores of CLs without PFA.

Table 5.3 Parameters of equivalent circuit modeling of EIS spectra of MEA2 at H_2/O_2 gas-feeding mode

MEA Type	O_2			
	$R_{\text{HF}} (\Omega\text{cm}^2)$	$R_{\text{ct}} (\text{A}) (\Omega\text{cm}^2)$	$R_{\text{ct}} (\text{C}) (\Omega\text{cm}^2)$	$R_{\text{mt}} (\Omega\text{cm}^2)$
without PFA	0.26	0.03	0.39	0.11
MEA2				
30PFA_C	0.28	0.06	0.46	0.07
20PFA_C	0.27	0.06	0.61	0.06
10PFA_C	0.24	0.04	0.43	0.07
5PFA_C	0.26	0.09	0.32	0.09

5.3.2. Effect of PFA Loading on Performance and Running Electrochemical Impedance Spectrum of PEMFC at H₂/Air Gas-feeding Mode

PFA Loaded Catalyst Layers on Both Electrodes (MEA1):

Figure 5.5 illustrates polarization and power density curves obtained for MEA1 at H₂/Air gas feeding mode. Performances of all MEAs reduced by half when the air was used instead of oxygen due to decreased partial pressure of the oxygen. It is well-known that increase in partial pressure of oxygen, not only enhances the electrode kinetics but also reduces the mass transport limitations (Ticianelli et al. 1988). Performances of PFA loaded CLs were compared with CLs without PFA. The current density at 0.9V for CLs without PFA was 39 mA/cm². The highest intrinsic activity was obtained for CLs without PFA. 5PFA_AC (31 mA/cm²) and 10PFA_AC (27 mA/cm²) had lower intrinsic activities than CLs without PFA. As PFA loading on CLs increased, Pt utilization decreased. Therefore, current densities of 20PFA_AC (17 mA/cm²) and 30PFA_AC (21 mA/cm²) were the lowest at 0.9 V. The maximum power density at 0.45 V was 0.60 W/cm² obtained for CLs without PFA. 5PFA_AC and 10PFA_AC had power densities of 0.54 and 0.48 W/cm² at 0.45 V, respectively. Power densities of 20PFA_AC and 30PFA_AC were the lowest and 0.35 W/cm², and 0.38 W/cm² at 0.45 V, respectively. As PFA weight percentage in the CLs increased, performances decreased. However, although weight percentage of PFA nanoparticles in 10PFA_AC was higher than 5PFA_AC, similar performances were attained. Similarly, performances of 30PFA_AC and 20PFA_AC were close to each other.

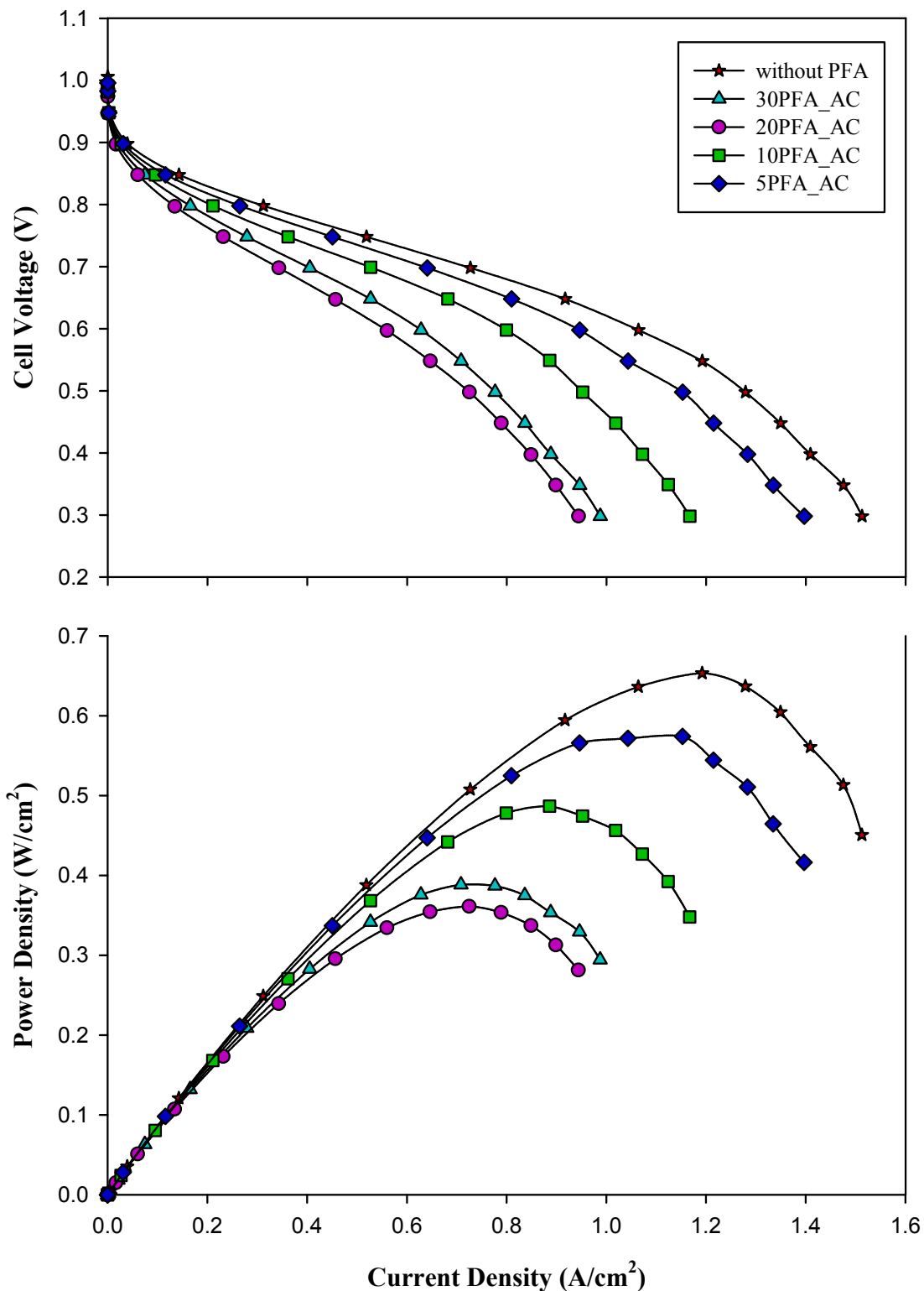


Figure 5.5 Polarization and power density curves of PEMFC for MEA1. Pt loading of anode and cathode electrodes was $1.2 \text{ mgPt}/\text{cm}^2$. Both anode and cathode catalyst layers were coated with PFA nanoparticles. PEMFC was operated at H_2 /Air gas-feeding mode.

Figure 5.6 illustrates EIS spectra of MEA1 measured at 0.5 V. Impedance spectrum of all CLs demonstrates only one arc at high-frequency data range. However, there were two arcs in H₂/O₂ feeding mode. The second arc corresponded to mass transfer limitations (R_{mt}). Mass transport limitation at the cCL was diminished, which is attributed to the high airflow rate. When air flow rate is generally much higher than the stoichiometric flow, it prevents cathode over flooding (Ciureanu & Roberge 2001) via promoting back diffusion of water. Parameters of equivalent circuit modeling of EIS spectra of MEA1 are shown in Table 5.4. Charge transfer resistances of all CLs at both anode and cathode were increased at least more than 2 times compared to H₂/O₂ feeding mode (Table 5.2), which indicates reduced reaction kinetics.

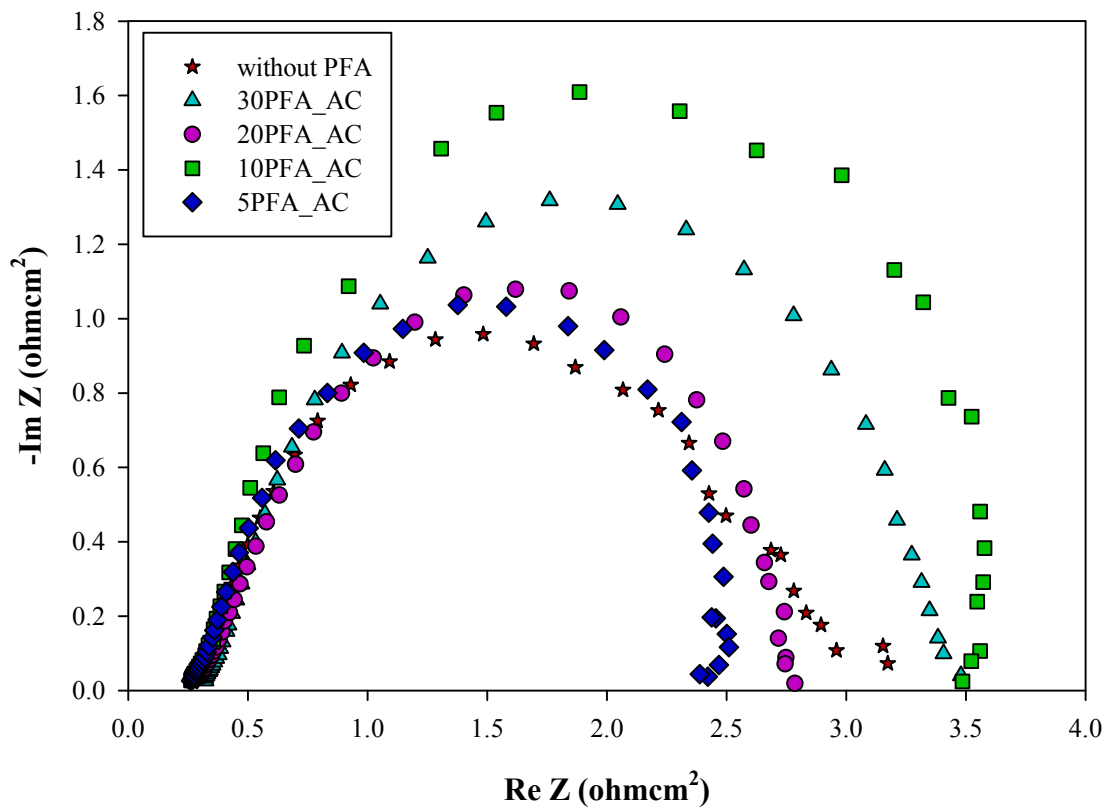


Figure 5.6 Electrochemical impedance spectra obtained for running fuel cell at 0.5 V. Pt loading of anode and cathode electrodes was 1.2 mg Pt/cm². Both anode and cathode catalyst layers were coated with PFA nanoparticles. PEMFC was operated at H₂/Air gas-feeding mode

The decrease in partial pressure of oxygen caused reduced reaction rate, accordingly, the rate of water generation decreased. Because, when oxygen was fed with nitrogen to the cell, oxygen had to diffuse also through the nitrogen to reach the triple phase boundary. This caused a decrease in reaction rate.

Table 5.4 Parameters of equivalent circuit modeling of EIS spectra of MEA1 at H₂/Air gas-feeding mode

MEA Type	Air		
	R _{HF} (Ωcm ²)	R _{ct} (A) (Ωcm ²)	R _{ct} (C) (Ωcm ²)
without PFA MEA1	0.25	0.11	2.51
30PFA_AC	0.28	0.30	2.88
20PFA_AC	0.27	0.41	2.11
10PFA_AC	0.24	0.35	3.05
5PFA_AC	0.24	0.31	1.97

High-frequency resistances of all CLs were similar. However, as PFA amount increased high-frequency resistance increased. Moreover, the high-frequency resistance of 5PFA_AC (0.24 Ωcm²) and 10PFA_AC (0.24 Ωcm²) was same and lower than the high-frequency resistance of CLs without PFA (0.25 Ωcm²). This indicates lower ohmic resistances of 5PFA_AC and 10PFA_AC with respect to CLs without PFA. The increase in membrane hydration is associated with increased concentration of liquid water at CL/membrane interface at the anode side. Hydrophobic nanoparticles in the anode CLs of 5PFA_AC and 10PFA_AC increased the retention time of water diffused from cathode side at CL/membrane interface. In addition to that higher hydrophilic properties of PFA nanoparticles (Chen et al. 2006) increased water uptake. This led to increased water concentration in the CLs. Consequently, ohmic resistance in the CLs decreased. 5PFA_AC (1.97 Ωcm²) and 20PFA_AC (2.11 Ωcm²) had lower charge transfer resistance at the cathode, while 10PFA_AC (3.05 Ωcm²) had the highest. Although CLs without PFA have higher Pt utilization than 5PFA_AC and 20PFA_AC, charge transfer resistance at cathode was

higher. This indicated that PFA nanoparticles in CLs mitigated flooding, which led to higher reaction rate than CLs without PFA.

PFA Loaded Catalyst Layer on Cathode Electrodes (MEA2):

Figure 5.7 illustrates polarization and power density curves obtained for MEA2 at H₂/Air gas feeding mode. Performances of all MEAs reduced by half, compared to MEAs operated with H₂/O₂ reaction gasses. The current density at 0.9V for CLs without PFA was 39 mA/cm². The highest intrinsic activity obtained for CLs without PFA. Current densities at the same voltage for 5PFA_C and 10PFA_C were 45 and 31 mA/cm². 20PFA_C and 30PFA_C were 17 and 25 mA/cm² at the same voltage. The maximum power density was 0.60 W/cm² at 0.45 V for CLs without PFA. 5PFA_C had a power density of 0.56 W/cm² at 0.45 V. Power density of 10PFA_C was 0.52 W/cm² at 0.45V. Friedman et al (Friedmann & Van Nguyen 2010), obtained ca. 0.52 W/cm² power density at 0.45 V for lower Pt loading at the cCL with 10 wt % PTFE at H₂/Air gas-feeding mode. They also prepared the catalyst ink with 2-step preparation method. Although Pt loading (1.2 mg/cm²) was three-fold in our study leading to mass transport limitations, power densities of cCLs were same. This is attributed to the higher proton conductivity of PFA nanoparticles according to PTFE nanoparticles. Power density of 20PFA_C and 30PFA_C were 0.36 W/cm² and 0.49 W/cm² at 0.45V. As PFA weight percentage increased, Pt utilization decreased, accordingly, performances decreased. However, although, 30PFA_C had a higher amount of hydrophobic nanoparticles, the power density of 30PFA_C was higher than 20PFA_C. The power density of 30PFA_C was also higher than 30PTFE_C and 30FEP_C. The increase in the performance of 30PFA_C is attributed to its enhanced catalytic activity.

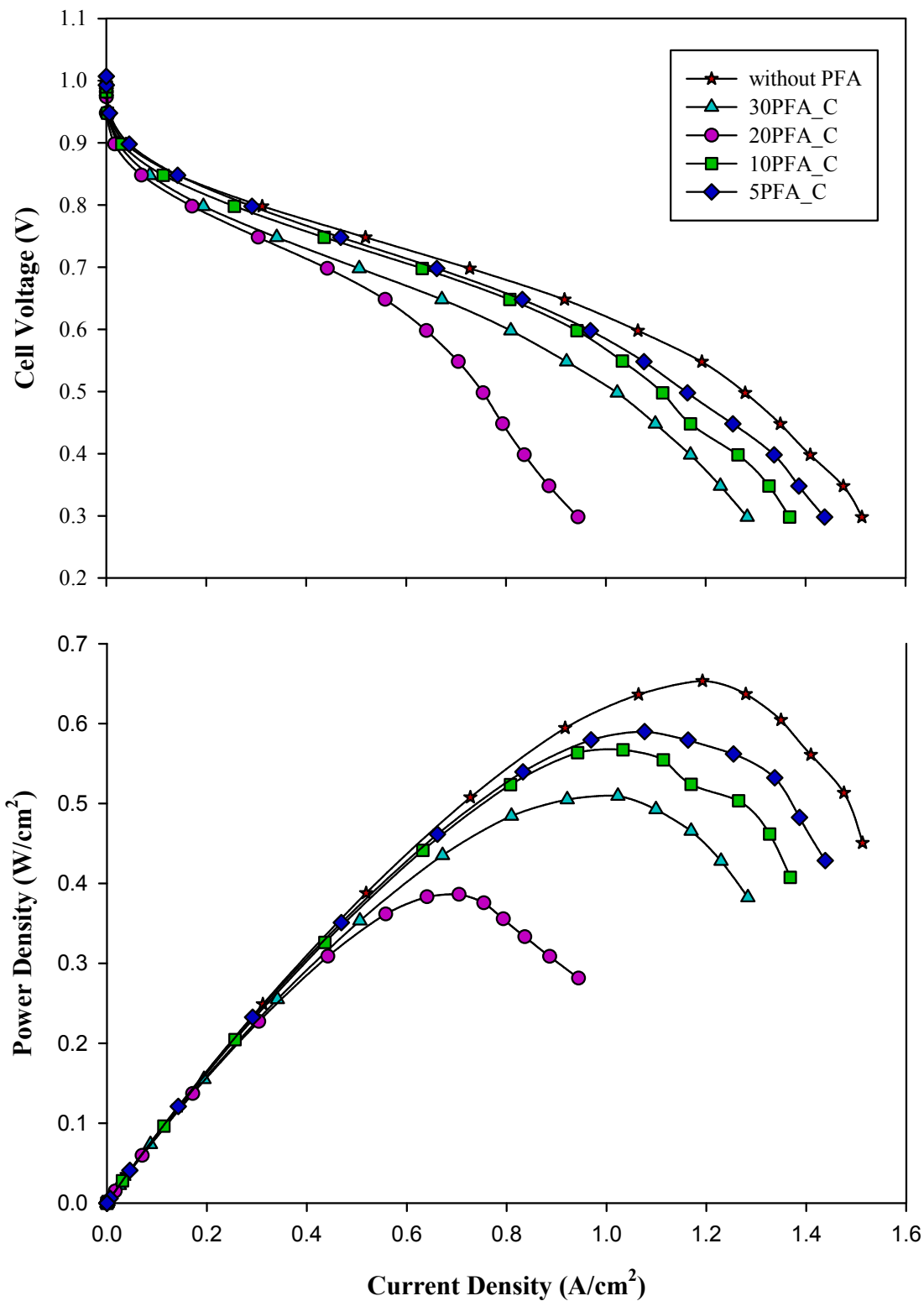


Figure 5.7 Polarization and power density curves of PEMFC for MEA2. Pt loading of anode and cathode electrodes was $1.2 \text{ mgPt}/\text{cm}^2$. Cathode catalyst layer was coated with PFA nanoparticles. PEMFC was operated at H_2 /Air gas-feeding mode

Figure 5.8 illustrates EIS spectra of MEA2 measured at 0.5 V. Impedance spectrum of all CLs demonstrates only one arc at high-frequency data range. Mass transport limitations associated with water accumulation in the pores of the GDL of cathode diminished also in this MEA configuration. This is attributed to the high airflow rate, because when air flow rate was higher than stoichiometric flow rate, it prevents cathode over flooding (Ciureanu & Roberge 2001) via promoting back diffusion of water.

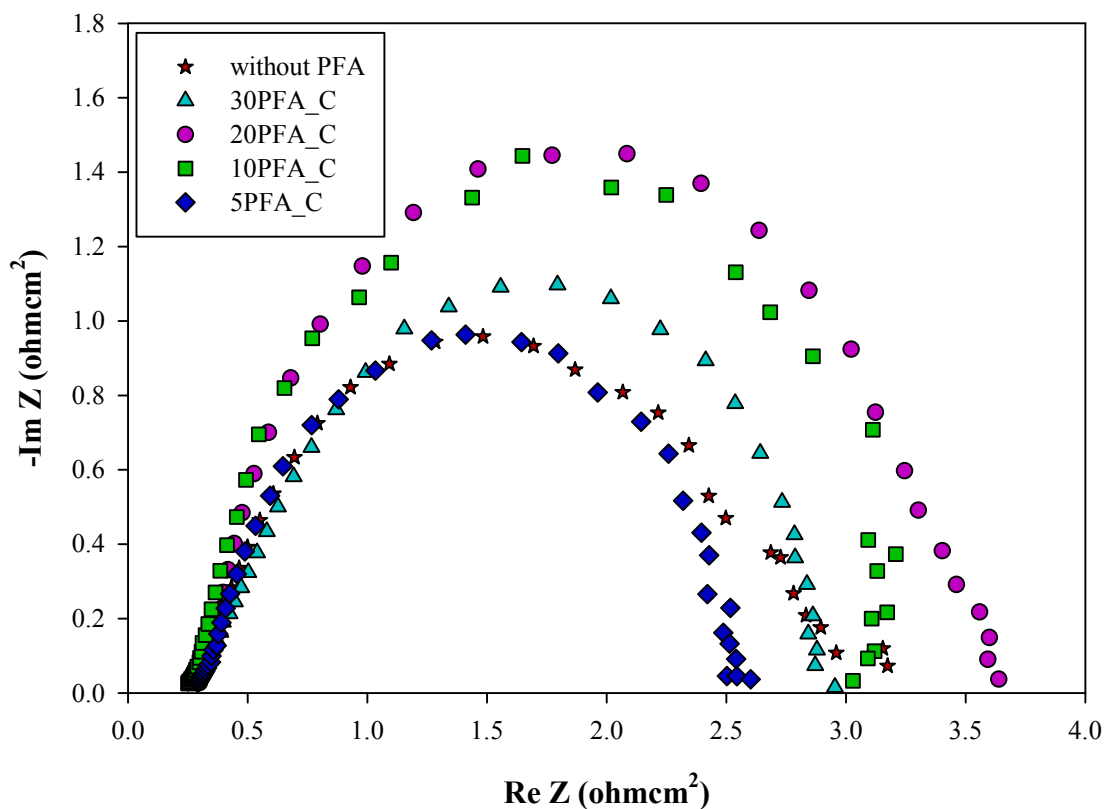


Figure 5.8 Electrochemical impedance spectra obtained running fuel cell at 0.5 V. Pt loading of anode and cathode electrodes was 1.2 mgPt/cm^2 . Cathode catalyst layer was coated with PFA nanoparticles. PEMFC was operated at H_2/Air gas-feeding mode

Parameters of equivalent circuit modeling of EIS spectra of MEA2 are shown in Table 5.5. High-frequency resistances of all CLs were similar, while the high-frequency resistance of 10PFA_C had the lowest. Charge transfer resistances at the

cathode of all CLs increased more than 4 times, which also indicates reduced reaction kinetics compared to H₂/O₂ feeding mode.

High-frequency resistances of all CLs were similar. Moreover, the high-frequency resistance of 10PFA_C (0.23 Ωcm²) was the lowest, while a high frequency of 30PFA_C (0.26 Ωcm²) was the highest. The lowest charge transfer resistance at cathode was obtained for 5PFA_C (2.12 Ωcm²) and 30PFA_C (2.11 Ωcm²). Although CLs without PFA have higher Pt utilization than 5PFA_C and 30PFA_C, charge transfer resistance of CLs without PFA (2.51 Ωcm²) was higher than 5PFA_C (2.12 Ωcm²) and 30PFA_C (2.11 Ωcm²) at the cathode. This indicated that 5PFA_C and 30PFA_C mitigated flooding, which led to higher reaction rate than CLs without PFA. The highest charge transfer resistance at cathode was obtained for 20PFA_C (3.19 Ωcm²). This is pointed out the disrupted ionic network, leading to the lowest reaction rate.

Table 5.5 Parameters of the equivalent circuit modeling of MEA2 at H₂/Air gas-feeding mode

MEA Type	Air		
	R _{HF} (Ωcm ²)	R _{ct} (A) (Ωcm ²)	R _{ct} (C) (Ωcm ²)
without PFA MEA2	0.25	0.11	2.51
30PFA_C	0.26	0.53	2.11
20PFA_C	0.24	0.15	3.19
10PFA_C	0.23	0.23	2.72
5PFA_C	0.25	0.18	2.12

5.4. Conclusions

PFA nanoparticles (5 wt %) included in the CL either anode and cathode or only cCLs provided meso-macro hydrophobic channeling which enhanced water management. This influence had been observed both for H₂/O₂ and at H₂/Air feeding mode. Therefore, the addition of PFA nanoparticles enhanced water management.

Attained performance of CLs hydrophobized with PFA nanoparticles confirms the performances of hydrophobic CLs including PTFE and FEP nanoparticles.

CHAPTER 6

DIAGNOSTIC CHARACTERISATION OF HYDROPHOBIC CATALYST LAYERS INCLUDING PTFE NANOPARTICLES OF HIGH-PERFORMANCE PEM FUEL CELL

In this chapter, Polytetrafluoroethylene (PTFE) nanoparticles added to catalyst may form hydrophobic channels in the CL structure. This modification is expected to enhance liquid water removal from the CL. Excess water production, especially, constrain the reactants mass transfer to the catalyst surface in high-performance PEM fuel cell electrodes. Membrane electrode assemblies were prepared with a commercial catalyst containing 70 wt % Pt on carbon, by ultrasonic spray coating technique. PEM fuel cell performance tests were carried out with membrane electrode assemblies that were prepared with varying catalyst ink compositions. The weight percentage of PTFE was changed from zero to 40% in order to explore the influence of the hydrophobic material in anode and cathode CLs on mass transport of reactants and product. PEM fuel cell performance testing was carried out with two different membrane electrode assembly configuration in order to identify the effect of PTFE in the anode and cathode catalyst layer structures on water transport mechanism and cell performance. In the first configuration (MEA1), PTFE nanoparticles were introduced to both anode and cathode catalyst layers. In the second configuration (MEA2), they were only present in cathode CL. Platinum loading on both anode and cathode CLs was adjusted to 0.4 mg/cm^2 for all cases studied. Performance test results together with electrochemical characterization with impedance spectroscopy of the fuel cell, gave clues to understanding the mass-transport mechanism and the influence of PTFE nanoparticles in the CL on

performance. PEM fuel cell tests were carried out at both H₂/O₂ and H₂/Air gas-feeding modes.

6.1. Introduction

To provide optimum transport path for electronic, ionic, gas and liquid phase in hydrophobic CL with PTFE nanoparticles. The goal of this work is to characterize high-performance electrodes with hydrophobic CLs prepared by ultrasonic coating technique with high Pt-containing commercial catalyst (70 wt % Pt/C). Here, we also investigated the effect of PTFE nanoparticle addition into the CL to enhance water management in high-performance PEM fuel cells. The experimental design has been used to optimize the composition of the CL. Fuel cell performance tests were carried out to determine the highest performance. Reaction kinetics and mass transport limitations were investigated with electrochemical impedance spectroscopy.

6.2. Materials and Methods

6.2.1. Catalyst Ink Preparation

The commercial catalyst was 70 wt % Pt on a carbon support. Catalyst ink of CLs without PTFE was prepared by adding water, Nafion solution (15 wt% 1100 EW, Ion Power, Inc., USA) and isopropyl alcohol (Sigma-Aldrich Co. LLC., USA) to Pt/C catalyst, respectively. Then, catalyst ink was mixed for 24 h in a water bath with a magnetic stirrer at room temperature. Hydrophobic catalyst inks were prepared via two-step preparation method (Friedmann & Nguyen 2008). In the first step, the catalyst was wetted with water, and then half amount of Nafion solution was added. The ink was mixed for 24 h in a water bath with a magnetic stirrer at room temperature. After mixing step, catalyst ink was dried in an oven (Binder GmbH, Germany). With the sample, the oven was heated from room temperature to 135 °C. It was held for 20 min at 135 °C, cooled down to 75 °C and hold for 20 min further at 75 °C. Afterward, it was cooled down to room temperature. In the second step, the dried catalyst ink was wetted with water and remained half of Nafion solution was added. Finally, PTFE dispersion (10 wt%), and isopropyl alcohol (IPA)

were added to the ink, respectively. The prepared ink was mixed for 24 h in a water bath with a magnetic stirrer at room temperature. Nafion fraction parameter (Antolini et al. 1999) (Nafion amount on dry basis) in the catalyst inks was fixed at 0.3. The weight percentage of PTFE in the catalyst ink varied 5 wt %, 10 wt %, 20 wt %, 30 wt % on dry basis. The ratio of total volume of water (ml) to total catalyst weight (g) in the catalyst ink was adjusted to 200. The ratio of total volume of IPA (ml) to the total volume of water (ml) in the catalyst ink was set to 3. For characterization, catalyst ink was dried in an oven under atmospheric pressure at 40 °C for 96 h and then was kept at 110 °C for 3 h.

6.2.2. MEA Configuration

Performance testing was carried out with two different membrane electrode assembly configurations. By this way, the effect of PTFE nanoparticles in anode and cathode catalyst layers on water transport mechanism was investigated, separately. In the first configuration (MEA1), PTFE nanoparticles were coated with both anode and cathode catalyst layers. In the second configuration (MEA2), PTFE nanoparticles were coated only on cCL. The Pt, Nafion, and PTFE nanoparticle loadings on CLs for prepared MEAs are summarized in Table 6.1.

Table 6.1 Pt, Nafion, and PTFE loadings in catalyst layers

Catalyst Ink	Loading (mg/cm ²)		
	Pt	Nafion	PTFE
without PTFE	0.4	0.26	-
40PTFE	0.4	0.31	0.62
30PTFE	0.4	0.46	0.46
20PTFE	0.4	0.37	0.25
10PTFE	0.4	0.31	0.10
10PTFE_2	0.4	0.18	0.09
5PTFE	0.4	0.28	0.05

Numbers before PTFE synonym represent the weight percentage of PTFE in the CL on a dry basis. For example, 5PTFE represents the CL prepared with the ink

containing 5 wt % PTFE on a dry basis. On the other hand, 30PTFE_AC represents the MEA that has 30 wt % PTFE on both anode and cathode catalyst layers. 30PTFE_C represents the MEA that had 30 wt % PTFE on only cCL.

6.2.3. Physical Characterization

Physical and morphological characterization of the catalysts was performed by using TGA-DTA, Nitrogen physisorption, XRD, SEM, TEM, and EDX analyses.

6.2.3.1. Determination of Pt amount

Inductively-Coupled Plasma-Mass Spectrometer (Perkin Elmer DRC II model ICP-MS) was used to determine the Pt amount of catalyst powders. Pt/C catalysts were dissolved in aqua regia prior to analysis.

6.2.3.2. TGA and DTA Measurements

Pt amount in the catalysts and thermal decomposition of the catalysts were determined by Thermogravimetric (TGA) and differential thermal analyses (DTA). A modular simultaneous TGA&DTA thermal analyzer (SETSYS Evolution TGA-DTA/DSC, Seteram Instrumentation, France) was used. Aluminum pans were used in all experiments. For TGA and DTA analyses, samples were heated from room temperature to 1000 °C with a heating ramp of 3 °C/min under airflow.

6.2.3.3. Nitrogen Physisorption Measurements

BET surface area, pore size distribution, and cumulative pore volume were determined with a surface area analyzer (Micromeritics TriStar II 3020 V1.04, Particle & Surface Sciences Pty. Limited, Australia). All samples were degassed at 110 °C for 3 h before analysis. Adsorption/desorption isotherms were measured at 196 °C. Pore size distribution data were calculated from desorption branches of Nitrogen isotherms by the Barrett Joyner Halenda (BJH) method.

6.2.3.4. XRD Measurements

The X-ray diffractograms of the catalysts were determined by an X-Ray Diffractometer (PW1840 of M/s Philips NV, Netherlands and Rigaku Ultima-IV,

Riguka Corp, Japan) equipped with a Cu X-ray tube. XRD measurements were performed in a range of 5° to 90° with a 2θ step of 0.1° .

6.2.3.5. SEM Measurements

SEM images of catalysts were taken by using high-resolution scanning electron microscope system (FEI QUANTA 400F Field Emission, FEI Company, USA) included secondary electrons (SE) in high vacuum modes. Energy-dispersive X-ray spectroscopy (EDX) of the catalyst samples were obtained by the instrument. In order to provide conductivity, ultrathin (5 nm) coating of gold/palladium alloy was deposited on samples by low vacuum sputter coating. Coated samples were fixed on aluminum holder before analysis.

SEM images of membrane electrode assemblies (MEAs) were obtained by using high-resolution scanning electron microscope system (FEI QUANTA 400F Field Emission, FEI Company, USA) included secondary electrons (SE) in high vacuum modes. The images were taken from the cross section of the membrane electrode assemblies. Samples were prepared by submerging half of the MEA into liquid nitrogen then breaking it into two parts. Ultrathin (5 nm) coating of gold/palladium alloy was deposited on samples by low vacuum sputter coating to provide conductivity. Coated samples were fixed on aluminum holder before analysis.

6.2.3.6. TEM Measurements

TEM images of catalyst powders were taken by using a high-resolution transmission electron microscope system (FEI Tecnai G2 F30, FEI Company, USA) for 70 wt % Pt/C operated at 120 kV. Samples used for TEM analysis were prepared by suspending the catalyst powder in ethanol and mixing with an ultrasonic probe. As the homogeneous mixture was obtained, the sample was loaded on the grid and dried completely before analysis.

6.2.4. Electrochemical Characterization

6.2.4.1. Electrochemical impedance spectroscopy analysis

A frequency response analyzer (FCI4/Series G, Gamry Instruments, USA) was connected to an electronic load (RBL 488, TDI-Dynaload, TDI Power, USA). A voltage follower circuit was used to isolate grounds and unwanted current flow between the output signal from the FRA and the analog input to the load. The sweeping frequency was ranged from 4 kHz down to 0.1 Hz with 10 points/decade. The amplitude of the AC current was kept at 5% of the DC current for H₂/O₂ feeding mode and 10% of the DC current for H₂/Air feeding mode. The impedance measurement was obtained at galvanostatic mode. Real and imaginary parts of frequency response were measured at fast mode to minimize fluctuations. After the data of polarization curve were obtained, the cell was held at 0.5 V for 1 h for stabilization, then real and imaginary part of frequency responses of the Nyquist plot was measured at 0.5 V.

6.2.4.2. Cyclic voltammetry analysis

Cyclic voltammetry (CV) measurements were performed in a three-electrode cell containing 0.1 M HClO₄ at 20 °C temperature. Bipotentiostat (Pine AFCBP1, Pine Instrument Company, USA) was used for the experiments. Working electrode was a glassy carbon disk with a 0.5 cm diameter cavity inserted into a Teflon holder. The reference electrode was made up of Ag/AgCl, filled with 0.1 M KCl solution and the counter electrode was a platinum wire. Prior to experiments, the electrolyte was purged with N₂ for 30 min. Working electrode was polished with 5-micron Alumina slurry (Micropolish, Buehler, ITW Company, USA) on a polisher (Microcloth, Buehler, ITW Company, USA) before every experiment. Platinum loading on working electrode was fixed at 28 μg Pt/cm². The concentration of the cyclic voltammetry ink of the catalysts was fixed at 2 mgcat/ml. The ink of the catalysts was prepared by mixing the catalysts with the mixture of 70/30 (v/v) Propanol/water. The aliquots were dried under air atmosphere at 40 °C for 30 min. Cyclic voltammograms were recorded at 50 mV/s scan rate from -0.30 V to 1.0 V. Potentials were referenced to normal hydrogen electrode for Ag/AgCl reference electrode at 25 °C.

6.2.5. Performance Tests

Catalyst inks were coated onto 34 BC gas diffusion layers (SGL Technologies GmbH, Germany) by using Sono-Tek ultrasonic coating instrument (Exactacoat DMC-2100, Sono-Tek Corporation, USA). The operating frequency was 48 kHz. Before coating, catalyst inks were inserted into a syringe pump and then were sprayed on the GDL at a flow rate of 0.3 ml/min. Gas diffusion layers were 315 mm thick and were hydrophobized with 5 wt% PTFE with standard MPL on one side. The Pt loading of anode and cathode electrodes was kept 0.4 mg Pt/cm² for all catalysts. After coating, electrodes were hot pressed onto the Nafion 212 membrane (Ion Power, Inc., USA) at 135 °C for 5min at 20 bars on the active area. The fabricated MEA was placed in a single cell with an active area of 5 cm² (Model: FC05-01 SP REF, Electro-Chem Inc., USA). Silicon gaskets (0.18 mm) were placed on both anode and cathode sides of the membrane between MEA and graphite plates consist of mixed serpentine flow fields. A single cell was tightened with a torque of 1.7 Nm on each bolt from corners. Performance tests were carried out by using a fuel cell test station. External humidification system was included in the test station. Reactant gasses were passing through a water column of a humidifier bottle, whereas temperatures of anode and cathode humidifiers were adjusted to 70 °C. Fuel cell temperature was adjusted to 70.2 °C. Back pressure (3 psi) was applied on both anode and cathode exhaust of the cell. The fuel cell was operated at both H₂/O₂ and H₂/Air gas feeding modes. The volumetric flow rate for hydrogen and oxygen was 0.1 slpm, and for air was 0.6 slpm. For MEA conditioning, the cell was operated at 0.3 V for 1 h, then at 0.5 V for 3.5 h. At the end of every hour, the cell was kept at OCV for 5 min, and then at 0.1 V for 5 min. Data for polarization curve were taken for three times using a visual basic program. Cell voltage varied from 1 to 0.3 V with a step size of 0.05 V for each MEA.

6.3. Results and Discussions

6.3.1. Physical Characterization

6.3.1.1. Nitrogen physisorption analysis

Figure 6.1 illustrates nitrogen adsorption/desorption isotherms for powders of commercial catalyst (Pt/C), commercial catalyst impregnated with Nafion (without PTFE), commercial catalyst impregnated with Nafion and PTFE included catalysts. All isotherms are compatible with isotherm of Type IV according to IUPAC classification which is typical for mesoporous structure (Brunauer et al. 1940; Sing 1985), (Kaneko 1994).

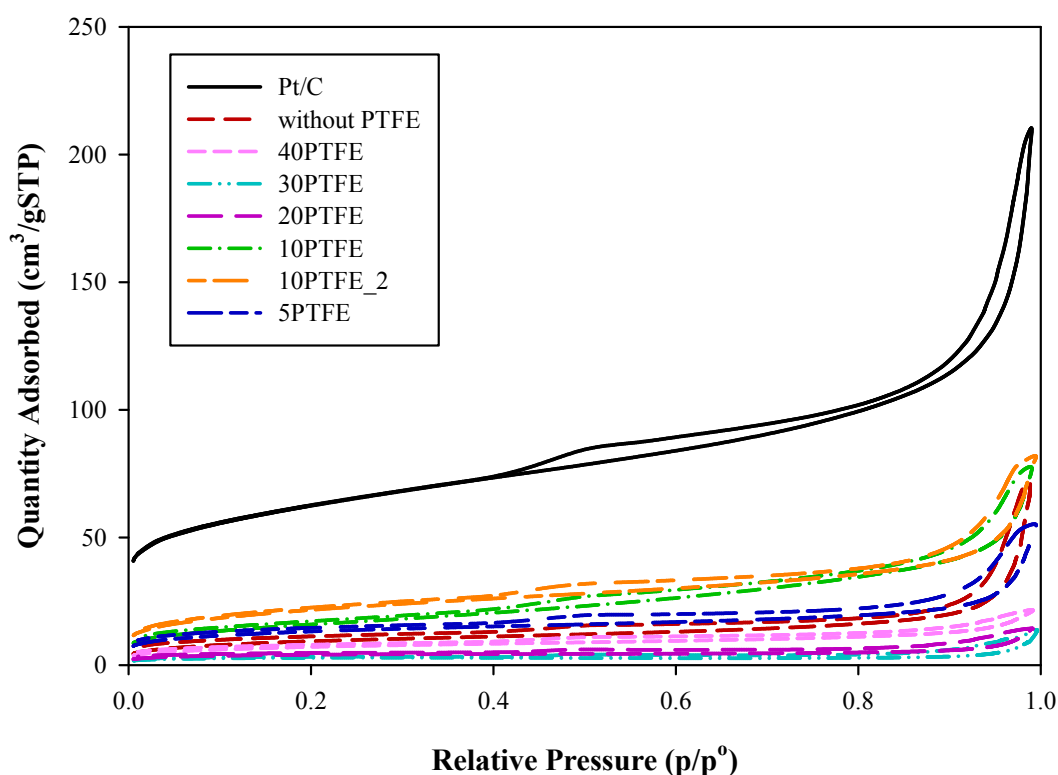


Figure 6.1 Adsorption/desorption isotherms for powders of commercial catalyst (Pt/C), commercial catalyst impregnated with Nafion (without PTFE), commercial catalyst impregnated with different Nafion and PTFE loadings

Furthermore, the hysteresis loops for the commercial catalyst (Pt/C), commercial catalyst impregnated with Nafion ionomer (without PTFE) and 10PTFE, 10PTFE_2, and 5PTFE, demonstrate hysteresis Type H3 according to IUPAC classification, is observed with aggregates of plate-like particles give rise to slit-shaped pores (Sing 1985). Furthermore, 40PTFE 30PTFE and 20PTFE demonstrates more like type H4 loop is often associated with narrow slit-like pores (Sing 1985). This is because most of the pore volume of slit-shaped pores was covered with Nafion and PTFE polymers leading to narrower pore width.

Pore diameters of all catalysts (see Figure 6.2) were spread into micro/meso/macroporous region.

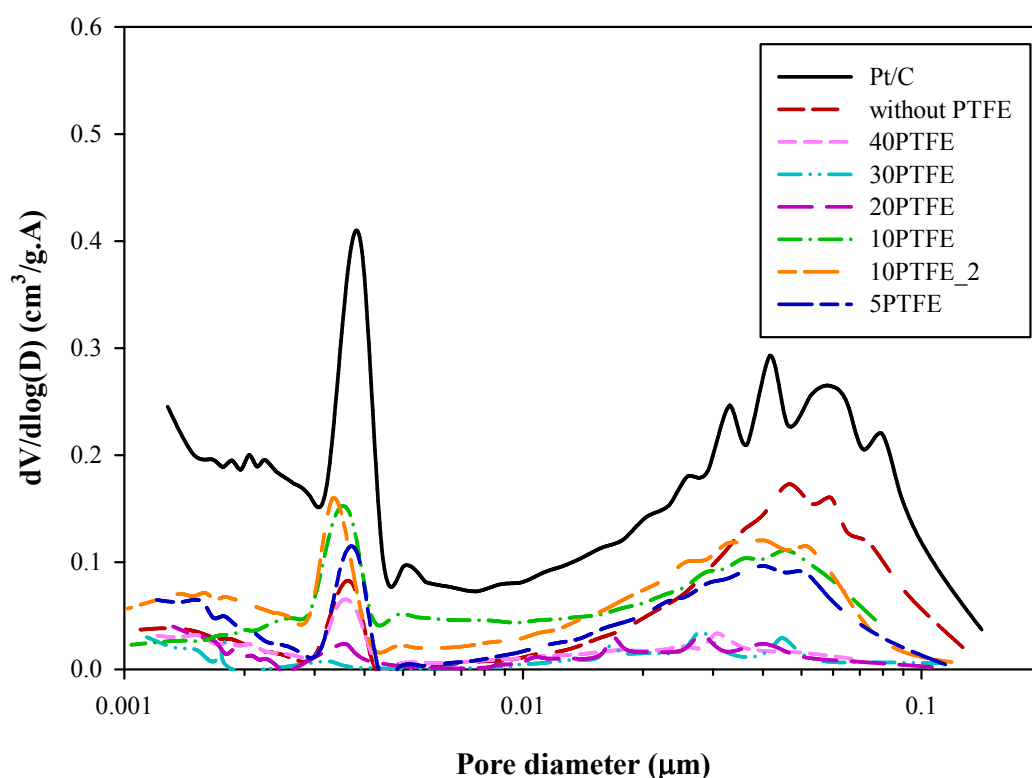


Figure 6.2 Pore size distributions for powders of commercial catalyst (Pt/C), commercial catalyst impregnated with Nafion (without PTFE), and commercial catalyst impregnated with different Nafion and PTFE loadings

The catalyst powder consisted of two distinctive pore distributions, where pores with a diameter distributed from 0.01 μm to 0.1 μm defined as primary pores, while pores with a diameter distributed from 0.1 μm to 1.0 μm defined as secondary pores. The primary pores represented to the pores in the aggregates, where the reaction takes place, while the secondary pores represented to the pores between aggregates assigned to gas diffusion (Watanabe et al. 1985). The highest cumulative pore volume was obtained for Pt/C. When Nafion impregnated to the commercial catalyst, it occupied most of the primary pores led to the decrease in cumulative pore volume. As the weight percentage of total polymer in the catalyst powder increased, cumulative pore volume reduced. The cumulative pore volume of 10PTFE, 10PTFE_2 was higher than the cumulative pore volumes of 5PTFE, and catalyst powder without PTFE below 0.1 μm . Mesoporous of 20PTFE and 30PTFE were completely closed below 0.1 μm . Although, 40PTFE had the same polymer loading (0.93 mg/cm^2) with 30PTFE (0.93 mg/cm^2), the cumulative pore volume of 40PTFE was higher than 30PTFE. Furthermore, 40PTFE had higher polymer loading than 20PTFE (0.62 mg/cm^2), mesopores of 40PTFE below 0.1 μm were slightly open compared to 20PTFE. This is attributed to the $X_{\text{PTFE/Nafion}}$ constant of the catalyst powders. The $X_{\text{PTFE/Nafion}}$ of 40PTFE was highest with a value of 2.0, while $X_{\text{PTFE/Nafion}}$ of 30PTFE and 20PTFE was 1.0 and 0.7, respectively. Nafion mainly occupied most of the primary pores, while PTFE settled in the secondary pores (Watanabe et al. 1985; Uchida 1996; Uchida 1995). This is interpreted as since the total polymer amount was similar when PTFE amount was higher than Nafion, cumulative pore volume was increased. This means that higher volume of the primary pores was free to access. Although 10PTFE_2 consisted of similar polymer loading (0.26 mg/cm^2) of the catalyst powder as in without PTFE (0.26 mg/cm^2), it had higher pore volume below 0.1 μm than catalyst powder without PTFE. This revealed that catalyst preparation with two-steps reduces pore blockage and provide more homogenous distribution. The pores of 20PTFE, 30PTFE, and 40PTFE between 0.1 μm and 1.0 μm were almost completely blocked, while the pores of 10PTFE_2, 10PTFE, 5PTFE, and catalyst powder without PTFE in the same range were open. This revealed that polymer amount included in 20PTFE, 30PTFE, and 40PTFE were pretty much, causing blockage of most of the secondary pores for gas diffusion.

6.3.1.2. XRD analysis

XRD patterns for powders of commercial catalyst (Pt/C), commercial catalyst impregnated with Nafion (without PTFE), and commercial catalyst impregnated with different Nafion and PTFE loadings are shown in Figure 6.3. All of the patterns clearly show the presence of the elemental platinum with the five characteristic peaks of face centered cubic crystalline platinum. The Bragg angles of ca. 40° , 46° , 67° , 81° , 86° correspond to (111), (200), (220), (311) (He 1997; Pozio et al. 2002), and (222) (Zhang et al. 2010) Pt facets, respectively. The intensity of diffraction peak of Pt (222) was weak only in the pattern of all catalysts. The peak appeared at the diffraction pattern for powder of commercial catalyst impregnated with Nafion (without PTFE) at ca. 17° Bragg angle was attributed to poly-fluorocarbon chains of Nafion ionomer (Jung et al. 2003). The broadness of the Nafion peak pointed out the amorphous structure of the polymer. The sharp peak occurred at ca. 18.4° Bragg angle corresponded to a crystalline component of PTFE (Lebedev et al. 2010). Nafion and PTFE peaks were overlapped at the diffraction pattern for powder of PTFE including catalysts, since corresponding Bragg angles of Nafion and PTFE were very close to each other. Determination of average diameter of Pt crystallite and total Pt surface area was described in Chapter 1.

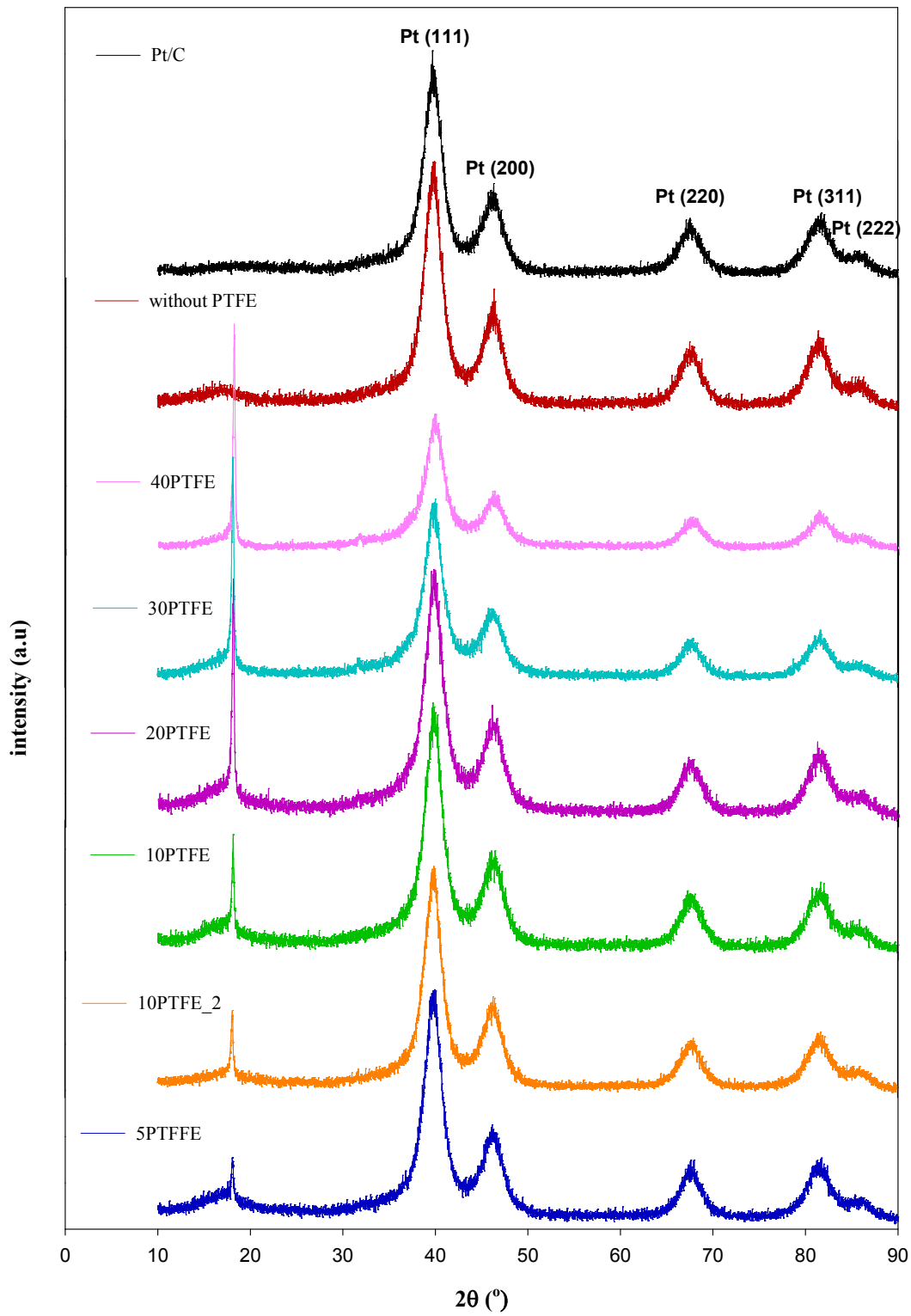


Figure 6.3 XRD patterns of powders of commercial catalyst (Pt/C), commercial catalyst impregnated with Nafion (without PTFE), and commercial catalyst impregnated with different Nafion and PTFE loadings

6.3.2. Cyclic Voltammetry Analysis

Figure 6.4 illustrates cyclic voltammograms of commercial catalyst (Pt/C), commercial catalyst impregnated with Nafion (without PTFE); commercial catalyst impregnated with six different Nafion and PTFE loadings.

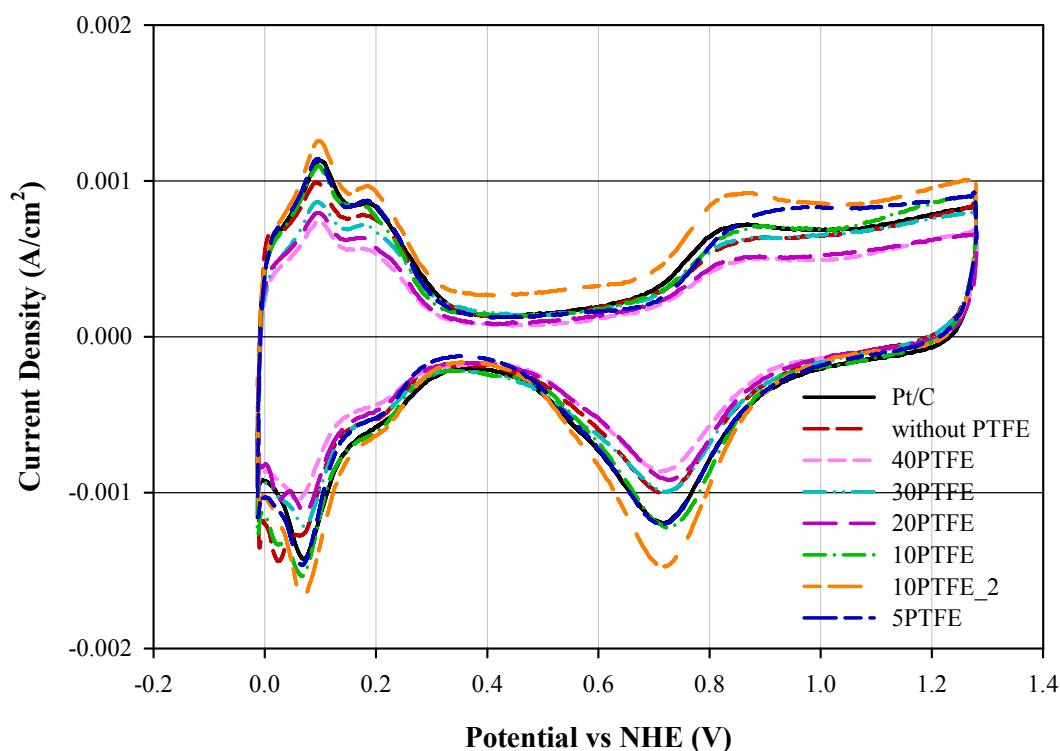


Figure 6.4 Cyclic voltammograms of commercial catalyst (Pt/C), commercial catalyst impregnated with Nafion (without PTFE), and commercial catalyst impregnated with different Nafion and PTFE loadings

Hydrogen adsorption/desorption peaks were observed from 0.0 to 0.4 V; while Pt oxidation was observed between 0.7 and 1.2 V at the cathodic direction and Pt reduction was observed at 0.9 and 0.4 V at anodic direction.

Electrochemical surface area and Pt utilization were calculated as described in Chapter 2.

Commercial catalyst (Pt/C) had the highest electrochemical surface area (65 m²/g). This was attributed to the highest Pt content (62 wt. %) in the commercial catalyst (Pt/C). The catalyst powder of the 10PTFE had the same electrochemical surface area (65 m²/g) with the commercial catalyst. Nafion addition to the

commercial catalyst (Pt/C) decreased the electrochemical surface area to 62 m²/g. Although the catalyst powder of 10PTFE contained the lower weight percentage of Pt (35 wt %) than catalyst powder without PTFE (43 wt %), it had slightly higher electrochemical surface area according to catalyst powder without PTFE. This is attributed to the difference in the catalyst preparation methods. The catalyst powder of 10PTFE was prepared in two steps, while the catalyst powder without PTFE was prepared in only one-step. By two-step ink preparation, more homogenous distribution of Pt was provided. The homogeneity of the Pt nanoparticles in the catalyst powder can be deduced from the differences in the Pt utilizations. The catalyst powder of 10PTFE had highest Pt utilization (84 %) among all catalyst powders; while the Pt utilization of commercial catalyst was 83 % and it was 78 % for the catalyst powder without PTFE. This means that 16 % of Pt nanoparticles in the powder of 10PTFE and 17 % and 22 % of Pt particles of the catalyst powders of commercial catalyst powder and commercial catalyst impregnated with Nafion (without PTFE) could not contribute to the reaction, respectively. This also revealed that electronic conduction of the Pt nanoparticles was highest with 84 % of all Pt nanoparticles and the accessibility for protons to 84 % of all Pt surface were highest (Zhang & Song 2008; Li & Pickup 2003).

Table 6.2 summarizes the physical characterization values; the weight ratio of Platinum to total polymer, the weight ratio of Platinum to Nafion, the weight ratio of PTFE to Nafion, the weight percentage of Pt, average Pt diameter, total Pt surface, multipoint BET surface area, cumulative pore volume, the average pore diameter of catalyst powders. The maximum Pt content was obtained for the commercial catalyst (62 wt %), with the inclusion of Nafion, the weight percentage of Pt decreased to 43 wt %. As the ratio of Pt to total polymer amount in the catalyst ($X_{Pt/TP}$) increased, the thickness of the CLs increased. The thinnest CLs were attained with the catalyst powder without PTFE and the catalyst powder of 10PTFE_2 because $X_{Pt/TP}$ of these CLs was highest (1.5). The CLs prepared with the catalyst powder of 5PTFE was 21 % thicker than the CLs prepared with the catalyst powder without PTFE and the catalyst powder of 10PTFE_2. The CLs prepared with the catalyst powder of 10PTFE was 36 % thicker than the CLs prepared with the catalyst powders without PTFE and catalyst powder of 10PTFE_2. Furthermore, the CLs prepared with the catalyst powder of 20PTFE was 56 % thicker than the CLs prepared with the catalyst

powder of 10PTFE_2. Finally, the thickest CLs prepared with the catalyst powders of 30PTFE and 40PTFE was more than two fold (72 %) thicker than the CLs prepared with 10PTFE_2.

Average Pt diameter of powders of commercial catalyst (Pt/C), commercial catalyst impregnated with Nafion (without PTFE) were 3.5 nm, and 3.7 nm and total Pt surface area were 79 m²/g, 75 m²/g, respectively (Table 6.2). Total Pt surface area and average Pt diameter for the commercial catalyst (Pt/C), obtained from XRD data, provided from the Product Company was 3.1 nm, which slightly lower than the value attained in the present study. Nafion impregnation in one-step caused agglomeration of Pt particles. Since Nafion was included into the commercial catalyst powder average Pt diameter increased. However, PTFE addition to Nafion impregnated catalyst did not influence the average Pt diameter; in addition, did not cause further agglomeration. Moreover, PTFE addition in two steps led to the decrease in average Pt diameter of 20PTFE (3.5 nm), 30PTFE (3.4 nm), and 40PTFE (3.3 nm). This revealed that since Pt amount in the catalyst powder was lower, Pt agglomeration reduced. The powders of 20PTFE (49 m²/g), 30PTFE (50 m²/g), and 40PTFE (47 m²/g) had higher electrochemical surface area than 5PTFE (43 m²/g) and 10PTFE_2 (42 m²/g). This is attributed to the smaller size of Pt particles in the catalyst powders of the 20PTFE, 30PTFE, and 40PTFE. Smaller Pt particles provided enhanced electrochemical surface area. The highest BET surface area was obtained for Pt/C was 210 m²/g. BET specification given by Product Company is 239.4 m²/g-cat, which is slightly higher than our value. Since the average Pt diameter of the commercial catalyst used in the present study was higher (3.5 nm), the multipoint BET surface area was lower than the values of the multipoint BET surface area declared by the Product Company. BET surface area reduced (84 %) when Nafion was included to the catalyst. On the other hand, average pore diameter increased from 5.2 nm to 8.5 nm. This indicated that Nafion ionomer occupied narrower pores, which also led to a reduction in BET surface area and contributions to cumulative pore volume were mostly by larger pores. Although, catalyst powder without PTFE and 10PTFE_2 had the same X_{Pt/TP} (1.5), BET surface area of 10PTFE_2 (75 m²/g) was more than 2.5 times higher than the BET surface area of catalyst powder without PTFE (33 m²/g).

Table 6.2 Physical characterization values of powders of commercial catalyst (Pt/C), commercial catalyst impregnated with Nafion (without PTFE), commercial catalyst impregnated with different Nafion and PTFE loadings

	Pt/C	Without PTFE	5PTFE	10PTFE	10PTFE_2	20PTFE	30PTFE	40PTFE
$X_{\text{PTFE/TP}}$	NaN	0.0	0.14	0.25	0.33	0.40	0.50	0.67
$X_{\text{C/(Nafion+C)}}$	1.0	0.44	0.42	0.40	0.54	0.35	0.31	0.40
$X_{\text{Pt/TP}}$	NaN	1.5	1.2	1.0	1.5	0.7	0.4	0.4
Pt wt % ^a	67	46	43	39	46	33	26	26
Pt wt % ^b	34	18	19	27	42	28	22	19
Pt wt % ^c	62	43	37	35	40	30	23	23
ESA ^d (m ² /g)	65	62	67	65	69	49	50	47
U _{Pt} ^d (%)	83	78	86	84	91	61	61	57
d _{Ptavg} ^e (nm)	3.5	3.7	3.6	3.6	3.7	3.5	3.4	3.3
SA _{Pt} ^e (m ² /g)	79	75	78	77	76	81	83	84
SA _{BET} ^f (m ² /g)	210	33	44	57	75	13	9	25
V _{poreCum} ^f (cm ³ /g)	0.35	0.11	0.09	0.12	0.13	0.024	0.023	0.035
V _{pporeCum} ^f (cm ³ /g)	0.16	0.02	0.03	0.05	0.05	0.010	0.006	0.019
V _{sporeCum} ^f (cm ³ /g)	0.19	0.09	0.06	0.07	0.08	0.014	0.017	0.016
dpore _{avg} ^f (nm)	5.2	8.5	5.3	6.2	4.7	4.3	5.0	3.6

^a Theoretical value

^b Determined by TGA analysis

^c Determined by ICP_MS analysis

^d Determined by CV analysis

^e Calculated from XRD data

^f Calculated from nitrogen physisorption data

This is attributed to $X_{C/(Nafion+C)}$ of 10PTFE_2 because it was 23% higher than $X_{C/Nafion}$ of catalyst powder without PTFE. This revealed that carbon amount is as critical as Pt amount in the catalyst powder. On the other hand, the average pore diameter of the catalyst powder without PTFE (8.5 nm) was almost two times higher than the average pore diameter of 10PTFE_2 (4.7 nm). This revealed that primary pores of the catalyst powder without PTFE ($0.02 \text{ cm}^3/\text{g}$) were almost closed according to secondary pores ($0.09 \text{ cm}^3/\text{g}$). This led to an increase in the contribution of larger pores (% 82) to the cumulative pore volume of catalyst powder without PTFE, while the contribution of the smaller pores decreased (% 18). In the case of the catalyst powder of 10PTFE_2, the percentage of the primary pores contributed to the cumulative pore volume (% 39) was higher than the primary pores contributed to the cumulative pore volume of the catalyst powder without PTFE (% 18). This is attributed to the PTFE amount in the catalyst powder of 10PTFE_2 ($X_{PTFE/TP} = 0.3$). Although they have the same polymer amount in the catalyst powder, the catalyst powder of 10PTFE_2 included PTFE in addition to Nafion. This led to an increase in the volume of primary pores. When PTFE was included in the catalyst powder, the weight percentage of Nafion decreased, by this way, a higher volume of the smaller pores was attained to be open. When the $X_{C/(Nafion+C)}$ in the catalyst powder was below 0.4, there was an order of magnitude decrease in the multipoint BET surface area. That is why; 30PTFE had revealed the lowest multipoint BET surface area ($9 \text{ m}^2/\text{g}$) with the lowest $X_{C/(Nafion+C)}$ (0.31). Consequently, the cumulative pore volume of 20PTFE ($13 \text{ m}^2/\text{g}$), 30PTFE ($9 \text{ m}^2/\text{g}$), 40PTFE ($25 \text{ m}^2/\text{g}$) was lower than 5PTFE ($44 \text{ m}^2/\text{g}$), 10PTFE ($57 \text{ m}^2/\text{g}$), and 10PTFE_2 ($75 \text{ m}^2/\text{g}$), because, most of the pores of 20PTFE, 30PTFE, 40PTFE were occupied with polymer.

6.3.3. TEM Analysis

TEM images of powders of commercial catalyst (Pt/C), commercial catalyst impregnated with Nafion (without PTFE), and commercial catalyst impregnated with different Nafion and PTFE loadings are shown in Figure 6.5.

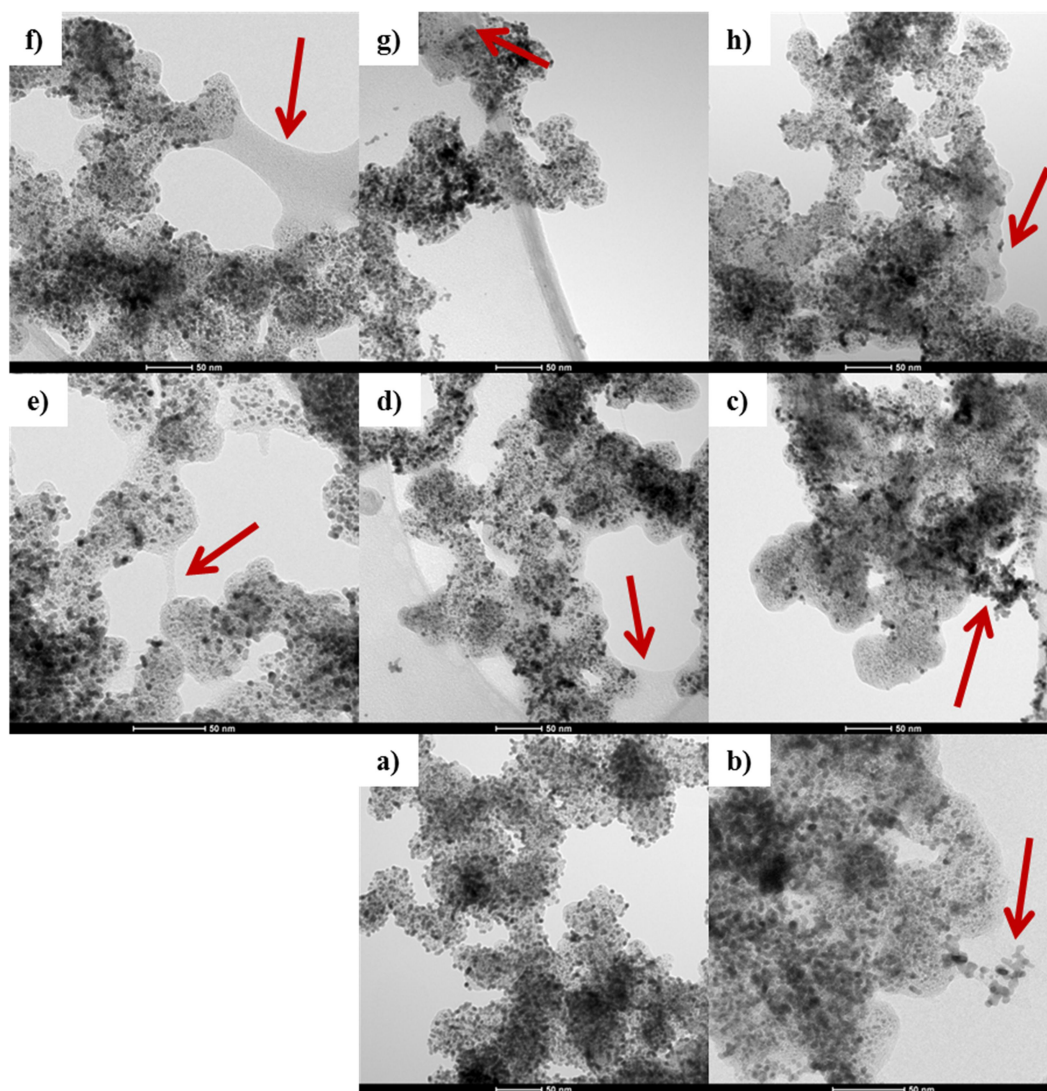


Figure 6.5 TEM images of powders of a)Pt/C, b) without PTFE, c) 5PTFE, d) 10PTFE, e) 10PTFE_2, f) 20PTFE, g) 30PTFE, h) 40PTFE

The image of the commercial catalyst is shown in Figure 6.5a. Black dots correspond to the dispersed Pt particles on gray carbon spheres. The red arrow on the image of catalyst powder without PTFE (Figure 6.5b) indicates the agglomerated Pt particles on Nafion ionomer. We can clearly observe that when Nafion impregnated

to the commercial catalyst, Pt agglomeration occurred. Pt agglomeration on Nafion can clearly be observed on the image of 5PTFE (Figure 6.5c). The red arrow on the images of 10PTFE (Figure 6.5d), 10PTFE_2 (Figure 6.5e), 20PTFE (Figure 6.5f), and 40PTFE (Figure 6.5h) show the empty surfaces where Pt particles cannot place on. These empty places may consist of PTFE nanoparticles.

6.3.4. SEM Analysis of Catalyst Powder

SEM images of powders of commercial catalyst (Pt/C), commercial catalyst impregnated with Nafion (without PTFE), and commercial catalyst impregnated with different Nafion and PTFE loadings are shown in Figure 6.6. The Pt particles in the commercial catalyst (Pt/C) were the smallest considering commercial catalyst impregnated with different Nafion (without PTFE) and PTFE loadings (Figure 6.6). Catalyst agglomeration occurred with Nafion addition to Pt/C catalyst was clearly observed when Figure 6.6a and Figure 6.6b is compared. Decline in the void spaces of the commercial catalyst when impregnated with Nafion was also examined from Figure 6.6b. The red arrow on the images of 10PTFE (Figure 6.6d), 10PTFE_2 (Figure 6.6e), 20PTFE (Figure 6.6f), 30PTFE (Figure 6.6g), and 40PTFE (Figure 6.6h) points out the PTFE fibers in the catalyst powder. EDX results represented the relative amount of the chemical compounds in the catalysts. For commercial catalyst (Pt/C), Pt, carbon, and oxygen peaks appeared in the EDX results (Figure 6.6a); while fluoride and sulfur peaks appeared in addition to Pt, carbon, and oxygen peaks for catalyst powders including the different amount of Nafion and PTFE. Since PTFE amount in the catalyst powders increased, the intensity of Fluorine peak increased (20PTFE, 30PTFE, and 40PTFE).

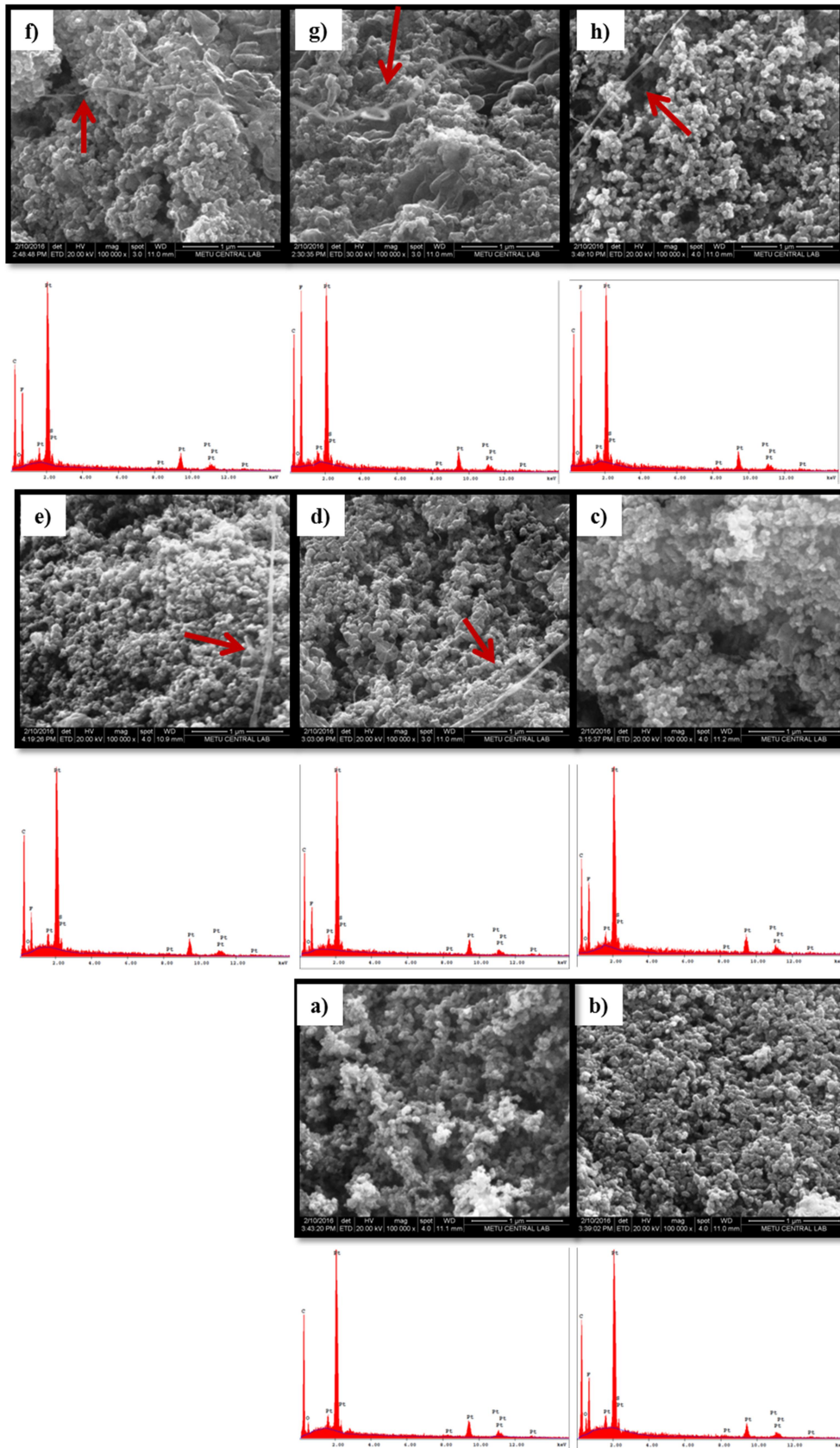


Figure 6.6 SEM images of powders of a)Pt/C, b) without PTFE, c) 5PTFE, d) 10PTFE, e) 10PTFE_2, f) 20PTFE, g) 30PTFE, h) 40PTFE

6.3.5. Effect of PTFE Loading on Performance and Running Electrochemical Impedance Spectrum of PEMFC at H₂/O₂ Gas-feeding Mode

PTFE Loaded Catalyst Layers on Both Electrodes (MEA1):

Polarization and power density curves for CLs with six different PTFE loadings, working at H₂/O₂ gas-feeding mode are shown in Figure 6.7. The performances of PTFE loaded CLs were compared with CLs without PTFE. The maximum power density at 0.45 V was 1.27 W/cm² for CLs without PTFE. Erkan et al. (Erkan & Eroglu 2015) obtained 0.88 W/cm² the maximum power density keeping Pt loading 0.4 mg/cm² on the CLs, which was prepared with 70 wt % Pt/C by an ultrasonic coating technique. In the present study, CLs were prepared with the same commercial catalyst keeping Pt loading 0.4 mg/cm² on the CLs and coating technique. However, performance attained in the present study was higher than (1.27 W/cm²) their study. The difference between performances of CLs without PTFE is attributed to the differences in ink preparation and MEA conditioning techniques. 10PTFE_2_AC (1.15 W/cm²) and 10PTFE_AC (1.13 W/cm²) had the closer performance to CLs without PTFE at 0.45 V. This is attributed to having similar X_{Pt/TP}, which is 1.5 for 10PTFE_2_AC and is 1.0 for 10PTFE_AC. The highest ratio of Pt to total polymer loading (X_{Pt/TP}) was 1.5 attained for the CLs without PTFE and for 10PTFE_2_AC, which provided the thinnest CLs decreasing mass transport limitations. However, when we look at Figure 6.7, we can see that 10PTFE_2_AC and 10PTFE_AC had the lowest slopes in the ohmic region compared to other PTFE included CLs. This pointed out the lower ohmic resistance. This is because PTFE nanoparticles in the CLs of 10PTFE_AC and 10PTFE_2_AC provided enhanced water management, which decrease the ohmic resistance of 10PTFE_2_AC and 10PTFE_AC. However, 10PTFE_AC had higher mass transfer limitation than 10PTFE_2_AC, which caused a sudden decrease in the current density in the mass transfer region. This is attributed to the X_{PTFE/TP} ratio, which is 0.25 for 10PTFE_AC and 0.33 for 10PTFE_2_AC. The higher amount PTFE in the thinner CLs of 10PTFE_2_AC (X_{Pt/TP}=1.5) provided improved water management, which mitigates flooding, and therefore, mass transport limitations diminished.

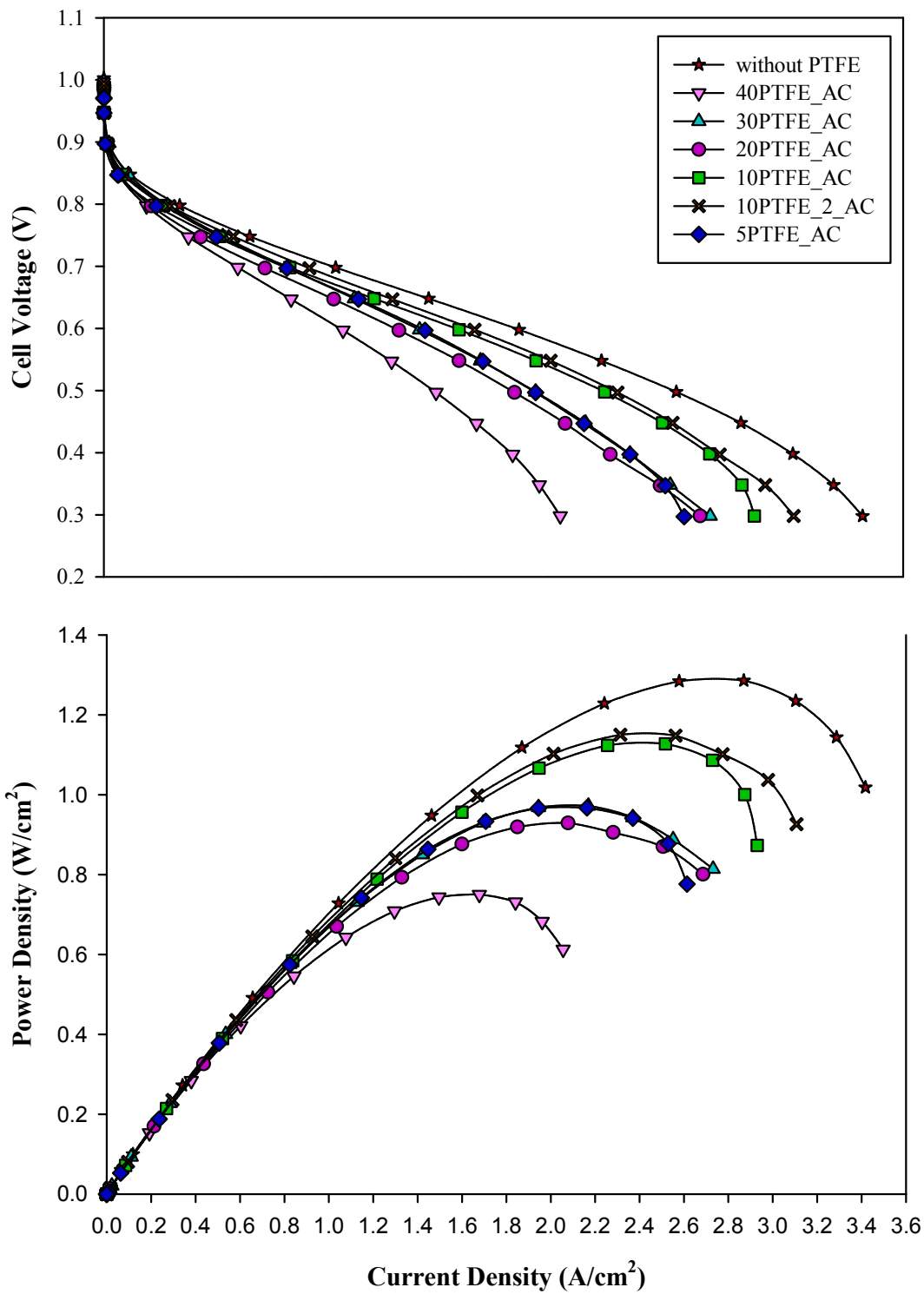


Figure 6.7 Polarization and power density curves of PEMFC for MEA1. Pt loading of anode and cathode electrodes was $0.4 \text{ mgPt}/\text{cm}^2$. PTFE nanoparticles were coated with both anode and cathode catalyst layers. H_2/O_2 gas-feeding mode was used

Song et al. (Song et al. 2010), studied with hydrophobic CLs with different PTFE loadings while keeping Pt loading at 0.4 mg/cm^2 . They obtained ca. 0.47 W/cm^2 power density for 5 wt % PTFE in CLs at 0.45 V. In the present study, for the same PTFE (5 wt %) loading with the same Pt loading, performance (0.97 W/cm^2) was almost twofold. This is attributed to 2-step ink preparation method, which reduces PTFE nanoparticles settled on electronic and ionic network leading to a reduction in triple phase boundaries. Electrode preparation technique with ultrasonic coating technique had also a significant impact on cell performance. Ultrasonic coating technique used in this study also led to enhanced performance. The power density of 20PTFE_AC was 0.93 W/cm^2 , and the power density of 30PTFE_AC was 0.97 W/cm^2 at 0.45 V, while the power density of 5PTFE_AC was 0.97 W/cm^2 . Although 30PTFE_AC had thicker CL with the $X_{\text{Pt/TP}}$ of 0.4 according to 20PTFE_AC and 5PTFE_AC, similar performance was attained with 20PTFE_AC and 5PTFE_AC. This is attributed the $X_{\text{PTFE/TP}}$ ratio, which was 0.4 for 20PTFE_AC and was 0.5 for 30PTFE_AC, while it was 0.1 for 5PTFE_AC. The higher amount of PTFE in the thicker CLs of 30PTFE_AC promoted better water management, which enhanced the cell performance. On the other hand, PTFE nanoparticles in the CLs of 5PTFE_AC could not be sufficient to mitigate flooding. Consequently, excess water in the pores of the CLs of 5PTFE_AC caused higher ohmic resistance causing decreased cell performance despite having higher $X_{\text{Pt/TP}}$. Improved water management also promoted decreased ohmic resistance for 20PTFE_AC and 30PTFE_AC compared to 5PTFE_AC. The power density of 40PTFE_AC (0.75 W/cm^2) was lower than 30PTFE_AC (0.97 W/cm^2) although their $X_{\text{Pt/TP}}$ was same (0.4). This identifies the similarity of the thickness of the CLs of 30PTFE_AC and 40PTFE_AC. The reduction in the cell performance of 40PTFE_AC is attributed to higher PTFE amount in the CLs. Although 30PTFE_AC and 40PTFE_AC consisted of the same CL thickness, $X_{\text{PTFE/TP}}$ of 40PTFE_AC (0.7) was higher than 30PTFE_AC (0.5). The higher amount of PTFE did not influence the cumulative pore volume because $X_{\text{C/(Nafion+C)}}$ of 40PTFE (0.4) was higher than the $X_{\text{C/(Nafion+C)}}$ of 30PTFE (0.31). The cumulative pore volume of 30PTFE_AC was $0.024 \text{ cm}^3/\text{g}$, while it was $0.035 \text{ cm}^3/\text{g}$ for 40PTFE_AC because 40PTFE_AC consisted of the lower amount of Nafion. This means that since the total polymer amount ($X_{\text{Pt/TP}}=0.4$) was same, PTFE amount of 40PTFE ($X_{\text{PTFE/TP}}=0.7$) was higher than 30PTFE

($X_{\text{PTFE/TP}}=0.5$). Therefore, the fraction of the primary pores (0.54) contributed to the cumulative pore volume of 40PTFE_AC was higher than the fraction of the secondary pores (0.46). However, when the highest thickness of the CLs coupled with the low amount of Pt utilization (%57) caused a reduction in the rate of chemical reaction.

Figure 6.8 illustrates EIS spectra of MEA1 measured at 0.5 V. Thin film diffusion has a preponderant effect on mass transport at this voltage (Ciureanu & Roberge 2001).

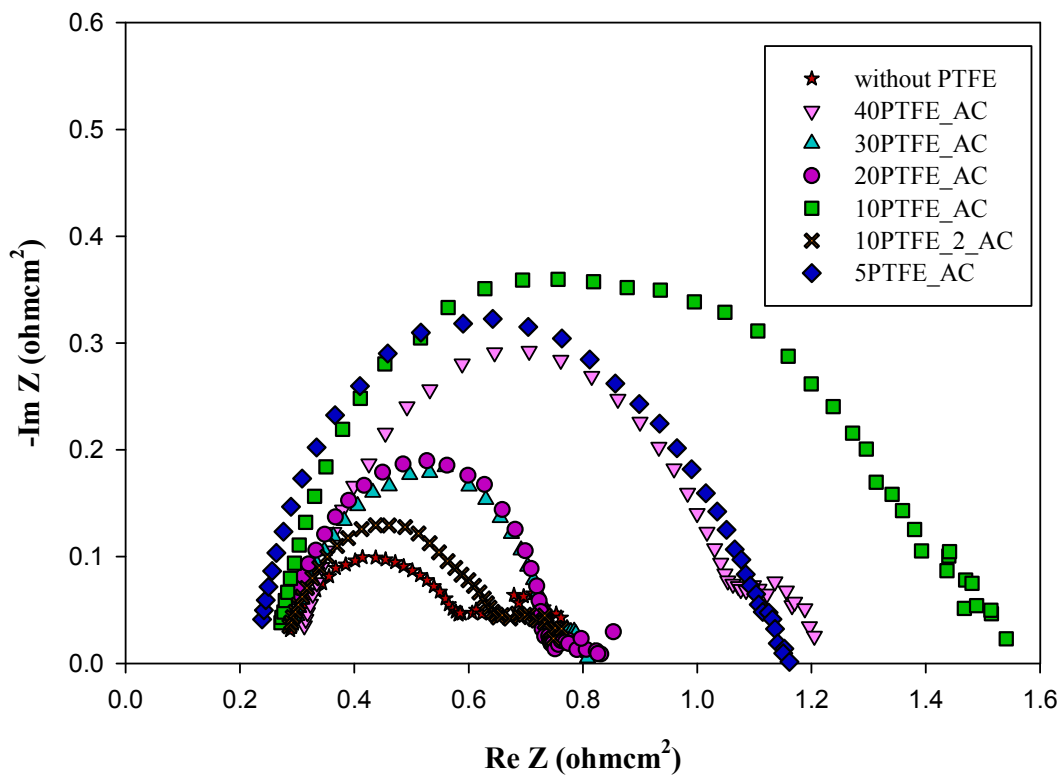


Figure 6.8 Electrochemical impedance spectra obtained for a running fuel cell at 0.5 V. Pt loading of anode and cathode electrodes was 0.4 mgPt/cm^2 . Both anode and cathode catalyst layers were coated with PTFE nanoparticles. H_2/O_2 gas-feeding mode was used

Except for 5PTFE_AC and 10PTFE_AC, all CLs demonstrated an impedance spectrum with a high-frequency arc followed by a low-frequency arc. The intercept of the high-frequency impedance arc on the real axis represents the total ohmic

resistance of the cell. The main contributor to the R_{HF} is the ohmic resistance of the membrane. The first arc represents the total charge transfer resistance at both anode (R_{ct} (A)) and cathode (R_{ct} (C)), however, charge transfer resistance at cCL is the dominated component. Moreover, mass transfer resistance represented with low-frequency arc, is related with oxygen/air diffusion in the cGDL (Park et al. 2006). Parameters of equivalent circuit modeling of EIS spectra for MEA1 are listed in Table 6.3. All of the MEAs demonstrated similar high-frequency resistances; however, 5PTFE_AC had the lowest, which indicates the lowest ohmic resistance of the membrane. 10PTFE_2_AC demonstrated the lowest charge transfer resistance after CLs without PTFE, which pointed out the highest reaction rate. The lower charge transfer resistances of CLs without PTFE ($0.33 \Omega \cdot \text{cm}^2$) and 10PTFE_2_AC ($0.38 \Omega \cdot \text{cm}^2$) is attributed to the thickness of the CLs of 10PTFE_2_AC ($X_{Pt/TP}=1.5$) and the CLs without PTFE ($X_{Pt/TP}=1.5$). The thicknesses of the CLs of these two MEAs were the lowest among all MEAs. This led to reduced mass transport limitation for both gas and liquid phase, which promote enhanced performance with higher reaction rate. On the other hand, 10PTFE_2_AC included higher $X_{C(\text{Nafion}+C)}$ with the value of 0.54, which pointed out the lower Nafion loading ($0.20 \text{ mg}/\text{cm}^2$) causing reduced ionic conduction. Lower ionic conduction is one of the reasons of reduced Pt utilization. In addition, hydrophobic nanoparticles in the CLs of 10PTFE_2_AC caused a decrease in Pt utilization (55 %) according to the CLs without PTFE (78 %). Therefore, charge transfer resistance of 10PTFE_2_AC was slightly higher than the charge transfer resistance of the CLs without PTFE. However, mass transport resistance of 10PTFE_2_AC ($0.12 \Omega \cdot \text{cm}^2$) was lower than the mass transfer resistance of the CLs without PTFE ($0.17 \Omega \cdot \text{cm}^2$). This revealed that PTFE nanoparticles in the CLs of 10PTFE_2_AC facilitated excess water removal. The thickness of the CLs increased for 5PTFE_AC (21 %) and 10PTFE_AC (56 %), however, the percentage of PTFE nanoparticles in the CLs of 5PTFE_AC ($X_{PTFE/TP}=0.14$) and 10PTFE_AC ($X_{PTFE/TP}=0.25$) decreased. Therefore, the charge transfer resistances of 5PTFE_AC ($0.93 \Omega \cdot \text{cm}^2$) and 10PTFE_AC ($1.30 \Omega \cdot \text{cm}^2$) were the highest among all CLs. The produced water at the triple phase boundaries occupied the secondary pores, where oxygen diffuses. This caused flooding at the catalyst/electrolyte interface, which hinders oxygen diffusion and slowed down the reaction because of reduced rate of reactant diffusion. Although

5PTFE_AC and 10PTFE_AC demonstrated highest charge transfer resistances, the mass transfer limitations at cGDL were diminished. This is interpreted as water accumulation in the pores of cGDL was eliminated. Therefore, oxygen can freely diffuse through the pores of cGDL, however, when reactant gas reached to cCL, it encountered the blocked pores with liquid water. The thickness of the CLs of 30PTFE_AC ($X_{Pt/TP}=0.4$) was 33 % thicker than the thickness of the CLs of 20PTFE_AC ($X_{Pt/TP}=0.6$). Furthermore, 30PTFE_AC included 25 % higher PTFE amount in the CLs ($X_{PTFE/TP}=0.5$) than the PTFE amount in the CLs of 20PTFE_AC ($X_{PTFE/TP}=0.4$). On the other hand, Nafion amount covering carbon nanoparticles of 30PTFE_AC was higher ($X_{C/(Nafion+C)}=0.31$) according to 20PTFE_AC ($X_{C/(Nafion+C)}=0.35$), which assured similar Pt utilization (61 %) despite higher amount of PTFE nanoparticles. Therefore, the charge transfer resistances were similar for 30PTFE_AC ($0.49 \Omega \cdot \text{cm}^2$) and 20PTFE_AC ($0.54 \Omega \cdot \text{cm}^2$). The higher amount of PTFE nanoparticles with these thicknesses of the CLs of 20PTFE_AC and 30PTFE_AC enhanced water management. Therefore mass transport limitations for 20PTFE_AC ($0.06 \Omega \cdot \text{cm}^2$) and 30PTFE_AC ($0.04 \Omega \cdot \text{cm}^2$) were decreased according to CLs without PTFE ($0.17 \Omega \cdot \text{cm}^2$). The charge transfer resistance of 40PTFE_AC ($0.78 \Omega \cdot \text{cm}^2$) was higher than 30PTFE_AC ($0.49 \Omega \cdot \text{cm}^2$). Although the thicknesses of the CLs of 40PTFE_AC and 30PTFE_AC ($X_{Pt/TP}=0.4$) was same, the amount PTFE nanoparticles in the CLs of 40PTFE_AC was 34 % higher than 30PTFE_AC. In addition to that 40PTFE_AC consisted of lower amount of Nafion encapsulating carbon nanoparticles ($X_{C/(Nafion+C)}=0.40$) compared to 30PTFE_AC ($X_{C/(Nafion+C)}=0.31$). Increase in PTFE nanoparticles in addition to reduced Nafion to carbon ratio caused a slight decrease in Pt utilization of 40PTFE_AC (47 %) compared to 30PTFE_AC (50 %). The reduced Pt utilization led to decreased amount of product water. When the water generation rate is low, a continuous hydraulic connection among water in pores is not formed, and therefore the product water is widely spread over the GDL in the isolated droplet form, increasing water saturation in the porous media (Cho & Mench 2012).

Table 6.3 Parameters of equivalent circuit modeling of EIS spectra of MEA1 at H₂/O₂ gas-feeding mode

MEA Type	O ₂			
	R _{HF} (Ωcm ²)	R _{ct} (A)(Ωcm ²)	R _{ct} (C)(Ωcm ²)	R _{mt} (Ωcm ²)
without PTFE MEA1	0.26	0.11	0.22	0.17
40PTFE_AC	0.28	0.03	0.75	0.15
30PTFE_AC	0.27	0.03	0.46	0.06
20PTFE_AC	0.26	0.09	0.45	0.04
10PTFE_AC	0.25	0.50	0.80	-
10PTFE_2_AC	0.27	-	0.38	0.12
5PTFE_AC	0.23	0.37	0.56	-

PTFE Loaded Catalyst Layer on Cathode Electrode (MEA2):

Polarization and power density curves for cathode CLs with six different PTFE loadings, working at H₂/O₂ gas-feeding mode are shown in Figure 6.8. The performances of PTFE loaded cathode CLs were compared with CLs without PTFE. The maximum power density at 0.45 V was 1.27 W/cm² for CLs without PTFE. 10PTFE_C (1.12 W/cm²) had the closer performance to CLs without PTFE at 0.45 V. This is attributed to having the similar X_{Pt/TP}, which is 1.0 for 10PTFE_C. The high ratio of Pt to total polymer loading (X_{Pt/TP}) provided thinner CLs, which reduce mass transport limitations. If we compare the X_{Pt/TP} constants, the thinnest cCL was attained for CLs without PTFE. This is interpreted as cCL without PTFE was less prone to mass transport limitations, while 10PTFE_C was more prone. Cathode catalyst layer of 5PTFE_C (X_{Pt/TP}=1.2) was 21 % thicker than the cCL without PTFE. However, it was also 17 % thinner than the cCL of 10PTFE_C. When we look at Figure 6.9, we can see that the performance of the 5PTFE_C (0.80 W/cm²) was very low compared to CLs without PTFE. However, such a decline in the power density was not observed for the V-I curve of cCLs. The lower power density of 5PTFE_C is attributed to the low amount of PTFE nanoparticles (X_{PTFE/TP}=0.14) in the cCL, which did not achieve to mitigate flooding. The cathode MPL also consisted of 5-weight percentage PTFE. It is more difficult for water molecules to invade hydrophobic pores compared to hydrophilic pores because hydrophobic nanoparticle in the pores has a higher surface tension and therefore repels the water.

After the water pressure accumulated at the entrance of the hydrophobic pores overcome the surface tension of the hydrophobic pores, liquid water can penetrate through the hydrophobic pores. Moreover, when liquid water once penetrates into the hydrophobic pore, high surface tension force liquid molecules to reduce their surface area and to be like a droplet form. Therefore, liquid molecules invaded hydrophobic pores move faster than in the hydrophilic pores. However, until liquid water invades the hydrophobic pores they occupy the entrance of the hydrophobic pores, which increased the retention time of water molecules in the CL and MPL. The PTFE nanoparticles in the both cathode MPL and cathode CL increased the retention time of water in the pores of cCL and cMPL due to increased capillary pressure. In addition to that, when cCL does not include hydrophobic nanoparticles, water pressure is the highest at the interface of the cCL and cMPL, which we call this pressure increase as capillary barrier effect. The peak point of the water pressure at the interface of cCL and cMPL increased the concentration gradient of water between the interface of membrane and cCL, and between the interface of cMPL and GDL at that point. This increased concentration gradient provided water molecules to move towards cGDL and anode side with back diffusion rapidly compared to cMPL without PTFE. In addition that by the addition of the same amount of PTFE nanoparticles into the CL, the concentration gradient which forces liquid water moves towards cathode GDL or anode GDL. When the same amount of PTFE nanoparticles were added into the cCL with cMPL, water pressure at the interface of cCL and cMPL decreased, because produced water was held at the entrance of hydrophobic pores of cCL. Therefore, the driving force of water molecules providing them move towards cGDL and aCL disappeared. This caused flooding at the cCL, which caused performance decrease due to accumulated water in the pores of cCL. 10PTFE_C had a closer performance to CL without PTFE, which had the lowest slope in the ohmic region. This pointed out the lower ohmic resistance. This is because the catalyst powder of 10PTFE_C had highest Pt utilization among all catalyst powders with a percentage of 84. This is because of the improved PTFE and Nafion distribution in the cCL, which increased the contribution of primary pores (42 %) to the cumulative pore volume. This allowed increased reaction rate in addition to enhanced water management, which decreased the ohmic resistance of 10PTFE_C.

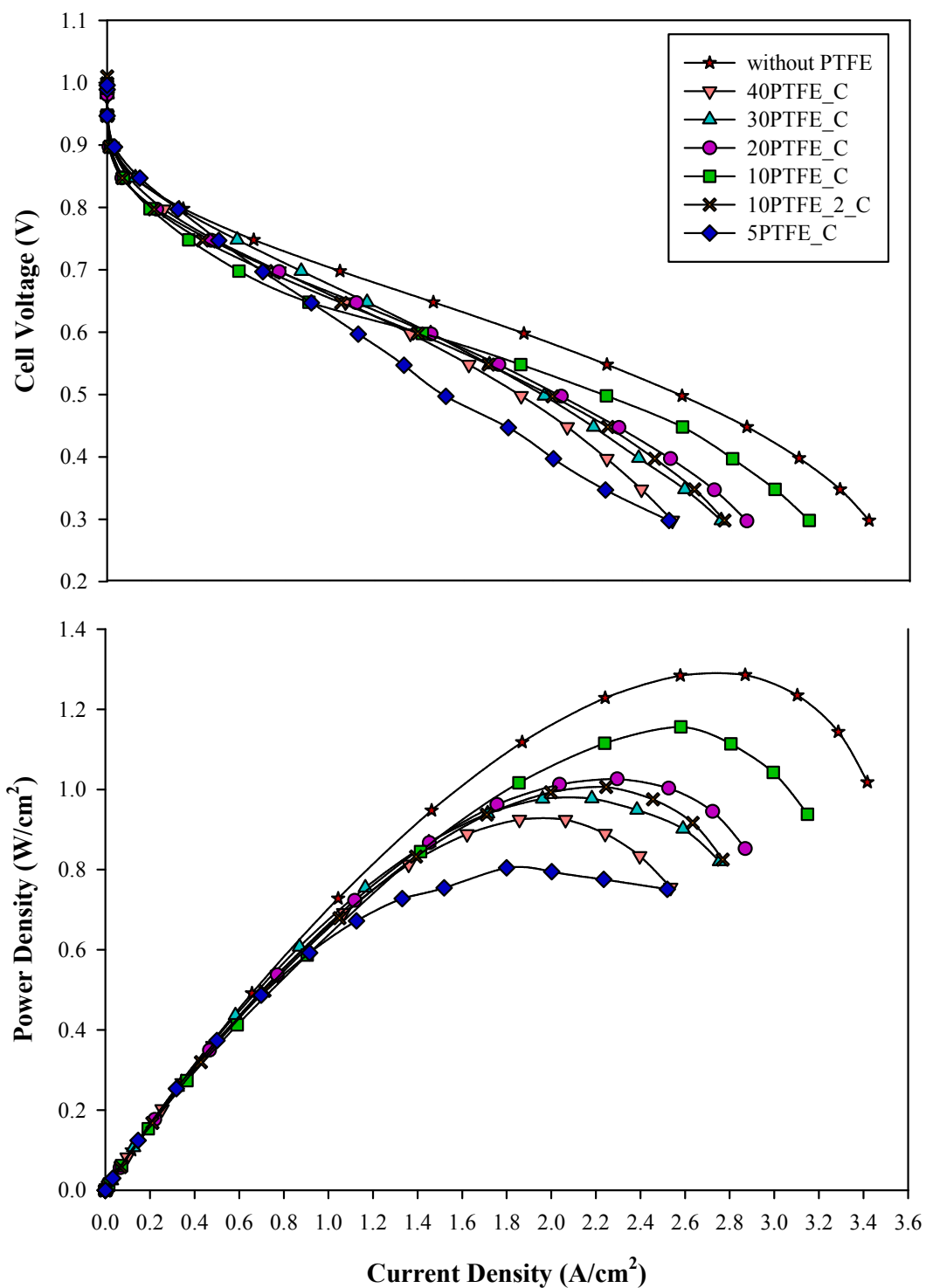


Figure 6.9 Polarization and power density curves of PEMFC for MEA2. Pt loading of anode and cathode electrodes was $0.4 \text{ mgPt}/\text{cm}^2$. Cathode catalyst layer was coated with PTFE nanoparticles. PEMFC was operated at H_2/O_2 gas feeding mode

Unlike to the previous case, which PTFE nanoparticles were included into both CLs (MEA1), in the present case (MEA2), 10PTFE_C (1.16 W/cm²) demonstrated higher performance than 10PTFE_2_C (1.01 W/cm²). The cCL of 10PTFE_2_C was 36 % thinner than the cCL of 10PTFE_C. In addition, 10PTFE_2_C had higher PTFE amount ($X_{\text{PTFE/TP}}=0.33$) in the cCL than 10PTFE_C ($X_{\text{PTFE/TP}}=0.25$). When PTFE nanoparticles were included to the aCL, they held the liquid water transported by back diffusion at the aCL/membrane interface. This keeps the membrane well humidified. In addition, the water concentration gradient between the aCL/membrane interface and aGDL decreased. This increased the retention time of liquid water in the pores of aCL and aGDL and decreased water removal rate from anode flow channels. Therefore, when aCL does not include PTFE nanoparticles water removal rate from anode side increased, in addition, the concentration gradient between cCL/membrane and aCL/membrane increased. This led to increasing in back diffusion rate of water, which may cause a decrease in membrane humidification. On the other hand, when cCL consisted of the higher amount of PTFE nanoparticles the retention time of water accumulated at the mouth of the hydrophobic pores in the CL increased. In addition, the ratio of the hydrophilic to hydrophobic pores decreased. This led increasing water saturation in the hydrophilic pores. Increased saturation of water caused an increase in the film thickness of water around aggregates and/or flooding of the pores. This may cause an increase in the effective diffusion coefficient of the reactant gas causing a decrease in the reaction rate. Therefore, with a thinner cCL and increased hydrophobicity (10PTFE_2_C), the retention time of water in the hydrophilic pores decreased, however, water saturation increased. This may cause swelling of the ionomer in the cCL. On the other hand holding time of water molecules at the mouth of the hydrophobic pores increased. Therefore, the ohmic resistance increased. Contrary to 10PTFE_2_C, with a thicker cathode CL and lower hydrophobicity (10PTFE_C), water saturation in the hydrophilic pores decreased and holding time of water at the pore mouth decreased while pore length increased. All these parameters influenced the ohmic resistance positively. Therdthianwong et al. (Therdthianwong et al. 2012) obtained ca. 0.45, 0.40, and 0.38 W/cm² for 0.1, 0.25 and 0.5 mg/cm² Pt loadings, respectively with 10 wt % PTFE in cCL at 0.45 V, working at H₂/O₂ gas-feeding mode. The power densities obtained for 10PTFE_C and 10PTFE_2_C was higher

more than two-fold in the present study. This is attributed to 2-step ink preparation method, which promotes PTFE nanoparticles settled in voids between catalyst agglomerates. By this way, disruption of the electronic and ionic network with a decline in Pt utilization was minimized. They obtained enhanced performance with PTFE added cCL compared to CLs without PTFE. They used a commercial catalyst with 20 wt % Pt/C while preparing the CLs. When we used the same commercial catalyst with the same Pt/C percentage (in Chapter 3), we also yielded higher performance with CLs including 30 wt % PTFE compared to CLs without PTFE. However, CLs prepared with 70 wt % Pt/C, the performance of the cCLs included even with 5 wt % PTFE was lower than the performance of CLs without PTFE. This is attributed to the high Pt percentage in the commercial catalyst, because, as Pt percentage increases in the commercial catalyst, total catalyst surface area per unit mass of the catalyst decreases (Marr & Li 1999). Furthermore, Platinum to Carbon ratio for 20 wt % Pt/C catalyst is 0.25, while it is 2 for 70 wt % P/C catalyst, which is almost ten times higher. Therefore, when PTFE nanoparticles are added to CLs, even if two step-catalyst ink preparation method is used, nanoparticles occupy electronically and ionomer network causing a loss in the electrochemical surface area and/or disruption of the network. The power density of 20PTFE_C was 1.03 W/cm², and the power density of 30PTFE_C was 0.98 W/cm² at 0.45 V. 10PTFE_2_C ($X_{Pt/TP}=1.5$), 20PTFE_C ($X_{Pt/TP}=0.60$), and 30PTFE_C ($X_{Pt/TP}=0.40$) demonstrated similar performance although they included a different amount of PTFE in the cCL with different thicknesses. The $X_{PTFE/TP}$ of the catalyst powder of 10PTFE_2_C was 0.33. The $X_{PTFE/TP}$ of the catalyst powder of 20PTFE_C was 0.40, while it was 0.5 for the catalyst powder of 30PTFE_C. 20PTFE_C had both moderate thickness for the cCL and moderate amount of PTFE nanoparticles in the cCL for the same Pt loading. The higher amount of the PTFE in the thicker cCL (20PTFE_C) than 10PTFE_2_C promoted better water management, which enhanced the cell performance. Nafion coverage of carbon nanoparticles ($X_{C/(Nafion+C)}=0.35$) of 20PTFE_C was higher than in the cCL of 10PTFE_2_C ($X_{C/(Nafion+C)}=0.54$). This led to increase in Pt utilization of 20PTFE_C (61 %) compared to 10PTFE_2_C (55%). Improved water management coupled with enhanced utilization promoted decreased ohmic resistance for 20PTFE_C compared to 10PTFE_2_C.

The power density of 40PTFE_C (0.93 W/cm^2) was slightly lower than 30PTFE_C (0.98 W/cm^2) although thicknesses of the cCL ($X_{\text{Pt/TP}}=0.4$). The $X_{\text{Pt/TP}}$ identifies the thickness of the cCL of 30PTFE_C and 40PTFE_C. The reduction in the cell performance of 40PTFE_C is attributed to higher PTFE amount in the cCL. Although 30PTFE_C and 40PTFE_C consisted of the same cCL thickness, PTFE amount of 40PTFE_C was higher ($X_{\text{PTFE/TP}}=0.67$) than 30PTFE_C ($X_{\text{PTFE/TP}}=0.5$). The excess amount of PTFE settled on the electronic and ionic network, which caused a reduction in the Pt utilization (57 %) causing an increase in the ohmic resistance and reduction in catalytic activity.

Figure 6.10 illustrates EIS spectra of MEA2 measured at 0.5V. Impedance spectrum of CLs demonstrates a high-frequency arc followed by a low-frequency arc.

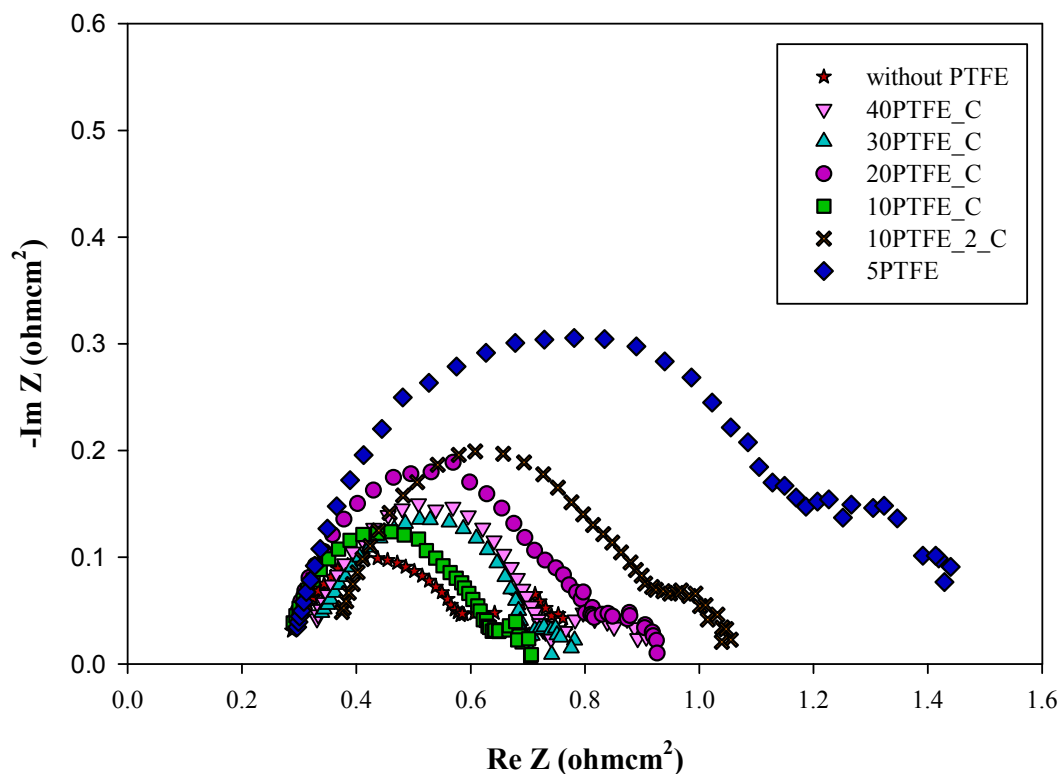


Figure 6.10 Electrochemical impedance spectra obtained at 0.5 V. Pt loading of anode and cathode electrodes was 0.4 mgPt/cm^2 . Cathode catalyst layer was coated with PTFE nanoparticles. PEMFC was operated at H_2/O_2 gas-feeding mode

This revealed that the pores of the cathode GDL of all MEAs were blocked by water. Parameters of equivalent circuit modeling of EIS spectra of MEA2 are shown in Table 6.4. The high-frequency resistance of 10PTFE_2_C was the lowest while R_{HF} of 10PTFE_2_C was the highest. The lowest performance of 5PTFE_C is attributed to the highest charge transfer resistance ($0.96 \Omega \cdot \text{cm}^2$) coupled with the highest mass transfer resistance ($0.25 \Omega \cdot \text{cm}^2$). This is because of flooding of the cCL and GDL of 5PTFE_C. On the other hand, the charge transfer resistance of 10PTFE_C ($0.39 \Omega \cdot \text{cm}^2$) was the closest to the cCL without PTFE ($0.33 \Omega \cdot \text{cm}^2$). This also revealed the higher performance of 10PTFE_C, which is closest to the cCLs without PTFE. Although the cCL of 10PTFE_C ($X_{Pt/TP}=1.0$) was 36 % thicker than the cCL without PTFE ($X_{Pt/TP}=1.5$), the mass transfer resistance of 10PTFE_C ($0.04 \Omega \cdot \text{cm}^2$) was lower than the cCL without PTFE ($0.17 \Omega \cdot \text{cm}^2$). This revealed that PTFE nanoparticles in the cCL of 10PTFE_C provided two-phase flow leading to lower water saturation in the pores of cGDL. Although the cCL of 20PTFE_C was % 43 thinner ($X_{Pt/TP}=0.7$) than 30PTFE_C and 40PTFE_C ($X_{Pt/TP}=0.4$), it demonstrated higher charge transfer resistance ($0.48 \Omega \cdot \text{cm}^2$) than 30PTFE_C ($0.41 \Omega \cdot \text{cm}^2$) and 40PTFE_C ($0.43 \Omega \cdot \text{cm}^2$). This is attributed to the lower amount of PTFE in the cCL of 20PTFE_C ($X_{PTFE/TP}=0.4$) with respect to 30PTFE_C ($X_{PTFE/TP}=0.50$) and 40PTFE_C ($X_{PTFE/TP}=0.67$). This revealed the amount of PTFE nanoparticles in the cCL of 20PTFE_C was not sufficient to mitigate flooding.

Table 6.4 Parameters of equivalent circuit modeling of EIS spectra of MEA2 at H_2/O_2 gas-feeding mode

MEA Type	O_2			
	$R_{HF} (\Omega \text{cm}^2)$	$R_{ct} (A)(\Omega \text{cm}^2)$	$R_{ct} (C)(\Omega \text{cm}^2)$	$R_{mt} (\Omega \text{cm}^2)$
without PTFE MEA2	0.26	0.11	0.22	0.17
40PTFE_C	0.29	0.14	0.29	0.19
30PTFE_C	0.30	0.16	0.25	0.07
20PTFE_C	0.27	0.09	0.39	0.17
10PTFE_C	0.27	0.33	0.06	0.04
10PTFE_2_C	0.33	0.24	0.41	0.07
5PTFE_C	0.28	0.11	0.85	0.25

6.3.6. Effect of PTFE Loading on Performance and Running Electrochemical Impedance Spectrum of PEMFC at H₂/Air Gas-feeding Mode

PTFE Loaded Catalyst Layer on Both Electrodes (MEA1):

Figure 6.11 illustrates polarization and power density curves obtained for MEA1 at H₂/Air gas feeding mode. Performances of all MEAs reduced by half, when the air was used instead of oxygen due to decreased partial pressure of the oxygen. The maximum power density at 0.45 V was 0.64 W/cm² attained for CLs without PTFE. 10PTFE_2_AC had a power density of 0.55 W/cm² at 0.45 V, which is the closest performance to the CLs without PTFE. This is attributed to having the same $X_{P/TP}$ caused a decrease in mass transport limitations, which is 1.5 for both MEAs. At H₂/O₂ feeding mode, 10PTFE_2_AC also demonstrated the closest performance to the CLs without PTFE with a power density of 1.15 W/cm². However, power density for 10PTFE_2_AC decreased by half when air used as the reactant gas at the cathode. This revealed that at both feeding modes, since PTFE nanoparticles were coated both sides, 10PTFE_2_AC demonstrated the highest performance, which is interpreted as 10PTFE_2_AC consisted of the optimum PTFE amount in the CLs. This means that in the thinnest CL with the $X_{P/TP}$ of 1.5, the optimum PTFE amount was the half the value of Nafion amount ($X_{PTFE/TP}$ of 0.33) for enhanced water management. Catalyst layers of 5PTFE_AC (0.46 W/cm²) were 17 % thinner than the CLs of 10PTFE_AC (0.48 W/cm²). However, PTFE amount of 5PTFE_AC ($X_{PTFE/TP}$ of 0.14) was 11 % lower than 10PTFE_AC ($X_{PTFE/TP}$ of 0.25). If we look at Figure 6.11, we can see that 5PTFE_AC and 10PTFE_AC demonstrated similar performances; however, 10PTFE_AC had higher mass transport limitations than 5PTFE_AC, while it demonstrated lower ohmic resistance than 5PTFE_AC. This is revealed that the thickness of CL ($X_{P/TP}$) and PTFE amount in the CLs ($X_{PTFE/TP}$) are competing parameters, which are influencing mass transport and ohmic resistances of the electrodes. The higher amount of PTFE nanoparticles included into the anode CL held the liquid water transported by back diffusion at the aCL/membrane interface. This keeps the membrane well humidified.

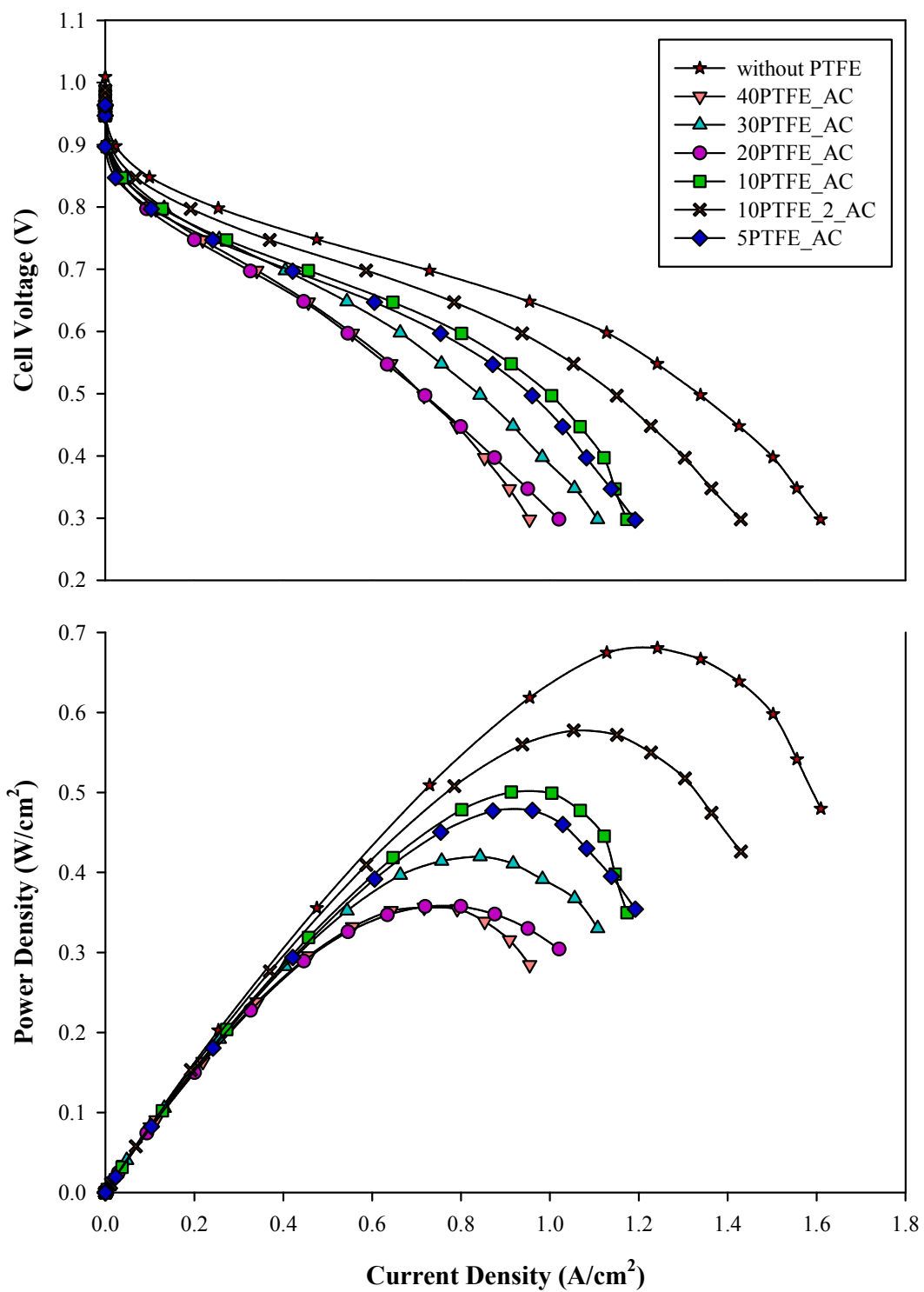


Figure 6.11 Polarization and power density curves of PEMFC for MEA1. Pt loading of anode and cathode electrodes was $0.4 \text{ mgPt}/\text{cm}^2$. Both anode and cathode catalyst layers include PTFE nanoparticles. PEMFC was operated at H_2 /Air gas-feeding mode

That is why ohmic resistance decreased. However, the higher amount of PTFE nanoparticles in the cCL facilitated water removal from cCL towards cathode GDL. Higher water saturation in the pores of cGDL led to reactant starvations, which is the main reason of the mass transport limitations. Song et al. (Song et al. 2010), obtained ca. 0.34 W/cm^2 power density for 5 wt % PTFE in both CLs at 0.45 V for 0.4 mg/cm^2 Pt loading, working at H_2/Air gas-feeding mode. Although the same PTFE loading was used in the CLs of 5PTFE_AC, power density was higher than the CLs of the study of (Song et al. 2010). This is attributed to 2-step ink preparation method (Friedmann & Nguyen 2008; Friedmann & Van Nguyen 2010).

The power density of 30PTFE_AC was 0.41 W/cm^2 and the power density of 20PTFE_AC was 0.36 W/cm^2 , which is same with the power density of 40PTFE_AC at 0.45 V. 30PTFE_AC demonstrated higher performance although including higher amount of PTFE in the CLs ($X_{\text{PTFE/TP}}$ of 0.5) than 20PTFE_AC ($X_{\text{PTFE/TP}}$ of 0.4). The thickness of the CLs of 30PTFE_AC ($X_{\text{Pt/TP}}=0.4$) was 43 % higher than 20PTFE_AC ($X_{\text{Pt/TP}}=0.7$), while the thicknesses of the CLs of 30PTFE_AC and 40PTFE_AC ($X_{\text{Pt/TP}}=0.4$) were the same. However, PTFE amount of in the CLs of 40PTFE_AC ($X_{\text{PTFE/TP}}=0.67$) was 34 % higher than the PTFE amount of 30PTFE_AC ($X_{\text{PTFE/TP}}=0.5$). Consequently, 30PTFE_AC had thickest CLs with moderate hydrophobicity with respect to 20PTFE_AC and 40PTFE_AC. The lower amount of the PTFE with respect to 40PTFE_AC in the same thickness (30PTFE_AC) promoted enhanced water management, which improved the cell performance. The higher amount of PTFE in the CLs caused higher mass transport limitations. The thickness of the CLs of 40PTFE_AC was highest among all the CLs. Since the pore length the highest, and water saturation is the low, capillary flow cannot be formed. Therefore, product water spread over the pores preventing gas transport, which caused mass transport limitations.

Figure 6.12 illustrates EIS spectra of MEA1 measured at 0.5V. Impedance spectra of all CLs demonstrate only one arc at high-frequency data range. This revealed that high airflow rate purges the accumulated water in the pores of cathode GDL. Therefore, low-frequency arc of all CLs disappeared. Parameters of equivalent circuit modeling of EIS spectra of MEA1 are shown in Table 6.5. 5PTFE_AC had the lowest high-frequency resistance, while 40PTFE_AC had the highest. The decrease in partial pressure of oxygen caused a reduction in the reaction rate,

accordingly, the rate of water generation decreased. Therefore, charge transfer resistances of all MEAs increased more than 6 times which also indicates reduced reaction kinetics.

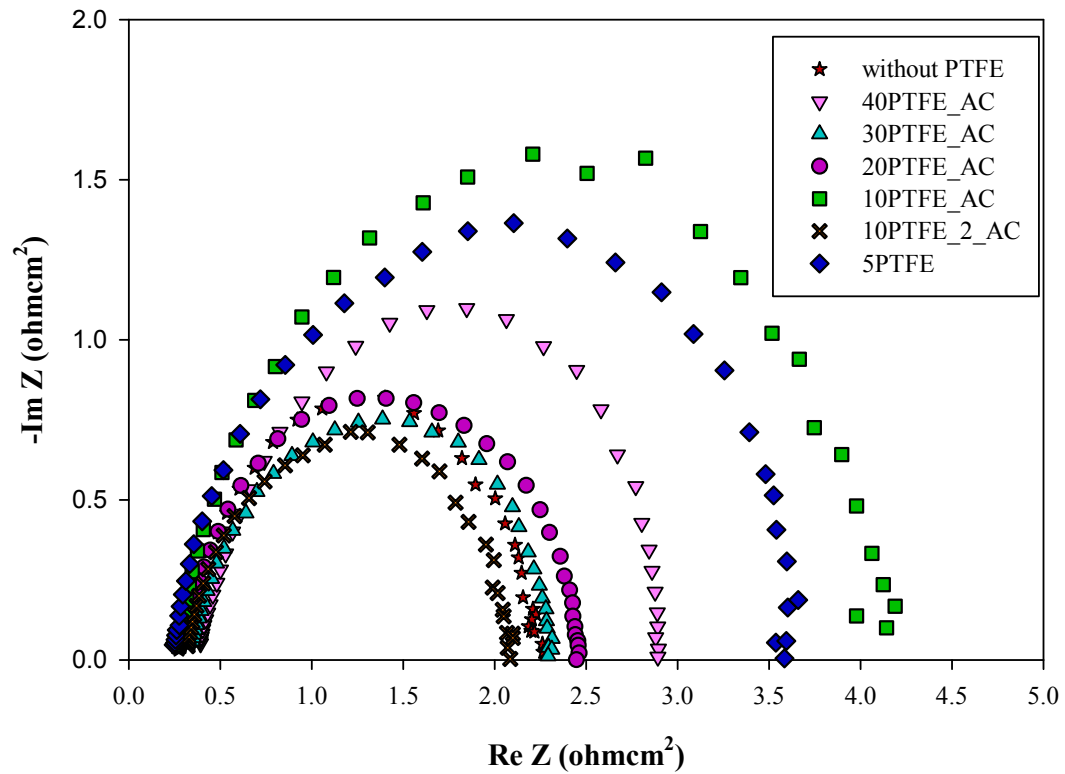


Figure 6.12 Electrochemical impedance spectra obtained for a running fuel cell at 0.5 V. Pt loading of anode and cathode electrodes was 0.4 mgPt/cm^2 . Both anode and cathode catalyst layers were coated with PTFE nanoparticles. PEMFC was operated at H_2/Air gas-feeding mode

10PTFE_2_AC had the lowest charge transfer resistance ($1.80 \text{ } \Omega \cdot \text{cm}^2$) among all CLs including FEP. The charge transfer resistance of the CL of 10PTFE_2_AC was also lower than the charge transfer resistance of the CL without PTFE ($2.0 \text{ } \Omega \cdot \text{cm}^2$). This revealed that 10PTFE_2_AC provided enhanced water management compared to CLs without PTFE. The highest charge transfer resistance was obtained for 10PTFE_AC ($3.87 \text{ } \Omega \cdot \text{cm}^2$) similar to H_2/O_2 feeding mode. The charge transfer resistances of 5PTFE_AC ($3.36 \text{ } \Omega \cdot \text{cm}^2$) and 40PTFE_AC ($2.53 \text{ } \Omega \cdot \text{cm}^2$) came after 10PTFE_AC with descending order. In the H_2/O_2 feeding mode, the charge transfer resistance of 5PTFE_AC was lower 40PTFE_AC, but right after 10PTFE_AC. This

revealed that high airflow rate mitigated flooding at cathode GDL of 10PTFE_AC, 5PTFE_AC, and 40PTFE_AC, but did not cause any decrease in water saturation in the cCL. Therefore, both the order and the degree of the charge transfer resistances of 10PTFE_AC, 5PTFE_AC, and 40PTFE_AC did not alter with high airflow rate. The charge transfer resistance of 20PTFE_AC ($2.23 \Omega \cdot \text{cm}^2$) had the higher than the charge transfer resistance of 30PTFE_AC ($1.98 \Omega \cdot \text{cm}^2$). The CLs of 30PTFE_AC ($X_{\text{Pt/TP}}=0.40$) was 43 % thicker than 20PTFE_AC ($X_{\text{Pt/TP}}=0.70$), accordingly, PTFE amount was 25 % higher with respect to 20PTFE_AC ($X_{\text{PTFE/TP}}=0.40$). However, a higher amount of PTFE nanoparticles in the CLs of 30PTFE_AC influenced the charge transfer resistance negatively, because high airflow rate mitigated flooding. Therefore, an excess amount of PTFE caused only reduction in the reaction rate.

Table 6.5 Parameters of equivalent circuit modeling of EIS spectra of MEA1 at H₂/Air gas-feeding mode

MEA Type	Air		
	$R_{\text{HF}} (\Omega \text{cm}^2)$	$R_{\text{ct}} (\text{A}) (\Omega \text{cm}^2)$	$R_{\text{ct}} (\text{C}) (\Omega \text{cm}^2)$
without PTFE MEA1	0.24	0.14	1.86
40PTFE_AC	0.37	0.65	1.88
30PTFE_AC	0.33	0.74	1.24
20PTFE_AC	0.24	0.05	2.18
10PTFE_AC	0.27	1.57	2.30
10PTFE_2_AC	0.31	0.62	1.18
5PTFE_AC	0.24	1.48	1.88

PTFE Loaded Catalyst Layer on Cathode Electrode (MEA2):

Figure 6.13 illustrates polarization and power density curves obtained for MEA2 at H₂/Air gas feeding mode. Performances of all MEAs reduced by half, compared to MEA2 operated with H₂/O₂ feeding mode. The maximum power density was 0.64 W/cm^2 at 0.45 V , which was obtained for the CLs without PTFE. 5PTFE_C had a power density of 0.55 W/cm^2 , while power density of 10PTFE_2_C was 0.45 W/cm^2 at 0.45 V . At H₂/O₂ feeding mode, 5PTFE_C demonstrated the

lowest performance with a power density of 0.8 W/cm^2 . However, power density for 5PTFE_C decreased almost by half when air used as the reactant gas at the cathode. This revealed that at H₂/Air feeding mode, since PTFE nanoparticles were coated only on the cathode side, 5PTFE_C with the $X_{\text{Pt/TP}}$ of 1.2 and with $X_{\text{PTFE/TP}}$ of 0.14 demonstrating highest performance among all PTFE included CLs (See Table 6.2). However, in the case of the H₂/O₂ feeding, PTFE nanoparticles in the cCL could not achieve to mitigate flooding. This is because reaction rate at H₂/O₂ feeding mode was higher than at H₂/Air feeding mode. Therefore, the concentration of the product water decreased due to decreased reaction rate. In addition to that, high airflow diminished the blockage of the pores of cGDL. Therefore, at H₂/Air feeding mode the low amount of PTFE nanoparticles achieved to decrease flooding. 10PTFE_2_C (0.45 W/cm^2) had the closer performance to 5PTFE_C (0.55 W/cm^2). The higher amount of ($X_{\text{PTFE/TP}}=0.33$) with thinner cCL for 10PTFE_2_C ($X_{\text{Pt/TP}}=1.5$) according to 5PTFE_C ($X_{\text{Pt/TP}}=1.2$) could not assure a reduction in the ohmic and mass transport limitations. If we look at Figure 6.12, we can see that above 1.0 mA/cm^2 , an abrupt decrease in the cell performance due to reactant starvation. Cathode catalyst layer of 5PTFE_C was thinner than the cCL of 10PTFE_C, while the PTFE amount of 5PTFE_C ($X_{\text{PTFE/TP}}$ of 0.14) was lower than 10PTFE_C ($X_{\text{PTFE/TP}}$ of 0.25). The higher amount of PTFE nanoparticles in the cCL of 10PTFE_C influenced the performance negatively because high airflow reduced pore blocking. Friedman et al. (Friedmann & Van Nguyen 2010), obtained ca. 0.52 W/cm^2 power density for the cCL with 10 wt % PTFE at 0.45 V for 0.55 mg/cm^2 Pt loading at H₂/Air gas-feeding mode, which is slightly higher than our performance. They obtained higher power density for increased Pt loading. They also prepared the catalyst ink with 2-step preparation method. Furthermore, they operated fuel cell with high airflow rate and interdigitated flow field, which creates higher gas pressure on the both anode and cathode sides to minimize the influence of flooding in the GDLs on the performance of the CLs. In their study, temperatures of anode and cathode humidifiers were also $20 \text{ }^\circ\text{C}$ higher than cell temperature. When external humidification is used, as the anode and cathode humidification temperatures are higher than the cell temperature, performance enhances (Wang et al. 2003).

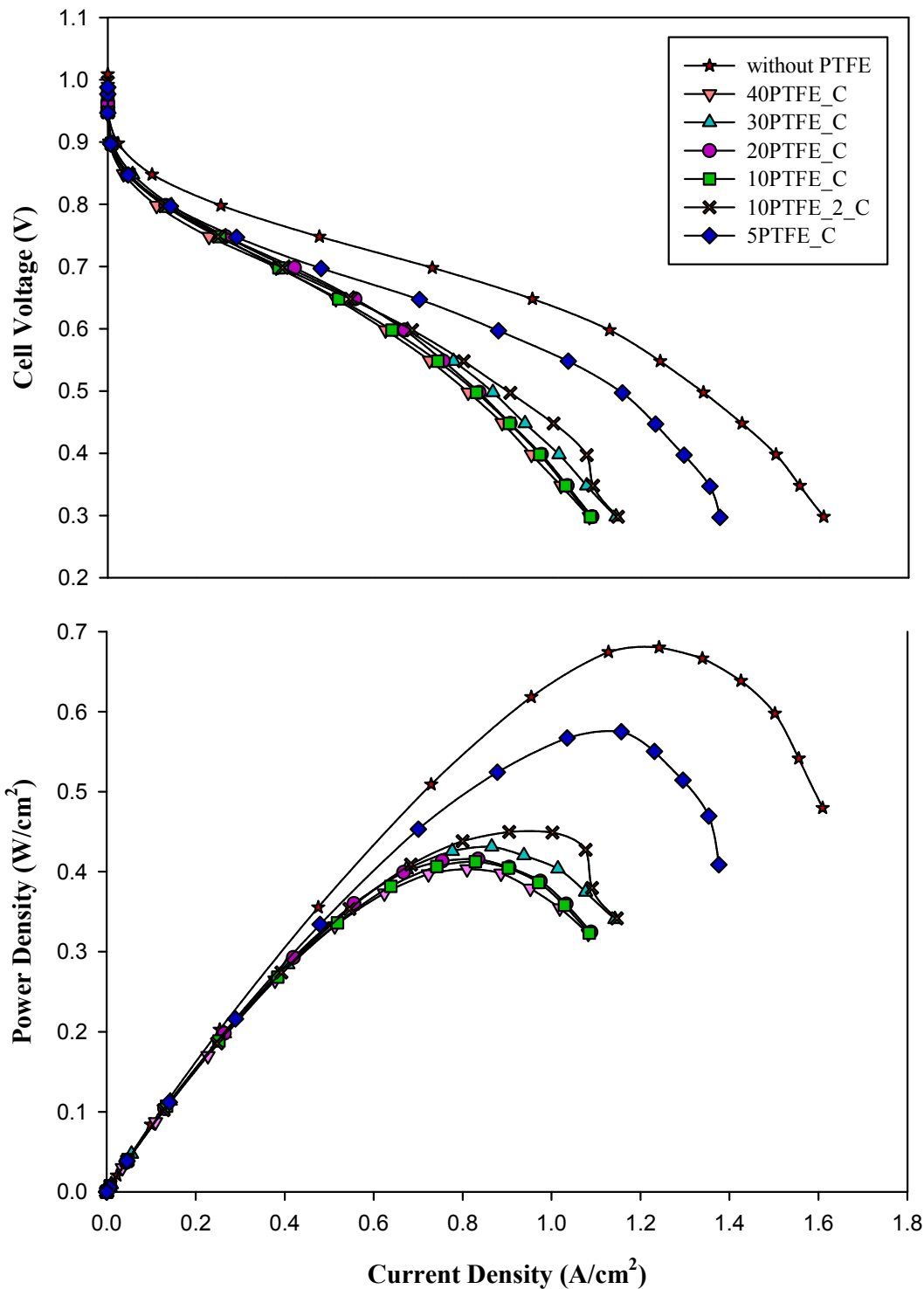


Figure 6.13 Polarization and power density curves of PEMFC for MEA2. Pt loading of anode and cathode electrodes was $0.4 \text{ mgPt}/\text{cm}^2$. Cathode catalyst layer was coated with PTFE nanoparticles. PEMFC was operated at H_2 /Air gas feeding mode

Therefore, reactant gas could easily reach the active catalyst sites, compensated the performance decrease. Friedman et al. (Friedmann & Van Nguyen 2010) obtained 0.60 W/cm^2 power density for 23 wt % PTFE in the cCL for 0.55 mg Pt/cm^2 loading, while they obtained 0.50 W/cm^2 power density for the cCL with 27.7 wt % PTFE at 0.45 V for 0.48 mg/cm^2 Pt loading. The increase in the performance is attributed to the higher Pt loading coupled with differences in flow plates and humidification temperature.

Figure 6.14 illustrates EIS spectra of MEA2 measured at 0.5 V. Impedance spectra of all CLs demonstrate only one arc at high-frequency data range. Mass transport limitations associated with pore blocking of cGDL were diminished also in this MEA configuration. This is attributed to the high airflow rate.

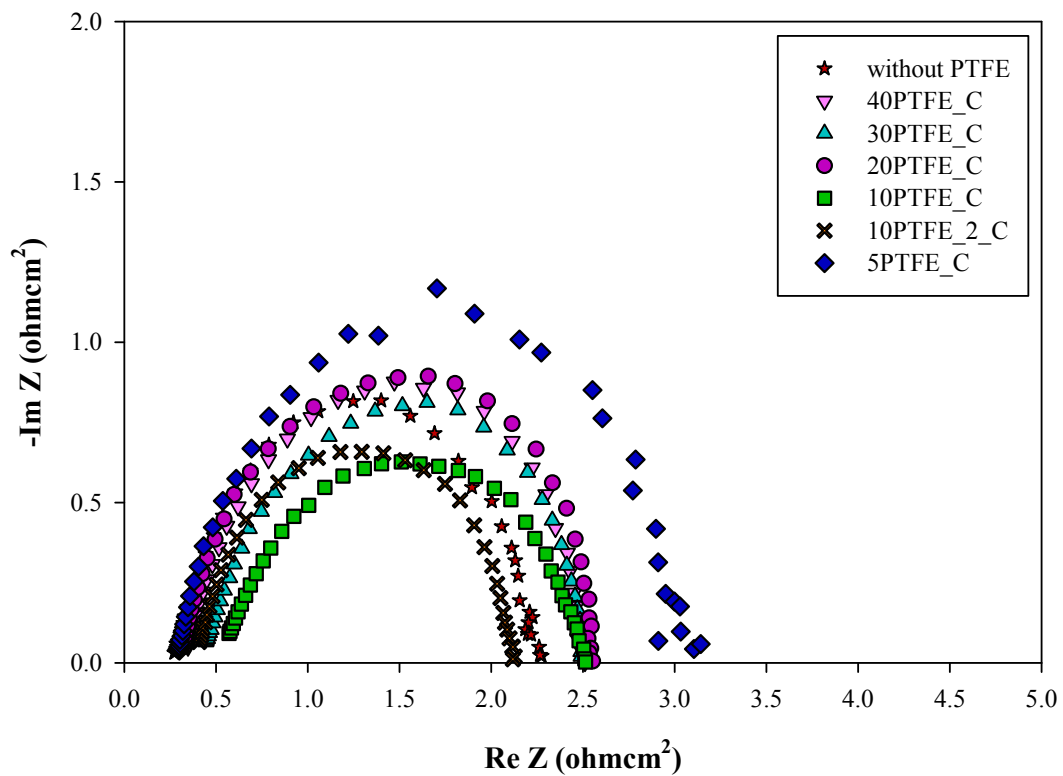


Figure 6.14 Electrochemical impedance spectra obtained for running fuel cell at 0.5 V. Pt loading of anode and cathode electrodes was 0.4 mgPt/cm^2 . Cathode catalyst layer was coated with PTFE nanoparticles. PEMFC was operated at H_2/Air gas-feeding mode

Parameters of equivalent circuit modeling of EIS spectra of MEA2 are shown in Table 6.6. The lowest high-frequency resistance was attained for the cCL without PTFE ($0.24 \Omega\cdot\text{cm}^2$), while 10PTFE_C had the highest high-frequency resistance ($0.53 \Omega\cdot\text{cm}^2$). Charge transfer resistances at the cathode of all CLs increased more than 6 times which also indicates reduced reaction kinetics as encountered with previous experiment set.

Table 6.6 Parameters of equivalent circuit modeling of EIS spectra of MEA1 at H₂/Air gas-feeding mode

MEA Type	Air		
	R _{HF} (Ωcm^2)	R _{ct} (A)(Ωcm^2)	R _{ct} (C)(Ωcm^2)
without PTFE MEA2	0.24	0.14	1.86
40PTFE_C	0.33	0.68	1.51
30PTFE_C	0.42	0.87	1.21
20PTFE_C	0.31	1.19	1.05
10PTFE_C	0.53	0.29	1.68
10PTFE_2_C	0.30	0.10	1.73
5PTFE_C	0.22	0.07	2.84

10PTFE_2_C had the lowest charge transfer resistance ($1.83 \Omega\cdot\text{cm}^2$), while 5PTFE_C had the highest ($2.91 \Omega\cdot\text{cm}^2$). This is interpreted as the PTFE amount in the cCL of 10PTFE_2_C ($X_{\text{PTFE/TP}}$ of 0.33) provided the optimum water saturation in the cCL. This led to decrease in the charge transfer resistance. Longer pores with the lower amount of PTFE in the cCL of 5PTFE_C ($X_{\text{PTFE/TP}}$ of 0.14) with respect to 10PTFE_2_C caused highest charge transfer resistance because of the higher water saturation in the pores of the cCL. On the other hand, the charge transfer resistance of 10PTFE_C ($1.97 \Omega\cdot\text{cm}^2$) was similar to the charge transfer resistance of the cCL without PTFE ($2.00 \Omega\cdot\text{cm}^2$). This is pointed out the similar water saturation around the aggregates. The charge transfer resistances of 30PTFE_C ($2.08 \Omega\cdot\text{cm}^2$) and 40PTFE_C ($2.11 \Omega\cdot\text{cm}^2$) was also similar to each other. This is attributed to the thickness of the cCL ($X_{\text{Pt/TP}}$ of 0.4). Their thicknesses were same with each other, but the PTFE amount in the cCL was different for 30PTFE_C ($X_{\text{PTFE/TP}}$ of 0.5) and

40PTFE_C ($X_{\text{PTFE/TP}}$ of 0.67). The higher amount of PTFE in the cCL of 40PTFE_C did not significantly alter the water saturation in the CL. The charge transfer resistance of 20PTFE_C ($2.34 \Omega \cdot \text{cm}^2$) was the highest after 5PTFE_C. Lower PTFE amount ($X_{\text{PTFE/TP}}$ of 0.4) with thinner cCL ($X_{\text{Pt/TP}}$ of 0.7). This is pointed out that PTFE amount in the cCL was not sufficient to mitigate flooding around the aggregates.

6.3.7. Cross-section Images of MEA after Performance Testing

SEM images of cross section area of the membrane electrode assemblies prepared with CLs with 1.2 mg/cm^2 Pt loading without PTFE, CLs with 0.4 mg/cm^2 Pt loading without PTFE, 5PTFE_AC with 1.2 mg/cm^2 Pt loading, 10PTFE_2_AC with 0.4 mg/cm^2 Pt loading are shown in Figure 6.15. The two-sided arrows on the images illustrate anode and cathode side of the MEAs. The thickness of the CLs with 1.2 mg/cm^2 Pt loading (Figure 6.15a) was higher than the thickness of the CLs with 0.4 mg/cm^2 Pt loading (Figure 6.15b). This revealed that the thickness of the CLs increased since the Pt loading were increased. When the CLs were thin, membrane deformation (shown with the red arrow on Figure 6.15 b) could be observed clearly. However, as the thickness of the CLs increased, especially on the cathode side, CLs were broken at some points indicated with red arrows on Figure 6.15a. This revealed that high Pt loading makes the CLs brittle according to thinner CLs. Surface morphology of the MEA of 5PTFE_AC after fuel cell testing is shown in Figure 6.15c. Membrane deformation due to swelling was not significant but brittleness of the anode and cathode CLs (shown with red arrows on the image) increased as PTFE nanoparticles were included into the CLs with high Pt loading. Surface morphology of the MEA after fuel cell testing of 10PTFE_2_AC is shown in Figure 6.15d. Membrane deformation due to swelling was not significant, cracks in the CLs (shown with red arrows on the image) was not observable as well. This revealed that deformation in the CLs can be tolerable with low Pt loading.

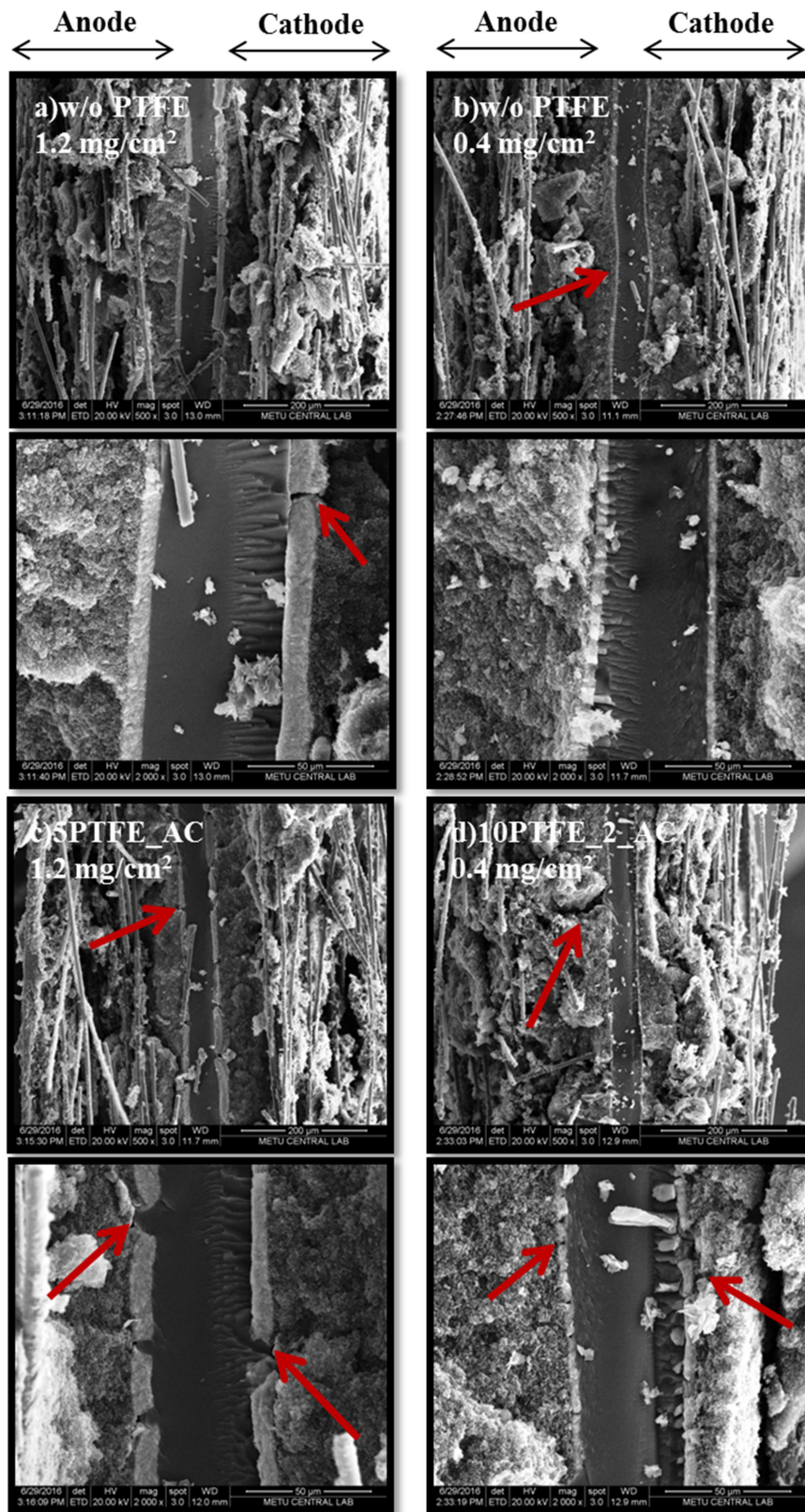


Figure 6.15 SEM images of the cross-section of the MEAs for a) without PTFE with 1.2 mg/cm^2 Pt loading, b) without PTFE with 0.4 mg/cm^2 Pt loading, c) 5PTFE_AC with 1.2 mg/cm^2 d) 10PTFE_2_AC with 0.4 mg/cm^2

6.4. Conclusions

Nafion addition to the commercial catalyst reduced a significant amount of the pore volume, however, PTFE addition to Nafion impregnated catalyst does not cause further reduction in the pore volume.

Total surface area of Pt particles in the catalyst powders does not alter with the addition of PTFE nanoparticles; even Pt percentage in the catalyst powder reduces by the addition of PTFE nanoparticles. This indicates that when Pt percentage in the commercial catalyst was higher, Pt agglomeration occurs, which causes reduced active surface area. Therefore, even if Pt percentage in the PTFE included catalyst powder is lower, total surface area of Pt nanoparticles remain constant.

2-step ink preparation method provides homogenous distribution of the Pt, Nafion, and PTFE nanoparticles, which enhances Pt utilization in the case of the low amount of Pt. In addition to that, for the catalyst powders including 5 wt % and 10 wt % PTFE, 2-step ink preparation method improved Pt utilization according to the commercial catalyst.

Cumulative pore volume has a great impact on the performance of the cell. When the percentage of the primary pores contributed to the cumulative pore volume increased, Pt utilization enhances, therefore cell performance increases.

The thickness of the CLs and the PTFE amount in the CLs are competing parameters dominating the water transport mechanisms at H₂/O₂ feeding mode. In the case of H₂/Air feeding mode, airflow rate was the dominant parameter influencing water movement in the pores of cGDL.

High airflow rate prevents pore blockage at the cathode GDL for both MEA configurations.

When air is used as the reactant gas of the CLs included into both MEA1 and MEA2 configurations, the charge transfer resistances increases up to 6 times of the charge transfer resistances of the CL operated at H₂/O₂ feeding mode.

5 wt. % PTFE was not sufficient to mitigate flooding for both MEA1 and MEA2 configurations at H₂/O₂ feeding mode.

The increase in the PTFE amount in the CLs made the CLs more brittle, which causes cracks in the CL-leading to electronic and ionic disruption.

Although PTFE included catalyst powders prepared with 2-step ink preparation, which provided enhanced Pt utilization, PTFE nanoparticles in CLs caused a reduction in the cell performance. The highest performance is always attained for the CLs without PTFE.

10 wt % PTFE inclusion into the cCL decreases the charge transfer resistance at both feeding modes which is the prove of the enhanced water management.

CHAPTER 7

CHARACTERIZATION OF HYDROPHOBIC CATALYST LAYERS INCLUDING FEP NANOPARTICLES IN THE SCOPE OF WATER MANAGEMENT AND PERFORMANCE OF PEM FUEL CELL

In this chapter, fluorinated ethylene propylene (FEP) nanoparticles were added to CL to facilitate excess water removal from the triple phase boundary in high Pt loading (0.4 mg/cm^2) proton exchange membrane fuel cell (PEMFC) electrodes. The loading of FEP in the catalyst ink was varied from zero to 30 weight percentage. High-performance electrodes for anode and cathode were prepared by ultrasonic spray coating technique with a commercial catalyst containing 70 wt % Pt on carbon. Different membrane electrode assemblies (MEAs) were prepared in order to differentiate the influence of hydrophobic nanoparticles on water transport and cell performance. In the first configuration (MEA1), FEP nanoparticles were added to both anode and cathode catalyst layers. In the second configuration (MEA2), FEP nanoparticles were added only to cCL. PEM fuel cell tests were carried out at both H_2/O_2 and H_2/Air gas-feeding modes.

7.1. Introduction

The objective of this work is to investigate the influence of FEP nanoparticles in CLs as a hydrophobic agent in a low-temperature PEM fuel cell. The electrodes were prepared by ultrasonic coating technique with high Pt-containing commercial catalyst (70 wt % Pt/C) with a high Pt loading (0.4 mg Pt/cm^2). Fuel cell performance tests were carried out to determine the influence of FEP nanoparticles

on high-performance PEM fuel cells. Impedance spectroscopy results have revealed the influence of FEP nanoparticles on reaction kinetics and water management.

7.2. Materials and Methods

Ink preparation, physical and electrochemical characterization methods in addition to performance tests are same as explained in Chapter 6.

7.2.1. MEA Configuration

Performance testing was carried out with two different membrane electrode assembly configurations. By this way, the effect of FEP nanoparticles in anode and cathode CLs on water transport mechanism was investigated, separately. In the first configuration (MEA1), both anode and cathode catalyst layers coated with FEP nanoparticles. In the second configuration (MEA2), FEP nanoparticles were coated only on cCL. The Pt, Nafion, and FEP nanoparticle loadings on CLs for prepared MEAs are summarized in Table 7.1.

Table 7.1 Pt, Nafion, and FEP loadings in catalyst layers

Catalyst Ink	Loading (mg/cm ²)		
	Pt	Nafion	FEP
without FEP	0.4	0.26	-
40FEP	0.4	0.31	0.62
30FEP	0.4	0.46	0.46
20FEP	0.4	0.37	0.25
10FEP	0.4	0.31	0.10
10FEP_2	0.4	0.18	0.09
5FEP	0.4	0.28	0.05

Numbers before FEP synonym represent the weight percentage of FEP in the CL on a dry basis. For example, 5FEP represents the CL prepared with the ink containing 5 wt % FEP on a dry basis. On the other hand, 30FEP_AC represents the

MEA that has 30 wt % FEP on both anode and cathode catalyst layers. 30FEP_C represents the MEA that had 30 wt % FEP on only cCL.

7.3. Results and Discussions

7.3.1. Physical Characterization

7.3.1.1. Nitrogen physisorption analysis

Figure 7.1 illustrates nitrogen adsorption/desorption isotherms for powders of commercial catalyst (Pt/C), commercial catalyst impregnated with Nafion (without FEP), commercial catalyst impregnated with Nafion and FEP included catalysts.

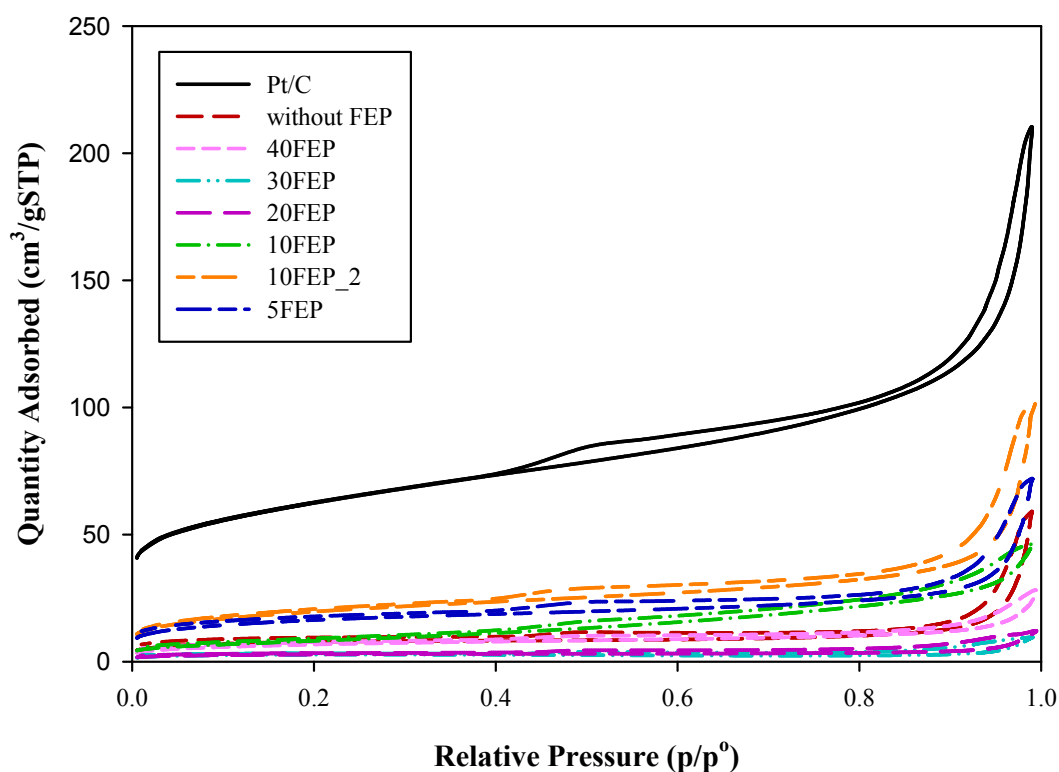


Figure 7.1 Adsorption/desorption isotherms for powders of commercial catalyst (Pt/C), commercial catalyst impregnated with Nafion (without FEP), commercial catalyst impregnated with different Nafion and FEP loadings

All isotherms are compatible with isotherm of Type IV according to IUPAC classification which is typical for mesoporous structure (Brunauer et al. 1940; Sing 1985), (Kaneko 1994). Furthermore, the hysteresis loops for the commercial catalyst (Pt/C), commercial catalyst impregnated with Nafion ionomer (without FEP), 10FEP_2, and 5FEP, demonstrated hysteresis Type H3 according to IUPAC classification. This means that these catalysts consist of aggregates of plate-like particles give rise to slit-shaped pores (Sing 1985). Moreover, 40FEP, 30FEP, 20FEP, and 10FEP demonstrates more like type H4 loop is often associated with narrow slit-like pores (Sing 1985). This is because most of the pore volume of the slit-shaped pores was occupied with Nafion and FEP polymers leading to narrower pore width.

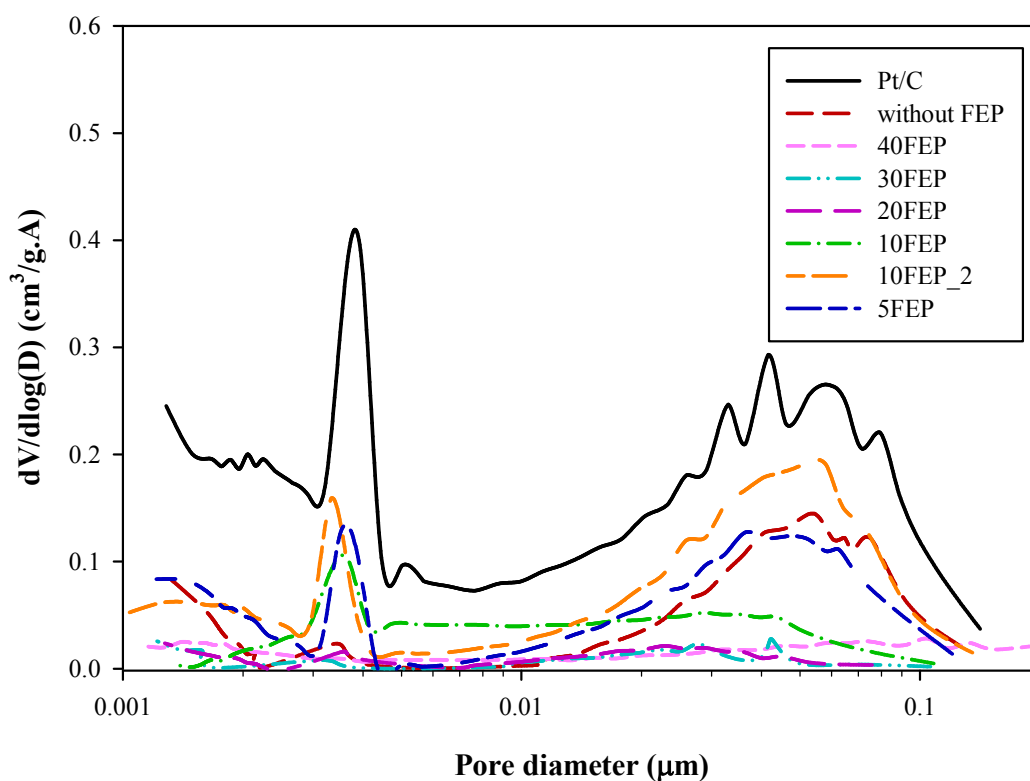


Figure 7.2 Pore size distributions for powders of commercial catalyst (Pt/C), commercial catalyst impregnated with Nafion (without FEP), and commercial catalyst impregnated with different Nafion and FEP loadings

The catalyst powder consisted of two distinctive pore distributions, where pores with a diameter distributed from 0.01 μm to 0.1 μm defined as primary pores, while pores with a diameter distributed from 0.1 μm to 1.0 μm defined as secondary pores. The primary pores represented to the pores in the aggregates, where the reaction takes place, while the secondary pores represented to the pores between aggregates assigned to gas diffusion (Watanabe et al. 1985). The highest cumulative pore volume was obtained for Pt/C. When Nafion impregnated to the commercial catalyst, it occupied most of the primary pores led to the decrease in cumulative pore volume. As the weight percentage of total polymer in the catalyst powder increased, cumulative pore volume reduced. The cumulative pore volume of 10FEP, 10FEP_2, and 5FEP was higher than the cumulative pore volume of 40FEP, 30FEP, 20FEP, and catalyst powder without FEP below 0.1 μm . Although 10FEP (0.41 mg/cm^2), 10FEP_2 (0.26 mg/cm^2), and 5FEP (0.33 mg/cm^2) consisted of similar polymer loadings with the catalyst powder without FEP (0.26 mg/cm^2), 10FEP, 10FEP_2, and 5FEP had higher pore volume below 0.1 μm . This revealed that catalyst preparation with two-steps reduces pore blockage and provide more homogenous distribution. Although, 40FEP had the same polymer loading (0.93 mg/cm^2) with 30FEP (0.93 mg/cm^2), the cumulative pore volume of 40FEP was higher than 30FEP. Furthermore, 40FEP had higher polymer loading than 20PTFE (0.62 mg/cm^2), mesopores of 40FEP below 0.1 μm were slightly open compared to 20FEP. This is attributed to the $X_{\text{FEP/Nafion}}$ constant of the catalyst powders. The $X_{\text{PTFE/Nafion}}$ of 40FEP was highest with a value of 2.0, while $X_{\text{FEP/Nafion}}$ of 30FEP and 20FEP was 1.0 and 0.7, respectively. Nafion mainly occupied most of the primary pores, while FEP settled in the secondary pores (Watanabe et al. 1985; Uchida 1996; Uchida 1995). This is interpreted as since the total polymer amount was similar when FEP amount was higher than Nafion, cumulative pore volume was increased. This means that higher volume of the primary pores was free to access. The pores of 20FEP, 30FEP, and 40FEP between 0.1 μm and 1.0 μm were almost completely blocked while the pores of 10FEP_2, 5FEP, and catalyst powder without FEP in the same range were open. This revealed that polymer loading of 20FEP (0.62 mg/cm^2), 30FEP (0.93 mg/cm^2), and 40FEP (0.93 mg/cm^2) were pretty much, causing blockage of most of the pores both in meso and macro region.

7.3.1.2. XRD analysis

XRD patterns for powders of commercial catalyst (Pt/C), commercial catalyst impregnated with Nafion (without FEP), and commercial catalyst impregnated with different Nafion and FEP loadings are shown in Figure 7.3. All of the patterns clearly show the presence of the elemental platinum with the five characteristic peaks of face centered cubic crystalline platinum. The Bragg angles of ca. 40° , 46° , 67° , 81° , 86° correspond to (111), (200), (220), (311) (He 1997; Pozio et al. 2002), and (222) (Zhang et al. 2010) Pt facets, respectively. The intensity of diffraction peak of Pt (222) was weak only in the pattern of all catalysts. The peak appeared at the diffraction pattern for powder of commercial catalyst impregnated with Nafion (without PTFE) at ca. 17° Bragg angle was attributed to poly-fluorocarbon chains of Nafion ionomer (Jung et al. 2003). The broadness of the Nafion peak pointed out the amorphous structure of the polymer. The peak occurred at ca. 17° Bragg angle corresponded to a crystalline and amorphous component of FEP (Sudarshan et al. 2007). The degree of crystallinity of FEP is about 45% (Latorrata et al. 2015). Nafion and FEP peaks were overlapped at the diffraction pattern of powder of FEP including catalysts since corresponding Bragg angles of Nafion and FEP were very close to each other. However, as FEP weight percentage increased in the powders, the intensity of the FEP peak increased indicating the higher amount of FEP.

Determination of average diameter of Pt crystallite and total Pt surface area was described in Chapter 1.

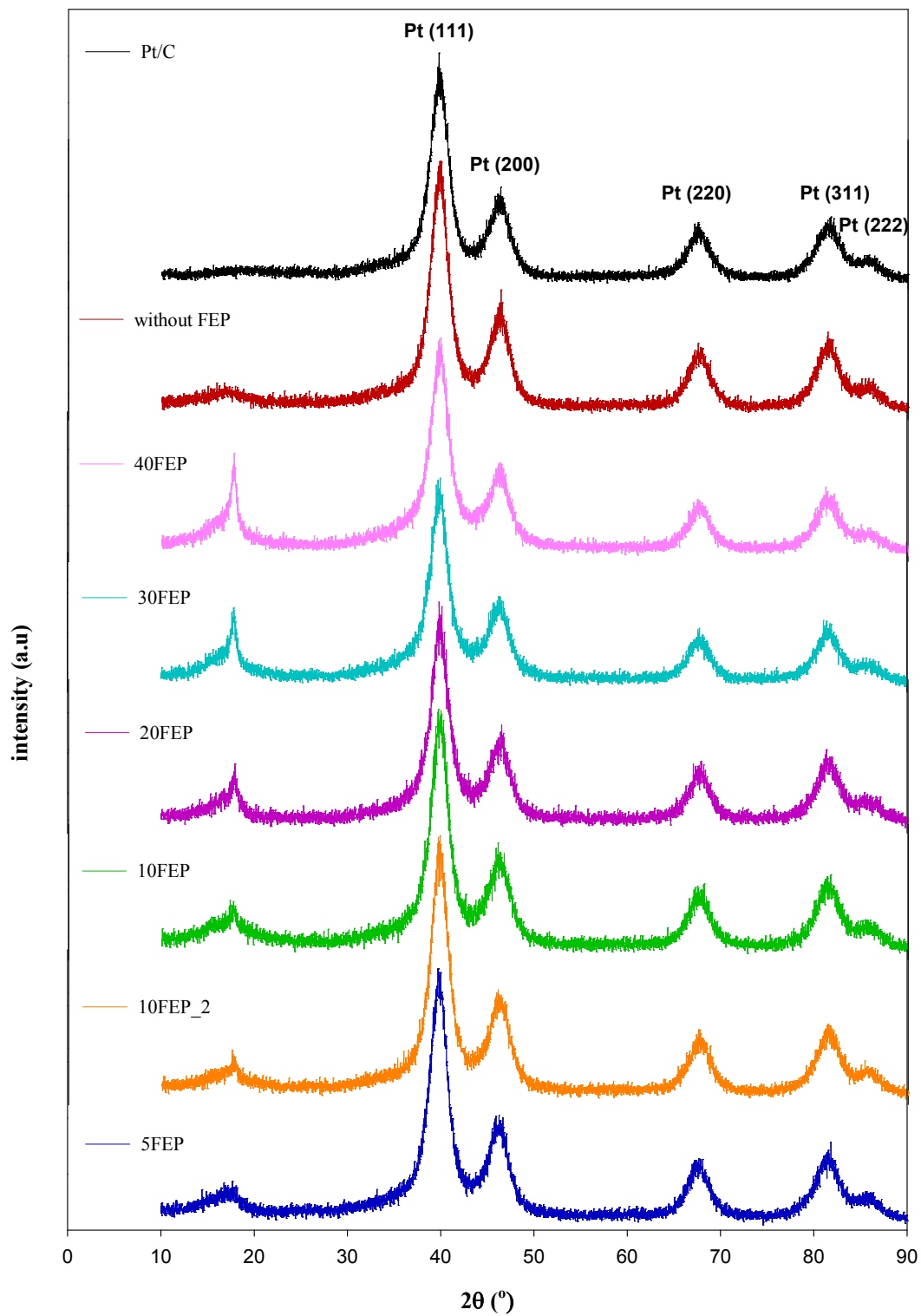


Figure 7.3 XRD patterns of powders of commercial catalyst (Pt/C), commercial catalyst impregnated with Nafion (without FEP), and commercial catalyst impregnated with different Nafion and FEP loadings

7.3.2. Cyclic Voltammetry Analysis

Figure 7.4 illustrates cyclic voltammograms of commercial catalyst (Pt/C), commercial catalyst impregnated with Nafion (without FEP); commercial catalyst impregnated with six different Nafion and FEP loadings.

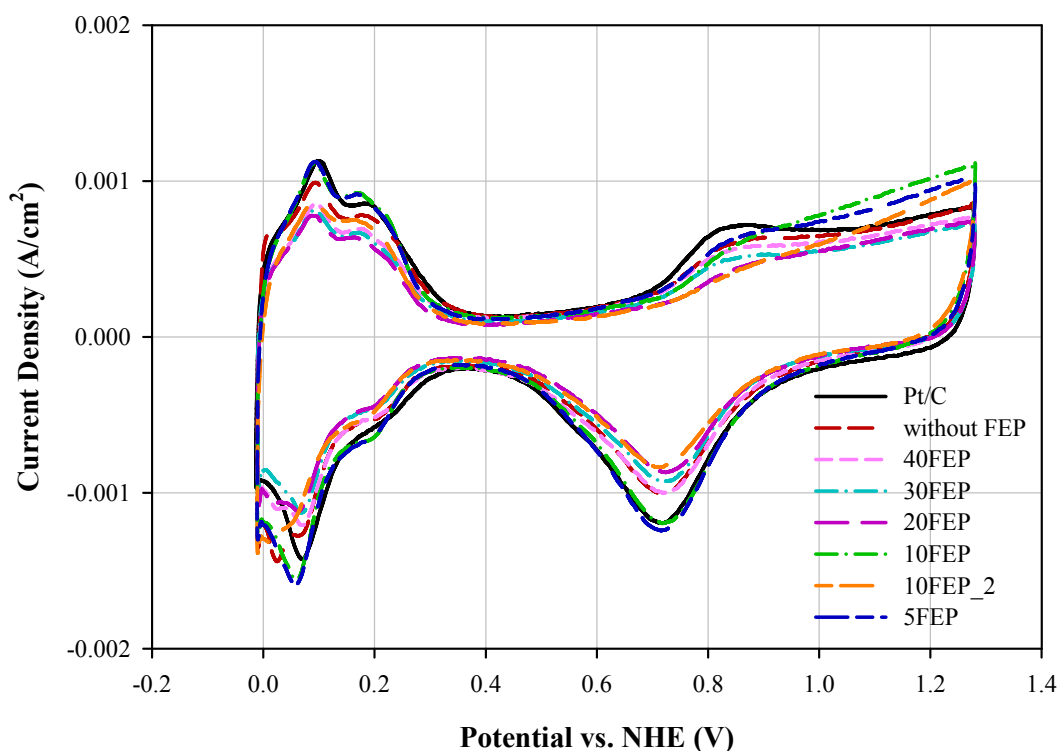


Figure 7.4 Cyclic voltammograms of commercial catalyst (Pt/C), commercial catalyst impregnated with Nafion (without FEP), and commercial catalyst impregnated with different Nafion and FEP loadings

Hydrogen adsorption/desorption peaks observed from 0.0 to 0.3 V both for the anodic and cathodic directions. Pt oxidation was observed between 0.7 and 1.2 V at the cathodic direction and Pt reduction was observed at 0.9 and 0.4 V at anodic direction.

Electrochemical surface area and Pt utilization were calculated as described in Chapter 2.

Commercial catalyst (Pt/C) had the highest electrochemical surface area (65 m²/g). This was attributed to the highest Pt content (62 wt. %) in the commercial

catalyst (Pt/C). The catalyst powders of the 5FEP (69 m²/g) and 10FEP (66 m²/g) had a slightly higher electrochemical surface area than the catalyst powder of commercial catalyst (65 m²/g). The weight percentage of Pt in the catalyst powder of 5FEP (37 wt %) was slightly higher than in the catalyst powder of 10FEP (35 wt %). This explained the higher surface area of the catalyst powder of the 5FEP. The catalyst powder of commercial catalyst impregnated with Nafion (without FEP) had higher Pt content according to 5FEP and 10FEP (43 wt %), however, its electrochemical surface area (62 m²/g) was lower than the catalyst powders of 5FEP and 10FEP. This is attributed to the difference in the catalyst preparation methods. By two-step ink preparation, electronic and ionic conduction of Pt nanoparticles of 5FEP and 10FEP enhanced. The catalyst powder of 5FEP and 10FEP had Pt utilization as 88 % and 87 %, respectively, which was higher than the Pt utilization of the commercial catalyst (83 %) and the catalyst powder without FEP (78 %). This revealed that 5 % of Pt particles were further actively in use in the electrochemical reaction in the catalyst powders of 5FEP and 10FEP.

Table 7.2 summarizes the physical characterization values; the weight ratio of Platinum to total polymer, the weight ratio of Platinum to Nafion, the weight ratio of FEP to Nafion, the weight percentage of Pt, average Pt diameter, total Pt surface, multipoint BET surface area, cumulative pore volume, the average pore diameter of catalyst powders. The maximum Pt content was obtained for the commercial catalyst (62 wt %), with the inclusion of Nafion, the weight percentage of Pt decreased to 43 wt %. As the ratio of Pt to total polymer amount in the catalyst ($X_{Pt/TP}$) increased, the thickness of the CLs increased. The thinnest CLs were attained with the catalyst powder without FEP and the catalyst powder of 10FEP_2 because $X_{Pt/TP}$ of these CLs was highest (1.5). Catalyst layers prepared with the catalyst powder of 5FEP was 21 % thicker than catalyst layers prepared with the catalyst powder without FEP and the catalyst powder of 10FEP_2. Catalyst layers prepared with the catalyst powder of 10FEP was 36 % thicker than catalyst layers prepared with the catalyst powders without FEP and catalyst powder of 10FEP_2. Furthermore, CLs prepared with the catalyst powder of 20FEP was 56 % thicker than the CLs prepared with the catalyst powder of 10FEP_2. Finally, the thickest CLs prepared with the catalyst powders of 30FEP and 40FEP was more than two fold (72 %) thicker than the CLs prepared with 10FEP_2.

Average Pt diameter of powders of commercial catalyst (Pt/C), commercial catalyst impregnated with Nafion (without FEP) were 3.5 nm, and 3.7 nm and total Pt surface area were 79 m²/g, 75 m²/g, respectively (Table 7.2). Since the ratio of Pt to total polymer in the catalyst powder was over 1.0, average Pt diameter was greater than 3.6 nm. This revealed that FEP addition to Nafion impregnated catalyst did not cause further agglomeration. Moreover, FEP addition in two steps led to the decrease in average Pt diameter of 20FEP (3.6 nm), 30FEP (3.5 nm), and 40FEP (3.4 nm). This revealed that since the Pt amount in the catalyst powder was lower, Pt agglomeration decreased.

The highest BET surface area was obtained for Pt/C was 210 m²/g. BET surface area reduced to 33 m²/g when Nafion was included to the catalyst. On the other hand, average pore diameter increased from 5.2 nm to 8.5 nm. This indicated that Nafion ionomer occupied narrower pores, which also led to a reduction in BET surface area and contributions to cumulative pore volume were mostly by larger pores. Since the catalyst powder included a higher amount of polymer coupled with the lower amount of carbon ($X_{C/(Nafion+C)} < 0.4$), the multipoint BET surface area decreased below 30 m²/g. The average pore diameter of 20FEP (4.7 nm), 30FEP (4.5 nm), 40FEP (4.7 nm) was lower than 5FEP (5.7 nm), 10FEP (7.3 nm), and 10PTFE_2 (6.6 nm). 30FEP had the lowest $X_{C/(Nafion+C)}$, which is 0.31; therefore, it had the lowest BET surface area (8 m²/g) among FEP included catalyst powders. This indicated that since the ratio of Pt to the total polymer ($X_{Pt/TP}$) was below 1.0, the $X_{C/(Nafion+C)}$ would be critical. Although, the catalyst powder without FEP and 10FEP_2 had the same $X_{Pt/TP}$ (1.5), BET surface area of 10FEP_2 (75 m²/g) was 2.5 times higher than the BET surface area of the catalyst powder without FEP (33 m²/g). This is attributed to $X_{C/(Nafion+C)}$ of 10FEP_2 because it was 23 % higher than $X_{C/(Nafion+C)}$ of the catalyst powder without FEP. The average pore volume of the catalyst powder without FEP is 8.5 nm, while the average pore volume of 10FEP_2 is 6.6 nm. This revealed that secondary pores were contributed to the cumulative pore volume of the catalyst powder without FEP (0.09 cm³/g), while primary pores were almost completely FEP (0.02 cm³/g).

Table 7.2 Physical characterization values of powders of commercial catalyst (Pt/C), commercial catalyst impregnated with Nafion (without FEP), commercial catalyst impregnated with different Nafion and FEP loadings

	Pt/C	Without FEP	5FEP	10FEP	10FEP_2	20FEP	30FEP	40FEP
$X_{\text{FEP/TP}}$	NaN	0.0	0.14	0.25	0.33	0.40	0.50	0.67
$X_{\text{C/(Nafion+C)}}$	1.0	0.44	0.42	0.40	0.54	0.35	0.31	0.40
$X_{\text{Pt/TP}}$	NaN	1.5	1.2	1.0	1.5	0.7	0.4	0.4
Pt wt % ^a	67	46	43	39	46	33	26	26
Pt wt % ^b	34	18	19	41	44	30	24	25
Pt wt % ^c	62	43	37	35	38	30	24	23
ESA ^d (m ² /g)	65	62	69	66	54	50	49	53
U _{Pt} ^d (%)	83	78	88	87	73	64	60	65
d _{Ptavg} ^e (nm)	3.5	3.7	3.6	3.7	3.7	3.6	3.5	3.4
SA _{Pt} ^e (m ² /g)	79	75	78	76	75	78	81	82
SA _{BET} ^f (m ² /g)	210	33	55	30	68	9	8	23
V _{poreCum} ^f (cm ³ /g)	0.35	0.11	0.12	0.07	0.17	0.018	0.014	0.04
V _{pporeCum} ^f (cm ³ /g)	0.16	0.02	0.04	0.03	0.05	0.007	0.004	0.01
V _{sporeCum} ^f (cm ³ /g)	0.19	0.09	0.08	0.04	0.12	0.011	0.010	0.03
dpore _{avg} ^f (nm)	5.2	8.5	5.7	7.3	6.6	4.7	4.5	4.7

^a Theoretical value

^b Determined by TGA analysis

^c Determined by ICP_MS analysis

^d Determined by CV analysis

^e Calculated from XRD data

^f Calculated from nitrogen physisorption data

In the case of 10FEP_2, the contribution of primary pores to the cumulative pore volume ($0.17 \text{ cm}^3/\text{g}$) was higher (29 %) according to the contribution of primary pores (18 %) to the cumulative pore volume of the catalyst powder without FEP. This indicated that Nafion occupied first primary pores than secondary pores in the catalyst powder. When FEP was included into the catalyst powder, the weight percentage of Nafion decreased, by this way, most of the primary pores were attained to be open. The BET surface area of 10FEP was $30 \text{ m}^2/\text{g}$, while the cumulative pore volume was $0.07 \text{ cm}^3/\text{g}$. The contribution of the primary pores to the cumulative pore volume (43%) was the highest among all FEP included catalyst powders. This revealed that since the multipoint BET surface area increased, accordingly cumulative pore volume increased until $X_{\text{FEP/Nafion}}$ was up to 0.5. When $X_{\text{FEP/Nafion}}$ exceeded 0.5, in the meanwhile, the $X_{\text{C/Nafion}}$ decreased below 0.7 and $X_{\text{Pt/TP}}$ decreased below 1.0, this led to a significant decrease in multipoint BET surface area. That is why; 30FEP had the lowest $X_{\text{C/Nafion}}$ (0.4), which revealed the lowest multipoint BET surface area ($8 \text{ m}^2/\text{g}$). This indicated that FEP addition to catalyst powder was encouraging until FEP amount does not exceed the half of the Nafion amount since $X_{\text{Pt/TP}}$ was above 1.0. The cumulative pore volume of 20FEP ($9 \text{ m}^2/\text{g}$), 30FEP ($8 \text{ m}^2/\text{g}$), 40FEP ($23 \text{ m}^2/\text{g}$) was lower than 5FEP ($44 \text{ m}^2/\text{g}$), 10FEP ($57 \text{ m}^2/\text{g}$), and 10FEP_2 ($75 \text{ m}^2/\text{g}$), because, most of the pores of 20FEP, 30FEP, 40FEP were occupied with polymer. Therefore, a higher amount of polymer in the catalyst powders of 20FEP, 30FEP, and 40FEP caused a decrease in electrochemical surface area, which was $64 \text{ m}^2/\text{g}$, $60 \text{ m}^2/\text{g}$, and $65 \text{ m}^2/\text{g}$, respectively.

7.3.3. TEM Analysis

TEM images of powders of commercial catalyst (Pt/C), commercial catalyst impregnated with Nafion (without FEP), and commercial catalyst impregnated with different Nafion and FEP loadings are shown in Figure 7.5. The image of the commercial catalyst is shown in Figure 7.5a. Black dots correspond to the dispersed Pt particles on gray carbon spheres. The red arrow on the image of catalyst powder without FEP (Figure 7.5b) indicates the agglomerated Pt particles on Nafion ionomer. The red arrow on the images of 5FEP (Figure 7.5c), 10FEP (Figure 7.5d), and 10FEP_2 (Figure 7.5e) show the empty surfaces where Pt particles cannot place on consisting of FEP nanoparticles. In addition to Pt agglomeration, Pt particles with

the smaller diameter can be detected from the image of 20FEP (Figure 7.5f), 30FEP (Figure 7.5g), and 40FEP (Figure 7.5h).

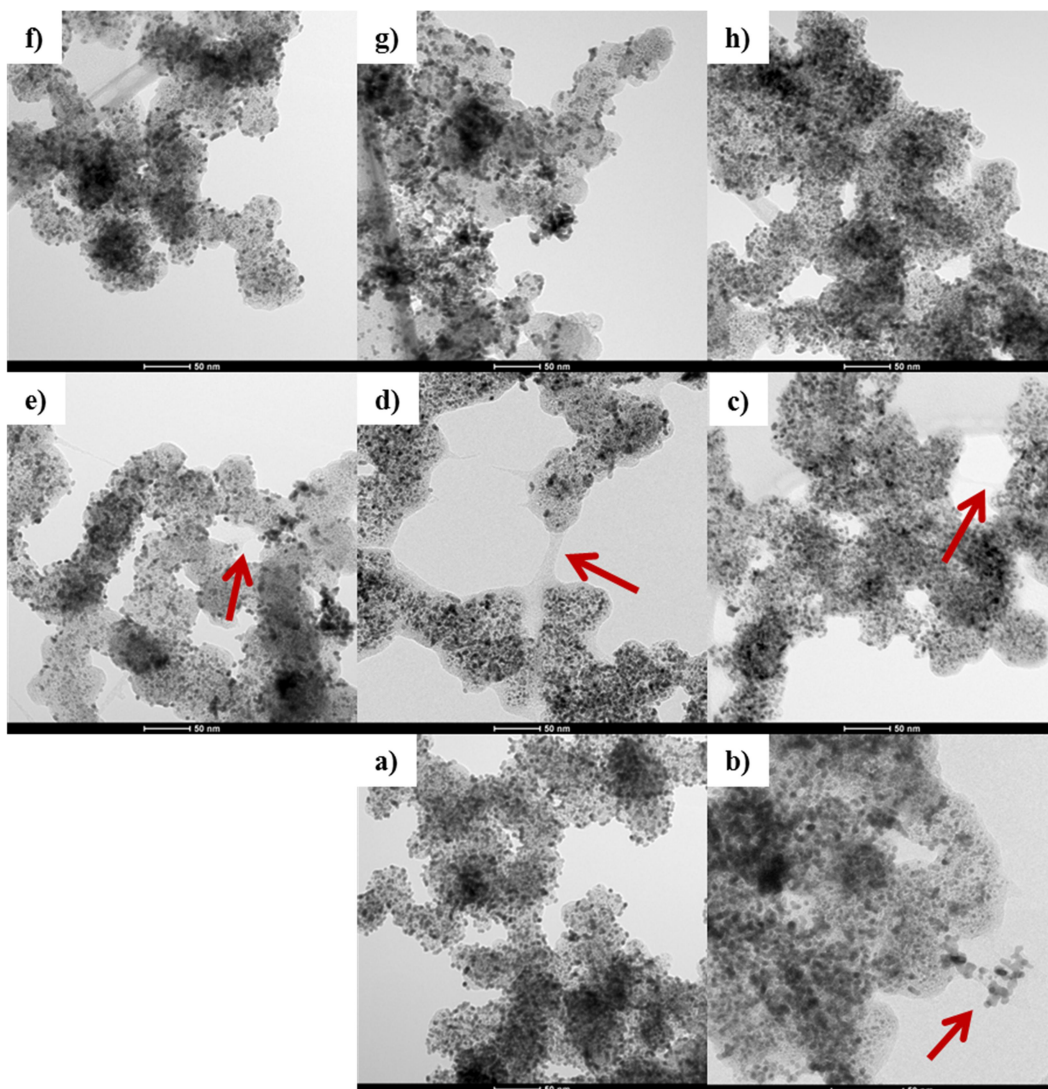


Figure 7.5 TEM images of powders of a)Pt/C, b) without FEP, c) 5FEP, d) 10FEP, e) 10FEP_2, f) 20FEP, g) 30FEP, h) 40FEP

7.3.4. SEM Analysis of Catalyst Powder

SEM images of powders of commercial catalyst (Pt/C), commercial catalyst impregnated with Nafion (without FEP), and commercial catalyst impregnated with different Nafion and FEP loadings are shown in Figure 7.6.

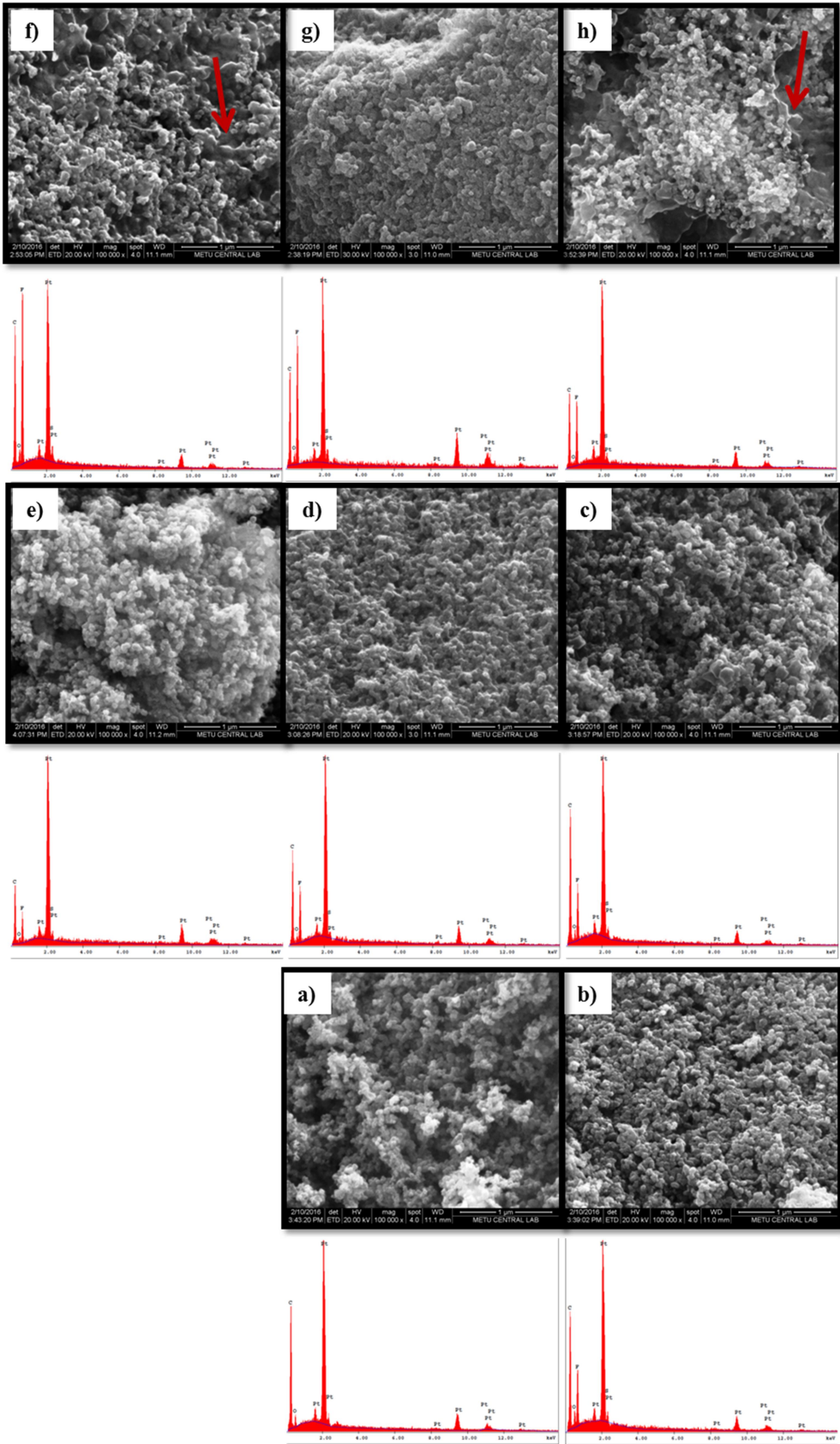


Figure 7.6 SEM images of powders of a) Pt/C, b) without FEP, c) 5FEP, d) 10FEP, e) 10FEP_2, f) 20FEP, g) 30FEP, h) 40FEP

The Pt particles in the commercial catalyst (Pt/C) were the smallest considering commercial catalyst impregnated with different Nafion (without FEP) and FEP loadings (Figure 7.6). Catalyst agglomeration occurred with Nafion addition to Pt/C catalyst was clearly observed when Figure 7.6a and Figure 7.6b is compared. Decline in the void spaces of the commercial catalyst when impregnated with Nafion and FEP inclusion was also examined from Figure 7.6b. The red arrow on the images of 20FEP (Figure 7.6f) and 40FEP (Figure 7.6h), points out the structural changes when FEP nanoparticles added to the commercial catalyst. FEP nanoparticles caused agglomeration by covering Pt particles. The geometry of the newly-formed agglomerates was similar to the sphere as like Pt particles. EDX results represented the relative amount of the chemical compounds in the catalyst powders. For commercial catalyst (Pt/C), Pt, carbon, and oxygen peaks appeared in the EDX results (Figure 7.6a); while fluoride and sulfur peaks appeared in addition to Pt, carbon, and oxygen peaks for catalyst powders including the different amount of Nafion and FEP. Since FEP amount in the catalyst powders increased, the intensity of Fluorine peak increased (20FEP, 30FEP, and 40FEP).

7.3.5. Effect of FEP Loading on Performance and Running Electrochemical Impedance Spectrum of PEMFC at H₂/O₂ Gas-feeding Mode

FEP Loaded Catalyst Layers on Both Electrodes (MEA1):

Polarization and power density curves for CLs with six different Nafion and FEP loadings, working at H₂/O₂ gas-feeding mode are shown in Figure 7.7. The performances of FEP loaded CLs were compared with CLs without FEP. The maximum power density at 0.45 V was 1.27 W/cm² for the CLs without FEP. 5FEP_AC and 10FEP_2_AC had closer performances to CLs without FEP with the power densities of 1.08 W/cm² and 1.03 W/cm² at 0.45 V, respectively. This is attributed to the similar $X_{Pt/TP}$ of 5FEP_AC (1.2) and $X_{Pt/TP}$ of 10FEP_2_AC (1.5) to $X_{Pt/TP}$ of catalyst powder without FEP (1.5). The similarity in $X_{Pt/TP}$ designated the thickness of the CLs similar. 5FEP_AC had 20 % thicker CLs than the CLs without FEP and the CLs of 10FEP_2_AC.

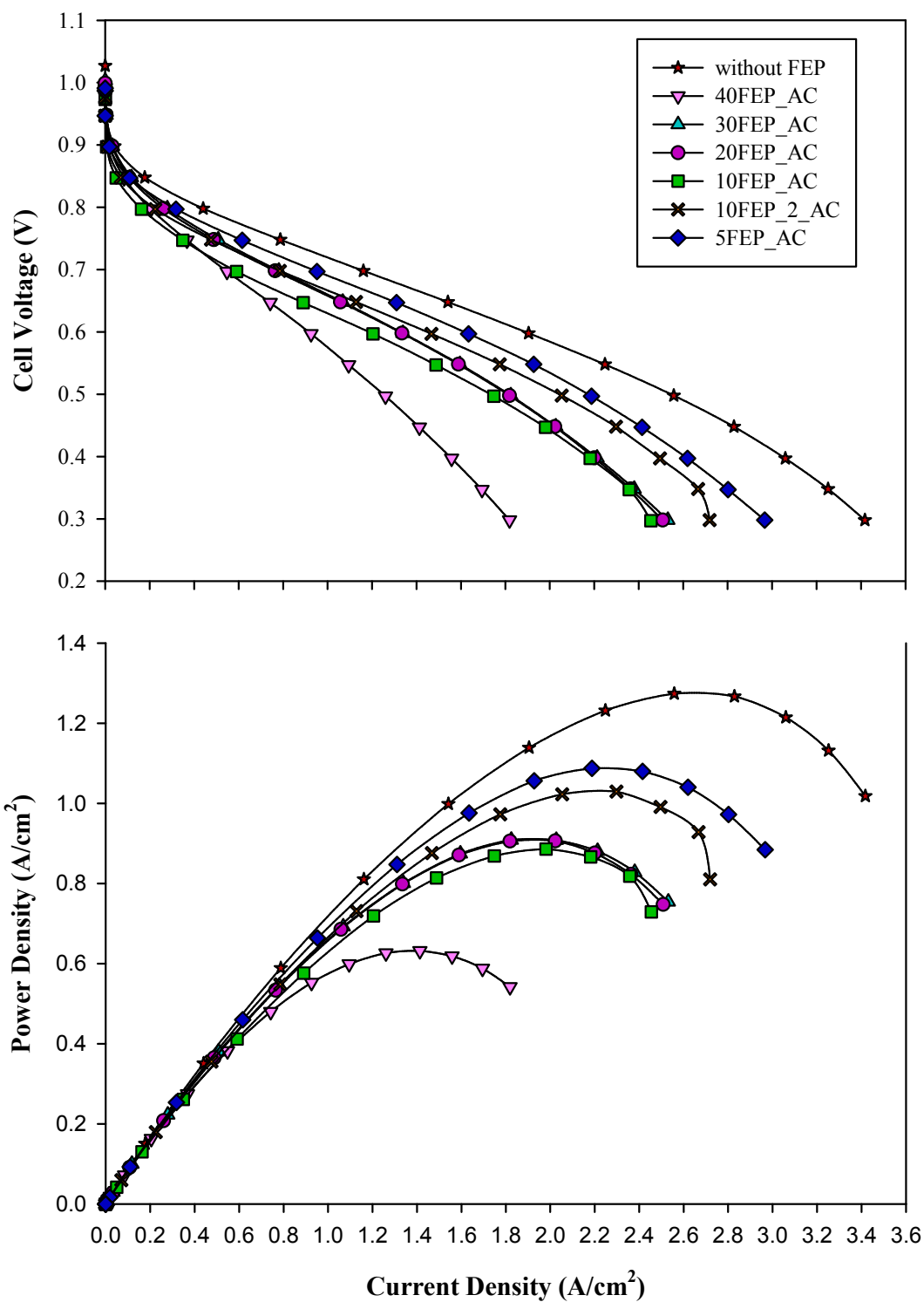


Figure 7.7 Polarization and power density curves of PEMFC for MEA1. Pt loading of anode and cathode electrodes was $0.4 \text{ mgPt}/\text{cm}^2$. Both anode and cathode catalyst layers were coated with FEP nanoparticles. H_2/O_2 gas-feeding mode was used

When we look at Figure 7.7, we can observe that 10FEP_2_AC had a flattened slope at the ohmic region indicating lower ohmic resistance than 5FEP_AC. This made 5FEP_AC more prone to flooding. However, FEP amount in the CLs of 5FEP_AC ($X_{\text{FEP/TP}} = 0.14$) was lower than 10FEP_2_AC ($X_{\text{FEP/TP}} = 0.33$). Although 10FEP_2_AC demonstrated lower ohmic resistance, higher Pt utilization of 5FEP_AC (87 %) assured enhanced performance. The power density of 20FEP_AC, and 30FEP_AC at 0.45V was 0.91 W/cm². Similarly, 10FEP_AC had a power density of 0.89 W/cm². Although 20FEP_AC ($X_{\text{Pt/TP}} = 0.7$) and 30FEP_AC ($X_{\text{Pt/TP}} = 0.4$) had thicker CLs, which influence gas transport negatively, they had similar performance to 10FEP_AC ($X_{\text{Pt/TP}} = 1.0$). This revealed that the FEP amount of 10FEP_AC ($X_{\text{FEP/TP}} = 0.25$) was not sufficient to mitigate flooding in the pores of the CLs. On the other hand, when we look at Figure 7.7, we can see that the ohmic resistance of 10FEP_AC was lower than 20FEP_AC and 30FEP_AC, while mass transport losses were higher than 20FEP_AC and 30FEP_AC. This is also attributed the $X_{\text{FEP/TP}}$ ratio. The $X_{\text{FEP/TP}}$ of 20FEP_AC was 0.4 while it was 0.25 for 10FEP_AC. On the other hand, 30FEP_AC had $X_{\text{FEP/TP}}$ of 0.5. When the amount FEP nanoparticles in the CL of were lower, this improved ionic conduction. Moreover, FEP nanoparticles in the CLs of 10FEP_AC ($X_{\text{Pt/TP}} = 1.0$) was not sufficient to mitigate water saturation. On the other hand, although 30FEP_AC had lower $X_{\text{Pt/TP}}$ (0.4) than 20FEP_AC (0.7), which cause thicker CLs, and then higher mass transport limitations, 30FEP_AC had similar performance to 20FEP_AC. In addition to that, had higher than 20FEP_AC (0.7). This revealed that the higher amount of FEP in the CLs of 30FEP_AC ($X_{\text{FEP/TP}}$ of 0.5) provided enhanced water management leading to higher performance. The power density of 40FEP_AC (0.63 W/cm²) was lower than 30FEP_AC (0.91 W/cm²) although their $X_{\text{Pt/TP}}$ was the same (0.4). The reduction in the cell performance of 40FEP_AC is attributed to higher FEP amount in the CLs. Although 30FEP_AC and 40FEP_AC consist of the same amount of polymer, $X_{\text{FEP/TP}}$ of 40FEP_AC (0.5) was 34 % higher than 30FEP_AC (0.50). The higher amount of FEP did not influence the cumulative pore volume negatively, because the cumulative pore volume of the catalyst powder of 30FEP_AC was 0.014 cm³/g, while it was 0.04 cm³/g for the catalyst powder of 40FEP_AC. However, the excess amount of FEP settled on the electronic and ionic network, which caused a reduction in the triple phase boundaries. If we look at

Figure 7.7, we can observe that the highest ohmic resistance was attained for 40FEP_AC, which led to a reduction in the cell performance.

Figure 7.8 illustrates EIS spectra of MEA1 measured at 0.5 V. Thin film diffusion has a preponderant effect on mass transport at this voltage (Ciureanu & Roberge 2001). Except for 10FEP_AC, all CLs demonstrated an impedance spectrum with a high-frequency arc followed by a low-frequency arc. Parameters of equivalent circuit modeling of EIS spectra for MEA1 are listed in Table 7.3. All of the MEAs demonstrated similar high-frequency resistances except 40FEP_AC. The higher amount of FEP nanoparticles in the aCL of 40FEP_AC prevent the introduction of H₂ gas humidified with water vapor, therefore membrane dehydrated.

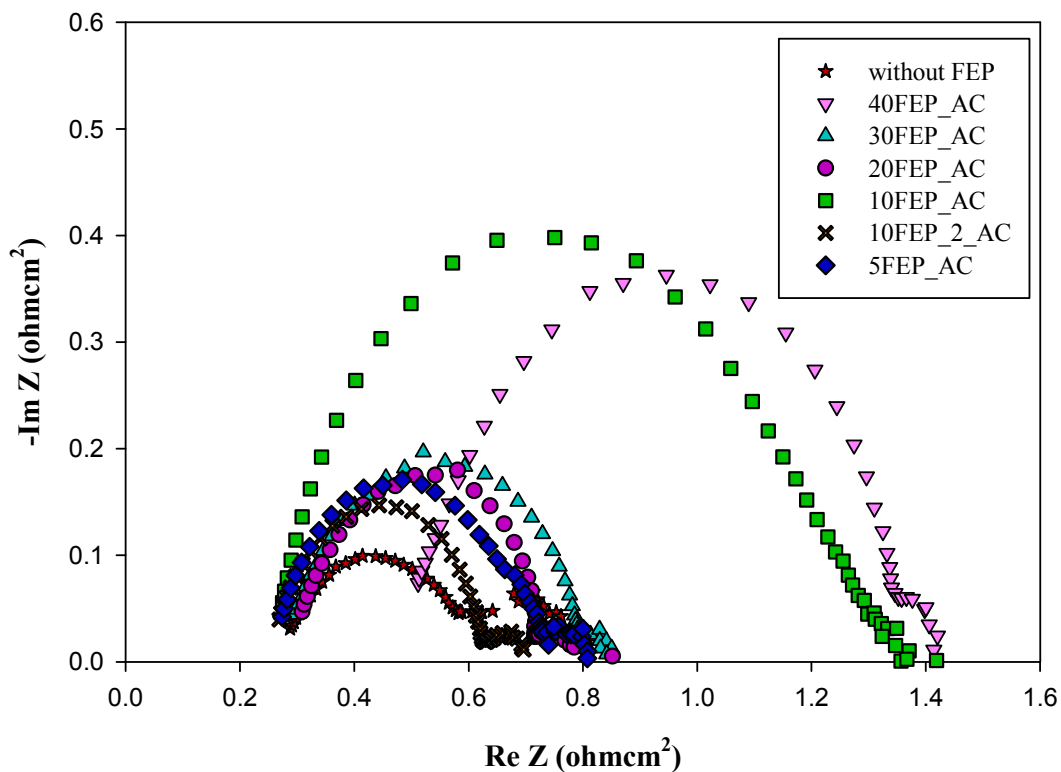


Figure 7.8 Electrochemical impedance spectra obtained for a running fuel cell at 0.5 V. Pt loading of anode and cathode electrodes was 0.4 mgPt/cm². Both anode and cathode catalyst layers were coated with FEP nanoparticles. H₂/O₂ gas-feeding mode was used

The highest charge transfer resistance ($1.15 \Omega\text{cm}^2$) was obtained for 10FEP_AC. FEP amount in the CLs of 10FEP_AC could not mitigate flooding in the CL; however, pore blockage due to higher water saturation diminished in the cGDL. This means that water removal rate from the cGDL was not sufficient to decrease the water saturation in the secondary pores, but the removal rate was sufficient to provide a funicular regime of water flow, which decreased the water saturation in the pores of cGDL. 40FEP_AC had also higher charge transfer resistance ($0.88 \Omega\text{cm}^2$), which is closer to 10FEP_AC. The reason for the higher charge transfer resistance of 40FEP_AC is related to higher FEP amount in the CLs, which caused disruption of the electronic and ionomer network. The reason for the mass transfer resistance at cGDL of 40FEP_AC is the unconnected water molecules spread over the pores, which blocked the gas access. The capillary flow of water from CLs towards cGDL could not be provided. The charge transfer resistance of 10FEP_2_AC ($0.37 \Omega\text{cm}^2$) was closer to the charge transfer resistance of the CLs without FEP ($0.33 \Omega\text{cm}^2$). The Pt utilization of the powders of these two CLs was 75 %. However, the Nafion coverage of 10FEP_2_AC ($X_{C/(\text{Nafion}+\text{C})}=0.54$) was lower than the CLs without FEP ($X_{C/(\text{Nafion}+\text{C})}=0.44$). This caused a decrease in ionic conduction.

Table 7.3 Parameters of equivalent circuit modeling of EIS spectra of MEA1 at H_2/O_2 gas-feeding mode

MEA Type	O_2			
	$R_{\text{HF}} (\Omega\text{cm}^2)$	$R_{\text{ct}} (\text{A})(\Omega\text{cm}^2)$	$R_{\text{ct}} (\text{C})(\Omega\text{cm}^2)$	$R_{\text{mt}} (\Omega\text{cm}^2)$
without FEP MEA1	0.26	0.11	0.22	0.17
40FEP_AC	0.48	0.07	0.81	0.07
30FEP_AC	0.28	0.07	0.53	0.04
20FEP_AC	0.29	0.14	0.30	0.14
10FEP_AC	0.25	0.78	0.37	-
10FEP_2_AC	0.25	0.04	0.33	0.08
5FEP_AC	0.26	0.20	0.30	0.06

Although reduced Nafion coverage 10FEP_2_AC had closer charge transfer resistance to the CLs without FEP. This revealed the improved water management.

Although 5FEP_AC had higher charge transfer resistance ($0.50 \text{ } \Omega\text{cm}^2$) than 10FEP_2_AC, it demonstrated higher cell performance. This is attributed to the higher Pt utilization (88 %) of 5FEP_AC than 10FEP_2_AC (73%). The increased charge transfer resistance of 5FEP_AC is attributed to the increased volume of the product water that increased water saturation around the aggregates. 30FEP_AC had higher charge transfer resistance ($0.60 \text{ } \Omega\text{cm}^2$) than the 20FEP_AC ($0.44 \text{ } \Omega\text{cm}^2$). This is attributed to the lower Pt utilization of 30FEP_AC (60 %).

FEP Loaded Catalyst Layer on Cathode Electrode (MEA2):

Polarization and power density curves for cathode CLs with six different FEP loadings, working at H_2/O_2 gas-feeding mode are shown in Figure 7.9. The maximum power density at 0.45 V was 1.27 W/cm^2 for CLs without FEP. 5FEP_C (1.11 W/cm^2) had the closer performance to CLs without FEP at 0.45 V. This is attributed to having the similar $X_{\text{Pt/TP}}$, which is 1.2 for 5FEP_C, while it is 1.5 for the CLs without FEP. The cCL of the 5FEP_C ($X_{\text{FEP/TP}}=0.14$) was 17 % thinner than the cCL of 10FEP_C ($X_{\text{FEP/TP}}=0.25$). However, FEP amount of 10FEP_C was 79 % higher than the FEP amount in the cCL of 5FEP_C. The higher amount of FEP nanoparticles in the cCL of 10FEP_C was not sufficient to mitigate flooding. This is interpreted as the cCL without FEP was least prone to mass transport limitations, while cCL of 5FEP_C was less prone to flooding than the 10FEP_C. This revealed that thinner cCL required fewer amounts of FEP nanoparticles to manage water movement. Consequently, 5FEP_C demonstrated higher cell performance than 10FEP_C (1.01 W/cm^2). However, 10FEP_2_C included thinner cCL than 5FEP_C and 10FEP_C, its performance was lower than both the cathode CLs of 5FEP_C and 10FEP_C. This is attributed to the higher amount of FEP ($X_{\text{FEP/TP}}=0.33$), because for such a thin cCL, a higher amount of FEP nanoparticles caused a decrease in Pt utilization (73 %). In addition, FEP nanoparticles cover Pt particles and decrease the activity of the cCL; therefore, for the thin cCLs, the higher amount of FEP nanoparticles influences the performance negatively.

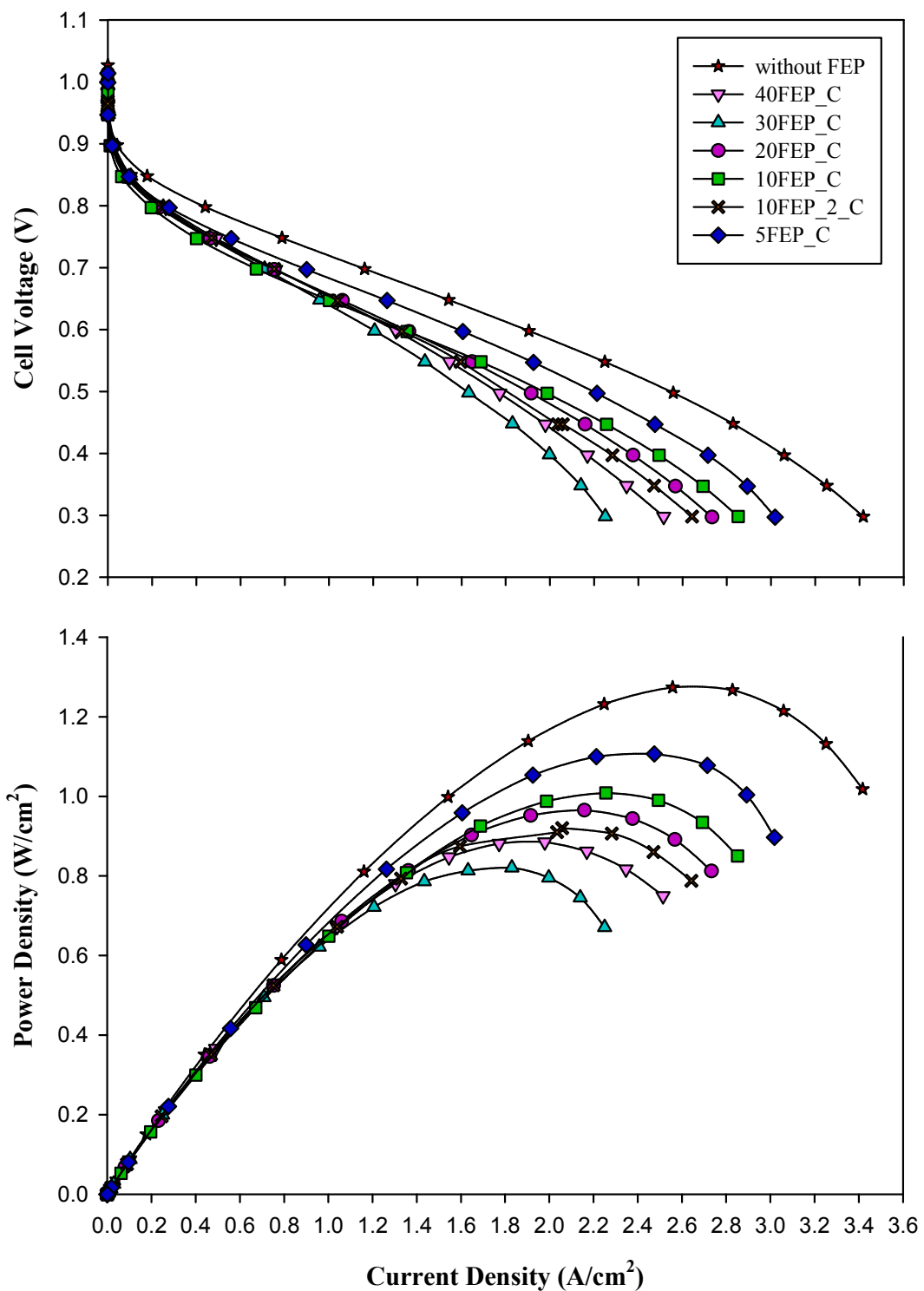


Figure 7.9 Polarization and power density curves of PEMFC for MEA2. Pt loading of anode and cathode electrodes was $0.4 \text{ mgPt}/\text{cm}^2$. Cathode catalyst layer was coated with FEP nanoparticles. PEMFC was operated at H_2/O_2 gas feeding mode

Although cCL of 20FEP_C (0.97 W/cm^2) was 54 % thicker than the cCL of 10FEP_2_C (0.92 W/cm^2), it demonstrated higher performance than 10FEP_2_C. This is because for a thicker cCL ($X_{\text{Pt/TP}}=0.7$) higher amount of FEP nanoparticles ($X_{\text{FEP/TP}}=0.4$) facilitated excess water removal. Moreover, 40FEP_C (0.89 W/cm^2) demonstrated higher power density than 30FEP_C (0.82 W/cm^2) although 40FEP_C ($X_{\text{Pt/TP}}=0.4$) had the same thickness of cCL with 30FEP_C ($X_{\text{Pt/TP}}=0.4$). In addition to 40FEP_C had higher FEP amount ($X_{\text{FEP/TP}}=0.67$) than 30FEP_C ($X_{\text{FEP/TP}}=0.5$). This revealed that higher FEP amount provided enhanced water management for the thicker cCL. On the other hand, the hydrophobicity of the cCL of 30FEP_C was not sufficient to mitigate flooding.

Figure 7.10 illustrates EIS spectra of MEA1 measured at 0.5 V. Except 10FEP_C, all CLs demonstrated an impedance spectrum with a high-frequency arc followed by a low-frequency arc. Parameters of equivalent circuit modeling of EIS spectra for MEA1 are listed in Table 7.4. All of the MEAs demonstrated similar high-frequency resistances. The highest charge transfer resistance ($1.09 \Omega\text{cm}^2$) was obtained for 10FEP_C. FEP amount in the CLs of 10FEP_C could not mitigate flooding in the CL; however pore blockages due to higher water saturation diminished in the cGDL similar to the result attained at H_2/O_2 feeding mode. This means that water removal rate from the cGDL was not sufficient to decrease the water saturation in the secondary pores, but the removal rate was sufficient to provide a funicular regime of water flow, which decreased the water saturation in the pores of cGDL at both feeding modes. Although 10FEP_2_C demonstrated lower charge transfer resistance ($0.61 \Omega\text{cm}^2$) than 10FEP_C ($1.09 \Omega\text{cm}^2$), 10FEP_C had higher performance than 10FEP_2_C, because the Pt utilization of 10FEP_C (73 %) was higher than 10FEP_2_C (87 %). On the other hand, mass transport limitation for gas transport was diminished in the cGDL of 10FEP_C, while 10FEP_2_C had high mass transfer resistance ($0.12 \Omega\text{cm}^2$) because of the blocked pores with liquid water. The charge transfer resistances of 30FEP_C and 40FEP_C were $0.68 \Omega\text{cm}^2$ and $0.53 \Omega\text{cm}^2$, respectively. Although 40FEP_C and 30FEP_C had the same thickness of the cCL, 30FEP_C demonstrated higher charge transfer resistance. This is related to lower Pt utilization of the powder of 30FEP_C (60 %) with respect to the catalyst powder of 40FEP_C (65 %). This means that the higher FEP amount in the CLs

40FEP_C ($X_{\text{FEP/TP}}=0.67$) provided enhanced water management compared to 30FEP_C ($X_{\text{FEP/TP}}=0.50$).

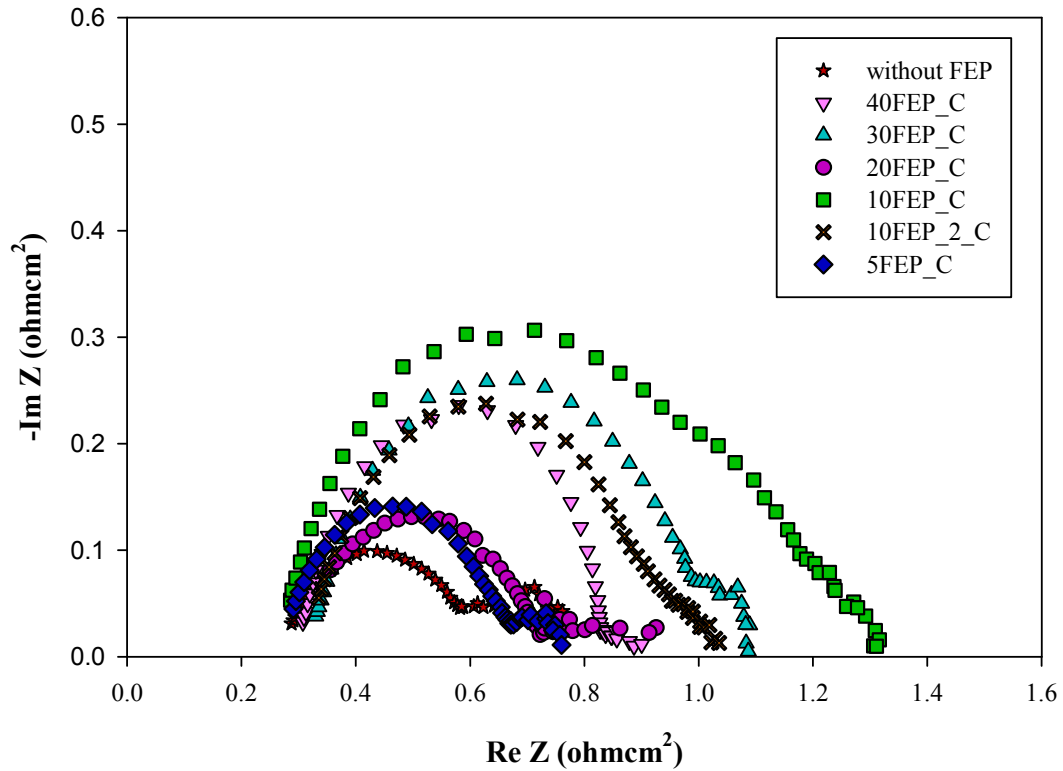


Figure 7.10 Electrochemical impedance spectra obtained at 0.5 V. Pt loading of anode and cathode electrodes was 0.4 mgPt/cm^2 . Cathode catalyst layer was coated with FEP nanoparticles. PEMFC was operated at H_2/O_2 gas-feeding mode

The enhancement of water management was also observed from the comparison of the cell performances. 40FEP_C demonstrated higher performance than 30FEP_C. The lowest charge transfer resistances were obtained for 5FEP_C ($0.40 \text{ } \Omega\text{cm}^2$) and 20FEP_C ($0.46 \text{ } \Omega\text{cm}^2$). The lower charge transfer resistances provided enhanced cell performance for 5FEP_C and 20FEP_C. The cCL of 20FEP_C was 42 % thicker than the cCL of 5FEP_C, while the FEP amount in the cCL of 20FEP_C ($X_{\text{FEP/TP}}=0.40$) was almost three times higher than in the cCL of 5FEP_C ($X_{\text{FEP/TP}}=0.14$). Increased amount of FEP nanoparticles in thicker cCL of 20FEP_C enhanced the performance.

Table 7.4 Parameters of equivalent circuit modeling of EIS spectra of MEA2 at H₂/O₂ gas-feeding mode

MEA Type	O ₂			
	R _{HF} (Ωcm ²)	R _{ct} (A)(Ωcm ²)	R _{ct} (C)(Ωcm ²)	R _{mt} (Ωcm ²)
without FEP MEA2	0.26	0.11	0.22	0.17
40FEP_C	0.29	0.08	0.45	0.09
30FEP_C	0.32	0.09	0.59	0.09
20FEP_C	0.28	-	0.46	0.11
10FEP_C	0.26	0.54	0.55	-
10FEP_2_C	0.32	0.01	0.60	0.12
5FEP_C	0.26	0.09	0.31	0.10

7.3.6. Effect of FEP Loading on Performance and Running Electrochemical Impedance Spectrum of PEMFC at H₂/Air Gas-feeding Mode

FEP Loaded Catalyst Layer on Both Electrodes (MEA1):

Polarization and power density curves for CLs with six different Nafion and FEP loadings, working at H₂/Air gas-feeding mode are shown in Figure 7.11. The performances of FEP loaded CLs were compared with the CLs without FEP. The maximum power density at 0.45 V was 0.64 W/cm² for the CLs without FEP. 5FEP_AC demonstrated closer performance to the CLs without FEP with the power densities of 0.47 W/cm². This is attributed to the low amount of FEP (X_{FEP/TP}=0.14) included into the 20 % thicker CLs of the 5FEP_AC (X_{PV/TP}=1.2), which made 5FEP_AC favorable than other FEP included CLs. 10FEP_2_AC demonstrated closer performance to 5FEP_AC with a power density of 1.03 W/cm² at 0.45 V. Although 10FEP_2_AC had 20 % thinner CL (X_{PV/TP}=1.5) than 5FEP_AC, which made it less prone to flooding, 10FEP_2_AC demonstrated lower performance. This attributed to the difference in the FEP amounts in the CLs. 10FEP_2_AC (X_{FEP/TP}=0.33) included higher amount of FEP compared to the CLs of 5FEP_AC (X_{FEP/TP}=0.14).

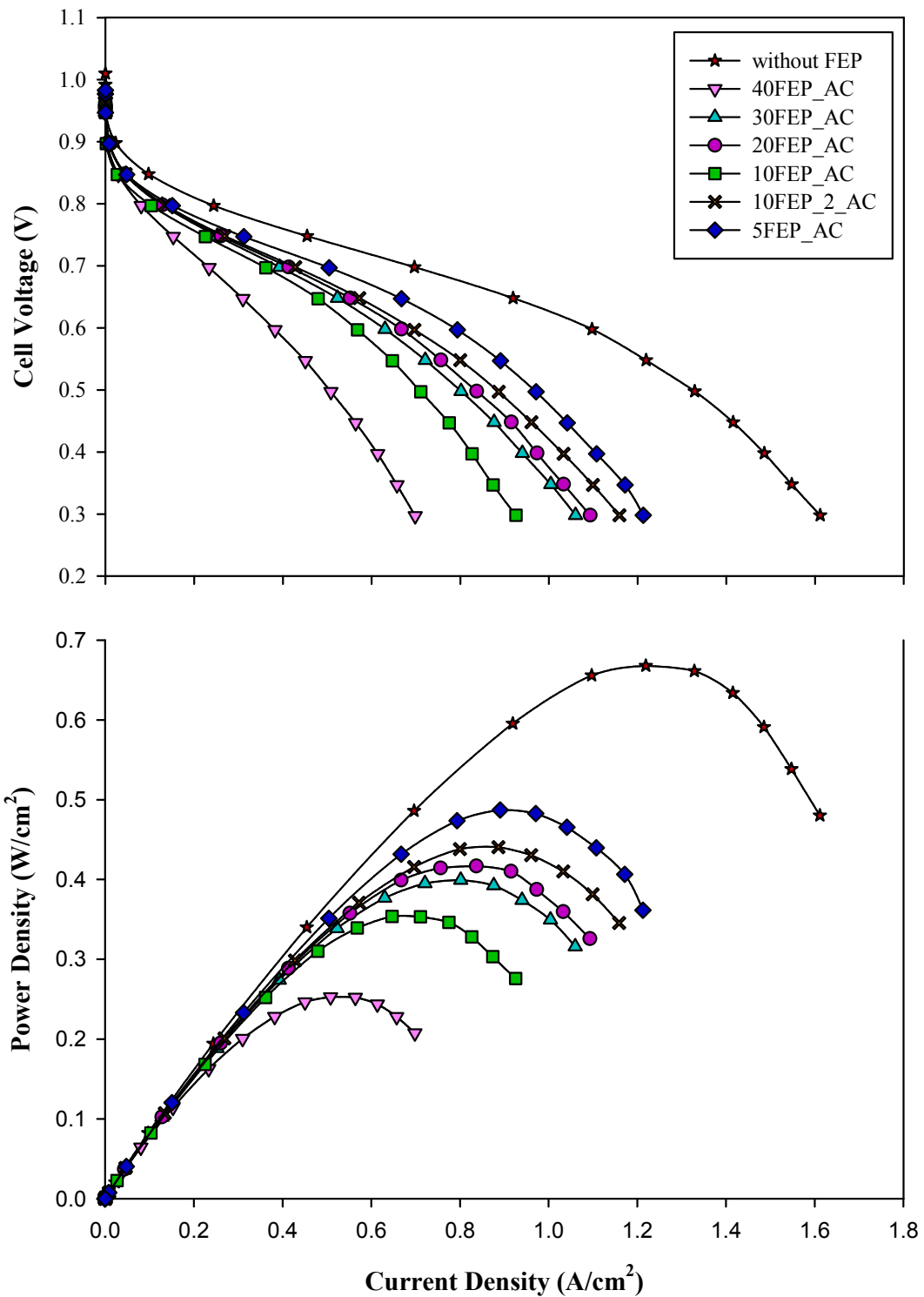


Figure 7.11 Polarization and power density curves of PEMFC for MEA1. Pt loading of anode and cathode electrodes was $0.4 \text{ mgPt}/\text{cm}^2$. Both anode and cathode catalyst layers were coated with FEP nanoparticles. PEMFC was operated at H_2 /Air gas-feeding mode

This revealed that higher amount of FEP in the CLs of 10FEP_2_AC served for decreasing catalytic activity than managing water movement. Therefore, the performance of 10FEP_2_AC was lower than the performance of 5FEP_AC. The similarity in $X_{Pt/TP}$ designated the thickness of the CLs similar. 5FEP_AC had 20 % thicker CLs than the CLs without FEP and 10FEP_2_AC. This made 5FEP_AC more prone to flooding. However, FEP amount in the CLs of 5FEP_AC ($X_{FEP/TP}=0.14$) was lower than 10FEP_2_AC ($X_{FEP/TP}=0.33$). This made the CLs of 5FEP_AC more active than 10FEP_2_AC. The Pt utilization of the catalyst powder of 5FEP_AC was higher (78 %) than 10FEP_2_AC (75 %). Although 10FEP_2_AC demonstrated lower ohmic resistance, higher activity of 5FEP_AC assured enhanced performance. The power densities of 20FEP_AC (0.41 W/cm^2), and 30FEP_AC (0.39 W/cm^2) at 0.45V was close to the power density of 10FEP_2_AC. Although 20FEP_AC ($X_{Pt/TP}=0.7$) and 30FEP_AC ($X_{Pt/TP}=0.4$) had thicker CLs, which influence gas transport negatively, they had similar performance to 10FEP_2_AC. This is attributed the $X_{FEP/Nafion}$ ratio. The $X_{FEP/Nafion}$ of 20FEP_AC was 0.7 while it was 1.0 for 30FEP_AC. As the CL thickness increased, the increase in the FEP amount was favorable for enhanced water management. Therefore, the performances of 20FEP_AC and 30FEP_AC were similar to but slightly lower than the performance of 10FEP_2_AC. In addition to that despite having thinner CLs ($X_{Pt/TP}=1.0$) with lower FEP amount ($X_{FEP/TP}=0.25$), 10FEP_AC demonstrated lower performance than 20FEP_AC and 30FEP_AC. This revealed that including the lower amount of FEP nanoparticles in the thicker CLs compared to 5FEP_AC and 10FEP_2_AC could not compensate the water movements in the case of high airflow rate. The power density of 40FEP_AC (0.25 W/cm^2) was lower than 30FEP_AC (0.39 W/cm^2) although their $X_{Pt/TP}$ was the same (0.4). The reduction in the cell performance of 40FEP_AC is attributed to higher FEP amount in the CLs. Although 30FEP_AC and 40FEP_AC consist of the same amount of polymer, $X_{FEP/TP}$ of 40FEP_AC was 34 % higher than 30FEP_AC (0.5). The excess amount of FEP was settled on the electronic and ionic network, which caused a reduction in the triple phase boundaries. If we look at Figure 7.11, we can observe that the highest ohmic resistance attained for 40FEP_AC, which led to a reduction in the cell performance.

Figure 7.12 illustrates EIS spectra of MEA1 measured at 0.5 V. Except 10FEP_C, all CLs demonstrated an impedance spectrum with a high-frequency.

Parameters of equivalent circuit modeling of EIS spectra for MEA1 are listed in Table 7.5. All of the MEAs demonstrated similar high-frequency resistances except 40FEP_AC. The higher amount of FEP nanoparticles in the aCL of 40FEP_AC prevent the introduction of H₂ gas humidified with water vapor, therefore membrane dehydrated.

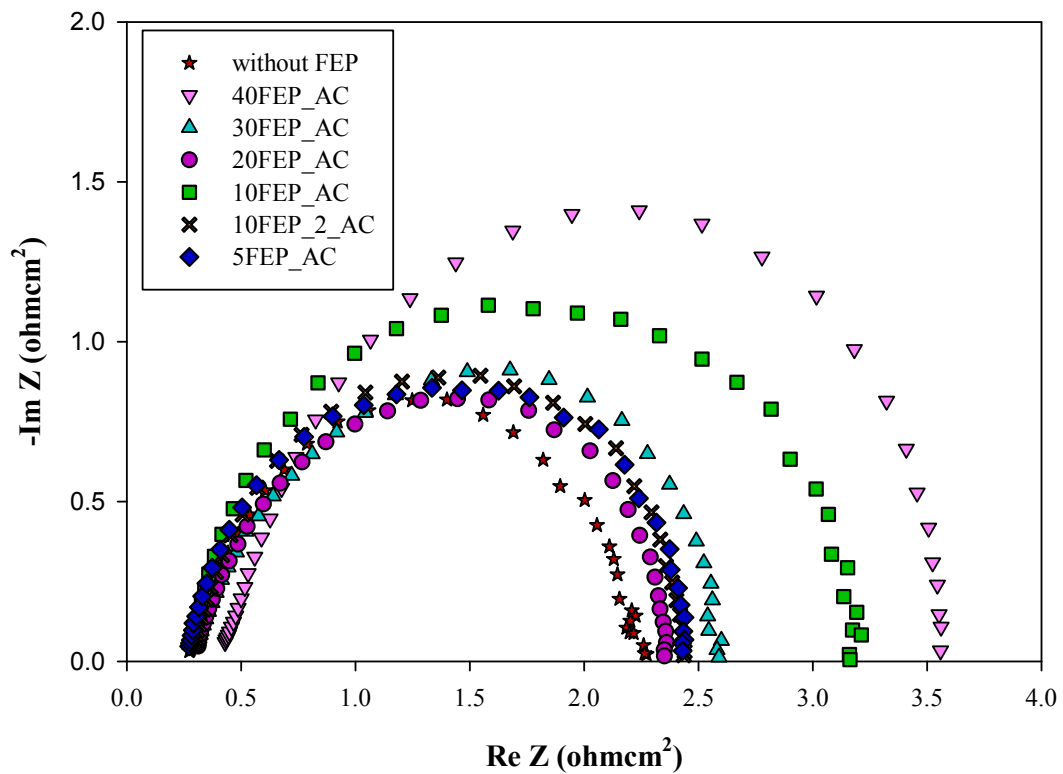


Figure 7.12 Electrochemical impedance spectra obtained for a running fuel cell at 0.5 V. Pt loading of anode and cathode electrodes was 0.4 mgPt/cm². Both anode and cathode catalyst layers were coated with FEP nanoparticles. PEMFC was operated at H₂/Air gas-feeding mode.

The highest charge transfer resistance (3.11 Ωcm²) was obtained for 40FEP_AC. FEP amount in the CLs of 40FEP_AC decreased the Pt utilization to 65 % with respect to the CLs without FEP (75 %). The decrease in the ionic and electronic conduction increased charge transfer resistance. Anode dehydration reduced with the high airflow rate because the higher amount of water was purged

with back diffusion. 10FEP_AC had also higher charge transfer resistance ($2.96 \Omega\text{cm}^2$), which is closer to 40FEP_AC. The lower performance of 10FEP_AC is attributed to the higher charge transfer resistance.

Table 7.5 Parameters of equivalent circuit modeling of EIS spectra of MEA1 at H₂/Air gas-feeding mode

MEA Type	Air		
	R _{HF} (Ωcm^2)	R _{ct} (A) (Ωcm^2)	R _{ct} (C) (Ωcm^2)
without FEP MEA1	0.24	0.14	1.86
40FEP_AC	0.40	0.43	2.72
30FEP_AC	0.29	1.21	1.12
20FEP_AC	0.29	0.99	1.10
10FEP_AC	0.28	0.94	2.02
10FEP_2_AC	0.25	0.07	2.13
5FEP_AC	0.26	0.97	1.21

The higher charge transfer resistance of 10FEP_AC revealed that the water removal rate towards the cGDL was not sufficient to decrease the water saturation in the secondary pores. This may be attributed to the high airflow rate, which caused hydraulic water drag from cathode towards anode side by providing high pressure at the cGDL/cMPL interface. The charge transfer resistance of 30FEP_AC ($2.33 \Omega\text{cm}^2$) was higher than 20FEP_AC ($2.09 \Omega\text{cm}^2$), because of thicker CLs with higher hydrophobicity. Therefore the reaction rate in the CLs of 20FEP_AC was higher than 30FEP_AC, which allowed enhanced performance. The charge transfer resistances of 10FEP_2_AC ($2.20 \Omega\text{cm}^2$) was similar to the charge transfer resistance of the 5FEP_AC ($2.18 \Omega\text{cm}^2$). The Pt utilization of the powder of the 10FEP_2_AC (75 %) was lower than 5FEP_AC (88 %). Furthermore, the Nafion coverage of 10FEP_2_AC ($X_{C/(Nafion+C)}=0.54$) was lower than 5FEP_AC ($X_{C/(Nafion+C)}=0.42$). This caused a decrease in ionic conduction. Although reduced Nafion coverage, 10FEP_2_AC had closer charge transfer resistance 5FEP_AC. This revealed the improved water management. Despite 5FEP_AC had thicker CLs with lower FEP amount ($X_{FEP/TP}=0.14$) with respect to 10FEP_2_AC ($X_{FEP/TP}=0.33$), the

charge transfer resistances were similar. However, 5FEP_AC demonstrated higher cell performance. This is attributed to the higher Pt utilization (88 %) of 5FEP_AC than 10FEP_2_AC (73%).

FEP Loaded Catalyst Layers on Cathode Electrode (MEA2):

Polarization and power density curves for cathode CLs with six different FEP loadings, working at H₂/Air gas-feeding mode are shown in Figure 7.13. The maximum power density at 0.45 V was 0.64 W/cm² for the CLs without FEP. 5FEP_C (0.45 W/cm²) demonstrated the closer performance to the CLs without FEP at 0.45 V. This is attributed to having the similar X_{Pt/TP}, which is 1.2 for 5FEP_C, while it is 1.5 for the CLs without FEP. This made cCL of 5FEP_C 20 % thicker than the cCL without FEP; however, low amount of FEP (X_{FEP/TP}=0.14) in the cCL allowed air to access active catalyst sites. Despite the thicknesses of cCL of 10FEP_C (X_{Pt/TP} =1.0) and 20FEP_C (X_{Pt/TP} =0.7) were various with different FEP amount 10FEP_C, they demonstrated closer performance (0.39 W/cm²). 10FEP_C had 30 % thinner cCL with 60 % lower amount of FEP nanoparticles (X_{FEP/TP}=0.25) compared to 20FEP_C (X_{FEP/TP}=0.4). Despite 10FEP_C had a thinner cCL mass transport resistance was higher than 20FEP_C (Figure 7.13). This revealed that FEP nanoparticles in the cCL of 10FEP_C could not achieve to mitigate flooding. 10FEP_2_C (0.35 W/cm²) and 30FEP_C (0.33 W/cm²) demonstrated closer performances. However, 30FEP_C had higher mass transport resistance. The thickness of the cCL of 30FEP_C (X_{Pt/TP} =0.4) was more than 3 times of the cCL of 10FEP_2_C (X_{Pt/TP} =1.5). On the other hand, FEP nanoparticles in the cCL of 30FEP_C were almost 2 times higher than the FEP nanoparticles in the cCL of 10FEP_2_C. However, that much of FEP nanoparticles in the cCL of 30FEP_C decreased the catalytic activity. The Pt utilization of 30FEP_C was 60 %, while the Pt utilization of 10FEP_2_C was 73 %. In addition to that, they could not achieve to reduce mass transport limitations for such a thickness of the cCL of 30FEP_C according to 10FEP_2_C. 40FEP_C (0.30 W/cm²) demonstrated lower power density than 30FEP_C (0.33 W/cm²) although 40FEP_C (X_{Pt/TP}=0.4) had the same thickness of cCL with 30FEP_C (X_{Pt/TP}=0.4).

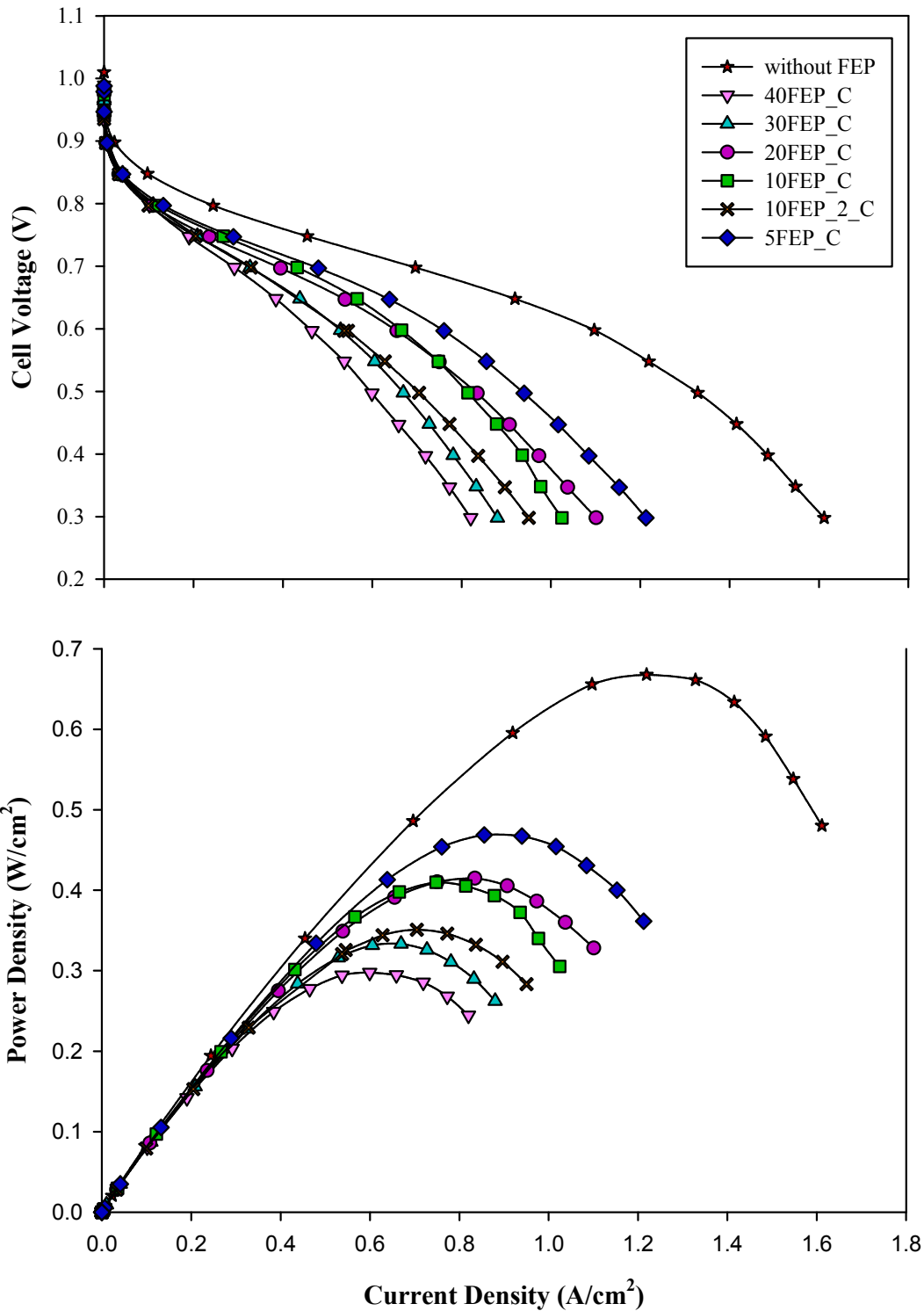


Figure 7.13 Polarization and power density curves of PEMFC for MEA2. Pt loading of anode and cathode electrodes was $0.4 \text{ mgPt}/\text{cm}^2$. Cathode catalyst layer was coated with FEP nanoparticles. PEMFC was operated at H_2 /Air gas feeding mode

This revealed that higher amount of FEP nanoparticles in the cCL of 40FEP_C ($X_{FEP/TP}=0.67$) in the same thickness of the cCL decreased cell performance.

Figure 7.14 illustrates EIS spectra of MEA1 measured at 0.5 V. All the CLs demonstrated an impedance spectrum with a high-frequency arc. Parameters of equivalent circuit modeling of EIS spectra for MEA1 are listed in Table 7.5.

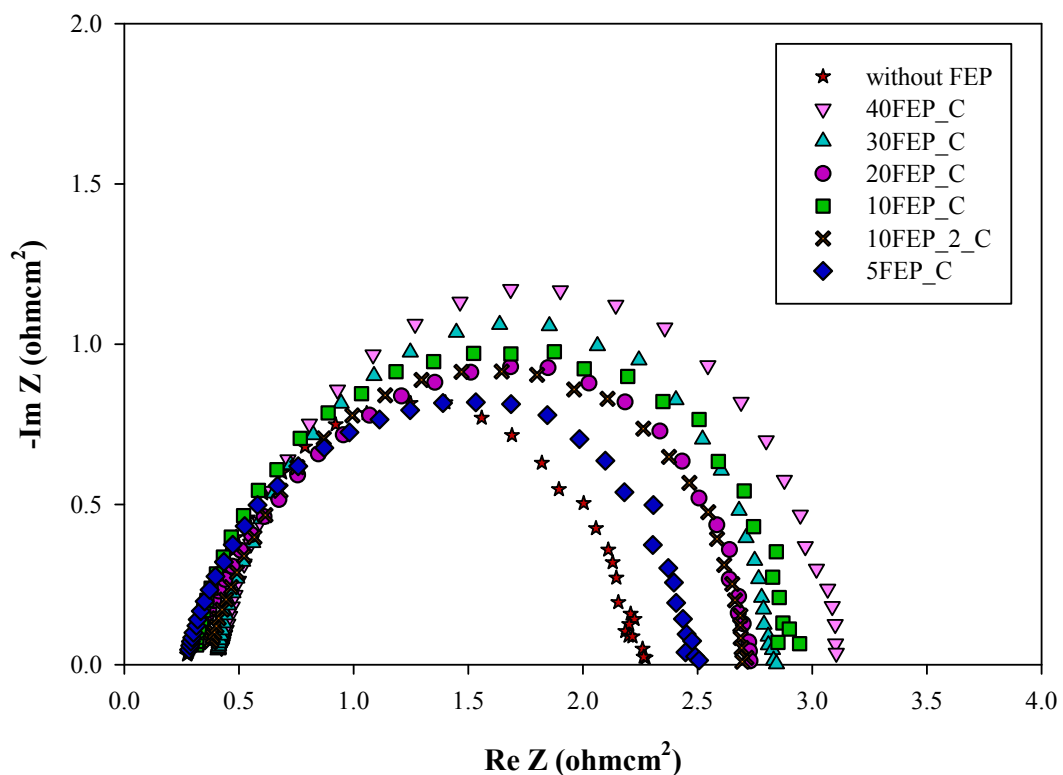


Figure 7.14 Electrochemical impedance spectra obtained for running fuel cell at 0.5 V. Pt loading of anode and cathode electrodes was 0.4 mgPt/cm^2 . Cathode catalyst layer was coated with FEP nanoparticles. PEMFC was operated at H_2/Air gas-feeding mode

All of the MEAs demonstrated similar high-frequency resistances except 30FEP_C ($0.40 \text{ } \Omega\text{cm}^2$). The highest charge transfer resistance ($2.80 \text{ } \Omega\text{cm}^2$) was obtained for 40FEP_C. The cCL of 40FEP_C thickest ($X_{Pt/TP}=0.4$) among all cCLs with highest FEP loading ($X_{FEP/TP}=0.67$). The charge transfer resistance of 10FEP_C

($2.66 \Omega\text{cm}^2$) was closest to 40FEP_C. The charge transfer resistance of 10FEP_C was higher because FEP amount in the cCLs of 10FEP_C ($X_{\text{FEP/TP}}=0.25$) could not mitigate flooding in the primary pores of the cCL. This caused a decrease in the reaction rate due to diffusion limitations. Therefore, the charge transfer resistance of 10FEP_C was higher. The charge transfer resistance of 30FEP_C ($2.48 \Omega\text{cm}^2$) was closer to the charge transfer resistance of 10FEP_C. The cCL of 30FEP_C was 60 % thicker than the cCL of 10FEP_C, while FEP amount in the cCL of 30FEP_C was % 40 higher than the FEP amount of the cCL of 10FEP_C. The higher amount of FEP nanoparticles in the cCL of 30FEP_C was not sufficient to decrease the water saturation in the secondary pores. Although the cCL of 20FEP_C was 56 % thicker than the cCL of 10FEP_2_C, while the FEP amount in the cCL of 20FEP_C was 14 % higher than 10FEP_2_C, the charge transfer resistance of cCL of 20FEP_C ($2.50 \Omega\text{cm}^2$) and 10FEP_2_C ($2.42 \Omega\text{cm}^2$) was similar. This is interpreted as the FEP amount in the cCL of 10FEP_2_C causing drying of Nafion ionomer. This led to decrease in ohmic resistances. We can observe the decrease in the ohmic resistance from Figure 7.13. The slope of the 10FEP_2_C in the ohmic region was steeper than 20FEP_C, which pointed out the higher ohmic resistance.

Table 7.6 Parameters of equivalent circuit modeling of EIS spectra of MEA1 at H₂/Air gas-feeding mode

MEA Type	Air		
	$R_{\text{HF}} (\Omega\text{cm}^2)$	$R_{\text{ct}} (\text{A})(\Omega\text{cm}^2)$	$R_{\text{ct}} (\text{C})(\Omega\text{cm}^2)$
without FEP MEA2	0.24	0.14	1.86
40FEP_C	0.31	0.15	2.65
30FEP_C	0.40	1.06	1.42
20FEP_C	0.27	1.06	1.44
10FEP_C	0.29	1.86	0.80
10FEP_2_C	0.32	0.04	2.38
5FEP_C	0.27	0.79	1.45

The charge transfer resistance of 5FEP_C ($2.24 \Omega\text{cm}^2$) was the lowest among all cCLs including FEP nanoparticles. The charge transfer resistance of the cCL of

5FEP_C was the closest to the charge transfer resistance of the cCL without FEP ($2.0 \Omega\text{cm}^2$). The cCL of 5FEP_C was 20 % thicker than the cCL without FEP. However, the cCL of 5FEP_C included a low amount of FEP ($X_{\text{FEP/TP}}=0.14$) with respect to the cCL without FEP. The increase in thickness of the cCL with FEP nanoparticles caused an increase in the charge transfer resistance.

7.3.7. Cross-section Images of MEA after Performance Testing

SEM images of cross section area of the membrane electrode assemblies prepared with commercial catalyst impregnated with Nafion (without FEP) with 1.2 mg/cm^2 Pt loading, without FEP with 0.4 mg/cm^2 Pt loading, 5FEP_AC with 1.2 mg/cm^2 Pt loading, 5FEP_AC with 0.4 mg/cm^2 Pt loading are shown in Figure 7.14. The two-sided arrows on the images illustrate anode and cathode side of the MEAs. Surface morphology of the MEA of 5FEP_AC after fuel cell testing is shown in Figure 7.15c. In addition, the surface morphology of the MEA after fuel cell testing of 5FEP_AC is shown in Figure 7.15d. The thickness of the CLs with 1.2 mg/cm^2 Pt loading (Figure 7.15c) was higher than the thickness of the CLs with 0.4 mg/cm^2 Pt loading (Figure 7.15d). This revealed that the thickness of the CLs increased since the Pt loading increased. Membrane deformation due to swelling was not significant for 5FEP_AC with 0.4 mg/cm^2 Pt loading. In addition, deformation in anode and cathode catalyst layers was not observable. However, since the Pt loading increased to 1.2 mg/cm^2 brittleness of the anode and cathode catalyst layers (shown with red arrows on the image) increased. FEP nanoparticles were softer than PTFE nanoparticles. Therefore, at low Pt loaded CLs, FEP nanoparticles did not cause any cracks at the CL. Therefore, $X_{\text{FEP/Nafion}}$ in the cCL may be lower than 1.0 to enhance cell performance in the case of high airflow rate.

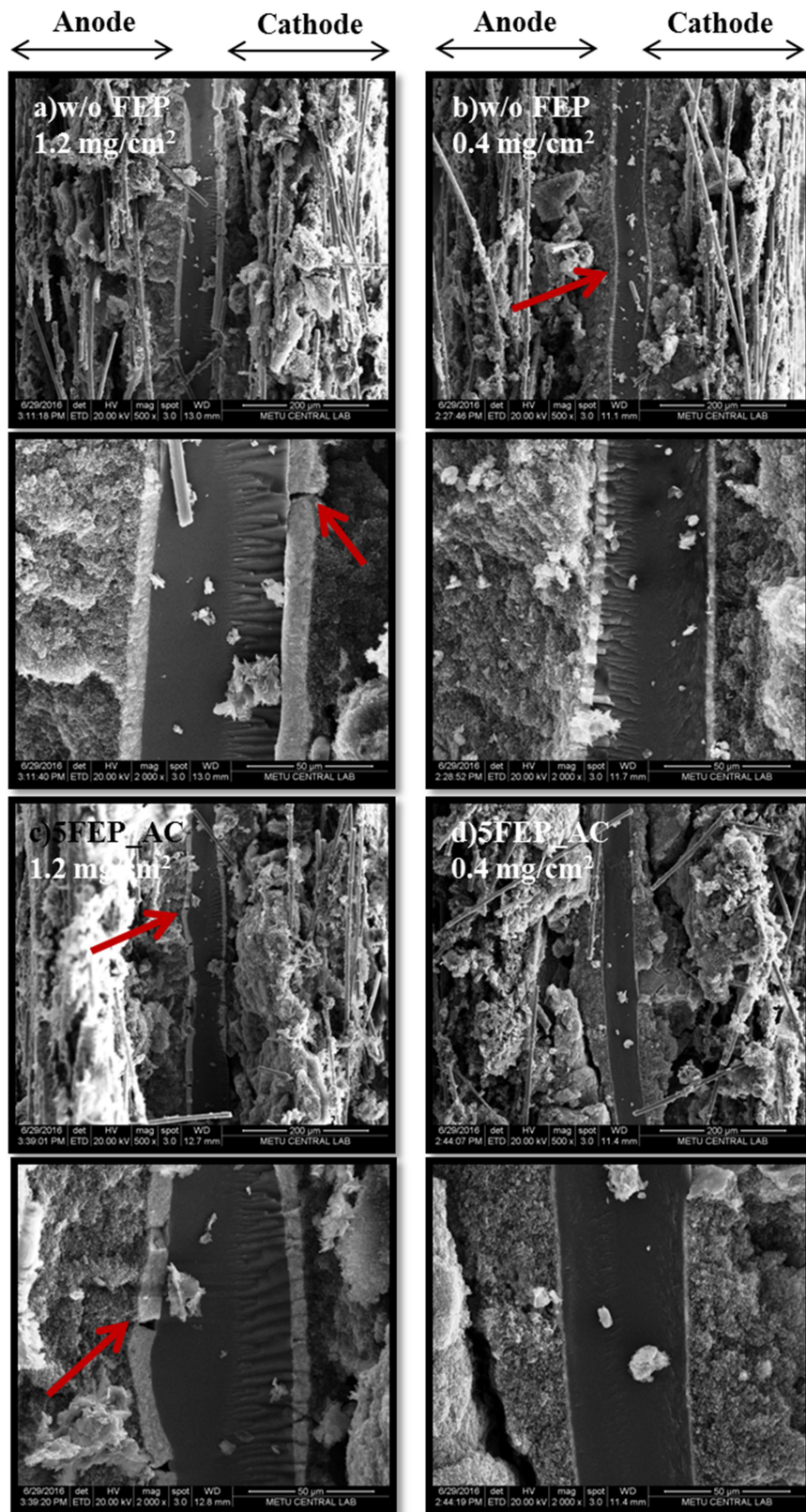


Figure 7.15 SEM images of the cross-section of the MEAs for a) without FEP with 1.2 mg/cm^2 Pt loading, b) without FEP with 0.4 mg/cm^2 Pt loading, c) 5FEP_AC with 1.2 mg/cm^2 d) 5FEP_AC with 0.4 mg/cm^2

7.4. Conclusions

In this chapter, for the FEP including CLs, the similar conclusion can be drawn with the PTFE including CLs. However, with FEP nanoparticles, the lower amount (5 wt. %) can be sufficient to mitigate flooding, because, in the structure of FEP nanoparticles, there are more hydrophobic sites than in the structure of PTFE nanoparticles. These hydrophobic sites also contribute to water management, which reduces the need for hydrophobic nanoparticles.

Nafion addition to the commercial catalyst reduced a significant amount of the pore volume, however, FEP addition to Nafion impregnated catalyst does not cause further reduction in the pore volume.

Total surface area of Pt particles in the catalyst powders does not alter with the addition of FEP nanoparticles; even Pt percentage in the catalyst powder reduces by the addition of FEP nanoparticles. This indicates that when Pt percentage in the commercial catalyst was higher, Pt agglomeration occurs, which causes reduced active surface area. Therefore, even if Pt percentage in the FEP included catalyst powder is lower, total surface area of Pt nanoparticles remain constant.

2-step ink preparation method provides homogenous distribution of the Pt, Nafion, and FEP nanoparticles, which enhances Pt utilization in the case of the low amount of Pt. In addition to that, for the catalyst powders including 5 wt % and 10 wt % FEP, 2-step ink preparation method improved Pt utilization according to the commercial catalyst.

Cumulative pore volume has a great impact on the performance of the cell. When the percentage of the primary pores contributed to the cumulative pore volume increased, Pt utilization enhances, therefore cell performance increases.

The thickness of the CLs and the FEP amount in the CLs are competing parameters dominating the water transport mechanisms at H₂/O₂ feeding mode. In the case of H₂/Air feeding mode, airflow rate was the dominant parameter influencing water movement in the pores of cGDL.

High airflow rate prevents pore blockage at the cathode GDL for both MEA configurations.

When air is used as the reactant gas of the CLs included into both MEA1 and MEA2 configurations, the charge transfer resistances increases up to 6 times of the charge transfer resistances of the CL operated at H₂/O₂ feeding mode.

5 wt. % FEP was sufficient to mitigate flooding for both MEA1 and MEA2 configurations at both feeding modes. The lowest charge transfer resistances among FEP included CL were obtained for the 5 wt. % included CL for both MEA configurations for both feeding modes, which is the proof of the enhanced water management.

The CLs including 20 wt % FEP demonstrated higher performances than expected because charge transfer resistances was the lower at both feeding modes and also for both MEA configurations. This is because the percentage of the primary pores contributed to the cumulative pore volume is higher than the other catalyst powders including FEP nanoparticles.

The increase in the FEP amount in the CLs made the CLs brittle, which causes cracks in the CL-leading to electronic and ionic disruption. However, the brittleness of the CLs is not as severe as the CLs including PTFE nanoparticles, because FEP nanoparticles were softer than PTFE nanoparticles.

Although FEP included catalyst powders prepared with 2-step ink preparation, which provided enhanced Pt utilization, FEP nanoparticles in CLs caused a reduction in the cell performance. The highest performance is always attained for the CLs without FEP.

CHAPTER 8

DETERMINATION THE EFFECTS OF HYDROPHOBIC CATALYST LAYERS INCLUDING PFA NANOPARTICLES TO WATER MANAGEMENT AND PERFORMANCE OF PEM FUEL CELL

In this chapter, poly(tetrafluoroethylene-co-perfluoro vinyl ether) (PFA) nanoparticles were added to CL to facilitate excess water removal from the triple phase boundary in high Pt loading (0.4 mg/cm^2) PEMFC electrodes. The loading of PFA in the catalyst ink was varied from zero to 40 weight percentage. High-performance electrodes for anode and cathode were prepared by ultrasonic spray coating technique with a commercial catalyst containing 70 wt % Pt on carbon. Different MEAs were prepared in order to differentiate the influence of hydrophobic nanoparticles on water transport and cell performance. In the first configuration (MEA1), PFA nanoparticles were added to both anode and cathode catalyst layers. In the second configuration (MEA2), PFA nanoparticles were added only to cCL. Anode catalyst layer prepared with commercial catalyst (Pt/C) impregnated with Nafion ionomer. PEM fuel cell tests were carried out at both H_2/O_2 and H_2/Air gas-feeding modes.

8.1. Introduction

The objective of this work is to investigate the influence of PFA nanoparticles in CLs as a hydrophobic agent in a low-temperature single PEM fuel cell. The electrodes were prepared by ultrasonic coating technique with high Pt-containing commercial catalyst (70 wt % Pt/C) with a high Pt loading (0.4 mg Pt/cm^2). Fuel cell

performance tests were carried out to determine the influence of PFA nanoparticles on high-performance PEM fuel cells. Impedance spectroscopy results have revealed the influence of PFA nanoparticles on reaction kinetics and water management.

8.2. Materials and Methods

Ink preparation, physical and electrochemical characterization methods in addition to performance tests are same as explained in Chapter 6.

8.2.1. MEA Configuration

Performance testing was carried out with two different membrane electrode assembly configurations. By this way, the effect of PFA nanoparticles in anode and cathode catalyst layers on water transport mechanism was investigated, separately. In the first configuration (MEA1), both anode and cathode catalyst layers coated with PFA nanoparticles. In the second configuration (MEA2), PFA nanoparticles were coated only on cCL. The Pt, Nafion, and PFA nanoparticle loadings on CLs for prepared MEAs are summarized in Table 8.1.

Table 8.1 Pt, Nafion, and PFA loadings in catalyst layers

Catalyst Ink	Loading (mg/cm ²)		
	Pt	Nafion	PFA
without PFA	0.4	0.26	-
40PFA	0.4	0.31	0.62
30PFA	0.4	0.46	0.46
20PFA	0.4	0.37	0.25
10PFA	0.4	0.31	0.10
10PFA_2	0.4	0.18	0.09
5PFA	0.4	0.28	0.05

Numbers before PFA synonym represent the weight percentage of PFA in the CL on a dry basis. For example, 5 PFA represents the CL prepared with the ink containing 5 wt % PFA on a dry basis. On the other hand, 30PFA _AC represents the

MEA that has 30 wt % PFA on both anode and cathode CLs. 30 PFA _C represents the MEA that had 30 wt % PFA on only cCL.

8.3. Results and Discussions

8.3.1. Physical Characterization

8.3.1.1. Nitrogen physisorption analysis

Figure 8.1 illustrates nitrogen adsorption/desorption isotherms for powders of commercial catalyst (Pt/C), commercial catalyst impregnated with Nafion (without PFA), commercial catalyst impregnated with different Nafion and PFA loadings.

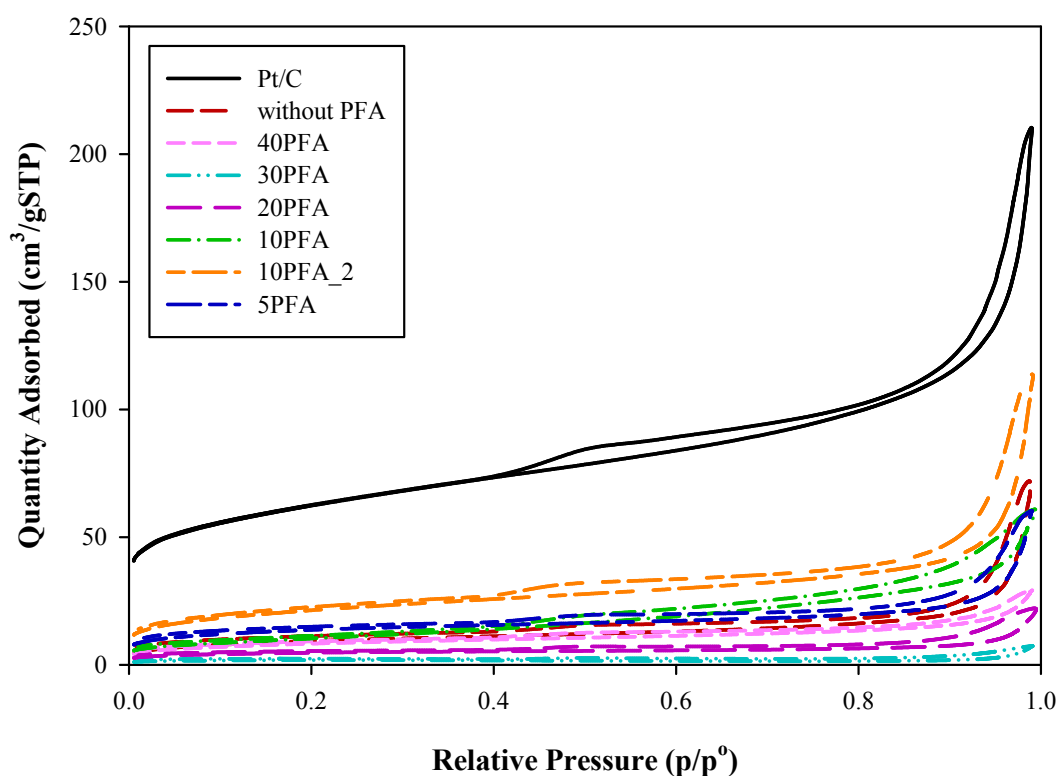


Figure 8.1 Adsorption/desorption isotherms for powders of commercial catalyst (Pt/C), commercial catalyst impregnated with Nafion (without PFA), commercial catalyst impregnated with different Nafion and PFA loadings

All isotherms are compatible with isotherm of Type IV according to IUPAC classification which is typical for the mesoporous structure of catalysts (Brunauer et al. 1940; Sing 1985), (Kaneko 1994). Furthermore, the hysteresis loops for the commercial catalyst (Pt/C), commercial catalyst impregnated with Nafion ionomer (without PFA), 5PFA, and 10PFA_2, demonstrated hysteresis Type H3 according to IUPAC classification, is observed with aggregates of plate-like particles give rise to slit-shaped pores (Sing 1985). Furthermore, 40PFA, 30PFA, 20PFA, and 10PFA demonstrate more like type H4 loop is often associated with narrow slit-like pores (Sing 1985). This is because walls of slit-shaped pores were covered with Nafion and PFA polymers leading to narrower pore width.

Figure 8.2 illustrates pore size distribution were spread into micro/meso/macroporous region. The catalyst powder consisted of two distinctive pore distributions, where pores with a diameter distributed from 0.01 μm to 0.01 μm defined as primary pores, while pores with a diameter distributed from 0.01 μm to 0.2 μm defined as secondary pores. The primary pores represented to the pores in the aggregates, where the reaction takes place, while the secondary pores represented to the pores between aggregates assigned to gas diffusion (Watanabe et al. 1985). The highest cumulative pore volume was obtained for Pt/C. When Nafion impregnated to the commercial catalyst, it occupied most of the primary pores led to the decrease in cumulative pore volume. As the weight percentage of total polymer in the catalyst powder increased, cumulative pore volume reduced. The cumulative pore volume of 10PFA (0.41 mg/cm^2), and 5PFA (0.33 mg/cm^2) was higher than the cumulative pore volume of catalyst powder without PFA (0.26 mg/cm^2) below 0.01 μm . This revealed that although they have similar polymer loadings, two-step ink preparation method provided more homogenous distribution of polymers. Therefore, more pores with the diameter below 0.01 μm were open for 10PFA and 5PFA. The pores of 30PFA (0.93 mg/cm^2) between 0.01 μm and 0.1 μm were almost completely blocked while the pores of 20PFA (0.62 mg/cm^2), and 40PFA (0.93 mg/cm^2) in the same range were slightly open. On the other hand, 40PFA had higher cumulative pore volume than 20PFA and 30PFA. This is attributed to the $X_{\text{PFA/Nafion}}$ constant of the catalyst powders. The $X_{\text{PFA/Nafion}}$ of 40PFA was highest with a value of 2.0, while $X_{\text{PFA/Nafion}}$ of 30PFA and 20PFA was 1.0 and 0.7, respectively. Nafion mainly occupied most of the primary pores, while PFA settled in the secondary pores

(Watanabe et al. 1985; Uchida 1996; Uchida 1995). This is interpreted as since the total polymer amount was similar when PFA amount was higher than Nafion, cumulative pore volume was increased.

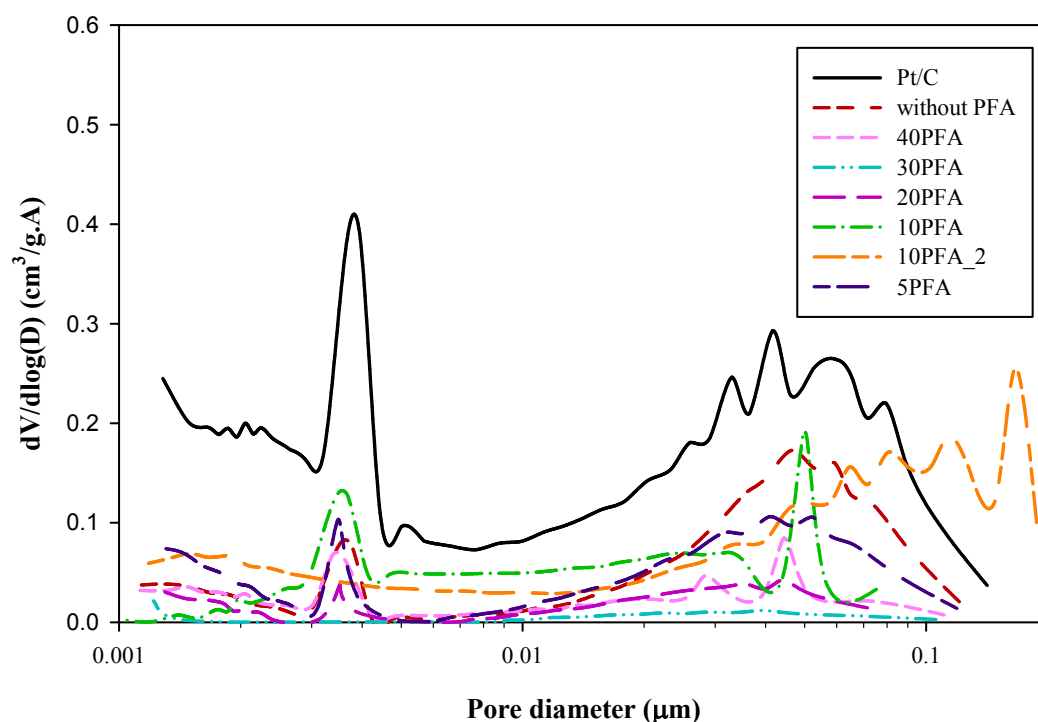


Figure 8.2 Pore size distributions for powders of commercial catalyst (Pt/C), commercial catalyst impregnated with Nafion (without PFA), and commercial catalyst impregnated with different Nafion and PFA loadings

This means that higher volume of the primary pores was free to access. Moreover, 10PFA_2 (0.26 mg/cm²) had higher cumulative pore volume than 10PFA (0.41 mg/cm²), 5PFA (0.33 mg/cm²), and catalyst powder without PFA (0.26 mg/cm²) in this range. The cumulative pore volume of 10PFA (0.41 mg/cm²), and 5PFA (0.33 mg/cm²) was higher than the cumulative pore volume of catalyst powder without PFA (0.26 mg/cm²) below 0.01 µm. This revealed that although they have similar polymer loadings, two-step ink preparation method provided more homogenous distribution of polymers. Therefore, more pores with the diameter below 0.01 µm were open for 10PFA and 5PFA. The pores of 30PFA (0.93 mg/cm²)

between 0.01 μm and 0.1 μm were almost completely blocked while the pores of 20PFA (0.62 mg/cm^2), and 40PFA (0.93 mg/cm^2) in the same range were slightly open. On the other hand, 40PFA had higher cumulative pore volume than 20PFA and 30PFA. Moreover, 10PFA_2 (0.26 mg/cm^2) had higher cumulative pore volume than 10PFA (0.41 mg/cm^2), 5PFA (0.33 mg/cm^2), and catalyst powder without PFA (0.26 mg/cm^2) in this range.

8.3.1.2. XRD analysis

XRD patterns for powders of commercial catalyst (Pt/C), commercial catalyst impregnated with Nafion (without PFA), and commercial catalyst impregnated with different Nafion and PFA loadings are shown in Figure 8.3. All of the patterns clearly show the presence of the elemental platinum with the five characteristic peaks of face centered cubic crystalline platinum. The Bragg angles of ca. 40° , 46° , 67° , 81° , 86° correspond to (111), (200), (220), (311) (He 1997; Pozio et al. 2002), and (222) (Zhang et al. 2010) Pt facets, respectively. The intensity of diffraction peak of Pt (222) was weak only in the pattern of all catalysts. The peak appeared at the diffraction pattern for powder of commercial catalyst impregnated with Nafion (without PTFE) at ca. 17° Bragg angle was attributed to poly-fluorocarbon chains of Nafion ionomer (Jung et al. 2003). The broadness of the Nafion peak pointed out the amorphous structure of the polymer. The peak occurred at ca. 18° Bragg angle corresponded to a crystalline (65%) and an amorphous component of PFA (Latorrata et al. 2015). Nafion and PFA peaks were overlapped at the diffraction pattern of powder of PFA including catalysts, since corresponding Bragg angles of Nafion and PFA were very close to each other. However, as PFA weight percentage increased in the powders, the intensity of the PFA peak increased indicating the higher amount of PFA.

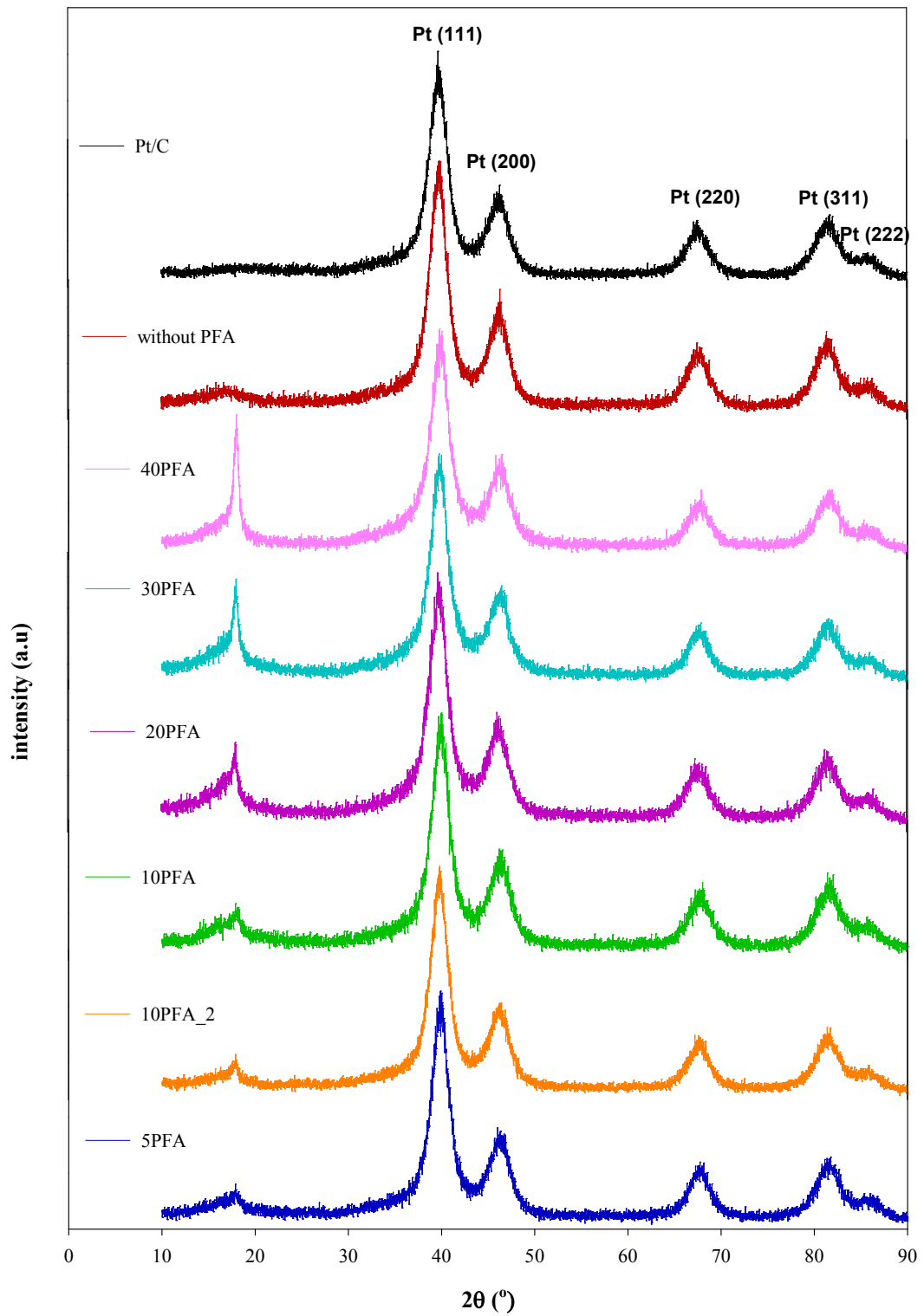


Figure 8.3 XRD patterns of powders of commercial catalyst (Pt/C), commercial catalyst impregnated with Nafion (without PFA), and commercial catalyst impregnated with different Nafion and PFA loadings

8.3.2. Cyclic Voltammetry Analysis

Figure 8.4 illustrates cyclic voltammograms of commercial catalyst (Pt/C), commercial catalyst impregnated with Nafion (without PFA); commercial catalyst impregnated with six different Nafion and PFA loadings.

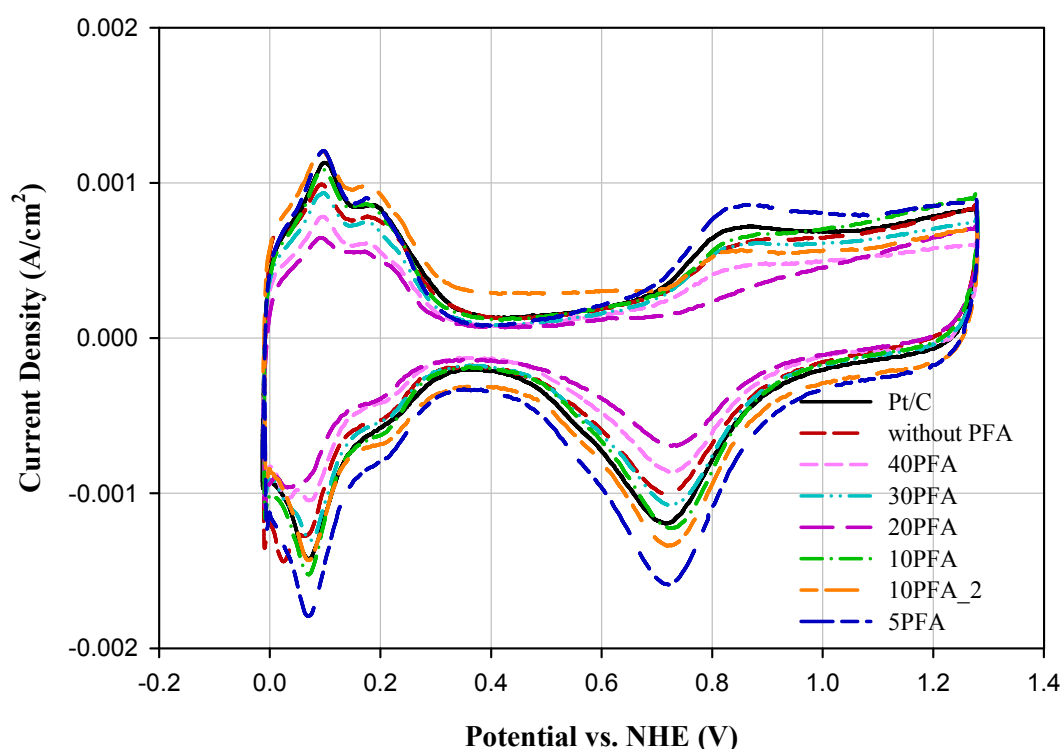


Figure 8.4 Cyclic voltammograms of commercial catalyst (Pt/C), commercial catalyst impregnated with Nafion (without PFA), and commercial catalyst impregnated with different Nafion and PFA loadings

Hydrogen adsorption/desorption peaks observed from 0.0 to 0.3 V both for the anodic and cathodic directions. Pt oxidation was observed between 0.7 and 1.2 V at the cathodic direction and Pt reduction was observed at 0.9 and 0.4 V at anodic direction.

Electrochemical surface area and Pt utilization were calculated as described in Chapter 2.

Commercial catalyst (Pt/C) had the highest electrochemical surface area (65 m²/g). This was attributed to the highest Pt content (62 wt. %) in the commercial

catalyst (Pt/C). The catalyst powders of the 10PFA (67 m²/g) had a slightly higher electrochemical surface area than the catalyst powder of commercial catalyst (65 m²/g). The catalyst powder of commercial catalyst impregnated with Nafion (without PFA) had higher Pt content according to 10PFA (43 wt %), however, its electrochemical surface area (62 m²/g) was lower than the catalyst powder of 10PFA. This is attributed to the difference in the catalyst preparation methods. By two-step ink preparation, electronic and ionic conduction of Pt nanoparticles 10FEP enhanced. The catalyst powder of 10PFA had Pt utilization of 87 %, which was higher than the Pt utilization of the commercial catalyst (83 %) and the catalyst powder without PFA (78 %). This revealed that the amount of Pt particles contributed to the electrochemical reaction was higher than in the catalyst powders of 10FEP.

Table 8.2 summarizes weight percentage of Pt, multipoint BET surface area, cumulative pore volume, and average pore diameter of catalyst powders. The maximum Pt content was obtained for the commercial catalyst, with the inclusion of Nafion and PFA polymers, the weight percentage of the Pt decreased. Furthermore, as the weight ratio of Pt to the total polymer in the catalyst powder decreased to 0.4, Pt weight percentage decreased to 24 %. Nafion addition to Pt/C catalyst (3.5 nm) caused Pt agglomeration (3.7 nm). This indicated that Nafion ionomer occupied narrower pores, which also led to a reduction in BET surface area and contributions to cumulative pore volume were mostly by larger pores. However, PFA addition to Nafion impregnated catalyst powder did not cause further agglomeration. Moreover, PFA addition in two steps led to the decrease in average Pt diameter of 20PFA (3.5 nm), 30PFA (3.5 nm), and 40PFA (3.4 nm) compared to catalyst powder without PFA (3.7 nm). This is attributed to the low Pt content of the catalysts. This revealed that since Pt amount in the catalyst powder was lower, Pt agglomeration decreased. The highest BET surface area was obtained for Pt/C was 210 m²/g. BET surface area reduced as the ratio of Pt to total polymer loading ($X_{Pt/TP}$) in the catalyst powder decreased below 1.0. On the other hand, average pore diameter increased from 5.2 nm to 8.5 nm.

Table 8.2 Physical characterization values of powders of commercial catalyst (Pt/C), commercial catalyst impregnated with Nafion (without PFA), commercial catalyst impregnated with different Nafion and PFA loadings

	Pt/C	Without PFA	5PFA	10PFA	10PFA_2	20PFA	30PFA	40PFA
$X_{\text{PFA/TP}}$	NaN	0.0	0.14	0.25	0.33	0.4	0.5	0.67
$X_{\text{C/(Nafion+C)}}$	1.0	0.44	0.42	0.40	0.54	0.35	0.31	0.40
$X_{\text{Pt/TP}}$	NaN	1.5	1.2	1.0	1.5	0.7	0.4	0.4
Pt wt % ^a	67	46	43	39	46	33	26	26
Pt wt % ^b	34	18	19	41	44	30	24	25
Pt wt % ^c	62	43	37	35	38	30	24	23
ESA ^d (m ² /g)	65	62	74	67	41	39	56	48
U _{Pt} ^d (%)	83	78	97	87	55	49	70	58
d _{Ptavg} ^e (nm)	3.5	3.7	3.7	3.6	3.7	3.5	3.5	3.4
SA _{Pt} ^e (m ² /g)	79	75	76	77	76	81	80	83
SA _{BET} ^f (m ² /g)	210	33	46	38	74	16	6	29
V _{poreCum} ^f (cm ³ /g)	0.35	0.11	0.1	0.09	0.17	0.03	0.011	0.05
V _{pporeCum} ^f (cm ³ /g)	0.16	0.02	0.03	0.04	0.04	0.01	0.003	0.02
V _{sporeCum} ^f (cm ³ /g)	0.19	0.09	0.07	0.05	0.13	0.02	0.008	0.03
dpore _{avg} ^f (nm)	5.2	8.5	5.6	7.4	6.7	5.5	4.9	4.3

^a Theoretical value

^b Determined by TGA analysis

^c Determined by ICP_MS analysis

^d Determined by CV analysis

^e Calculated from XRD data

^f Calculated from nitrogen physisorption data

This indicated that Nafion ionomer occupied narrower pores, which also led to a reduction in BET surface area and contributions to cumulative pore volume were mostly by larger pores. However, although, the ratio of Pt to total polymer loading ($X_{Pt/TP}$) of 10PFA_2 (1.5) was equal to the catalyst powder without PFA (1.5), 10PFA_2 had higher BET surface area ($74 \text{ m}^2/\text{g}$) than catalyst powder without PFA ($33 \text{ m}^2/\text{g}$). This is revealed that with the two-step ink preparation method (Friedmann & Nguyen 2008), Nafion and PFA polymers were distributed better in 10PFA_2 than in the catalyst powder without PFA. 30PFA had the lowest BET surface area due to the lowest ratio of carbon to Nafion (0.4). This indicated that since the ratio of Pt to the total polymer ($X_{Pt/TP}$) was below 1.0, the $X_{C/(Nafion+C)}$ would be critical. The average pore diameter of 20PFA (5.5 nm), 30PFA (4.9 nm), and 40PFA (4.3 nm) was smaller than 5PFA (5.6 nm), 10PFA_2 (7.4 nm), and 10PFA (6.7 nm). When the $X_{PFA/TP}$ exceeded 0.3, average pore diameter average pore diameter reduced below 5.6 nm. As the ratio of Pt to total polymer amount in the catalyst ($X_{Pt/TP}$) increased, the thickness of the CLs increased. The thinnest CLs were attained with the catalyst powder without PFA and the catalyst powder of 10PFA_2 because $X_{Pt/TP}$ of these CLs was highest (1.5). The CLs prepared with the catalyst powder of 5PFA was 21 % thicker than the CLs prepared with the catalyst powder without PFA and the catalyst powder of 10PFA_2. The CLs prepared with the catalyst powder of 10PFA was 36 % thicker than the CLs prepared with the catalyst powders without PFA and catalyst powder of 10PFA_2. Furthermore, the CLs prepared with the catalyst powder of 20PFA was 56 % thicker than the CLs prepared with the catalyst powder of 10PFA_2. Finally, the thickest CLs prepared with the catalyst powders of 30PFA and 40PFA was more than two fold (72 %) thicker than the CLs prepared with 10PFA_2.

When $X_{PFA/TP}$ increased in the catalyst powder, the weight percentage of Nafion decreased, by this way, most of the smaller pores were attained to be open. The multipoint BET surface area of 20PFA ($0.03 \text{ cm}^3/\text{g}$), 30PFA ($0.01 \text{ cm}^3/\text{g}$), and 40PFA ($0.05 \text{ cm}^3/\text{g}$) was smaller than 5PFA ($0.09 \text{ cm}^3/\text{g}$), 10PFA_2 ($0.09 \text{ cm}^3/\text{g}$), and 10PFA ($0.18 \text{ cm}^3/\text{g}$). When $X_{PFA/TP}$ exceeded 0.3, in the meanwhile, the $X_{C/(Nafion+C)}$ decreased below 0.4, this led to a significant decrease in multipoint BET surface area because, and most of the pores of 20PFA, 30PFA, 40PFA were

occupied with the polymer. That is why; 30PFA had the lowest $X_{C/(Nafion+C)}$ (0.31), which revealed the lowest multipoint BET surface area ($6 \text{ m}^2/\text{g}$).

8.3.3. TEM Analysis

TEM images of powders of commercial catalyst (Pt/C), commercial catalyst impregnated with Nafion (without PFA), and commercial catalyst impregnated with different Nafion and PFA loadings are shown in Figure 8.4.

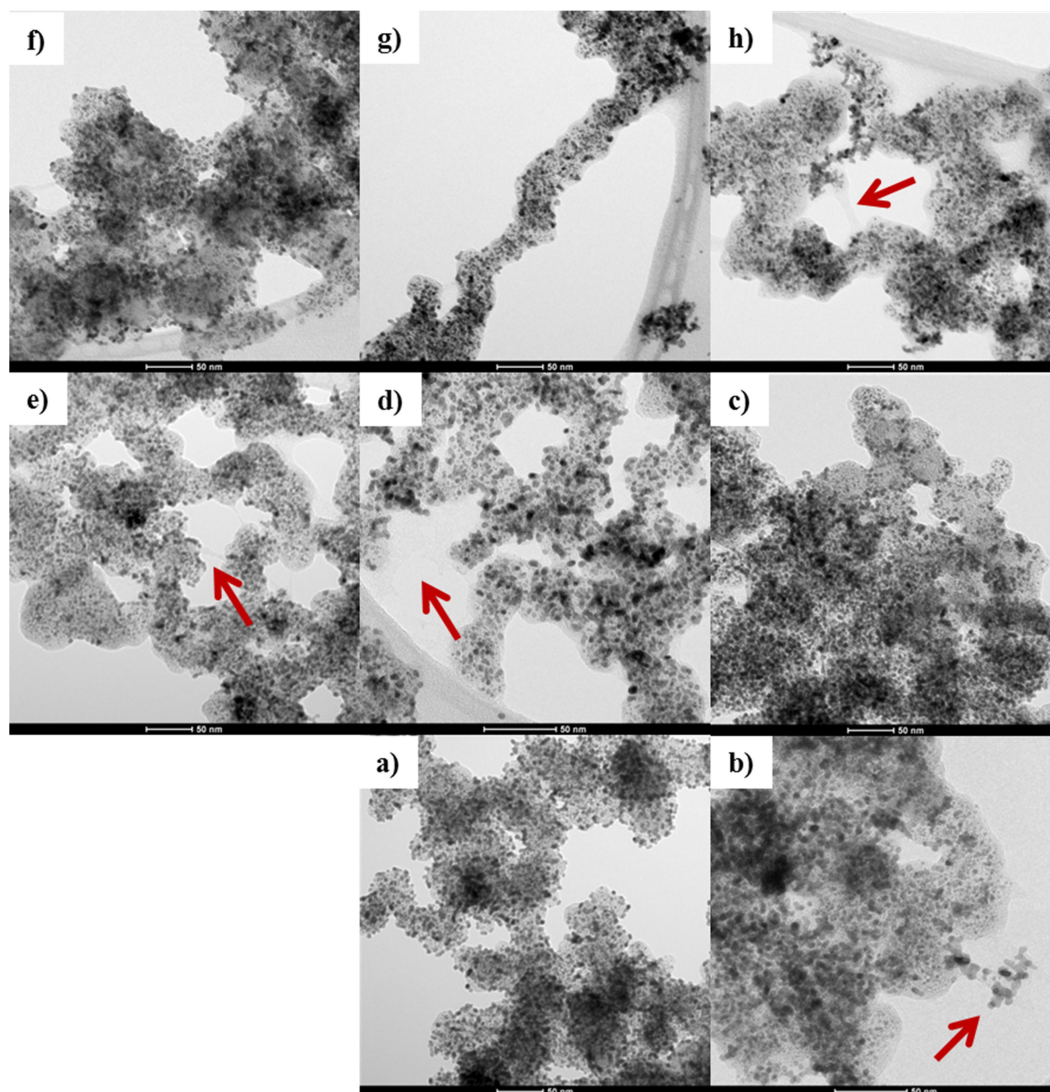


Figure 8.5 TEM images of powders of a)Pt/C, b) without PFA, c) 5PFA, d) 10PFA, e) 10PFA_2, f) 20PFA, g) 30PFA h) 40PFA

The image of the commercial catalyst is shown in Figure 8.4a. Black dots correspond to the dispersed Pt particles on gray carbon spheres. We can clearly observe that when Nafion impregnated to the commercial catalyst (Figure 8.4b), Pt agglomeration occurred. The red arrow on the images of 10PFA (Figure 8.4d), 10PFA_2 (Figure 8.4e), and 40PFA (Figure 8.4h) show the empty surfaces where Pt particles cannot place on. These empty places may consist of PFA nanoparticles.

8.3.4. SEM Analysis of Catalyst Powder

SEM images of powders of commercial catalyst (Pt/C), commercial catalyst impregnated with Nafion (without PFA), and commercial catalyst impregnated with different Nafion and PFA loadings are shown in Figure 8.5. EDX results illustrate the elemental composition of the samples, which include Pt, carbon, fluorine, sulfur, and oxygen peaks. The Pt particles in the commercial catalyst (Pt/C) were the smallest considering commercial catalyst impregnated with different Nafion (without PFA) and PFA loadings (Figure 8.5). Catalyst agglomeration occurred with Nafion addition to Pt/C catalyst was clearly observed when Figure 8.5b. 5PFA has smaller Pt particles with the smaller pores compared to other PFA included catalyst powders. The increase in Pt agglomeration with an increase in PFA amount was not significant. This is attributed to preparation method. The preparation of the catalyst ink in two-step provided homogenous distribution. The structural changes in the catalyst powder were indicated with a red arrow on the images of 10PFA (Figure 8.5d), 20PFA (Figure 8.5f), and 40PFA (Figure 8.5h). PFA nanoparticles caused agglomeration by covering Pt particles. The geometry of the newly-formed agglomerates was similar to the sphere as like Pt particles. Decline in the void spaces with the addition of PFA nanoparticles was clearly observed in the SEM image of 40PFA (Figure 8.5h). EDX results represented the relative amount of the chemical compounds in the catalyst powders. For commercial catalyst (Pt/C), Pt, carbon, and oxygen peaks appeared in the EDX results (Figure 8.5a); while fluoride and sulfur peaks appeared in addition to Pt, carbon, and oxygen peaks for catalyst powders including the different amount of Nafion and PFA. Since PFA amount in the catalyst powders increased, the intensity of Fluorine peak increased (20PFA, 30PFA, and 40PFA).

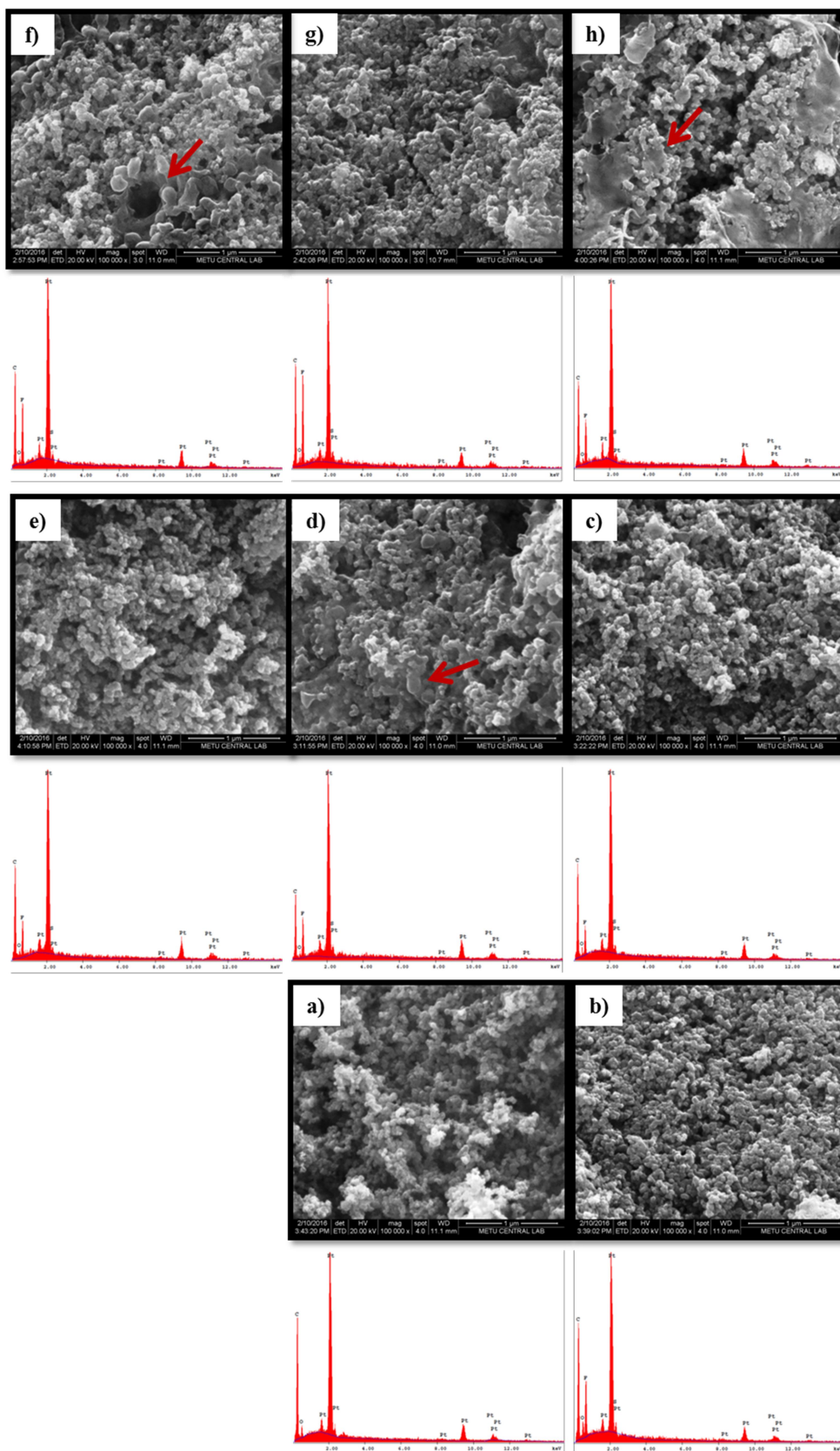


Figure 8.6 SEM images and energy-dispersive X-ray spectroscopy (EDX) of powders of a) Pt/C, b) without PFA c) 5PFA, d) 10PFA, e) 10PFA_2, f) 20PFA, g) 30PFA and h) 40PFA

8.3.5. Effect of PFA Loading on Performance and Running Electrochemical Impedance Spectrum of PEMFC at H₂/O₂ Gas-feeding Mode

PFA Loaded Catalyst Layers on Both Electrodes (MEA1):

Polarization and power density curves for CLs with six different Nafion and PFA loadings, working at H₂/O₂ gas-feeding mode are shown in Figure 8.7. The performances of PFA loaded CLs were compared with CLs without PFA. The maximum power density at 0.45 V was 1.27 W/cm² for the CLs without PFA. 10PFA_2_AC had closer performances to CLs without PFA with the power densities of 1.19 W/cm² at 0.45 V. This is attributed to the same X_{Pt/TP} of 1.5. This means that the thicknesses of the CLs of 10PFA_2_AC and the CLs without PFA were same with the same Pt loading. Thinnest CL indicated the lowest mass transport limitations. Although their CLs had the same thickness, PFA nanoparticles in the CLs of 10PFA_2_AC (X_{PFA/TP}=0.33) caused activity losses. The power density of 10PFA_AC and 5PFA_AC at 0.45V was 1.07 W/cm² and 1.0 W/cm², respectively. 10PFA_AC had X_{Pt/TP} of 1.0, while 5PFA_AC had X_{Pt/TP} of 1.2. This means that 10PFA_AC had 17 % thicker CLs than 10PFA_2_AC led to higher mass transport limitations. However, the X_{PFA/TP} ratio of 10PFA_AC (0.25) was higher than 5PFA_AC (0.14). The higher amount of PFA nanoparticles provided improved water management promoting a reduction in the ohmic resistance due to reduced mass transport limitations. Despite the thickness of the CLs were different, the performances of 20PFA_AC (0.92 W/cm²) and 30PFA_AC (0.93 W/cm²) were very close to each other at 0.45 V. The X_{PFA/TP} of 20PFA_AC was 0.7 while it was 0.4 for 30PFA_AC. This indicated that 30PFA_AC had 43 % thicker CLs than 20PFA_AC causing higher mass transport limitations. However, 30PFA_AC had similar performance to 20PFA_AC. Moreover, above 2.0 A/cm², the performance of 30PFA_AC exceeded the performance of 20PFA_AC. This revealed that higher amount of PFA nanoparticles (X_{PFA/TP} of 0.5) provided enhanced water management at higher current densities in the CLs of 30PFA_AC. The power density of 40PFA_AC (0.76 W/cm²) was the lowest among all CLs. This is attributed to the highest X_{PFA/TP} of 40PFA_AC (0.67).

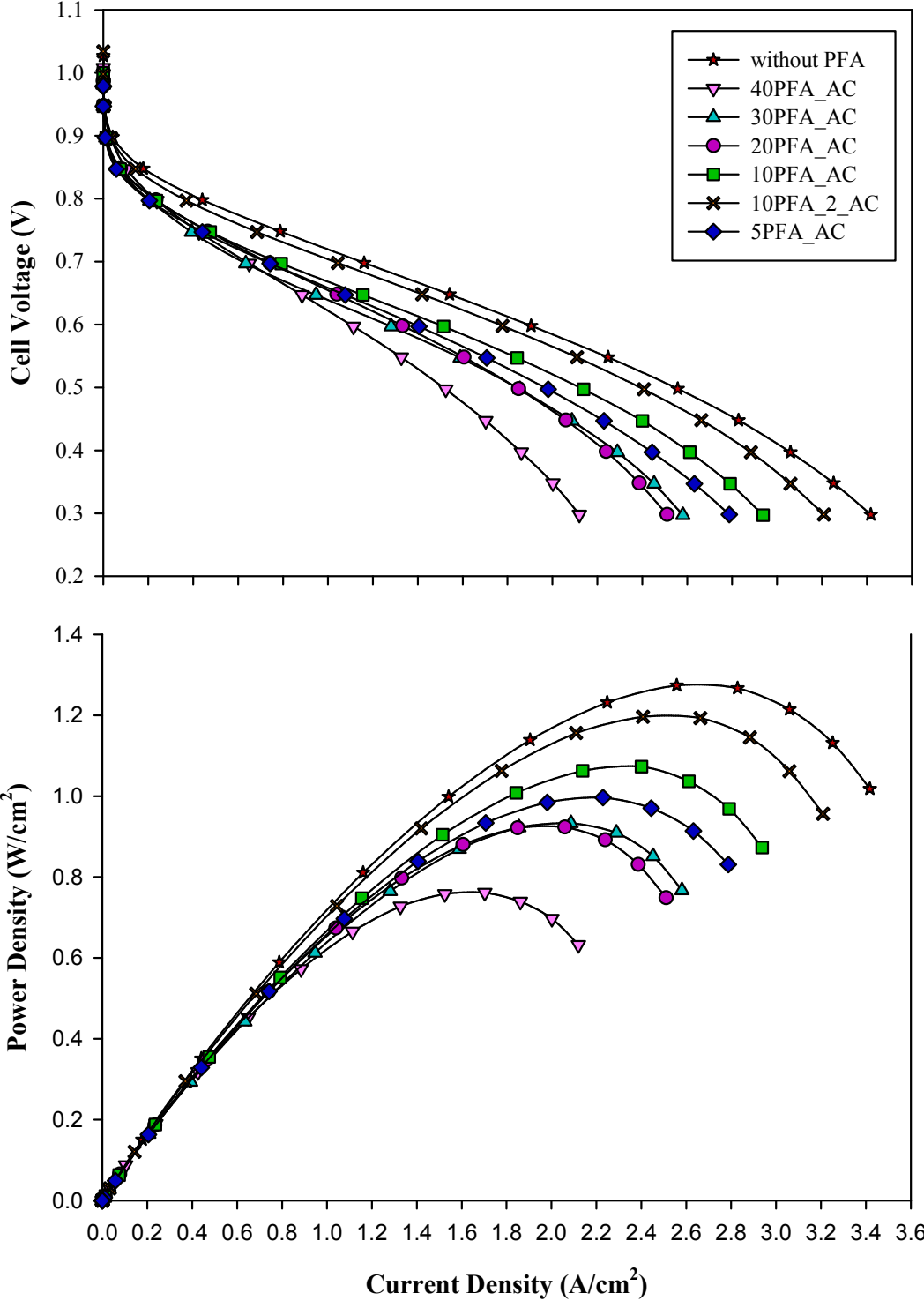


Figure 8.7 Polarization and power density curves of PEMFC for MEA1. Pt loading of anode and cathode electrodes was 0.4 mgPt/cm². Both anode and cathode catalyst layers coated with PFA nanoparticles. H₂/O₂ gas-feeding mode was used

The excess amount of PFA was settled on the electronic and ionic network, which caused a reduction in the triple phase boundaries. This also led to increasing in the ohmic resistance.

Figure 8.8 illustrates EIS spectra of MEA1 measured at 0.5 V at which thin film diffusion has a preponderant effect on mass transport. All CLs demonstrated an impedance spectrum with a high-frequency arc followed by a low-frequency arc. This revealed that the pores of the cGDLs of all MEAs were blocked with water molecules. Parameters of equivalent circuit modeling of EIS spectra for MEA1 are listed in Table 8.3.

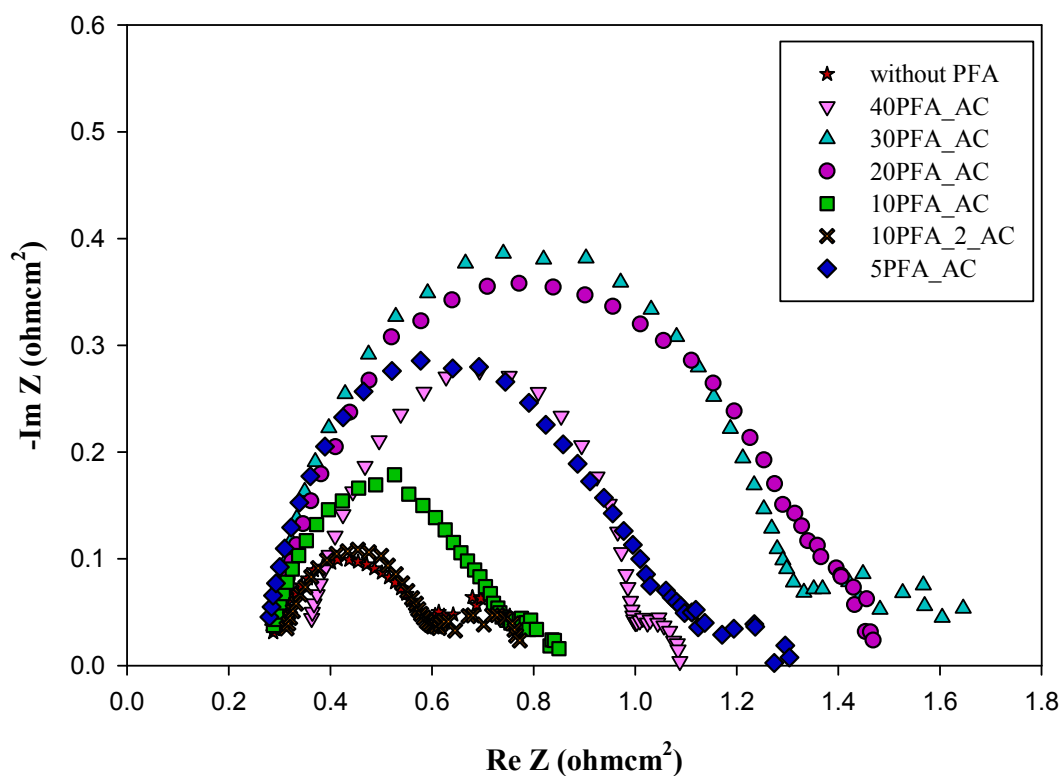


Figure 8.8 Electrochemical impedance spectra obtained for a running fuel cell at 0.5 V. Pt loading of anode and cathode electrodes was 0.4 mgPt/cm^2 . Both anode and cathode catalyst layers were coated with PFA nanoparticles. H_2/O_2 gas-feeding mode was used.

All of the MEAs demonstrated similar high-frequency resistances; however, 40PFA_AC had the highest high-frequency resistance. The higher amount of PFA nanoparticles in the aCL of 40PFA_AC prevent the introduction of H₂ gas humidified with water vapor, therefore membrane dehydrated. The highest charge transfer resistances was obtained for 30PFA_AC (1.18 Ωcm²) and 20PFA_AC (1.13 Ωcm²). Although the CLs of 30PFA_AC were 43 % thicker than the CLs of 20PFA_AC, while PFA amount was % 20 higher, the charge transfer resistances were closer each other. The amount of PFA nanoparticles in the CLs of 30PFA_AC mitigated flooding in the cCL. On the other hand, mass transfer resistance of 20PFA_AC (0.07 Ωcm²) was almost half the value of the mass transfer resistance of 30PFA_AC (0.18 Ωcm²). This revealed that water molecules blocked the higher amount of pores in the cathode GDL of 30PFA_AC. Although 5PFA_AC (0.71 Ωcm²) and 40PFA_AC (0.69 Ωcm²) included a different amount of PFA nanoparticles in the different thicknesses of the CLs, they had similar charge transfer resistances. This is because the amount of PFA nanoparticles in the cCL of 5PFA_AC was not sufficient to mitigate flooding in the CL. The excess amount of water invaded primary and secondary pores, which caused diffusion limitations. Therefore, reaction rate reduced. On the other hand, the amount of PFA nanoparticles in the cCL of 40PFA_AC high enough to push the water molecules towards the cGDL leading to dry ionomer around the catalyst aggregates.

Table 8.3 Parameters of equivalent circuit modeling of EIS spectra of MEA1 at H₂/O₂ gas-feeding mode

MEA Type	O ₂			
	R _{HF} (Ωcm ²)	R _{ct (A)} (Ωcm ²)	R _{ct (C)} (Ωcm ²)	R _{mt} (Ωcm ²)
without PFA MEA1	0.26	0.11	0.22	0.17
40PFA_AC	0.34	0.08	0.61	0.06
30PFA_AC	0.27	0.32	0.86	0.18
20PFA_AC	0.28	0.24	0.89	0.07
10PFA_AC	0.27	0.08	0.37	0.12
10PFA_2_AC	0.29	0.02	0.29	0.18
5PFA_AC	0.27	0.01	0.70	0.32

The charge transfer resistance of 10PFA_AC ($0.45 \text{ } \Omega\text{cm}^2$) was higher than the charge transfer resistances of 10PFA_2_AC ($0.31 \text{ } \Omega\text{cm}^2$) and the CLs without PFA. This is attributed to the thickness of the CLs. The CL of 10PFA_AC ($X_{\text{Pt/TP}}$ of 1.2) was 20 % thicker than the CLs of 10PFA_2_AC ($X_{\text{Pt/TP}}$ of 1.5) and the CLs without PFA ($X_{\text{Pt/TP}}$ of 1.5). Furthermore, the amount of PFA nanoparticles ($X_{\text{PFA/TP}}$ of 0.25) of 10PFA_AC was 24 % lower than the PFA amount in the CLs of 10PFA_2_AC ($X_{\text{PFA/TP}}$ of 0.33). This revealed that PFA amount in the cCL of 10PFA_AC was not sufficient to mitigate flooding. The lowest charge transfer resistance was attained for 10PFA_2_AC ($0.31 \text{ } \Omega\text{cm}^2$). It is lower than the charge transfer resistance of the CLs without PFA ($0.33 \text{ } \Omega\text{cm}^2$). This revealed that PFA nanoparticles in the CLs of 10PFA_2_AC provided enhanced water management, which led to lower charge transfer resistance.

PFA Loaded Catalyst Layer on Cathode Electrode (MEA2):

Polarization and power density curves for CLs with six different Nafion and PFA loadings, working at H_2/O_2 gas-feeding mode are shown in Figure 8.9. The maximum power density at 0.45 V was 1.27 W/cm^2 for the CLs without PFA. 20PFA_C had closer performances to CLs without PFA with the power densities of 1.17 W/cm^2 at 0.45 V. Although 20PFA_C had thicker cCL ($X_{\text{Pt/TP}}$ of 0.7), it demonstrated higher performance at 0.45 V than 5PFA_C (1.10 W/cm^2), 10PFA_C (1.10 W/cm^2), and 10PFA_2_C (1.14 W/cm^2). This is attributed to the higher PFA amount in the cCL ($X_{\text{PFA/TP}}=0.4$). Despite having longer pore path, the higher amount of PFA nanoparticles provided improved water management promoting a reduction in the ohmic resistance. However, when the current density exceeded 2.6 mA/cm^2 , severe mass transport limitation was observed. This revealed that above 2.6 mA/cm^2 PFA nanoparticles could not facilitate water removal for this thickness of cCL. 10PFA_C demonstrated closer performance to 20PFA_C with a power density of 1.14 W/cm^2 . Furthermore, above 2.6 mA/cm^2 10PFA_C was less prone to flooding than 20PFA_C. This is attributed to the thickness of the cCL of 10PFA_C ($X_{\text{Pt/TP}}$ of 1.0). The thickness of the cCL of 10PFA_C was 30 % thinner than 20PFA_C.

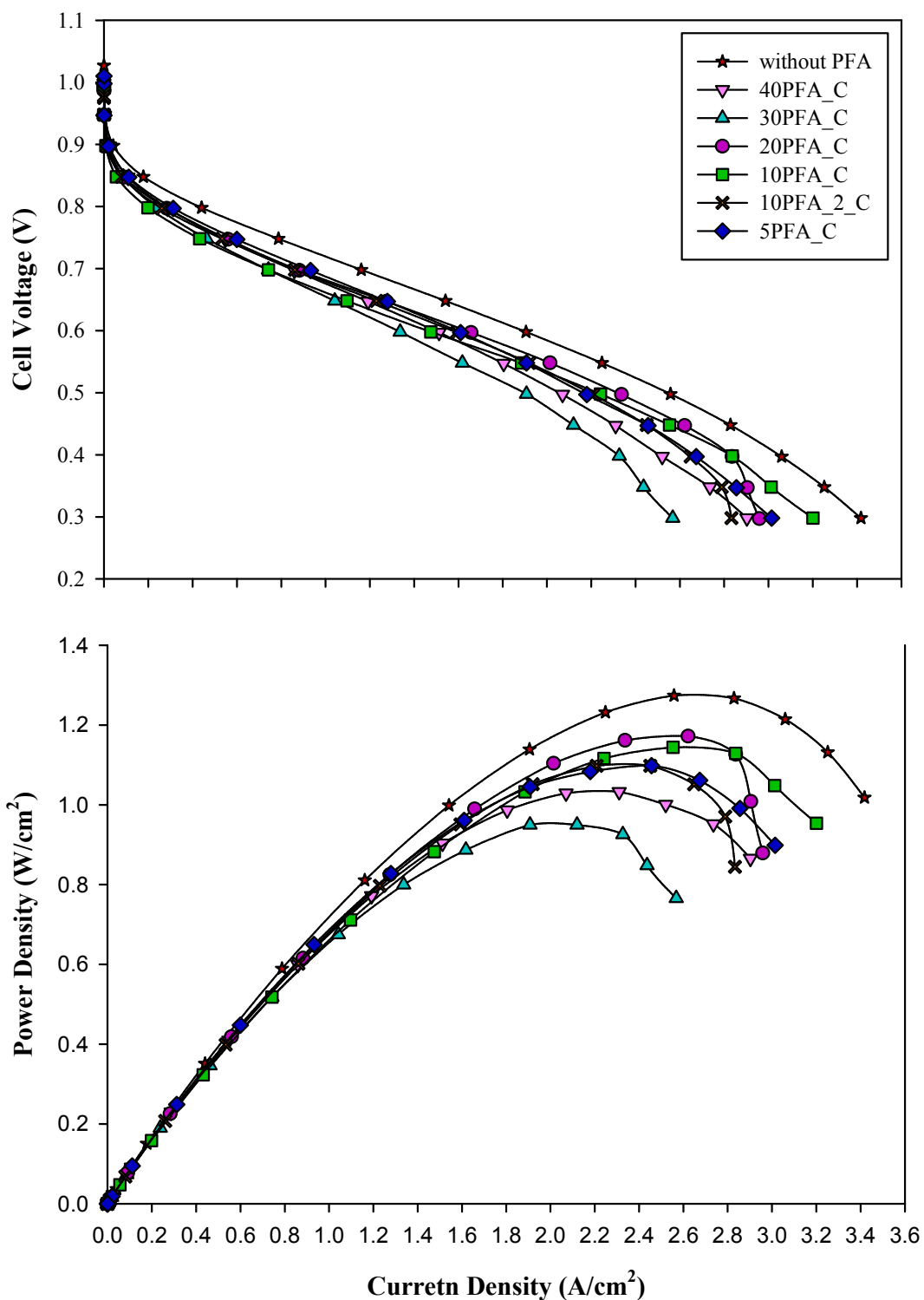


Figure 8.9 Polarization and power density curves of PEMFC for MEA2. Pt loading of anode and cathode electrodes was $0.4 \text{ mgPt}/\text{cm}^2$. Cathode catalyst layer was coated with PFA nanoparticles. H_2/O_2 gas-feeding mode was used

Thinner cCL provided mitigated flooding at higher current densities, despite including the lower amount of PFA ($X_{\text{PFA/TP}}=0.25$). This revealed that the thickness of the cCL has a great impact on the mass transport of gas and liquid. Although the cCL of 10PFA_C ($X_{\text{Pt/TP}}$ of 1.0) was thicker than the cCLs of 5PFA_C ($X_{\text{Pt/TP}}$ of 1.2) and 10PFA_2_C ($X_{\text{Pt/TP}}$ of 1.5), the lowest ohmic resistance was attained for 10PFA_C. The hydrophobicity of the cCL of 10PFA_2_C ($X_{\text{PFA/TP}}=0.33$) was higher than the cCL of 5PFA_C ($X_{\text{PFA/TP}}=0.14$) as well. If we look at Figure 8.9, we can see at the concentration polarization region that the pores of the cCL of the 10PFA_2_C were flooding which increase mass transport resistance. Higher hydrophobicity with thicker CL influenced the water management negatively at higher current densities (above 2.6 mA/cm^2). The power density of 40PFA_C (1.03 W/cm^2) was higher than 30PFA_C (0.95 W/cm^2), although they have the same thickness of the cCL ($X_{\text{Pt/TP}}$ of 0.4). Higher hydrophobicity in the cCL of 40PFA_C ($X_{\text{PFA/TP}}=0.67$) was promoted enhanced water management with respect to 30PFA_C ($X_{\text{PFA/TP}}=0.5$). This revealed that since the PFA nanoparticles were included to only cCL, higher hydrophobicity at thicker cCLs was more capable of managing water movement.

Figure 8.10 illustrates EIS spectra of MEA2 measured at 0.5 V at which thin film diffusion has a preponderant effect on mass transport. All CLs demonstrated an impedance spectrum with a high-frequency arc followed by a low-frequency arc. This revealed that the pores of the cGDLs of all MEAs were blocked with water molecules. Parameters of equivalent circuit modeling of EIS spectra for MEA1 are listed in Table 8.4. All of the MEAs demonstrated similar high-frequency resistances except 20PFA_C, which indicating the higher ohmic resistance of the membrane. The highest charge transfer resistance was obtained for 30PFA_C ($0.58 \text{ } \Omega\text{cm}^2$). Although the thickness of the cCL of 30PFA_C ($X_{\text{Pt/TP}}$ of 0.4) was the same as the thickness of the cCL of 40PFA_C, while the PFA amount of 40PFA_C was % 34 higher than 30PFA_C, the charge transfer resistance of 30PFA_C was higher than 40PFA_C ($0.40 \text{ } \Omega\text{cm}^2$). This revealed that the amount of PFA nanoparticles in the CLs of 30PFA_C could not mitigate flooding in the cCL. On the other hand, mass transfer resistance of 30PFA_C ($0.06 \text{ } \Omega\text{cm}^2$) was similar to the mass transfer resistance of 40PFA_C ($0.08 \text{ } \Omega\text{cm}^2$). This revealed that despite 30PFA_C had higher charge transfer resistance than 40PFA_C, which pointed out flooding in the cCL, water saturation in the pores of cGDL was similar. The charge transfer resistance of

5PFA_C ($0.47 \text{ } \Omega\text{cm}^2$) and 10PFA_2_C ($0.49 \text{ } \Omega\text{cm}^2$) was similar despite the thicknesses of the cCLs were different with the different amount of PFA nanoparticles. The thickness of the cCL of 10PFA_2_C ($X_{\text{Pt/TP}}$ of 1.5) was 20 % thinner than the cCL of 5PFA_C ($X_{\text{Pt/TP}}$ of 1.2), while the PFA amount was 58 % higher than 5PFA_C. The amount of PFA nanoparticles in the cCL of 5PFA_C was not sufficient to mitigate flooding in the cCL. The excess amount of water invaded primary and secondary pores, which caused diffusion limitations. Therefore, reaction rate reduced.

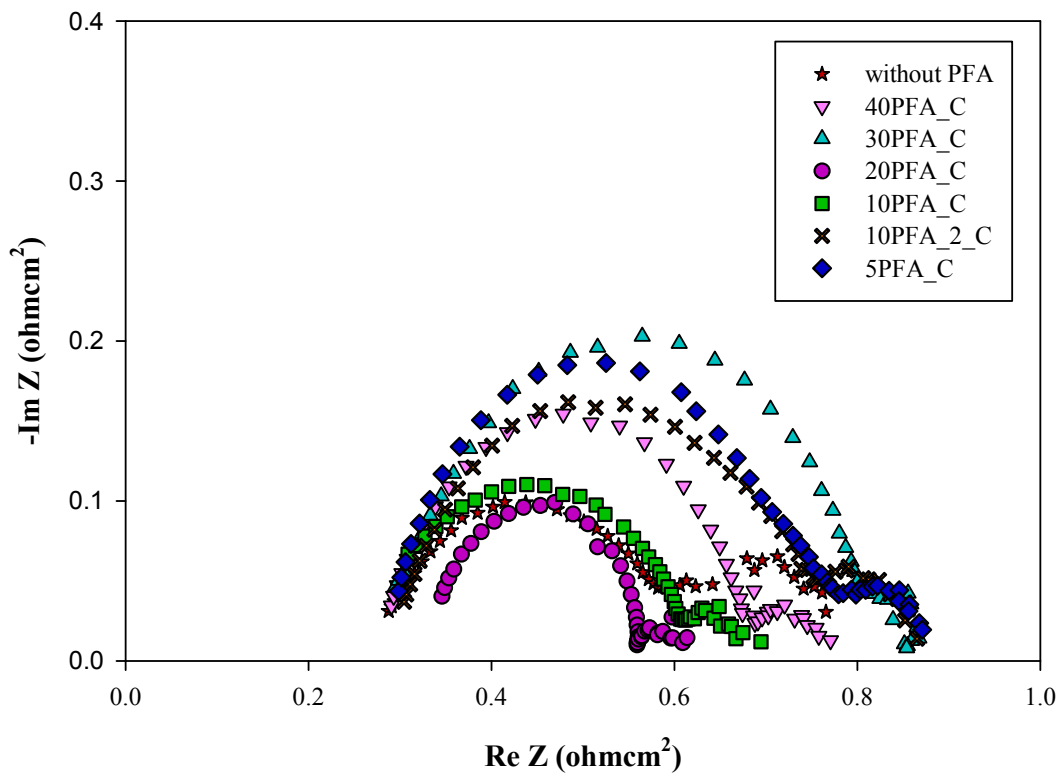


Figure 8.10 Electrochemical impedance spectra obtained at 0.5 V. Pt loading of anode and cathode electrodes was 0.4 mgPt/cm^2 . Cathode catalyst layer was coated with PFA nanoparticles. PEMFC was operated at H_2/O_2 gas-feeding mode

On the other hand, the amount of PFA nanoparticles in the cCL of 10PFA_2_C higher than required amount, which pushes the water molecules towards the cGDL leading to dehydration of ionomer around the aggregates of the

catalysts. Although in this case, charge transfer resistance increased. The charge transfer resistance of 20PFA_C ($0.27 \Omega\text{cm}^2$) was lower than the charge transfer resistances of 10PFA_C ($0.39 \Omega\text{cm}^2$) and the CLs without PFA ($0.33 \Omega\text{cm}^2$). The cCL of 20PFA_C ($X_{\text{Pt/TP}}$ of 0.7) was 30 % thicker than the cCL of 10PFA_C ($X_{\text{Pt/TP}}$ of 1.0) and the CLs without PFA ($X_{\text{Pt/TP}}$ of 1.5).

Table 8.4 Parameters of equivalent circuit modeling of EIS spectra of MEA2 at H_2/O_2 gas-feeding mode

MEA Type	O_2			
	$R_{\text{HF}} (\Omega\text{cm}^2)$	$R_{\text{ct}} (\text{A})(\Omega\text{cm}^2)$	$R_{\text{ct}} (\text{C})(\Omega\text{cm}^2)$	$R_{\text{mt}} (\Omega\text{cm}^2)$
without PFA	0.26	0.11	0.22	0.17
MEA2				
40PFA_C	0.27	0.08	0.32	0.08
30PFA_C	0.23	0.09	0.49	0.06
20PFA_C	0.30	0.04	0.23	0.04
10PFA_C	0.23	0.04	0.35	0.09
10PFA_2_C	0.28	0.09	0.38	0.11
5PFA_C	0.29	0.05	0.44	0.09

Furthermore, the amount of PFA nanoparticles ($X_{\text{PFA/TP}}$ of 0.4) of 20PFA_C was 38 % higher than the PFA amount in the CLs of 10PFA_C ($X_{\text{PFA/TP}}$ of 0.25). This revealed that PFA amount in the cCL of 10PFA_C was low to mitigate flooding. The lowest charge transfer resistance was attained for 20PFA_C ($0.27 \Omega\text{cm}^2$). It is lower than the charge transfer resistance of the CLs without PFA ($0.33 \Omega\text{cm}^2$). This revealed that PFA nanoparticles in the CLs of 20PFA_C provided enhanced water management, which led to lower charge transfer resistance.

8.3.6. Effect of PFA Loading on Performance and Running Electrochemical Impedance Spectrum of PEMFC at H₂/Air Gas-feeding Mode

PFA Loaded Catalyst Layers on Both Electrodes (MEA1):

Polarization and power density curves for CLs with six different Nafion and PFA loadings, working at H₂/Air gas-feeding mode are shown in Figure 8.11. The maximum power density at 0.45 V was 0.64 W/cm² for the CLs without PFA. 10PFA_2_AC had closer performances to the CLs without PFA with the power densities of 0.53 W/cm² at 0.45 V. This is attributed to the thickness of the CLs, which is lowest ($X_{Pt/TP}$ of 1.5). 10PFA_AC demonstrated higher performance, which is closer to 10PFA_2_AC with a power density of 0.51 W/cm² at 0.45 V. Although 5PFA_AC had thinner CLs ($X_{Pt/TP}$ of 1.2), it demonstrated lower performance than 10PFA_AC ($X_{Pt/TP}$ of 1.0). This is attributed to the lower PFA amount in the CLs of 5PFA_AC ($X_{PFA/TP}=0.14$), which was not sufficient to provide excess water removal. 20PFA_AC and 30PFA_AC demonstrated closer performance to 5PFA_AC with power densities of 0.42 W/cm² and 0.39 W/cm², respectively. 20PFA_AC had a slightly higher performance than 30PFA_AC because 20PFA_AC ($X_{Pt/TP}$ of 0.7) had thinner CLs than 30PFA_AC ($X_{Pt/TP}$ of 0.4), which made 20PFA_AC less prone to flooding. Despite having the same thickness of the CLs of 30PFA_AC ($X_{Pt/TP}$ of 0.4), 40PFA_AC demonstrated lower performance than 30PFA_AC. Higher hydrophobicity in the CLs of 40PFA_AC caused higher ohmic resistance because of reduced electronic and ionic conduction.

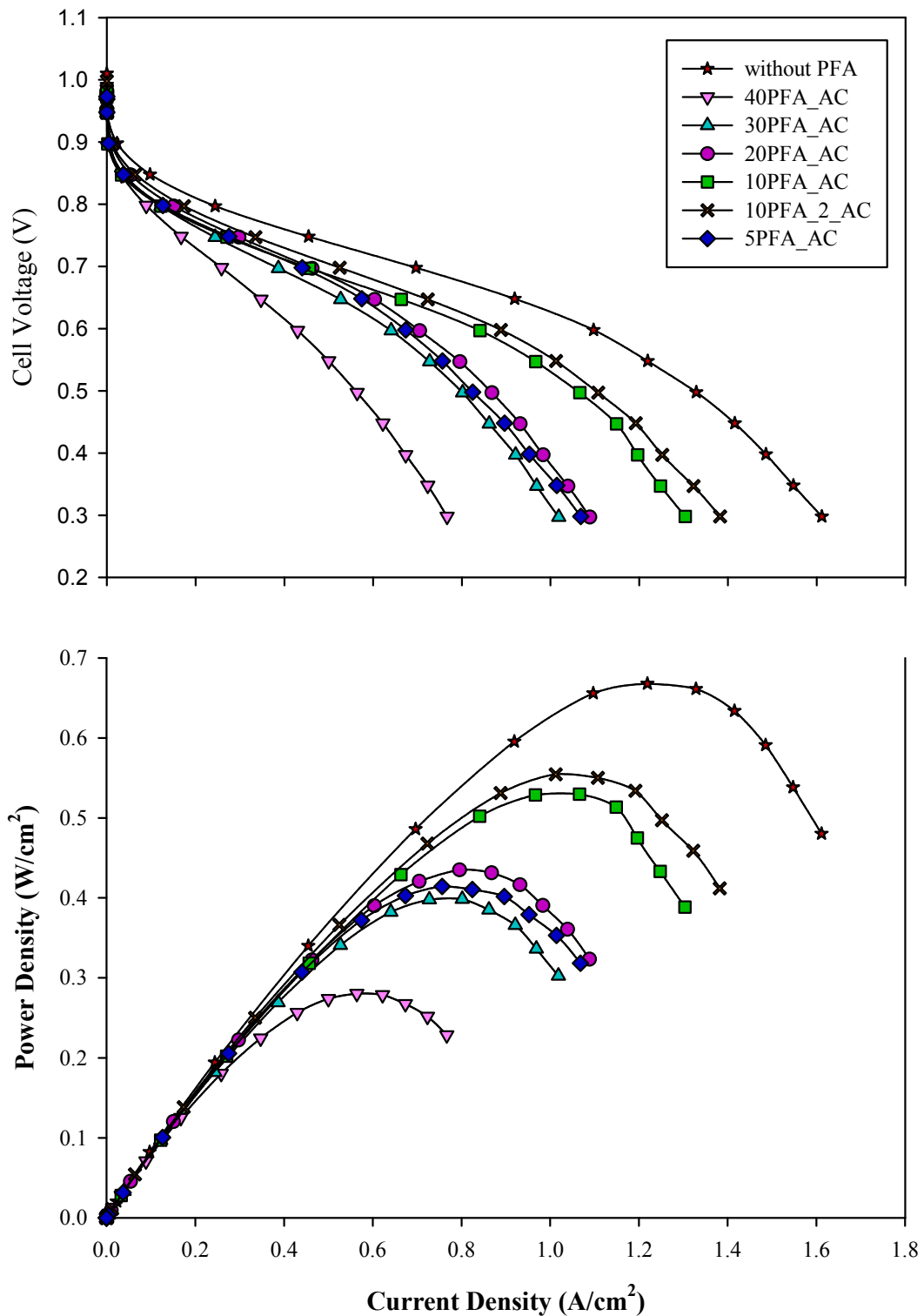


Figure 8.11 Polarization and power density curves of PEMFC for MEA1. Pt loading of anode and cathode electrodes was $0.4 \text{ mgPt}/\text{cm}^2$. Both anode and cathode catalyst layers were coated with PFA nanoparticles. PEMFC was operated at H_2/Air gas-feeding mode

Figure 8.12 illustrates EIS spectra of MEA1 measured at 0.5 V at which thin film diffusion has a preponderant effect on mass transport. All CLs demonstrated an impedance spectrum with a high-frequency arc. This revealed that mass transport limitations due to the pore blockage of the cGDLs were eliminated with high airflow rate. Parameters of equivalent circuit modeling of EIS spectra for MEA1 are listed in Table 8.5. All of the MEAs demonstrated similar high-frequency resistances except 40PFA_AC.

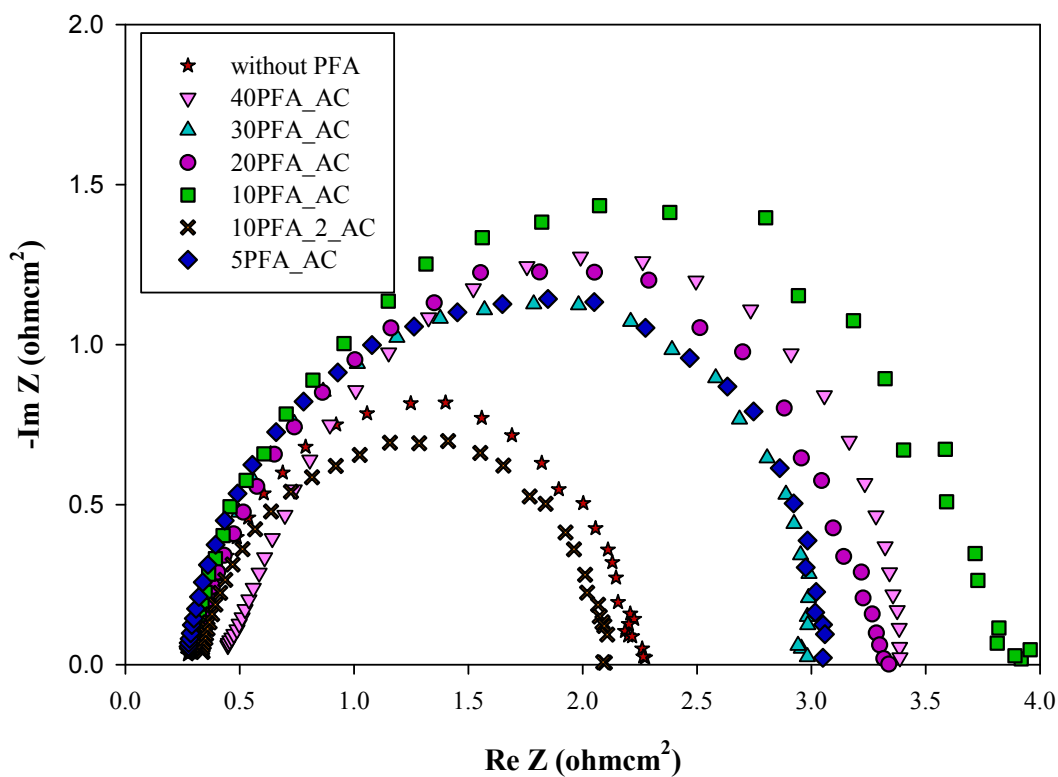


Figure 8.12 Electrochemical impedance spectra obtained for a running fuel cell at 0.5 V. Pt loading of anode and cathode electrodes was 0.4 mgPt/cm^2 . Both anode and cathode catalyst layers were coated with PFA nanoparticles. PEMFC was operated at H_2/Air gas-feeding mode

The high-frequency resistance of 40PFA_AC was the highest. The higher amount of PFA nanoparticles in the aCL of 40PFA_AC prevent the introduction of H_2 gas humidified with water vapor, therefore membrane dehydrated. In addition to

that higher amount of PFA nanoparticles in the CL, purge required water molecules towards the GDL, which caused dehydration of the ionomer in the CLs. The highest charge transfer resistance was obtained for 10PFA_AC ($3.69 \Omega\text{cm}^2$). The CLs of 10PFA_AC were thinner than the CLs of 40PFA_AC ($X_{\text{Pt/TP}}$ of 0.4), 30PFA_AC ($X_{\text{Pt/TP}}$ of 0.4), and 20PFA_AC ($X_{\text{Pt/TP}}$ of 0.7). In addition to that, PFA amount was the lowest compared to 40PFA_AC ($X_{\text{PFA/TP}}$ of 0.67), 30PFA_AC ($X_{\text{PFA/TP}}$ of 0.5), and 20PFA_AC ($X_{\text{PFA/TP}}$ of 0.4). This revealed that despite having thinner CLs, the amount of PFA nanoparticles was not sufficient to reduce water saturation in the pores of CLs. This led to additional diffusion limitations for oxygen to access triple phase boundaries. 40PFA_AC had higher charge transfer resistance ($2.98 \Omega\text{cm}^2$) than all CLs except 10PFA_AC. This is because the PFA amount in the CLs was the highest leading to dehydration of ionomer in the CLs. When the required water amount was not present in the cCL, protons could not be transported to the triple phase boundaries, and then the electrochemical reaction could not occur. On the other hand, charge transfer resistance of 20PFA_AC ($3.03 \Omega\text{cm}^2$) was higher than the charge transfer resistance of 30PFA_AC ($2.66 \Omega\text{cm}^2$).

Table 8.5 Parameters of equivalent circuit modeling of EIS spectra of MEA1 at H₂/Air gas-feeding mode

MEA Type	Air		
	$R_{\text{HF}} (\Omega\text{cm}^2)$	$R_{\text{ct}} (\text{A}) (\Omega\text{cm}^2)$	$R_{\text{ct}} (\text{C}) (\Omega\text{cm}^2)$
without PFA MEA1	0.24	0.14	1.86
40PFA_AC	0.42	0.42	2.56
30PFA_AC	0.30	1.07	1.59
20PFA_AC	0.28	1.10	1.93
10PFA_AC	0.23	0.05	3.64
10PFA_2_AC	0.23	0.09	1.81
5PFA_AC	0.27	1.38	1.44

This revealed that although CLs of 30PFA_AC ($X_{\text{Pt/TP}}$ of 0.4) was thicker than the CLs of 20PFA_AC ($X_{\text{Pt/TP}}$ of 0.7), the higher amount of PFA nanoparticles in the CLs of 30PFA_AC provided enhanced water management. Although,

5PFA_AC ($2.82 \Omega\text{cm}^2$) had thinner CLs than 20PFA_AC and 30PFA_AC, the charge transfer resistance of 5PFA_AC was similar to them. This is attributed to the lower amount of PFA nanoparticles in the CLs of 5PFA_AC ($X_{\text{PFA/TP}}$ of 0.14). PFA nanoparticles in the CLs of 5PFA_AC, could not achieve to mitigate flooding in the cCL, this caused high charge transfer resistance. The lowest charge transfer resistance was attained for the CLs of 10PFA_2_AC ($1.90 \Omega\text{cm}^2$). The charge transfer resistance of 10PFA_2_AC was lower than the charge transfer resistance of the CLs without PFA. This revealed that PFA nanoparticles in the CLs of 10PFA_2_AC provided enhanced water management and facilitated excess water removal.

PFA Loaded Catalyst Layer on Cathode Electrode (MEA1):

Polarization and power density curves for CLs with six different Nafion and PFA loadings, working at H₂/Air gas-feeding mode are shown in Figure 8.13. The maximum power density at 0.45 V was 0.64 W/cm^2 for the CLs without PFA. 10PFA_2_C and 20PFA_C had closer performances to the CLs without PFA with the power densities of 0.50 W/cm^2 and 0.49 W/cm^2 at 0.45 V, respectively. 10PFA_2_C had the cCL ($X_{\text{Pt/TP}}$ of 1.5) with the half thickness of the cCL of 20PFA_C ($X_{\text{Pt/TP}}$ of 0.7). However, PFA amount in the cCL of 10PFA_2_C was 40 % lower than the PFA amount in the cCL of 20PFA_C. Therefore, 10PFA_2_C had higher hydrophobicity in the cCL than 20PFA_C. This provided enhanced water management with the thinner cCL. The lower amount of PFA amount in the thinner cCL of 10PFA_2_C provided enhanced water management. 5PFA_C, 10PFA_C, and 30PFA_C demonstrated closer performance with power densities of 0.45 W/cm^2 , 0.46 W/cm^2 , and 0.44 W/cm^2 , respectively. 10PFA_C had a slightly higher performance than 5PFA_C, because 10PFA_C ($X_{\text{Pt/TP}}$ of 1.0) had 20 %thicker CL than 5PFA_C ($X_{\text{Pt/TP}}$ of 1.2), with 50 % higher PFA amount. Higher hydrophobicity in the 20 % thicker cCL of 10PFA_C provides enhanced water management. On the other hand, 30PFA_C had a cCL with three-fold thicker ($X_{\text{Pt/TP}}$ of 0.4) than the cCL of 5PFA_C ($X_{\text{Pt/TP}}$ of 1.2).

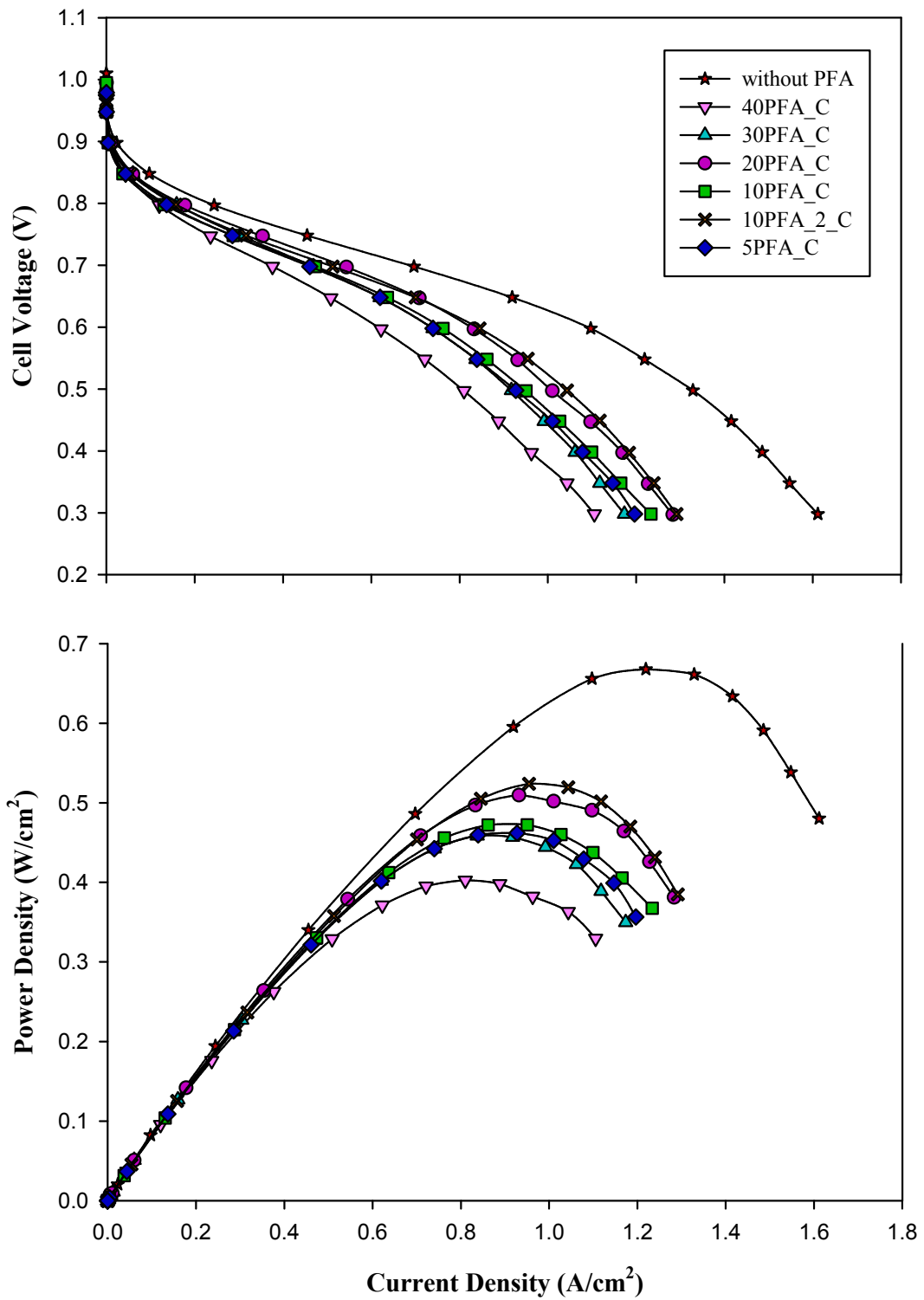


Figure 8.13 Polarization and power density curves of PEMFC for MEA2. Pt loading of anode and cathode electrodes was $0.4 \text{ mgPt}/\text{cm}^2$. Cathode catalyst layer was coated with PFA nanoparticles. PEMFC was operated at H_2/Air gas feeding mode

However, PFA amount in the cCL of 30PFA_C ($X_{PFA/TP}=0.5$), was 5 times higher than the PFA amount in the cCL of 5PFA_C ($X_{PFA/TP}=0.14$). Higher hydrophobicity in the thicker cCL provided enhanced water management although catalytic activity was lower than 5PFA_C. Despite having 40PFA_C the same thickness of CLs ($X_{Pt/TP}$ of 0.4) with the cCL of 30PFA_C, it demonstrated lower performance than 30PFA_C. Higher hydrophobicity in the CLs of 40PFA_C ($X_{PFA/TP}=0.67$) caused higher ohmic resistance because of settling on the electronic and ionic network.

Figure 8.14 illustrates EIS spectra of MEA2 measured at 0.5 V at which thin film diffusion has a preponderant effect on mass transport.

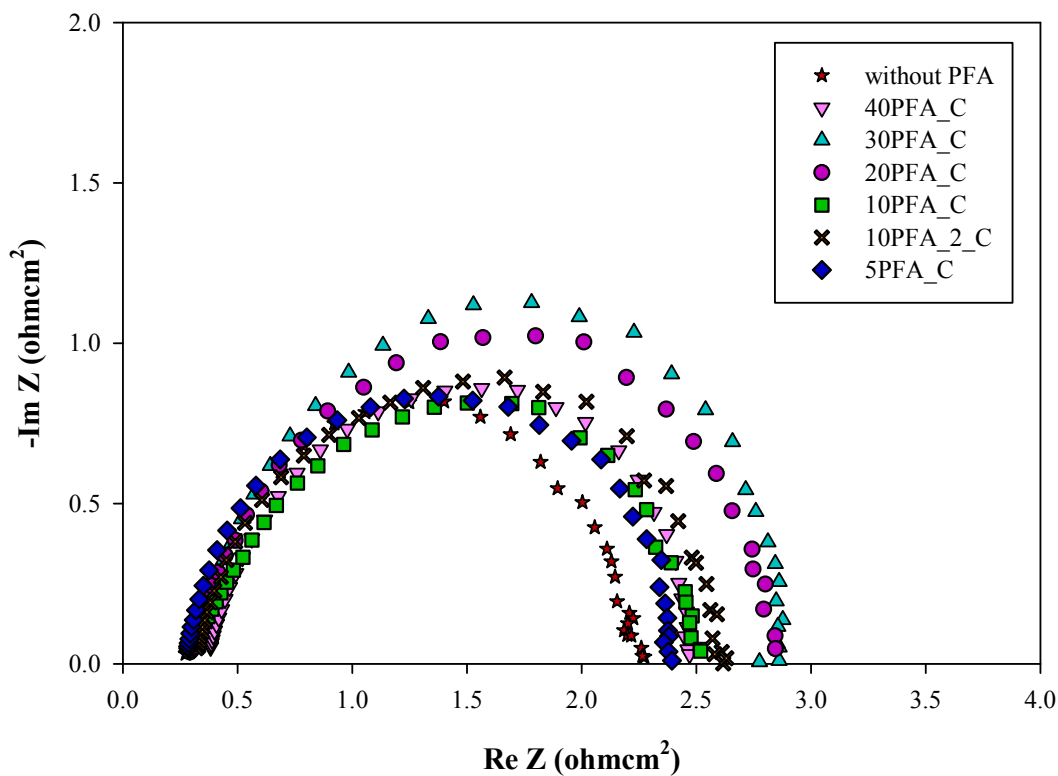


Figure 8.14 Electrochemical impedance spectra obtained for a running fuel cell at 0.5 V. Pt loading of anode and cathode electrodes was 0.4 mgPt/cm². Both anode and cathode catalyst layers were coated with PFA nanoparticles. PEMFC was operated at H₂/Air gas-feeding mode

All CLs demonstrated an impedance spectrum with only a high-frequency arc. This revealed that high airflow rate eliminated mass transport limitations due to the pore blockage of the cGDLs. Parameters of equivalent circuit modeling of EIS spectra for MEA2 are listed in Table 8.6. All of the MEAs demonstrated similar high-frequency resistances except 40PFA_C. The high-frequency resistance of 40PFA_C was the highest. The PFA nanoparticles in the cCL purged required water molecules towards the cGDL, which caused dehydration of the ionomer in the CLs. The highest charge transfer resistance was attained for 30PFA_C ($2.58 \Omega\text{cm}^2$). The thickness of the cCL of 30PFA_C ($X_{\text{Pt/TP}}$ of 0.4) was same as the thickness of the cCL of 40PFA_C ($X_{\text{Pt/TP}}$ of 0.4); however, PFA amount of 30PFA_C ($X_{\text{PFA/TP}}$ of 0.5) was lower than 40PFA_C ($X_{\text{PFA/TP}}$ of 0.67). For the same thickness of the cCL, the amount of PFA in the cCL of 30PFA_C was not sufficient to reduce the film thickness around the aggregates leading to diffusion limitations. The charge transfer resistance of 20PFA_C ($2.59 \Omega\text{cm}^2$) was the same to the charge transfer resistance of 30PFA_C. 20PFA_C had 43 % thinner cCL ($X_{\text{Pt/TP}}$ of 0.7) with 20 % lower PFA amount ($X_{\text{PFA/TP}}$ of 0.4) according to 30PFA_C. The lower amount of PFA in the cCL of 20PFA_C was not sufficient to mitigate flooding.

Table 8.6 Parameters of equivalent circuit modeling of EIS spectra of MEA2 at H₂/Air gas-feeding mode

MEA Type	Air		
	$R_{\text{HF}} (\Omega\text{cm}^2)$	$R_{\text{ct}} (\text{A})(\Omega\text{cm}^2)$	$R_{\text{ct}} (\text{C})(\Omega\text{cm}^2)$
without PFA MEA2	0.24	0.14	1.86
40PFA_C	0.37	0.91	1.19
30PFA_C	0.27	0.42	2.16
20PFA_C	0.29	1.09	1.50
10PFA_C	0.24	0.28	2.04
10PFA_2_C	0.31	0.18	2.16
5PFA_C	0.25	0.02	2.13

The cCL of 10PFA_2_C ($X_{\text{Pt/TP}}$ of 1.5) was the thinner than 40PFA_C ($X_{\text{Pt/TP}}$ of 0.4), 10PFA_C, ($X_{\text{Pt/TP}}$ of 1.0) and 5PFA_C ($X_{\text{Pt/TP}}$ of 1.2). However, the charge

transfer resistance of 10PFA_2_C ($2.34 \Omega\text{cm}^2$) was higher than 40PFA_C ($2.10 \Omega\text{cm}^2$), 10PFA_C, ($2.32 \Omega\text{cm}^2$) and 5PFA_C ($2.15 \Omega\text{cm}^2$). Despite having thinner cCL, the charge transfer resistance was highest among all. This revealed that PFA amount in such a thin cCL of 10PFA_2_C was high causing dehydration of ionomer in the cCL. The lowest charge transfer resistance was attained for CLs without PFA. This revealed that in this MEA configuration with the addition of PFA nanoparticles, enhanced water management could not be achieved.

8.3.7. Cross-section Images of MEA after Performance Testing

SEM images of cross section area of the membrane electrode assemblies prepared with commercial catalyst impregnated with Nafion (without PFA) with 1.2 mg/cm^2 Pt loading, without PFA with 0.4 mg/cm^2 Pt loading, 5PFA_C with 1.2 mg/cm^2 Pt loading, 20PFA_C with 0.4 mg/cm^2 Pt loading are shown in Figure 8.15. The two-sided arrows on the images illustrate anode and cathode side of the MEAs. Surface morphology of the MEA of 5PFA_C after fuel cell testing is shown in Figure 8.15c. In addition, the surface morphology of the MEA after fuel cell testing of 20PFA_C is shown in Figure 8.15d. The thickness of the CLs with 1.2 mg/cm^2 Pt loading (Figure 8.15c) was higher than the thickness of the CLs with 0.4 mg/cm^2 Pt loading (Figure 8.15d). This revealed that the thickness of the CLs increased since the Pt loading increased. The membrane has a similar thickness along the whole length, which indicated insignificant deformation due to swelling for 5PFA_C with 1.2 mg/cm^2 Pt loading. Some cracks in the CLs of 5PFA_C can be observable (shown with red arrows on the image) on the image. However, deformation in anode and cathode catalyst layers of 20PFA_C was not observable. This revealed that since the Pt loading increased to 1.2 mg/cm^2 brittleness of the anode and cathode catalyst layers increased. PFA nanoparticles have similar physical characteristics to FEP nanoparticles, which were softer than PTFE nanoparticles. Therefore, at low Pt loaded CLs, PFA nanoparticles did not cause any cracks at the CL.

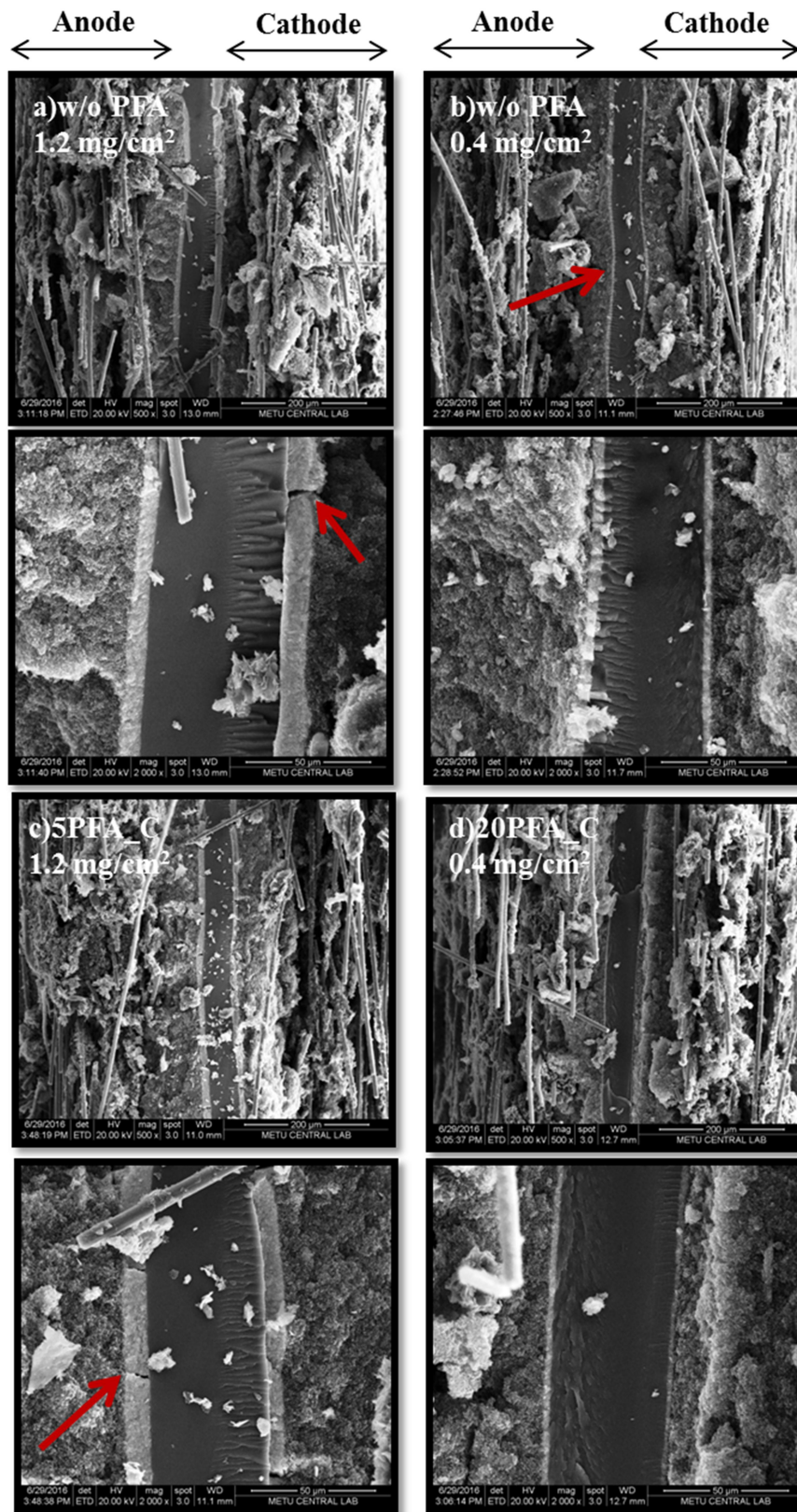


Figure 8.15 SEM images of the cross-section of the MEAs for a) without PFA with 1.2 mg/cm² Pt loading, b) without PFA with 0.4 mg/cm² Pt loading, c) 5PFA_C with 1.2 mg/cm² d) 20PFA_C with 0.4 mg/cm²

8.4. Conclusions

In this chapter, for the PFA including CLs, the similar conclusion can be drawn with the PTFE and FEP including CLs. Controversially to FEP results, but similar to PTFE results, 10 wt. % of PFA nanoparticles can mitigate flooding, because, PFA nanoparticles are less hydrophobic than FEP nanoparticles similar to PTFE nanoparticles. Therefore, low amount of PFA nanoparticles (5 w %) was not sufficient to facilitate excess water removal.

Nafion addition to the commercial catalyst reduced a significant amount of the pore volume, however, PFA addition to Nafion impregnated catalyst does not cause further reduction in the pore volume.

Total surface area of Pt particles in the catalyst powders does not alter with the addition of PFA nanoparticles; even Pt percentage in the catalyst powder reduces by the addition of PFA nanoparticles. This indicates that when Pt percentage in the commercial catalyst was higher, Pt agglomeration occurs, which causes reduced active surface area. Therefore, even if Pt percentage in the PFA included catalyst powder is lower, total surface area of Pt nanoparticles remains constant.

Cumulative pore volume has a great impact on the performance of the cell. When the percentage of the primary pores contributed to the cumulative pore volume increased, Pt utilization enhances, therefore cell performance increases. 2-step ink preparation method provides homogenous distribution of the Pt, Nafion, and PFA nanoparticles, which enhances Pt utilization in the case of the low amount of Pt. In addition to that, for the catalyst powders including 10 wt % PFA, 2-step ink preparation method improved Pt utilization according to the commercial catalyst.

The thickness of the CLs and the PFA amount in the CLs are competing parameters dominating the water transport mechanisms at H₂/O₂ feeding mode. In the case of H₂/Air feeding mode, airflow rate was the dominant parameter influencing water movement in the pores of cGDL.

High airflow rate prevents pore blockage at the cathode GDL for both MEA configurations.

When air is used as the reactant gas of the CLs included into both MEA1 and MEA2 configurations, the charge transfer resistances increases up to 6 times of the charge transfer resistances of the CL operated at H₂/O₂ feeding mode.

The CLs including 20 wt % PFA demonstrated higher performances than expected because charge transfer resistances was the lower at both feeding modes and also for both MEA configurations.

The increase in the PFA amount in the CLs made the CLs brittle, which causes cracks in the CL-leading to electronic and ionic disruption. However, the brittleness of the CLs is not as severe as the CLs including PTFE nanoparticles, because PFA nanoparticles were softer than PFA nanoparticles.

Although PFA included catalyst powders prepared with 2-step ink preparation, which provided enhanced Pt utilization, PFA nanoparticles in CLs caused a reduction in the cell performance. The highest performance is always attained for the CLs without PFA.

CHAPTER 9

CONCLUSIONS AND RECOMMENDATIONS

Commercial catalyst (Pt/C), commercial catalyst impregnated with Nafion without hydrophobic agent and hydrophobic catalyst powders including PTFE, FEP, PFA were characterized by thermogravimetric analysis, differential thermal analysis, ICP_MS (Inductively Coupled Plasma – Mass Spectrometer), X-ray diffraction, nitrogen physisorption, scanning electron microscope, transmission electron microscopy, energy dispersive X-ray spectroscopy, cyclic voltammetry analyses. In addition, performance tests and electrochemical impedance spectrometry for running fuel cell were carried out with oxygen or atmospheric air, and hydrogen. SEM analysis showed the change in the structure of MEA after performance tests. The influence of FEP and PFA nanoparticles incorporated to the CLs confirm the physical and electrochemical results obtained with PTFE nanoparticles.

Thermogravimetric analysis indicated that hydrophobic nanoparticles did not accelerate catalyst decomposition, moreover, increased the thermal stability of the catalyst. XRD analysis revealed that Nafion impregnation to 20 wt % Pt/C powder increased Pt agglomeration, therefore, decreased total Pt surface area. However, in the case of a commercial catalyst including 70 wt % Pt a significant agglomeration is not observed, therefore, a significant decrease in the total surface area of the Pt nanoparticles is not observed. Cyclic voltammetry analysis revealed that Nafion impregnation to Pt/C catalyst, decreased electrochemical surface area, however, enhanced Pt utilization for the catalyst powders prepared with 20 wt % Pt/C. However, hydrophobic nanoparticle addition to the commercial catalyst impregnated with Nafion decreased electrochemical surface area as well as Pt utilization for the

catalyst powders prepared with 20 wt % Pt/C. On the other hand, neither a significant decrease in the electrochemical surface area nor Pt utilization is not obtained for the catalyst powders prepared with a commercial catalyst including 70 wt % Pt. This is attributed to the high Pt content of the commercial catalyst. Since the Pt content of the commercial catalyst is high, Pt nanoparticles aggregate and cause a reduction in the Pt surface area. When Pt percentage in the catalyst powder decreased, with 2-step ink preparation method, well the distribution of Pt particles can be provided. Therefore, an increase in the diameter of Pt particles and decrease in the total surface area of Pt particles is not observed, because of this, the negative effect of hydrophobic nanoparticle addition to the Pt utilization of the catalyst powder cannot detect. While SEM and TEM images of the catalyst powders prepared with 20 wt % Pt/C illustrate Pt agglomeration, Pt agglomeration at the images of catalyst powders prepared with 70 wt % Pt/C isn't shown. Nitrogen physisorption analysis revealed that Nafion addition decreases the cumulative pore volume by occupying most of the primary pores of catalyst powders prepared with both commercial catalysts. The higher amount of hydrophobic nanoparticle addition (above 10 wt %) to the powder of Nafion impregnated commercial catalyst for both commercial catalysts, further decreases the cumulative pore volume. However, hydrophobic nanoparticle amount below 10 wt % Pt does not make a significant change in the cumulative pore volume. Performances of the hydrophobic catalyst powders including 10 wt % hydrophobic nanoparticle (10PTFE, 10FEP, and 10PFA) higher performance. This is attributed to the higher cumulative pore volume constructed with a higher percentage of primary pores (above 40 %). A higher percentage of primary pores contributed to the cumulative pore volume enhanced the cell performance, because primary pores behave as a reaction volume, while secondary pores behave as transport channels. Carbon amount in the commercial catalyst including 20 wt % Pt is almost 2.5 times higher than the carbon amount in the commercial catalyst including 70 wt % Pt, a cumulative pore volume of a commercial catalyst including 70 wt % Pt. However, a cumulative pore volume of a commercial catalyst including 70 wt % Pt is 23 % higher than the cumulative pore volume of the commercial catalyst including 20 wt % Pt. This is attributed to the high surface area carbon involved in the high Pt content commercial catalyst.

Enhanced performance is provided with 30 wt % PTFE in the low Pt content commercial catalyst with respect to commercial catalyst impregnated with Nafion (30PTFE_AC). This pointed out that two-phase flow is provided with 30 wt % hydrophobic nanoparticle addition. However, enhanced performance cannot be attained even with five and 10-wt % hydrophobic nanoparticle addition into the high Pt content commercial catalyst. This is attributed to the differences in the Pt and carbon content of the catalyst powders. As the Pt content in the commercial catalyst increases, agglomeration of Pt particles increases leading to decrease in the total surface area of the Pt. On the other hand, the cumulative pore volume of 30PTFE_AC prepared with low Pt content commercial catalyst is 73 % higher than the cumulative pore volume of 30PTFE_AC prepared with high Pt content commercial catalyst. This is attributed to the differences in the carbon content of the commercial catalysts. Even if 30PTFE_AC prepared with 70 wt % Pt/C including high surface area carbon, both the volume of the primary and secondary pores is lower than 30PTFE_AC prepared with 70 wt % Pt/C. This points out that high percentage of carbon provides higher pore volume for hydrophobic catalyst powders. This reveals that there is an upper point for Pt/C ratio for commercial catalysts used for hydrophobic CLs. If the Pt/C ratio exceeds one, enhanced performance with hydrophobic nanoparticle addition cannot be attained.

Electrode preparation technique has a great impact on cell performance. Ultrasonic coating technique used in this study provides homogenous distribution of catalysts at the surface of the GDL. In addition to that, with that atomizing technique, reproducibility of the electrodes can be provided. Therefore, this technique helps improving cell performance.

Reactant gas introduced to cathode has a great impact on the cell performance. As air used at cathode instead of oxygen, cell performance decreased to its half value of the value obtained with oxygen. When oxygen introduces to the cathode side with nitrogen, the concentration of oxygen accessed to active sites in a one-unit time decrease, this leads to decrease in performance per time. On the other hand, oxygen has to diffuse through also nitrogen to reach the active sites. This brings additional diffusion limitations to thin film diffusion, which increases the charge transfer resistance of CLs operated with air up to six times of the values that operated with oxygen. On the other hand, high airflow rate increases the gas pressure

at cGDL/cFL interface. Increased gas pressure promotes increased back diffusion rate of water by pushing accumulated water in the pores of cGDL towards cCL. By this way, blocked pores are opened to gas transport, which diminishing flooding at cathode GDL. Therefore, mass transfer resistance due to pore blockage at cGDL is eliminated with high airflow rate.

Due to its higher hydrophilic sites within the hydrophobic backbone in addition to the higher hydrophobicity of FEP nanoparticles with respect to PTFE and PFA nanoparticles might be more advantageous when used at lower amounts (5 wt %) according to PTFE and PFA nanoparticles (10 wt%). When the hydrophobic nanoparticle amount exceeds over 10 wt % in the CLs, the pores are almost closed with hydrophobic nanoparticles, which causes a severe reduction in the cumulative pore volume. This leads to decreased in the cell performance.

There is not any significant difference between the performances of the MEA1 and MEA2 configurations even the type of hydrophobic nanoparticles and the oxidant gas changes. The charge, mass transfer, and high-frequency resistances are also similar for both MEA configurations for all type of hydrophobic nanoparticles and for both oxidant gasses. This is because the hydrophobic nanoparticles in the CLs behave like a capillary barrier, which try to control the water transport through the pores. They do not influence the total water concentration in the cell. Therefore, a significant influence of hydrophobic nanoparticles in anode CL cannot be detected. However, a higher amount of hydrophobic nanoparticles in the aCL may prevent membrane humidification. On the other hand, a lower amount of hydrophobic nanoparticles in the aCL may enhance the membrane humidification. Furthermore, not only hydrophobic nanoparticles but also the thickness of the cCL has a preponderant effect on water management. There is an optimum ratio between the thickness of the cCL and the hydrophobicity. As a future work, the optimum ratio of catalyst layer thickness to hydrophobic nanoparticle amount can be studied.

The impedance spectroscopy results obtained at 0.5 V give us an idea about the thickness of water film around the aggregates. To determine the effect of hydrophobic nanoparticles on the catalytic activity of CLs, the cell voltage should be higher than 0.6 V. Therefore, the results obtained at 0.5 V predominantly represent the concentration polarization region of the V-I curves. This points out that correlating charge transfer resistance with cell performance or catalytic activity of

the cell will not give the correct answer. On the other hand, there are several discussions about the philosophy of the low-frequency arc. Some researchers think that low-frequency arc is related to the back diffusion rate of water, some other researchers think that it represents the mass transport limitations at the triple phase boundaries, and finally some researchers think that it is related to mass transport limitations encountered in the pores of cGDL. After all these experiments, I think that the high-frequency arc (charge transfer resistances) obtained in this study give us an idea about the mass transport limitations at the triple phase boundaries. On the other hand, low-frequency arc is related to the accumulated water in the pores of cathode GDL, because all the experiments carried out with air revealed that when airflow is higher than the stoichiometric ratio, the low-frequency arc disappears.

The equivalent circuit modeling is very important to interpret the impedance spectroscopy data. In my dissertation, I used an equivalent circuit data including four resistances, representing high-frequency resistance, charge transfer resistance of anode, charge transfer resistance of cathode, and mass transport resistance, respectively. However, most of the researchers neglect the charge transfer resistance of anode. I did not neglect the charge transfer resistance of anode, because, the raw data of impedance spectroscopy results mostly did not form a perfect arc, which can fit the equivalent circuit model of randles cell. At some arcs, there is a steeper region at the initial point of the high-frequency arc, which may represent the charge transfer resistance of anode. Therefore, I need to add an additional resistance for the charge transfer resistance of anode. However, the total of the charge transfer resistances of anode and cathode give the exact magnitude of the charge transfer resistance. On the other hand, instead of infinite Warburg diffusion with a line with a slope of 45° in the low-frequency region, finite Warburg diffusion with a low-frequency arc is observed. This means a complete flooding is not observed even with the CLs without hydrophobic nanoparticle. This may attribute to the hydrophobic agent, which is already included in the powder of commercial catalyst by the Product Company. As a future work, the research of water management with hydrophobic CL will be performed with a Pt/C catalyst powder, which is produced in the laboratory.

REFERENCES

- Antolini, E. et al., 1999. Influence of Nafion loading in the catalyst layer of gas-diffusion electrodes for PEFC. *Journal of Power Sources*, 77(2), pp.136–142.
- Antolini, E. et al., 2001. Physical and morphological characteristics and electrochemical behaviour in PEM fuel cells of PtRu /C catalysts. *Journal of Solid State Electrochemistry*, 5(2), pp.131–140.
- Avcioglu, G.S. et al., 2015. High performance PEM fuel cell catalyst layers with hydrophobic channels. *International Journal of Hydrogen Energy*, 40(24), pp.7720–7731.
- Barbir, F., 2005. PEM Fuel Cells: Theory and Practice.
- Baturina, O.A., Aubuchon, S.R. & Wynne, K.J., 2006. Thermal Stability in Air of Pt/C Catalysts and PEM Fuel Cell Catalyst Layers. *Chemistry of Materials*, 18(6), pp.1498–1504.
- Bayrakçeken, A. et al., 2008. Pt-based electrocatalysts for polymer electrolyte membrane fuel cells prepared by supercritical deposition technique. *Journal of Power Sources*, 179, pp.532–540.
- Bayrakceken, A., Turker, L. & Eroglu, I., 2008. Improvement of carbon dioxide tolerance of PEMFC electrocatalyst by using microwave irradiation technique. *International Journal of Hydrogen Energy*, 33(24), pp.7527–7537.
- Benziger, J. et al., 2005. Water flow in the gas diffusion layer of PEM fuel cells. *Journal of Membrane Science*, 261(1-2), pp.98–106.
- Blanco, M. & Wilkinson, D.P., 2014. Investigation of the effect of microporous layers on water management in a proton exchange membrane fuel cell using novel diagnostic methods. *International Journal of Hydrogen Energy*, 39(29), pp.16390–16404.
- Brunauer, S. et al., 1940. On a Theory of the van der Waals Adsorption of Gases. *J*

Am Chem Soc, 62(7), pp.1723–1731.

Bunmark, N. et al., 2010. Assisted water management in a PEMFC with a modified flow field and its effect on performance. *International Journal of Hydrogen Energy*, 35(13), pp.6887–6896.

Le Canut, J.-M., Abouatallah, R.M. & Harrington, D. a., 2006. Detection of Membrane Drying, Fuel Cell Flooding, and Anode Catalyst Poisoning on PEMFC Stacks by Electrochemical Impedance Spectroscopy. *Journal of The Electrochemical Society*, 153(5), p.A857.

Chen, J. et al., 2006. Suitability of some fluoropolymers used as base films for preparation of polymer electrolyte fuel cell membranes. *Journal of Membrane Science*, 277(1-2), pp.249–257.

Chen, J., Matsuura, T. & Hori, M., 2004. Novel gas diffusion layer with water management function for PEMFC. *Journal of Power Sources*, 131(1-2), pp.155–161.

Cheng, X. et al., 1999. Investigation of platinum utilization and morphology in catalyst layer of polymer electrolyte fuel cells. *Journal of Power Sources*, 79(1), pp.75–81.

Cho, K.T. & Mench, M.M., 2010. Fundamental characterization of evaporative water removal from fuel cell diffusion media. *Journal of Power Sources*, 195(12), pp.3858–3869.

Cho, K.T. & Mench, M.M., 2012. Investigation of the role of the micro-porous layer in polymer electrolyte fuel cells with hydrogen deuterium contrast neutron radiography. *Physical chemistry chemical physics : PCCP*, 14(12), pp.4296–302.

Ciureanu, M., Mikhailenko, S.D. & Kaliaguine, S., 2003. PEM fuel cells as membrane reactors: kinetic analysis by impedance spectroscopy. *Catalysis Today*, 82(1-4), pp.195–206.

Ciureanu, M. & Roberge, R., 2001. Electrochemical impedance study of PEM fuel cells. Experimental diagnostics and modeling of air cathodes. *Journal of Physical Chemistry B*, 105(17), pp.3531–3539.

- Cooper, K.R. & Smith, M., 2006. Electrical test methods for on-line fuel cell ohmic resistance measurement. *Journal of Power Sources*, 160(2), pp.1088–1095.
- Dai, W. et al., 2009. A review on water balance in the membrane electrode assembly of proton exchange membrane fuel cells. *International Journal of Hydrogen Energy*, 34(23), pp.9461–9478.
- Devrim, Y. et al., 2013. Nafion/titanium silicon oxide nanocomposite membranes for PEM fuel cells. *International Journal of Energy Research*, 37(5), pp.435–442.
- Do, D.D., 1998. Adsorption Analysis: Equilibria and Kinetics. *Chemical Engineering*, 2(Imperial College Press), p.913.
- Erkan, S. & Eroglu, I., 2015. Ultrasonic Spray Coating Technique for High-Performance PEM Fuel Cell Electrode Manufacturing. In I. Dincer et al., eds. *Progress in Clean Energy, Volume 2, Novel Systems and Applications*. Springer International Publishing, pp. 481–492.
- Fei, G. et al., 2012. Radiolytic preparation of PFA-g-PVBSA membranes as a polymer electrolyte membrane. *Nuclear Instruments and Methods in Physics Research Section B: Beam Interactions with Materials and Atoms*, 274, pp.83–86.
- Fiçicilar, B., Bayrakçeken, A. & Eroğlu, I., 2009. Effect of Pd loading in Pd-Pt bimetallic catalysts doped into hollow core mesoporous shell carbon on performance of proton exchange membrane fuel cells. *Journal of Power Sources*, 193(1), pp.17–23.
- Forner-Cuenca, A. et al., 2015. Engineered Water Highways in Fuel Cells: Radiation Grafting of Gas Diffusion Layers. *Advanced Materials*, 27(41), pp.6317–6322.
- Freire, T.J.P. & Gonzalez, E.R., 2001. Effect of membrane characteristics and humidification conditions on the impedance response of polymer electrolyte fuel cells. *Journal of Electroanalytical Chemistry*, 503, pp.57–68.
- Friedmann, R. & Nguyen, T. Van, 2008. Optimization of the Cathode Catalyst Layer Composition using a Novel 2-step Preparation Method. *ECS Transactions*, 16(2), pp.2021–2029.
- Friedmann, R. & Van Nguyen, T., 2010. Optimization of the Microstructure of the

- Cathode Catalyst Layer of a PEMFC for Two-Phase Flow. *Journal of The Electrochemical Society*, 157(2), pp.B260–B265.
- Gasteiger, H.A. et al., 2005. Activity benchmarks and requirements for Pt, Pt-alloy, and non-Pt oxygen reduction catalysts for PEMFCs. *Applied Catalysis B: Environmental*, 56(1-2 SPEC. ISS.), pp.9–35.
- Gubler, L., Gürsel, S.A. & Scherer, G.G., 2005. Radiation Grafted Membranes for Polymer Electrolyte Fuel Cells. *Fuel Cells*, 5(3), pp.317–335.
- He, C., 1997. Evaluation of Platinum-Based Catalysts for Methanol Electro-oxidation in Phosphoric Acid Electrolyte. *Journal of The Electrochemical Society*, 144(3), p.970.
- Ji, M. & Wei, Z., 2009. A Review of Water Management in Polymer Electrolyte Membrane Fuel Cells. *Energies*, 2(4), pp.1057–1106.
- Jiao, K. & Li, X., 2011. Water transport in polymer electrolyte membrane fuel cells. *Progress in Energy and Combustion Science*, 37(3), pp.221–291.
- Joo, J. et al., 2014. Controlled water flooding of polymer electrolyte fuel cells applying superhydrophobic gas diffusion layer. *Current Applied Physics*, 14(10), pp.1374–1379.
- Jung, D.H. et al., 2003. Preparation and performance of a Nafion®/montmorillonite nanocomposite membrane for direct methanol fuel cell. *Journal of Power Sources*, 118(1-2), pp.205–211.
- Kaneko, K., 1994. Determination of pore size and pore size distribution. *Journal of Membrane Science*, 96(1-2), pp.59–89.
- Kang, S.A. et al., 2009. Preparation of crosslinked polystyrene-grafted PFA films by a simultaneous irradiation method. *Journal of Industrial and Engineering Chemistry*, 15(4), pp.516–519.
- Kang, S.A. et al., 2010. Radiolytic preparation of poly(styrene sulfonic acid) - Grafted poly(tetrafluoroethylene-co-perfluorovinyl vinyl ether) membranes with highly cross-linked networks. *Nuclear Instruments and Methods in Physics Research, Section B: Beam Interactions with Materials and Atoms*, 268(22), pp.3458–3463.

- Kim, S. & Mench, M.M., 2009. Investigation of temperature-driven water transport in polymer electrolyte fuel cell: Thermo-osmosis in membranes. *Journal of Membrane Science*, 328(1-2), pp.113–120.
- Kitahara, T. et al., 2014. Triple microporous layer coated gas diffusion layer for performance enhancement of polymer electrolyte fuel cells under both low and high humidity conditions. *Journal of Power Sources*, 248, pp.1256–1263.
- Kitahara, T., Nakajima, H. & Mori, K., 2012. Hydrophilic and hydrophobic double microporous layer coated gas diffusion layer for enhancing performance of polymer electrolyte fuel cells under no-humidification at the cathode. *Journal of Power Sources*, 199, pp.29–36.
- Kurzweil, P. & Fischle, H.J., 2004. A new monitoring method for electrochemical aggregates by impedance spectroscopy. *Journal of Power Sources*, 127(1-2), pp.331–340.
- Lappan, U., Geißler, U. & Uhlmann, S., 2007. Pre-Irradiation Grafting of Styrene into Modified Fluoropolymers. *Macromolecular Symposia*, 254(1), pp.254–259.
- Latorrata, S. et al., 2015. Design of properties and performances of innovative gas diffusion media for polymer electrolyte membrane fuel cells. *Progress in Organic Coatings*, 78, pp.517–525.
- Latorrata, S. et al., 2014. Novel superhydrophobic microporous layers for enhanced performance and efficient water management in PEM fuel cells. *International Journal of Hydrogen Energy*, 39(10), pp.5350–5357.
- Lebedev, Y. et al., 2010. X-ray powder diffraction study of polytetrafluoroethylene. *Crystallography Reports*, 55(4), pp.609–614.
- Lee, J., Hinebaugh, J. & Bazylak, A., 2012. The Impact of an MPL on Water Management of an Operating PEMFC Using Synchrotron X-Ray Radiography. *ASME 2012 10th International Conference on Fuel Cell Science, Engineering and Technology*, p.205.
- Li, A. et al., 2010. Effects of hydrophobicity of the cathode catalyst layer on the performance of a PEM fuel cell. *Electrochimica Acta*, 55(8), pp.2706–2711.
- Li, A. & Chan, S.H., 2013. Understanding the role of cathode structure and property

- on water management and electrochemical performance of a PEM fuel cell. *International Journal of Hydrogen Energy*, 38(27), pp.11988–11995.
- Li, G.C. & Pickup, P.G., 2003. Ionic conductivity of PEMFC electrodes - Effect of Nafion loading. *Journal of the Electrochemical Society*, 150(11), pp.C745–C752.
- Li, H. et al., 2008. A review of water flooding issues in the proton exchange membrane fuel cell. *Journal of Power Sources*, 178(1), pp.103–117.
- Li, W. et al., 2003. Preparation and Characterization of Multiwalled Carbon Nanotube-Supported Platinum for Cathode Catalysts of Direct Methanol Fuel Cells. *The Journal of Physical Chemistry B*, 107(26), pp.6292–6299.
- Li, X., Sabir, I. & Park, J., 2007. A flow channel design procedure for PEM fuel cells with effective water removal. *Journal of Power Sources*, 163(2), pp.933–942.
- Lim, C. & Wang, C.Y., 2004. Effects of hydrophobic polymer content in GDL on power performance of a PEM fuel cell. *Electrochimica Acta*, 49(24), pp.4149–4156.
- Liu, C.-H. et al., 2009. Effect of hydrophobic gas diffusion layers on the performance of the polymer exchange membrane fuel cell. *Journal of Power Sources*, 191(2), pp.489–494.
- Marr, C. & Li, X., 1999. Composition and performance modelling of catalyst layer in a proton exchange membrane fuel cell. *Journal of Power Sources*, 77(1), pp.17–27.
- Martins Belchor, P., Camargo Forte, M.M. & Ortiz Suman Carpenter, D.E., 2012. Parallel serpentine-baffle flow field design for water management in a proton exchange membrane fuel cell. *International Journal of Hydrogen Energy*, 37(16), pp.11904–11911.
- Modestov, A.D. et al., 2009. Influence of Catalyst Layer Binder on Catalyst Utilization and Performance of Fuel Cell with Polybenzimidazole-HPO₄ Membrane. *Journal of The Electrochemical Society*, 156(5), p.B650.
- Mukerjee, S., Srinivasan, S. & Appleby, A.J., 1993. Effect of sputtered film of

- platinum on low platinum loading electrodes on electrode kinetics of oxygen reduction in proton exchange membrane fuel cells. *Electrochimica Acta*, 38(12), pp.1661–1669.
- Nam, J.H. et al., 2009. Microporous layer for water morphology control in PEMFC. *International Journal of Heat and Mass Transfer*, 52(11-12), pp.2779–2791.
- Nasef, M.M. et al., 2000. Cation exchange membranes by radiation-induced graft copolymerization of styrene onto PFA copolymer films. II. Characterization of sulfonated graft copolymer membranes. *Journal of Applied Polymer Science*, 76(1), pp.1–11.
- Nasef, M.M., 2014. Radiation-grafted membranes for polymer electrolyte fuel cells: Current trends and future directions. *Chemical Reviews*, 114(24), pp.12278–12329.
- Nasef, M.M. & Saidi, H., 2002. Post-mortem analysis of radiation grafted fuel cell membrane using X-ray photoelectron spectroscopy. *Journal of New Materials for Electrochemical Systems*, 5(3), pp.183–189.
- Nasef, M.M. & Saidi, H., 2003. Preparation of crosslinked cation exchange membranes by radiation grafting of styrene/divinylbenzene mixtures onto PFA films. *Journal of Membrane Science*, 216(1-2), pp.27–38.
- Nguyen, T. V., Natarajan, D. & Jain, R., 2006. Optimized Catalyst Layer Structure for PEM Fuel Cells. *ECS Transactions*, 1(6), pp.501–508.
- Van Nguyen, T. & Knobbe, M.W., 2003. A liquid water management strategy for PEM fuel cell stacks. *Journal of Power Sources*, 114(1), pp.70–79.
- Owejan, J. et al., 2007. Effects of flow field and diffusion layer properties on water accumulation in a PEM fuel cell. *International Journal of Hydrogen Energy*, 32(17), pp.4489–4502.
- Paganin, V.A. et al., 1998. Modelistic interpretation of the impedance response of a polymer electrolyte fuel cell. *Electrochimica Acta*, 43(24), pp.3761–3766.
- Park, S., Lee, J.W. & Popov, B.N., 2012. A review of gas diffusion layer in PEM fuel cells: Materials and designs. *International Journal of Hydrogen Energy*, 37(7), pp.5850–5865.

- Park, S., Lee, J.W. & Popov, B.N., 2006. Effect of carbon loading in microporous layer on PEM fuel cell performance. *Journal of Power Sources*, 163(1 SPEC. ISS.), pp.357–363.
- Park, S. & Popov, B.N., 2011. Effect of a GDL based on carbon paper or carbon cloth on PEM fuel cell performance. *Fuel*, 90(1), pp.436–440.
- Park, S.B. & Park, Y. il, 2012. Fabrication of gas diffusion layer (GDL) containing microporous layer using flourinated ethylene prophylyene (FEP) for proton exchange membrane fuel cell (PEMFC). *International Journal of Precision Engineering and Manufacturing*, 13(7), pp.1145–1151.
- Pasaogullari, U. & Wang, C.-Y., 2004. Two-phase transport and the role of microporous layer in polymer electrolyte fuel cells. *Electrochimica Acta*, 49(25), pp.4359–4369.
- Pivovar, B.S., 2006. An overview of electro-osmosis in fuel cell polymer electrolytes. *Polymer*, 47(11), pp.4194–4202.
- Pozio, A. et al., 2002. Comparison of high surface Pt / C catalysts by cyclic voltammetry. , 105(May 2001), pp.13–19.
- Prabhuram, J. et al., 2004. Synthesis and physical/electrochemical characterization of Pt/C nanocatalyst for polymer electrolyte fuel cells. *Journal of Power Sources*, 134(1), pp.1–6.
- Qi, Z. & Kaufman, A., 2002. Improvement of water management by a microporous sublayer for PEM fuel cells. *Journal of Power Sources*, 109(1), pp.38–46.
- Rager, T., Schnyder, B. & Tsukada, A., 2002. Radiation-grafted membrane / electrode assemblies with impro v ed interface. , 48, pp.247–254.
- Samms, S., Wasmus, S. & Savinell, R., 1996. Thermal stability of Nafion® in simulated fuel cell environments. *Journal of The Electrochemical Society*, 143(5), pp.1498–1504.
- Şayin, E.S., Bayrakçeken, A. & Eroğlu, İ., 2012. Durability of PEM fuel cell electrocatalysts prepared by microwave irradiation technique. *International Journal of Hydrogen Energy*, 37(21), pp.16663–16672.
- Schmidt, T. & Gasteiger, H., 1998. Characterization of High Surface Area

- Electrocatalysts Using a Rotating Disk Electrode Configuration. *Journal of Electrochemical Society*, 145(7), pp.2354–2358.
- Şengül, E. et al., 2008. Effect of Gas Diffusion Layer Characteristics and Addition of Pore-Forming Agents on the Performance of Polymer Electrolyte Membrane Fuel Cells. *Chemical Engineering Communications*, 196(1-2), pp.161–170.
- Shin, J. et al., 2014. Highly cross-linked poly(styrene sulfonic acid)-grafted poly(tetrafluoroethylene-co-perfluoropropyl vinyl ether) membranes with various thicknesses and their application to direct methanol fuel cell. *High Performance Polymers*, 26(4), pp.488–495.
- Sing, K.S.W., 1985. Reporting physisorption data for gas/solid systems with special reference to the determination of surface area and porosity (Recommendations 1984). *Pure and Applied Chemistry*, 57(4), pp.2201–2218.
- Song, W. et al., 2010. A new hydrophobic thin film catalyst layer for PEMFC. *Solid State Ionics*, 181(8-10), pp.453–458.
- Song, W. et al., 2014. Effect of polytetrafluoroethylene distribution in the gas diffusion layer on water flooding in proton exchange membrane fuel cells. *Chinese Journal of Catalysis*, 35(4), pp.468–473.
- Springer, E. et al., 1996. Characterization of Polymer Electrolyte Fuel Cells Using AC Impedance Spectroscopy. *Journal of The Electrochemical Society*, 143(2), pp.587–599.
- Staiti, P. et al., 1992. Influence of electrodic properties on water management in a solid polymer electrolyte fuel cell. *Journal of Applied Electrochemistry*, 22, pp.663–667.
- Sudarshan, K. et al., 2007. Positron annihilation spectroscopic studies of fluorinated ethylene propylene copolymer-g-polystyrene. *Polymer*, 48(21), pp.6434–6438.
- Therdthianwong, A., Saenwiset, P. & Therdthianwong, S., 2012. Cathode catalyst layer design for proton exchange membrane fuel cells. *Fuel*, 91(1), pp.192–199.
- Thomas, J.M. & Thomas, W.J., 2015. *Principle and Practice of Heterogeneous Catalysis*,
- Ticianelli, E.A. et al., 1988. Methods to Advance Technology of Proton Exchange

- Membrane Fuel Cells. *J. Electrochem. Soc.*, 135(9), p.2209.
- Trabold, T.A. et al., 2006. In situ investigation of water transport in an operating PEM fuel cell using neutron radiography: Part 1 - Experimental method and serpentine flow field results. *International Journal of Heat and Mass Transfer*, 49(25-26), pp.4712–4720.
- Uchida, M., 1996. Effects of Microstructure of Carbon Support in the Catalyst Layer on the Performance of Polymer-Electrolyte Fuel Cells. *Journal of The Electrochemical Society*, 143(7), p.2245.
- Uchida, M., 1995. Investigation of the Microstructure in the Catalyst Layer and Effects of Both Perfluorosulfonate Ionomer and PTFE-Loaded Carbon on the Catalyst Layer of Polymer Electrolyte Fuel Cells. *Journal of The Electrochemical Society*, 142(12), p.4143.
- Vinodh, R. et al., 2010. A novel anion exchange membrane from polystyrene (ethylene butylene) polystyrene: Synthesis and characterization. *Materials Science and Engineering: B*, 167(1), pp.43–50.
- Wagner, N. et al., 1998. Electrochemical impedance spectra of solid-oxide fuel cells and polymer membrane fuel cells. *Electrochim. Acta*, 43(24), pp.3785–3793.
- Wang, L. et al., 2003. A parametric study of PEM fuel cell performances. *International Journal of Hydrogen Energy*, 28(11), pp.1263–1272.
- Wang, X. & Van Nguyen, T., 2010. Modeling the Effects of the Microporous Layer on the Net Water Transport Rate Across the Membrane in a PEM Fuel Cell. *Journal of The Electrochemical Society*, 157(4), p.B496.
- Wang, X.L. et al., 2006. Micro-porous layer with composite carbon black for PEM fuel cells. *Electrochimica Acta*, 51(23), pp.4909–4915.
- Watanabe, M., Tomikawa, M. & Motoo, S., 1985. Experimental analysis of the reaction layer structure in a gas diffusion electrode. *Journal of Electroanalytical Chemistry and Interfacial Electrochemistry*, 195(1), pp.81–93.
- Weber, A.Z. et al., 2014. A Critical Review of Modeling Transport Phenomena in Polymer-Electrolyte Fuel Cells. *Journal of the Electrochemical Society*, 161(12), pp.F1254–F1299.

- Weber, A.Z., Darling, R.M. & Newman, J., 2004. Modeling Two-Phase Behavior in PEFCs. *Journal of The Electrochemical Society*, 151(10), p.A1715.
- Weber, A.Z. & Newman, J., 2005. Effects of Microporous Layers in Polymer Electrolyte Fuel Cells. *Journal of The Electrochemical Society*, 152(4), p.A677.
- Weng, F.B., Su, A. & Hsu, C.Y., 2007. The study of the effect of gas stoichiometric flow rate on the channel flooding and performance in a transparent fuel cell. *International Journal of Hydrogen Energy*, 32(6), pp.666–676.
- Wilson, M. & Gottesfeld, S., 1992. Thin-film catalyst layers for polymer electrolyte fuel cell electrodes. *Journal of applied electrochemistry*, 22(1), pp.1–7.
- Yan, W.M. et al., 2007. Effects of fabrication processes and material parameters of GDL on cell performance of PEM fuel cell. *International Journal of Hydrogen Energy*, 32(17), pp.4452–4458.
- Yan, W.-M. et al., 2010. Optimal microporous layer for proton exchange membrane fuel cell. *Journal of Power Sources*, 195(17), pp.5731–5734.
- Yau, T.C. et al., 2011. Effects of cathode gas diffusion layer design on polymer electrolyte membrane fuel cell water management and performance. *Journal of Power Sources*, 196(22), pp.9437–9444.
- Yuan, X. et al., 2007. AC impedance technique in PEM fuel cell diagnosis-A review. *International Journal of Hydrogen Energy*, 32(17), pp.4365–4380.
- Zhang, J. & Song, C., 2008. Electrocatalytic Oxygen Reduction Reaction. In J. Zhang, ed. *PEM Fuel Cell Electrocatalysts and Catalyst Layers*. London: Springer London, pp. 89–183.
- Zhang, J.Z., Hongsirikarn, K. & Goodwin, J.G., 2011. Effect and siting of Nafion® in a Pt/C proton exchange membrane fuel cell catalyst. *Journal of Power Sources*, 196(19), pp.7957–7966.
- Zhang, W. et al., 2010. Novel ACNT arrays based MEA structure-nano-Pt loaded ACNT/Nafion/ACNT for fuel cell applications. *Chemical communications (Cambridge, England)*, 46(26), pp.4824–4826.

CURRICULUM VITAE

Gokce S. Avcioglu

Chemical Engineering,
Middle East Technical University,
Ankara, 06800, Turkey
+90-312-210-4372
gavcioglu@gmail.com

EDUCATION and TRAINING

PhD, Chemical Engineering,
Middle East Technical University, Ankara, Turkey, September 2016,
Thesis Title:
**‘Characterization and Diagnostic Techniques for Optimization of Water
Management of PEMFC’**
Supervisor; Prof. Dr. Inci Eroglu
Co-supervisor; Asst. Prof. Dr. Berker Ficicilar
CGPA: 3.43/4.00

MSc, Chemical Engineering,
Middle East Technical University, Ankara, Turkey, September 2010
Thesis Title:
**‘Scale up Panel Photobioreactors for Hydrogen Production by PNS
Bacteria’**

Supervisor; Prof. Dr. Inci Eroglu

Co-supervisor; Dr. Ebru Ozgur

CGPA: 3.07/4.00

BSc, Chemical Engineering,

Ankara University, Ankara, Turkey, February 2007

CGPA: 3.07/4.00

High School Diploma,

Icel Anatolian High School, Mersin, Turkey, June 2001

CGPA: 4.14/5.00

RESEARCH EXPERIENCE

Doctoral Researcher, Fuel Cell Research Laboratory, 2010-2016

Department of Chemical Engineering

Middle East Technical University, Ankara, Turkey

Research advisors: Prof. Dr. Inci Eroglu

Asst. Prof. Dr. Berker Ficicilar

Graduate Researcher, Hydrogen Research Laboratory, 2007-2010

Department of Chemical Engineering

Middle East Technical University, Ankara, Turkey

Research advisors: Prof. Dr. Inci Eroglu

Dr. Ebru Ozgur

PUBLICATIONS

Avcioglu S G., Ficicilar B., Eroglu I. Influence of FEP nanoparticles in catalyst layer on water management and performance of PEM fuel cell with high Pt loading. Submitted to International Journal of Hydrogen Energy, (2016)

Avcioglu S G., Ficicilar B., Eroglu I. Effect of PTFE nanoparticles in catalyst layer on PEM fuel cell performance. International Journal of Hydrogen Energy, 41, 10010-10020, (2016)

Avcioglu S G., Ficicilar B., Bayrakceken A., Eroglu I. High performance PEM fuel cell catalyst layers with hydrophobic channels. International Journal of Hydrogen Energy, 40, 7720-7731, (2015)

Avcioglu S.G., Ozgur E., Gunduz U., Yucel M., Eroglu I. Biohydrogen production in an outdoor panel photobioreactor on dark fermentation effluent of molasses. International Journal of Hydrogen Energy, 36(17), 11360-11368, (2011)

ORAL PRESENTATIONS

Avcioglu S.G., Ficicilar B., Eroglu I. Katalizör Tabakasına Eklenen Hidrofobik Nanopartiküllerin PEM Yakıt Piliinde Hidrojen ve Havadan Doğrudan Elektrik elde edilmesine Etkisi, **National Chemical Engineers Congress**, Izmir, Turkey, 2016

Avcioglu S.G., Ficicilar B., Eroglu I. Influence of PTFE Nanoparticles on Mass Transport in High Performance PEM Fuel Cell Electrodes. **21st World Hydrogen Energy Conference**, Zaragoza, Spain, 2016

Avcioglu S.G., Ficicilar B., Eroglu I. Katalizör tabakasına eklenen hidrofobik nanopartiküllerin PEM yakıt pili performansına etkisi. **National Hydrogen Technologies Congress**, Istanbul, Turkey, 2015

Avcioglu S.G., Ficicilar B., Eroglu I. Effect of PTFE nanoparticles in catalyst layer on PEM fuel cell performance. **International Symposium on Materials for Energy Storage and Conversion**, Ankara, Turkey, 2015

Avcioglu S.G., Ozturk A., Ficicilar B., Bayrakceken A., Kincal S., Eroglu I. Experimental and modeling studies on the effect of inclusion of hydrophobic

nanoparticles To catalyst layer for enhanced water management in PEMFCs. **20th World Hydrogen Energy Conference**, Gwangju, Korea, 2014

Avcioglu S.G., Barim B. S., Ficicilar B., Bayrakceken A., Eroglu I. High Performance PEM Fuel Cell Catalyst Layers with Hydrophobic Channels. **13th International Conference on Clean Energy**, Istanbul, Turkey, 2014

Avcioglu S.G., Ozgur E., Gunduz U., Yucel M., Eroglu I. Biohydrogen Production in an Outdoor Panel Photobioreactor on Dark Fermentation Effluent of Molasses by *R. capsulatus* hup-. **International Conference on Hydrogen Production**, Istanbul, Turkey, 2010.

Avcioglu S.G., Androga D.D., Uyar B., Ozgur E., Gunduz U., Yücel M., Eroglu I. Continuous Hydrogen Production by *R. capsulatus* on Acetate in Panel Photobioreactors. **Hydrogen Power Theoretical and Engineering Solutions International Symposium**, Lisbon, Italy, 2009.

POSTER PRESENTATIONS

Avcioglu S.G., Ficicilar B., Bayrakceken A., Eroglu I. Effect of hydrophobic nanoparticles in cathode catalyst layer on PEM fuel cell performance. **20th World Hydrogen Energy Conference**, Gwangju, Korea, 2014

Avcioglu S.G., Ficicilar B., Eroglu I. Multi-step Reaction Mechanisms for Anode and Cathode Electrodes of a H₂/O₂ PEM Fuel Cell. **5th National Catalysis Congress**, Adana, Turkey, 2014

Avcioglu S G., Ficicilar B., Bayrakceken A., Eroglu I. Engineering of PEM Fuel Cell Catalyst Layer with Hydrophobic Nanoparticles. **9th Nanoscience and Nanotechnology Conference**, Erzurum, Turkey, 2013

Avcioglu S.G., Ozkan E., Sagir E., Ozgur E., Gunduz U., Yucel M., Eroglu I. Hydrogen Production in an Outdoor Panel Photobioreactor on Dark Fermentation Effluent of Molasses. **6th Chemical Engineering Conference for Collaborative Research in Eastern Mediterranean Countries**, Antalya, Turkey, 2010

Avcioglu S.G., Androga D.D., Uyar B., Ozgur E., Gunduz U., Yucel M., Eroglu I. Continuous Hydrogen Production by *R. capsulatus* on Acetate in Panel Photobioreactors in Outdoor Conditions. **International Symposium on Biotechnology: Developments and Trends**, Ankara, Turkey, 2009

HONORS and AWARDS

Exceptional Oral Presentation in 20th World Hydrogen Energy Conference, Gwangju, Korea, 2014

Exceptional Poster Presentation in 20th World Hydrogen Energy Conference, Gwangju, Korea, 2014

Thesis of the Year Award, Middle East Technical University, Ankara, Turkey, 2009-2010

FELLOWSHIPS

Doctoral Fellowship, Turkish Scientific and Technological Research Council, TUBITAK Project: 113M205

Doctoral Fellowship, Turkish Scientific and Technological Research Council, TUBITAK Project: 109M221

Graduate Fellowship, HYVOLUTION, the EU 6th Framework Integrated Project: 019825

MEMBERSHIPS

Member, National Association of Hydrogen Energy Technologies, **2015-present**

Student Member, International Association for Hydrogen Energy, **2015-2016**

Member, Turkish Chamber of Chemical Engineers, **2007-present**

REFERENCES

Prof. Dr. Inci Eroglu, Department of Chemical Engineering, Middle East Technical University, ieroglu@metu.edu.tr

Asst. Prof. Dr. Berker Ficilar, Department of Chemical Engineering, On Dokuz Mayis University, berker.ficilar@omu.edu.tr